Applied Surface Science 458 (2018) 446–453

Contents lists available at ScienceDirect

Applied Surface Science

journal homepage: www.elsevier.com/locate/apsusc

Full Length Article

Reducing sheet resistance of self-assembled transparent graphene films by defect patching and doping with UV/ozone treatment

Tijana Tomašević-Ilić[a,*], Đorđe Jovanović[a], Igor Popov[a,b], Rajveer Fandan[c], Jorge Pedrós[c], Marko Spasenović[a], Radoš Gajić[a]

[a] Graphene Laboratory (GLAB) of the Center for Solid State Physics and New Materials, Institute of Physics, University of Belgrade, Pregrevica 118, 11080 Belgrade, Serbia
[b] Institute for Multidisciplinary Research, University of Belgrade, Kneza Višeslava 1, 11030 Belgrade, Serbia
[c] Departamento de Ingeniería Electrónica and Instituto de Sistemas Optoelectrónicos y Microtecnología, Universidad Politécnica de Madrid, Madrid 28040, Spain

ARTICLE INFO

Keywords:
Graphene films
Liquid phase exfoliation
Langmuir-Blodgett assembly
UV/ozone treatment
Defect patching
Transparent conductors

ABSTRACT

Liquid phase exfoliation followed by Langmuir-Blodgett self-assembly (LBSA) is a promising method for scalable production of thin graphene films for transparent conductor applications. However, monolayer assembly into thin films often induces a high density of defects, resulting in a large sheet resistance that hinders practical use. We introduce UV/ozone as a novel photochemical treatment that reduces sheet resistance of LBSA graphene threefold, while preserving the high optical transparency. The effect of such treatment on our films is opposite to the effect it has on mechanically exfoliated or CVD films, where UV/ozone creates additional defects in the graphene plane, increasing sheet resistance. Raman scattering shows that exposure to UV/ozone reduces the defect density in LBSA graphene, where edges are the dominant defect type. FTIR spectroscopy indicates binding of oxygen to the graphene lattice during exposure to ozone. In addition, work function measurements reveal that the treatment dopes the LBSA film, making it more conductive. Such defect patching paired with doping leads to an accessible way of improving the transparent conductor performance of LBSA graphene, making solution-processed thin films a candidate for industrial use.

1. Introduction

Graphene, with its high optical transparency and low sheet resistance, is an excellent choice for transparent electrodes in various optoelectronic devices [1]. For such applications, transparency in the visible part of the spectrum should be above 80%, while the sheet resistance should be low enough for practical use, all while keeping production costs to a minimum. In the past decade, numerous research efforts were performed to achieve production of thin graphene films usable in practical applications [2–4]. Although chemical vapor deposition (CVD) yields graphene sheets of high quality that can be scaled for industrial use [5], the method is generally regarded as costly [6] and alternative methods are being sought that satisfy the quality/cost tradeoff. Liquid phase exfoliation (LPE) [7] is the most perspective way of obtaining large quantities of exfoliated graphite in solution at reasonable production costs. Nevertheless, all solution-processed graphene needs to be controllably assembled into thin films of satisfactory quality for transparent conductor applications. A number of film assembly strategies exist, such as evaporation-based assembly, assisted, and micropatterned assembly [8]. Each specific thickness and arrangement of graphene sheets in a thin film directly affects physical properties of the film [9] and device performance. Langmuir-Blodgett (LB) and Langmuir-Schaefer (LS) deposition, based on surface-tension induced self-assembly of nanoplatelets at an interface of two liquids or a gas and a liquid, are prime candidate methods for production of large-scale, highly transparent thin graphene films [10,11]. However, all self-assembled films suffer from a large density of defects that often leads to a high sheet resistance of deposited film. Conversely, the large defect density offers an opportunity for surface treatment such as annealing, chemical doping and functionalization [3,12], all of which can reduce sheet resistance or produce other desirable effects. The susceptibility of a film to treatment as well as its initial sheet resistance depend on the nature of the prevalent defects, such as impurities, vacancies, nanoplatelet edges, and topological defects, as well as the defect density. For example atoms located at the edges of a graphene sheet exhibit higher reactivity compared to those in the basal plane, making the ratio of the density of edge atoms to basal-plane atoms the determining factor for the efficiency of surface modification [13]. It is thus imperative to carefully study the nature and density of defects in any thin film transparent conductor, especially when considering physical or

* Corresponding author.
E-mail address: ttijana@ipb.ac.rs (T. Tomašević-Ilić).

https://doi.org/10.1016/j.apsusc.2018.07.111
Received 13 March 2018; Received in revised form 3 July 2018; Accepted 16 July 2018
Available online 17 July 2018
0169-4332/

chemical treatment to enhance the film's practical usability.

Here, we report characterization of the defect type of Langmuir-Blodgett self-assembled (LBSA) films from LPE graphene and subsequent defect patching with UV/ozone (UVO) treatment. We observe the effects that photochemical oxidation has on our films exposed to ozone, a very important gas adsorbate that significantly alters the properties of materials through doping, affecting the performance of electronic devices [14–16]. As shown earlier, oxidation spreads from edges inwards across the entire surface of graphene flakes [17]. When applied even for a short time to mechanically exfoliated and monolayer CVD graphene, UVO leads to significant defect generation resulting in an increase of sheet resistance [18,19]. Ozone reacts with the edge sites of CVD graphene until reaching a saturation point. Beyond saturation, the basal plane becomes more susceptible to oxidation, resulting in the replacement and relief of carbon atom defects. We find that nanoplatelet edges are the dominant defect type in our films, in contrast to CVD-grown graphene and earlier reported mechanically exfoliated graphene, where charged impurities and covalently bonded adatoms are the limiting factor for carrier mobility [20]. We treat the film surface with UVO and find that the sheet resistance decreases by a factor of 3, while optical transparency throughout the visible part of the spectrum remains high (> 80%) and virtually unchanged. Measurements of the surface work function indicate that doping is responsible for the decrease in sheet resistance. FTIR spectroscopy confirms formation of oxygen-containing groups after UVO treatment. With a careful analysis of Raman spectra, we find that the density of defects decreases with treatment, yielding an increase in the carrier mean free path, while edges remain the dominant defect type, all indicating that the ozone binds predominantly to the edges of graphene nanoplatelets. We perform the same UVO treatment on CVD graphene and show that on monolayer CVD graphene, UVO has a detrimental effect on sheet resistance. We also treat thick CVD-grown multilayer graphene films, which prove to be robust against UVO treatment, although such films have very low optical transparency. Furthermore, in order to understand the experimental results we theoretically analyze deposition of an ozone molecule on the edges of a wide graphene nanoribbon (GNR) as a nanosystem that well approximates LBSA film. After we determine the deposition mechanism, we present electronic and transport properties of such oxidized ribbons. Hence, transport and work function measurements indicate increased film doping, AFM indicates that no major macroscopically observable morphological changes are made on the film, Raman resolutely points to edge patching as the dominant interaction mechanism, while FTIR shows that oxygen binding to the graphene lattice occurs during treatment. Our experimental study is firmly backed by ab-initio calculations that indicate that ozone species binding to edges will increase film conductivity. We thus conclude that UVO treatment is a good option for reducing sheet resistance of LBSA LPE graphene films, bringing the electronic performance of these sheets closer to that of CVD graphene which is produced at a higher cost.

2. Methods

A graphene dispersion was prepared from graphite powder (Sigma Aldrich, product no. 332461) from a concentration of 18 mg ml^{-1} in N-Methyl-2-pyrrolidone (NMP, Sigma Aldrich, product no. 328634), exposed to 14 h of sonication in a low-power sonic bath. The resulting dispersion was centrifuged for 60 min at 3000 rpm in order to reduce the concentration of unexfoliated graphite. The resulting dispersions were used to form films approximately 3 nm thick by LBSA, in the same way that we demonstrated in our previous work [12,21]. A small amount of graphene dispersion is added to a water-air interface and after the film is formed, it is slowly scooped onto the target substrate (Fig. 1a). Glass and SiO_2/Si are used as substrates.

For single-layer CVD studies, we used commercially available monolayer CVD graphene grown on 20 µm thick copper foil (Graphene Supermarket) and transferred onto SiO_2/Si substrate with a home-built automatic transfer system using ammonium persulfate ($(NH_4)_2S_2O_8$) 0.3 M as copper etchant [22]. For multilayer CVD studies, we used multilayer graphene with an average thickness of 105 nm (about 300 monolayers) grown on 25 µm-thick nickel foil (Graphene Supermarket). We etched away the nickel foil in a 0.25 M solution of ferric chloride ($FeCl_3$) in water, yielding a floating multilayer graphene film which was scooped out of the solution onto a SiO_2/Si substrate in the same way as already reported for multilayer graphene condenser microphones [23].

Photochemical oxidation (UVO treatment) is performed by exposing the graphene films to ultraviolet radiation and ozone for 3, 5, 15 and 30 min at a 50 °C chamber temperature and ambient pressure in a Novascan UV/ozone Cleaner by converting oxygen from ambient air to ozone using a high intensity mercury lamp (Fig. 1b). We perform the treatment in a standard commercially available UVO cleaner and acknowledge that while varying the intensity of the radiation and/or the concentration of ozone gas may lead to interesting results, it will be part of a subsequent study.

For optical characterization, UV–VIS spectra were taken using a Perkin-Elmer Lambda 4B UV/VIS Spectrophotometer. The oxidation process was characterized using a TriVista 557 S&I GmbH Micro Raman spectrometer (λ = 532 nm) at room temperature. FTIR spectra were measured with a Thermo Scientific Nicolet 6700 FT-IR spectrometer in the diffuse reflectance infrared Fourier transform (DRIFT) mode. The resistance of each sample was measured in a two-point probe configuration and the sheet resistance was obtained by considering sample geometry factors. The work function measurement is performed with Kelvin probe force microscopy (KPFM, NTEGRA Spectra), prior to and after photochemical treatment of our graphene films.

The calculations are done using density functional-based tight binding method (DFTB) [24,25] with self-consistent charge correction as implemented in the DFTB+ code [26]. Spin polarization was included in calculations. This method has a proven record of various applications to graphene and graphene nanoribbons [27–30]. Transport properties are calculated by DFTB augmented with the Green's functions formalism [31]. Since the atomic structure of LBSA graphene is dominated by edges, we consider GNR a suitable nanosystem that well approximates the nanoflakes in our experiment. For this purpose we model a wide GNR with width 2 nm. The interaction between electronic clouds of two GNR edges is small for such a wide ribbon, hence its electronic properties are equal to the asymptotic limit of wide ribbons

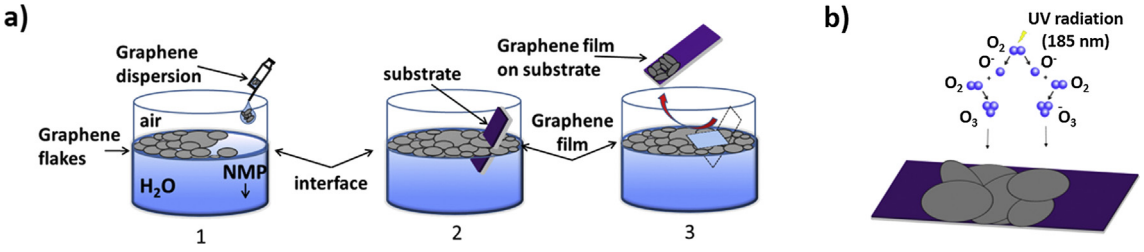

Fig. 1. (a) Schematic of Langmuir-Blodgett self-assembly (LBSA) on a water-air interface (1: film formation, 2: substrate immersion, 3: film deposition), NMP is N-Methyl-2-pyrrolidone; (b) Schematic of film exposure to photochemical oxidation.

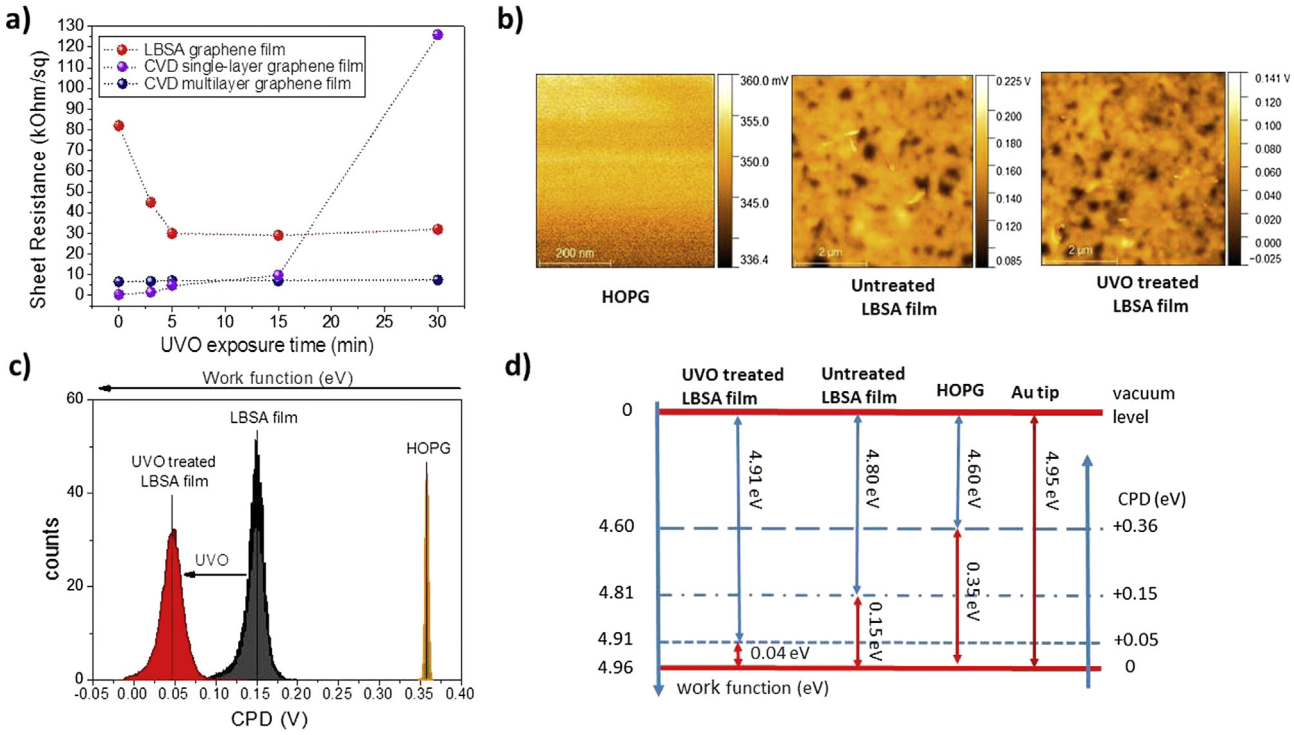

Fig. 2. (a) Sheet resistance of LBSA, CVD-grown single- and multilayer graphene films as a function of UVO exposure time, (b) KPFM map of HOPG, untreated, and UVO treated LBSA film, (c) KPFM histograms of LBSA graphene film before (grey) and after (red) UVO treatment, (c) Schematic of the relation between measured CPDs and their corresponding work functions.

[32]. The periodic (infinite) edges of GNR correspond to the flakes in the experiment, which have large circumferences, i.e. long edges. Utilization of GNR instead of nanoflakes per se is not only physically equivalent but also numerically much more tractable.

3. Results and discussion

Fig. 2a depicts the sheet resistance of graphene films upon exposure to UVO. Prior to exposure, the sheet resistance of LBSA graphene (red circles) is above 80 kΩ/sq. Upon exposure, the sheet resistance decreases rapidly within the first 5 min, reaching a value below 30 kΩ/sq, an approximately 3-fold reduction. At those exposure levels, oxidation reaches a saturation point and remains stable for longer exposure times. Single layer CVD graphene exhibits a pronouncedly different behavior (violet circles), starting from a very low value of sheet resistance which gently rises after 5 mins of exposure, dramatically increasing for longer exposures. After 15 min of treatment, sheet resistance of CVD graphene is still 3–4 times smaller than that of LBSA graphene, whereas after 30 min of exposure LBSA graphene exhibits 4 times smaller sheet resistance. Multilayer CVD graphene (blue circles) has a sheet resistance of ~8 kΩ/sq, which changes only slightly even for long exposures to UVO.

It is expected that CVD graphene compared to LBSA graphene boasts a lower sheet resistance, which is inherently related to carrier mobility. Carrier mobility is inversely proportional to the density of scattering defects, which should be small in CVD graphene. LBSA graphene morphology has an abundancy of nanoplatelet edges [21] that act as scattering centers and have a detrimental effect on initial sheet resistance. However, with UVO treatment, that resistance decreases, pointing to a reaction of ozone with existing defects [17]. On CVD graphene, the few edge sites are quickly fully saturated by ozone molecules, forcing the molecules to deposit their energy by formation of defects or through adsorption, thus creating new point defects on the basal plane, having a detrimental effect on sheet resistance [19]. In multilayer graphene, UVO has little effect on sheet resistance because the ozone molecules react with the top layers only, whereas charge transport takes place through the entire volume of the sheet.

To examine the origins of decreasing sheet resistance with UVO treatment, we measure the surface work function (WF) with KPFM. Fig. 2b depicts KPFM maps of the contact potential difference (CPD)

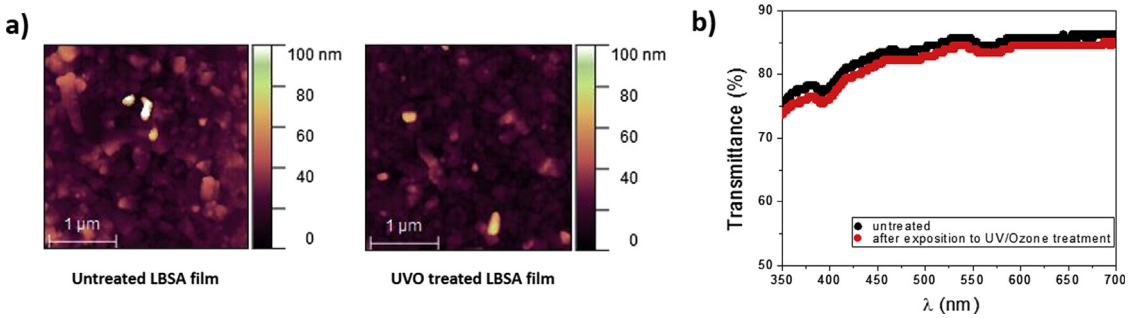

Fig. 3. (a) 3 × 3 μm^2 topograph of HOPG, untreated, and UVO treated LBSA film, (b) Transmittance of a LBSA graphene film in the visible range on a glass substrate, before (black) and after (red) 5 min exposure to UVO.

between the sample and the tip, before and after UVO exposure. Note the different colormap scale, that indicates a lower CPD between the sample and the metallized AFM tip for treated samples compared to untreated samples. To measure the absolute value of the WF, we use as a reference the work function of highly ordered pyrolytic graphite (HOPG), a tabulated value of 4.6 eV [33,34]. In order to determine the average CPD of the measured surface, histograms of KPFM maps were used and fitted to a Gaussian distribution (Fig. 2c). The mean WFs of the tip, HOPG, untreated, and treated films are plotted against the vacuum level in Fig. 2d. The exact procedure is detailed in our previous work [21]. It is evident that UVO increases the WF from 4.8 eV to 4.9 eV, shifting the Fermi level downwards by ~100 meV. It is this additional UVO-induced p-doping that leads to an increased carrier concentration, in turn causing decreased sheet resistance [35].

Aside from improving the sheet resistance, for transparent conductor applications it is important that the optical transparency of the treated film remains high. Fig. 3a depicts AFM topography of the same areas of the film that were used to measure the WF. No difference is observed in the film morphology as an effect of UVO exposure. Fig. 3b depicts the transmittance spectrum of the pristine and treated UVO film. The film has good transparency throughout the visible part of the spectrum, with 80–85% transmittance. The transmittance of the film is barely affected by the treatment. For comparison, monolayer CVD would have transmittance on the order of ~97%, whereas multilayer CVD transmits under 10% of light in the visible, according to manufacturer specifications. Hence, single layer CVD graphene has the overall best performance for transparent conductor applications, although cost remains a limiting factor for wide-scale use, whereas multilayer CVD has little use for such applications due to its low transparency. LBSA graphene holds the middle ground, with acceptable electronic and optical performance (especially after UVO treatment) with projected low costs of fabrication and good scalability. It is important to note that the unchanged transparency coupled with a reduced sheet resistance leads to a threefold increase in the figure of merit (FOM) for transparent conductor applications [36].

Fig. 4 shows FTIR spectra for untreated and UVO treated films. It is clear that the intensities of peaks associated with oxygen-containing groups increase after UVO exposure. We distinguish a change in shape and total peak area of a broad band in the 3000–3700 cm^{-1} region after UVO treatment, corresponding to the presence of hydroxyl and carboxyl groups as well as water. Also, a peak appears at 1825 cm^{-1} after 30 min of UVO exposure indicating the formation of interacting oxygen groups (OH and C═O). Another evident change after 30 min of exposure occurs near 800 cm^{-1}, in a spectral region associated to the formation of epoxides (C—O—C) at graphene edges, according to a previous report [37]. The overlapping spectral features of ethers, epoxides, carboxyles and hydroxyl groups complicate spectral interpretation in the 1000–1300 cm^{-1} region where there is a strong SiO_2 absorption band.

The opposite effect that UVO has on CVD and LBSA graphene demands an inquiry into the effect of reactive site morphology on reactions with ozone. LBSA graphene morphology is dominated by nanoplatelet edge defects, whereas CVD yields graphene that has a few edges, in which chemical reactions should be governed by point defects such as charged impurities and covalently bonded adatoms [36]. To clarify the nature of reactive defects and their evolution during UVO treatment, we apply Raman spectroscopy, a versatile tool for characterization of graphene-based materials [38].

Fig. 5a depicts Raman spectra of LBSA graphene as a function of UVO exposure. The spectra feature four pronounced bands: D at ~1343 cm^{-1}, G at ~1579 cm^{-1}, D' at ~1614 cm^{-1} and the 2D band at ~2694 cm^{-1}. Furthermore, several combinations of these bands are also observed: D + D“ at ~ 2450 cm^{-1} and D + D' at ~2935 cm^{-1} (Fig. 5b), where D” is signature of a phonon belonging to the LA branch, typically observed at ~1100 cm^{-1} [39]. The D and G bands are well resolved for all samples. The 2D peak is a typical signal arising in multilayer graphene. However, Raman spectra show evident changes of the intensity of the D mode with UVO exposure. Fig. 5c depicts the ratio

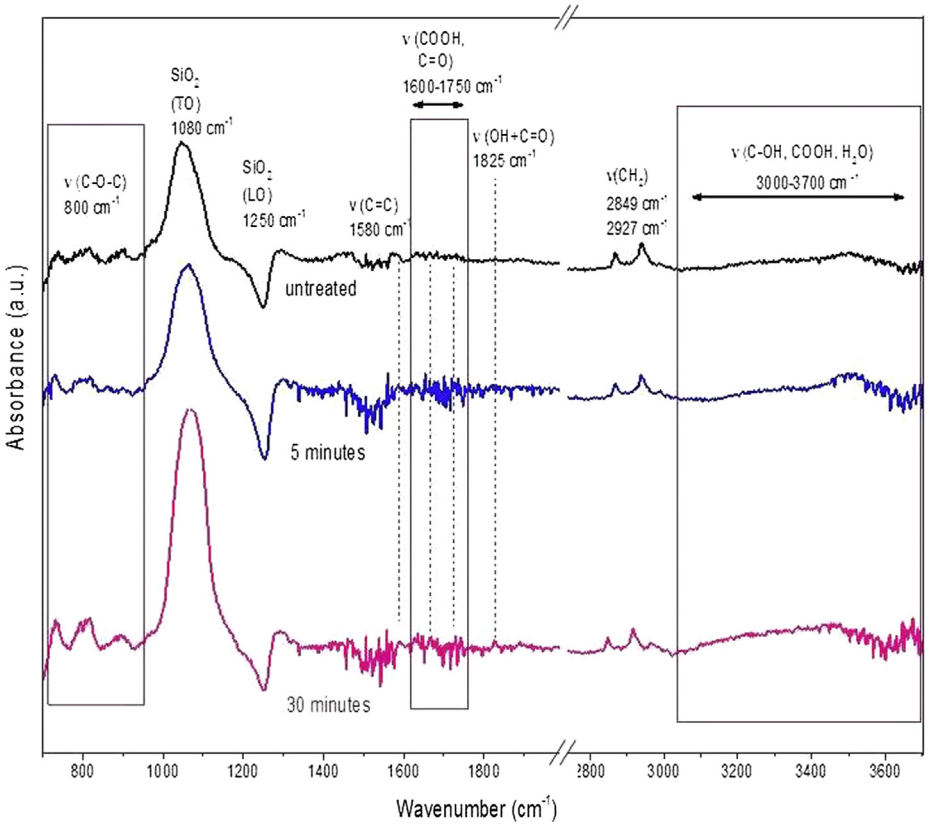

Fig. 4. Reflection infrared spectra of untreated (black), 5 min (blue) and 30 min (pink) UVO exposed LBSA graphene films. We indicate vibrational modes for hydroxyls (possible C—OH, COOH and H_2O contributions) at 3000–3700 cm^{-1}, carbonyl (C═O) and carboxyls (COOH) at 1600–1750 cm^{-1}, sp^2-hybridized (C═C) at 1580 cm^{-1} and epoxides (C—O—C) at 800 cm^{-1}. Vibrational modes of SiO_2 (LO and TO) appear at 1250 and 1080 cm^{-1}, respectively. The areas marked with rectangles are regions in which the most prominent spectral changes occur after UVO exposure.

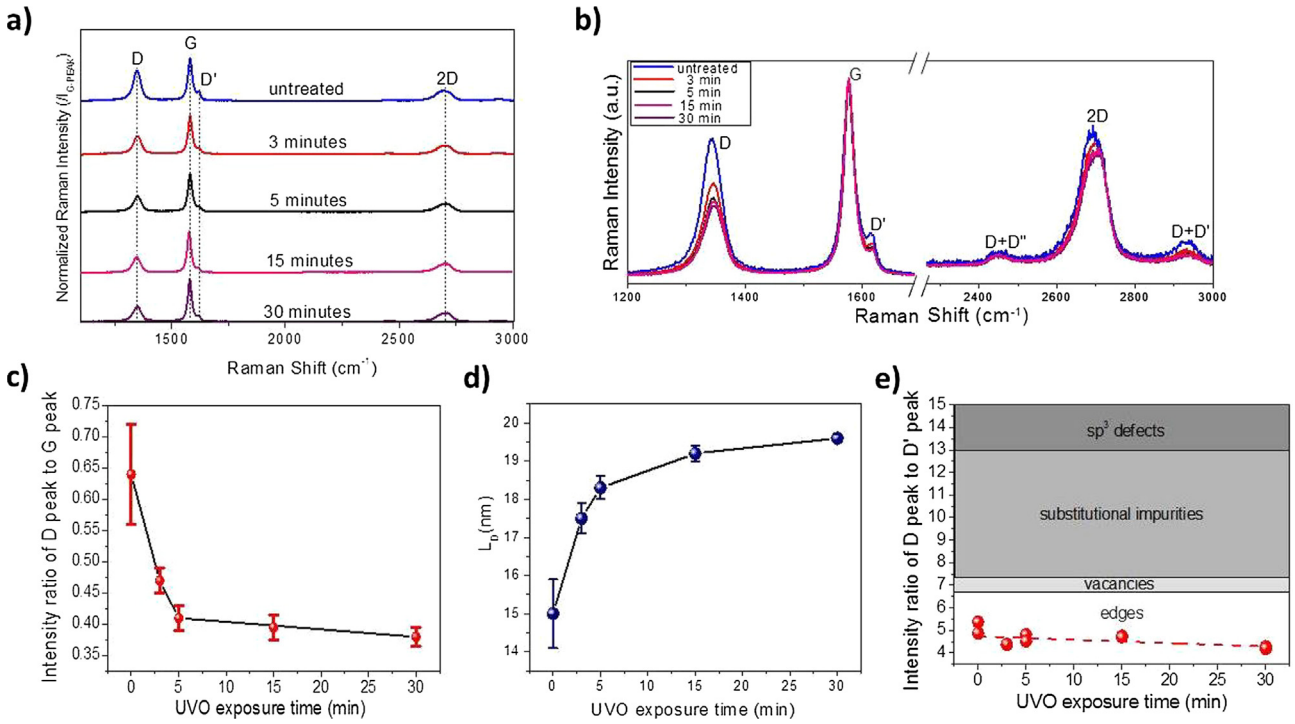

Fig. 5. (a) Representative Raman spectra of LBSA graphene as a function of UVO exposure time. We recorded Raman spectra in various regions to eliminate spot-to-spot variations in the obtained spectra. The spectra show four main bands: D, G, D', and 2D, as well as some weak combinations of these modes. (b) Close-up view of the main bands, (c) The D/G intensity ratio of the films as a function of UVO exposure. The D/G ratio is calculated from integrated peak areas. (d) Interdefect distance as a function of UVO exposure time. The error bar represents the standard deviation of five measurements, (e) The D/D' ratio as a function of UVO exposure time.

of the D peak to the G peak calculated from integrated peak areas, often used to monitor defect evolution in graphene. We observe a large decrease of this ratio during UVO exposure, indicating a reduction in defect density. The D/G intensity ratio evolution shows the same trend as sheet resistance, with a rapid change within the first 5 min of exposure, followed by saturation. The reduction of defect density with UVO exposure in LBSA graphene is opposite from our results on CVD graphene (Figs. S1 and S2) and the literature on monolayer graphene [12,13]. LBSA graphene thus responds in a unique way to an oxidizing environment, with ozone binding to existing defects leading to improved electrical performance.

Supplementary data associated with this article can be found, in the online version, at https://doi.org/10.1016/j.apsusc.2018.07.111.

The ratio I_D/I_G can be converted to the carrier mean free path (L_D), as long as the laser wavelength is known [40]:

$$L_D^2(nm)^2 = (1.8 \pm 0.5) \times 10^{-9} \lambda_L^4 \left(\frac{I_D}{I_G}\right)^{-1} \quad (1)$$

For the wavelength used in this study (λ_L = 532 nm), we plot L_D as a function of exposure time in Fig. 5d. L_D in LBSA graphene increases from 15 nm to 19.5 nm upon UVO exposure, again indicating defect patching. Before and after exposure, the mean free path is smaller than our average flake diameter (previously reported as 120 nm [21]), which points to defects within the nanoplatelets, either through edges of sheets that are stacked on top of each other, or through other point-like defects that we cannot observe with AFM and SEM.

Possible defects in graphene include topological defects (such as pentagon-heptagon pairs), boundaries, vacancies, substitutional impurities, and sp^3 defects [41]. Topological defects have the lowest formation energy [41], and they are always present in LPE graphene sheets as a result of the cavitation process [42]. As the ratio between the intensity of the D and the D' mode is very sensitive to the type of defect, with a value of 3.5 for edges, 7 for vacancies, between 7 and 13 for substitutional impurities, and 13 for sp^3 defects [43,44], we measure this value to deduce the nature of defects in our sample. We observe that the ratio of the D-peak intensity to the D'-peak intensity in our films is nearly constant at a value of 4.8 ± 0.5, regardless of UVO exposure. The measured ratio indicates that edges are the dominant defect type in our films, ruling out vacancies, substitutional impurities, and sp^3 defects, in agreement with previously published data for LPE graphene [42]. There is little change in defect type with photochemical oxidation (Fig. 5e), although the defect density decreases, indicating that ozone most likely reacts with the existing defects and patches them.

In LBSA graphene, flakes may bundle in stacks with varying thickness and lateral dimensions, edge geometries with varying saturation levels (bound oxygen, hydrogen, or other chemical groups), and a wide variety of possible defects. From these virtually infinite possibilities, for our DFTB+ calculation we choose an example of a GNR with bare zig-zag edges and with width of 2 nm. Electronic properties of graphene depend sensitively on physical and chemical modification of edges [45–47]. It was shown that roughness at zig-zag edges does not significantly influence their conductance in contrast to armchair edges [48–50]. The simple choice of a zig-zag GNR is for demonstration purpose only, i.e. to uncover the basic physics of the experimental results, without intent to cover all aspects of the experimental reality. The initial atomic structure consists of the GNR with an ozone molecule placed parallel to the edge. After geometry optimization of the system we obtained a transition configuration (TC) using the dimer method [51]. Optimization of the TC geometry led to the next (meta)stable geometry. The nudged elastic band (NEB) method [52,53] is used for evaluation of the potential barrier between the configurations. Using this procedure we obtained three (meta)stable configurations. The reaction is presented in Fig. 6a and b. Firstly, one of the two O-O bonds in O_3 breaks, which is followed by a rotation of the O—O dimer around a C—C axis by 180°, as illustrated with the insets in Fig. 6a. The product of the reaction is the GNR edge with three separate O adatoms at the nearest sites of the edge (the configuration will be called 3O in the

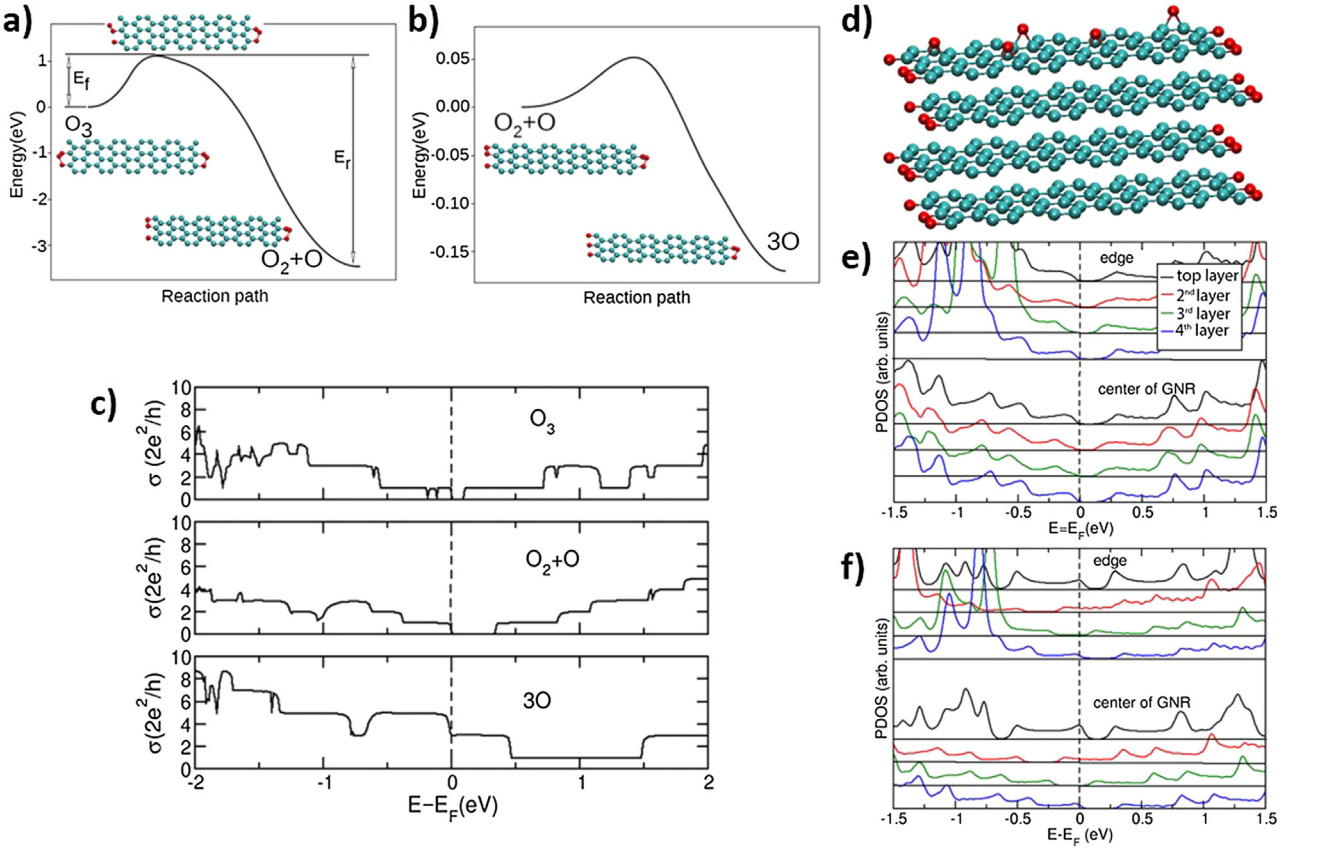

Fig. 6. (a) and (b) Potential energy surface of the cascaded reaction of an O_3 molecule with a GNR zig-zag edge (O_3 configuration). Breaking of an O—O bond in the ozone molecule and rotation of O—O dimer about C-O dimer (transition state), which settles the intermediate (3O) state, are shown in (a). The consequent association of two neighboring O atoms, yielding the O_2 + O configuration, is presented in (b). The reaction is analyzed only on one edge (the left edge in the insets). (c) Conductance at zero bias of the GNR with the three configurations. (d) Illustration of the stack with four layers of GNRs with O_2 + O edge configuration doped in-plane by five oxygen atoms. Projected density of states of the stack without (e) and with (f) in-plane doping. Panels (e) and (f) distinguish contributions to PDOS from GNR edges and lines of central carbon atoms.

remaining text). The potential barrier for the reaction is $E_f = 1.11$ eV, while the energy for the reverse reaction is $E_r = 4.58$ eV. At a temperature of 50 °C, which was used in our experiment, both forward and reverse reactions are impossible. However, the exposure of the sample to UV radiation may assist the reaction. The forward reaction is exothermic with $\Delta E = -3.47$ eV. Two of the three O atoms attached at the edge can associate into an O_2 molecule, as indicated in Fig. 6b. The potential barrier is much smaller in this case, being only $E_f = 0.05$ eV. The reverse reaction is also viable with $E_r = 0.22$ eV. The reaction is exothermic as well, with $\Delta E = -0.17$ eV. The final product of the cascaded reaction consisting of an O_2 molecule and an adatom at the GNR edge will be designated as O_2 + O configuration in following text. Therefore both configurations, O_2 + O and 3O, being nearly isoenergetic, can coexist at the same time. The reaction is somewhat different from the one obtained in [54], but it is expected since the paper considered zig-zag edges in a small hydrogenated carbon cluster in contrast to the infinite ribbon without edge saturation that we consider.

The conductance of the three configurations (the initial O_3 and the two reaction products O_2 + O and 3O) is shown in Fig. 6c. While a pristine zig-zag GNR (not shown in the figure) does not have an electronic band gap, a gap opens upon deposition of O_3 at a GNR edge. We set the Fermi level (E_F) to the top of the valence band in the initial O_3 and O_2 + O configurations. The electronic gaps are around 0.10 eV and 0.35 eV, respectively, whereas the conductance at E_F is one quantum for both cases. This corresponds to a sheet resistance of 12.9 kΩ. Breaking of the O—O bond in the O_2 + O configuration causes a significantly different conductance. The 3O configuration does not exhibit a gap, while the conductance is increased by a factor of 3 or 5, since E_F is positioned at the border of regions with two distinct conductance values. The 3- to 5-fold increase of conductance of a free-standing GNR indicates a possible mechanism of decreasing sheet resistance in our experiment. Note that there is not a one-to-one correspondence between experiment and theory as transport through LBSA graphene is more complex, involving stacks of GNRs with a variety of edges, and transport between stacks which is perhaps based on quantum tunneling. However the increase of conductance is in positive correlation with our experiments. All configurations exhibit p-type doping, in agreement with experiment.

A complete analysis of electronic properties of stacks of flakes (or GNRs) would require consideration of flakes with numerous combinations of edge structures, physical dimensions of flakes and their different mutual orientations, varying number of GNRs in stacks. After obtaining the conductance inside and between stacks a set of stacks could be modeled with an equivalent electrical circuit and their resistance calculated. This comprehensive study will be published elsewhere. Here, for demonstration only, we opt for a single structure, a Bernal stacking of four GNRs with an O_2 + O edge configuration as shown in Fig. 6d. We compare projected density of states (PDOS) of the stack in the plane of the top layer, without and with oxidation in Fig. 6e and f, respectively. The O adatoms responsible for the in-plane oxidation make epoxy groups as found previously in [55]. Upper four subgraphs in each panel represent PDOS at the GNR edge, while the lower four sub-graphs show PDOS at the center of GNR. Colors of the graphs distinguish four GNRs in the stack (named layers in Fig. 5e and f). Both

edges and the middle of GNRs contribute to PDOS in the range from E_F – 0.5 eV to E_F + 0.5 eV. Edges have much larger contributions for energies below E_F – 0.5 eV, hence conductance is expected to be dominated by edges for a bias voltage larger than ~1 V. The stack without in-plane oxidation exhibits a uniform PDOS among layers, with E_F positioned at the top of the valence band. In contrast, the oxidation of the top layer alternatively dopes the layers with p and n character. Since PDOS at E_F is non-zero in three out of four layers, we expect a much larger low-bias conductance of the in-plane oxidized stack than the one without in-plane oxidation. Note that the transport properties analyzed in this section are applicable only to the plane parallel to GNRs in the stack. The conductance in the perpendicular direction has a tunneling character, with expected much larger electric resistance.

4. Conclusion

In contrast to the degrading effects it has on CVD graphene, photochemical oxidation (UV/ozone treatment) of LBSA graphene leads to a decrease in defect density, which together with doping reduces sheet resistance while retaining high optical transparency. We find that edges are the dominant defect type in LBSA graphene, with little influence of other defects such as vacancies, impurities, or sp^3 defects that are common limiting factors for electronic performance of CVD and mechanically exfoliated graphene. Our study thus shows that graphene film morphology and defect landscape play a crucial role in the effect that UV/ozone treatment has on the film. This accessible treatment improves the performance of LBSA graphene, which is key to embedding such materials in durable devices especially those involving direct exposure to ultraviolet radiation and ozone gas. Our novel observation is expected to contribute to the technological acceptance of thin films based on solution-processed 2D materials.

Acknowledgments

This work is supported by the Serbian MPNTR through Projects OI 171005 and III 45018, by Qatar National Research Foundation through Project NPRP 7-665-1-125, and by the Innovation Fund through the Collaborative Grant Scheme. R.F. acknowledges support from European Union's Horizon 2020 Research and Inovation Programme under Marie Sklodowska-Curie Grant Agreement No 642688. J.P. acknowledges support from Spanish MINECO (Grant RyC-2015-18968 and project GRAFAGEN, ENE2013-47904-C3). D. J. And J. P. acknowledge support from the International Erasmus+ project 2015-2-ES01-KA107-022648. We acknowledge Dr. Davor Lončarević for FTIR measurements.

References

[1] F. Bonaccorso, Z. Sun, T. Hasan, A.C. Ferrari, Graphene photonics and optoelectronics, Nat. Photonics 4 (2010) 611–622.
[2] W. Ren, H.M. Cheng, The global growth of graphene, Nat. Nanotech. 9 (2014) 726–730.
[3] Q. Zheng, J.-K. Kim, Graphene for Transparent Conductors: Synthesis, Properties and Applications, Springer, New York, 2015.
[4] I. Banerjee, T. Faris, Z. Stoeva, P.G. Harris, J. Chen, A.K. Sharma, A.K. Ray, Graphene films printable on flexible substrates for sensor applications, 2D Mater. 4 (2017) 015036.
[5] T. Kobayashi, et al., Production of a 100-m-long high-quality graphene transparent conductive film by roll-to-roll chemical vapor deposition and transfer process, Appl. Phys. Lett. 102 (2013) 023112.
[6] E.L. Wolf, Practical Productions of Graphene, Supply and Cost, Applications of Graphene, Springer, New York, 2014, pp. 19–38.
[7] C. Backes, T.M. Higgins, A. Kelly, C. Boland, A. Harvey, D. Hanlon, J.N. Coleman, Guidelines for exfoliation, characterization and processing of layered materials produced by liquid exfoliation, Chem. Mater. 29 (2017) 243–255.
[8] J. Zhu, M.C. Hersam, Assembly and electronic applications of colloidal nanomaterials, Adv. Mater. 29 (2017) 1603895.
[9] S. Craciun, M. Russob, S. Yamamotoc, Taruchac, Tuneable electronic properties in graphene, Nano Today 6 (2011) 42–60.
[10] X. Li, G. Zhang, X. Bai, X. Sun, X. Wang, E. Wang, H. Dai, Highly conducting graphene sheets and Langmuir-Blodgett films, Nat. Nanotech. 3 (2008) 538–542.
[11] S.-K. Lee, H.Y. Jang, S. Jang, E. Choi, B.H. Hong, J. Lee, S. Park, J.-H. Ahn, All graphene-based thin film transistors on flexible plastic substrates, Nano Letters 12 (2012) 3472–3476.
[12] T. Tomašević-Ilić, J. Pešić, I. Milošević, J. Vujin, A. Matković, M. Spasenović, R. Gajić, Transparent and conductive films from liquid phase exfoliated graphene, Opt. Quant. Electron. 48 (2016) 319.
[13] M.R. Axet, R.R. Bacsa, B.F. Machado, P. Serp, Adsorption on and Reactivity of Carbon Nanotubes and Graphene, in: F. D'Souza, K.M. Kadish (Eds.), Handbook of Carbon Nano Materials, Volume 5: Graphene — Fundamental Properties, World Scientific, Singapore, 2014, pp. 39–183.
[14] I. Nasrallah, K.K. Banger, Y. Vaynzof, M.M. Payne, P. Too, J. Jongman, J.E. Anthony, H. Sirringhaus, Effect of ozone on the stability of solution-processed anthradithiophene-based organic field-effect transistors, Chem. Mater. 26 (2014) 3914–3919.
[15] P.J.D. Peterson, A. Aujla, K.H. Grant, A.G. Brundle, M.R. Thompson, J.V. Hey, R.J. Leigh, Practical use of metal oxide semiconductor gas sensors for measuring nitrogen dioxide and ozone in Urban environments, Sensors 17 (2017) 1653.
[16] Y. Xia, Y. Pan, H. Zhang, J. Qiu, Y. Zheng, Y.H. Chen, W. Huang, Graphene oxide by UV-Ozone treatment as efficient hole extraction layer for highly efficient and stable polymer solar cells, ACS Appl. Mater. Interfaces 9 (2017) 26252–26256.
[17] J.P. Froning, P. Lazar, M. Pykal, Q. Li, M. Dong, R. Zboril, M. Otyepka, Direct mapping of chemical oxidation of individual graphene sheets through dynamic force measurements at the nanoscale, Nanoscale 9 (2017) 119.
[18] E.X. Zhang, A.K.M. Newaz, B. Wang, C.X. Zhang, D.M. Fleetwood, K.I. Bolotin, R.D. Schrimpf, S.T. Pantelides, M.L. Alles, Ozone-exposure and annealing effects on graphene-on-SiO_2 transistors, Appl. Phys. Lett. 101 (2012) 121601.
[19] S. Zhao, P. Sumedh, S.P. Surwade, Z. Li, H. Liu, Photochemical oxidation of CVD-grown single layer graphene, Nanotechnology 23 (2012) 355703.
[20] N.M.R. Peres, Colloquium: The transport properties of graphene: An introduction, Rev. Mod. Phys. 82 (2010) 2673–2700.
[21] A. Matkovic, et al., Enhanced sheet conductivity of Langmuir-Blodgett assembled graphene thin films by chemical doping, 2D Mater. 3 (2016) 015002.
[22] A. Bosca, J. Pedros, J. Martínez, T. Palacios, F. Calle, Automatic graphene transfer system for improved material quality and efficiency, Sci. Reports 6 (2016) 21676.
[23] D. Todorović, A. Matković, M. Milićević, D. Jovanović, R. Gajić, I. Salom, M. Spasenović, Multilayer graphene condenser microphone, 2D Mater. 2 (2015) 045013.
[24] D. Porezag, T. Frauenheim, T. Kohler, G. Seifert, R. Kaschner, Construction of tight-binding-like potentials on the basis of density-functional theory: application to carbon, Phys. Rev. B 51 (1995) 12947.
[25] G. Seifert, D. Porezag, T. Frauenheim, Calculations of molecules, clusters, and solids with a simplified LCAO-DFT-LDA scheme, Int. J. Quantum Chem. 58 (1996) 185.
[26] B. Aradi, B. Hourahine, T. Frauenheim, DFTB+, a sparse matrix-based implementation of the DFTB method, J. Phys. Chem. 111 (2007) 5678.
[27] A. Zobelli, V. Ivanovskaya, P. Wagner, I.S. -Martinez, A. Yaya, C.P. Ewels, A comparative study of density functional and density functional tight binding calculations of defects in graphene, Phys. Stat. Sol. 249 (2012) 276.
[28] I. Popov, I. Đurišić, M. Belić, Designing topological defects in 2D materials using scanning probe microscopy and a self-healing mechanism: a density functional-based molecular dynamics study, Nanotechnology 28 (2017) 495706.
[29] E. Erdogan, I. Popov, C.G. Rocha, G. Cuniberti, S. Roche, G. Seifert, Engineering carbon chains from mechanically stretched graphene-based materials: Phys, Rev. B 83 (2011) 041401.
[30] E. Erdogan, I. Popov, G. Seifert, Robust electronic and transport properties of graphene break nanojunctions, Phys. Rev. B 83 (2011) 245417.
[31] S. Datta, Electronic Transport in Mesoscopic Systems, Cambridge University Press, Cambridge, 1997.
[32] Y.-W. Son, M.L. Cohen, S.G. Louie, Energy Gaps in Graphene Nanoribbons, Phys. Rev. Lett. 97 (2006) 216803.
[33] Y.-J. Yu, Y. Zhao, S. Ryu, L.E. Brus, K.S. Kim, P. Kim, Tuning the graphene work function by electric field effect, Nano Letters 9 (2009) 3430–3434.
[34] T. Takahashi, H. Tokailin, T. Sagawa, Angle-resolved ultraviolet photoelectron spectroscopy of the unoccupied band structure of graphite, Phys. Rev. B 32 (1985) 8317.
[35] A. Kasry, M.A. Kuroda, G.J. Martyna, G.S. Tulevski, A.A. Bol, Chemical doping of large-area stacked graphene films for use as transparent conducting electrodes, ACS Nano 4 (2010) 3839–3844.
[36] S. De, J.N. Coleman, Are there fundamental limitations on the sheet resistance and transmittance of thin graphene films? ACS Nano 4 (2010) 2713–2720.
[37] M. Acik, G. Lee, C. Mattevi, A. Pirkle, R.M. Wallace, M. Chhowalla, K. Cho, Y. Chabal, The role of oxygen during thermal reduction of graphene oxide studied by infrared absorption spectroscopy, J. Phys. Chem. C 115 (2011) 19761–19781.
[38] A.C. Ferrari, D.M. Basko, Raman spectroscopy as a versatile tool for studying the properties of graphene, Nat. Nanotech. 8 (2013) 235–246.
[39] L.G. Concado, A. Jorio, E.H. Martins Ferreira, F. Stavale, C.A. Achete, R.B. Capaz, M.V.O. Moutinho, A. Lombardo, T.S. Kulmala, A.C. Ferrari, Quantifying defects in graphene via raman spectroscopy at different excitation energies, Nano Letters 11 (2011) 3190–3196.
[40] L.E.F. Foa Torres, Stephan Roche, J.-C. Charlier, Introduction to Graphene-Based Nanomaterials: From Electronic Structure to Quantum Transport, Cambridge University Press Cambridge, 2014.
[41] L. Li, S. Reich, J. Robertson, Defect energies of graphite: density-functional calculations, Phys. Rev. B 72 (2005) 184109.
[42] M.V. Bracamonte, et al., On the nature of defects in liquid-phase exfoliated graphene on the nature of defects in liquid-phase exfoliated graphene, J. Phys. Chem. C 118 (2014) 15455–15459.
[43] A. Eckmann, A. Felten, A. Mishchenko, L. Britnell, R. Krupke, K.S. Novoselov,

C. Casiraghi, Probing the nature of defects in graphene by raman spectroscopy, Nano Letters 12 (2012) 3925–3930.
[44] A. Eckmann, A. Felten, I. Verzhbitskiy, R. Davey, C. Casiraghi, Raman study on defective graphene: effect of the excitation energy, type, and amount of defects, Phys. Rev. B 88 (2013) 035426.
[45] O. Hod, V. Barone, J.E. Peralta, G.E. Scuseria, Enhanced half-metallicity in edge-oxidized zigzag graphene nanoribbons, Nano Letters 7 (2007) 2295.
[46] G. Lee, K. Cho, Electronic structures of zigzag graphene nanoribbons with edge hydrogenation and oxidation, Phys. Rev. B 79 (2009) 165440.
[47] F.C. Sodi, G. Csanyi, S. Piscanec, A.C. Ferrari, Edge-functionalized and substitutionally doped graphene nanoribbons: Electronic and spin properties, Phys. Rev. B 77 (2008) 165427.
[48] D.A. Areshkin, D. Gunlycke, C.T. White, Ballistic transport in graphene nanostrips in the presence of disorder: importance of edge effects, Nano Letters 7 (2007) 204.
[49] F.M. Royas, D. Jacob, J.F. Rossier, J.J. Palacios, Coherent transport in graphene nanoconstrictions, Phys. Rev. B 74 (2006) 195417.
[50] T.C. Li, S.-P. Lu, Quantum conductance of graphene nanoribbons with edge defects, Phys. Rev. B 77 (2008) 085408.
[51] G. Henkelman, H. Jonsson, A dimer method for finding saddle points on high dimensional potential surfaces using only first derivatives, J. Chem. Phys. 111 (1999) 7010.
[52] H. Jonsson, G. Mills, K.W. Jacobsen, Nudged elastic band method for finding minimum energy paths of transitions, in: B.J. Berne, G. Cicotti, D.F. Coker (Eds.), Classical and Quantum Dynamics in Condensed Phase Systems, World Scientific, Singapore, 1998, pp. 385–404.
[53] G. Henkelman, B.P. Uberuaga, H. Jonsson, A climbing-image NEB method for finding saddle points and minimum energy paths, J. Chem. Phys. 113 (2000) 9901.
[54] K. Xu, P.D. Ye, Theoretical study on the oxidation mechanism and dynamics of the zigzag graphene nanoribbon edge by oxygen and ozone, J. Phys. Chem. C 118 (2014) 10400–10407.
[55] Ž. Šljivančanin, A.S. Milošević, Z.S. Popović, F.R. Vukajlović, Binding of atomic oxygen on graphene from small epoxy clusters to a fully oxidized surface, Carbon 54 (2013) 482.

Applied Surface Science 710 (2025) 163753

Contents lists available at ScienceDirect

Applied Surface Science

journal homepage: www.elsevier.com/locate/apsusc

Unraveling the effects of terbium doping on the electronic structure and conductivity of $BiFeO_3$ thin films

Bojan Stojadinović [a,*], Igor Popov [b], Borislav Vasić [a], Dejan Pjević [c], Milena Rosić [c], Nenad Tadić [d], Zorana Dohčević-Mitrović [a]

[a] Institute of Physics Belgrade, University of Belgrade, Pregrevica 118, 11080 Belgrade, Serbia
[b] Institute for Multidisciplinary Research, University of Belgrade, Kneza Višeslava 1, 11000 Belgrade, Serbia
[c] "Vinča" Institute of Nuclear Sciences, National Institute of the Republic of Serbia, University of Belgrade, Mike Petrovića Alasa 12-14, 11351 Belgrade, Serbia
[d] Faculty of Physics, University of Belgrade, Studentski trg 12-16, 11000 Belgrade, Serbia

ARTICLE INFO

Keywords:
$BiFeO_3$ thin films
Tb doping
Oxygen vacancies
Conductivity
Electronic structure
Density functional theory (DFT)

ABSTRACT

The structural and electrical properties of sol–gel synthetized $Bi_{1-x}Tb_xFeO_3$ films (x = 0, 0.05, 0.1, 0.2) were analyzed combining experimental observations and density functional theory, with an aim to elucidate the influence of Tb dopant on conduction properties of the films. $Bi_{1-x}Tb_xFeO_3$ films have a rhombohedral crystal structure, as identified from X-ray diffraction and Raman spectroscopy. Raman and X-ray photoelectron spectroscopy revealed that 10% Tb-doped film had significantly lower concentration of oxygen vacancies. This sample showed notably lower leakage current compared to other ones. Conductive atomic force microscopy measurements confirmed the lowest conductivity of 10% Tb-doped film. Density functional theory calculations provide atomic-level insights into the electronic structure and are consistent with experimental findings. Undoped and ~5% doped films are conductive due to high density of surface oxygen vacancy conducting states, whereas the conductivity of ~20% Tb-doped film originates from increased density of Tb conductive states near the Fermi level. In contrast, in ~10% Tb-doped film, lack of states responsible for electronic transport was found. These results highlight the necessity of judicious selection of doping concentrations to suppress vacancy-assisted as well as dopant-induced conduction paths and provide valuable guidelines for designing future $BiFeO_3$-based multiferroic materials with high resistivity.

Contents

* Corresponding author.
E-mail address: bojans@ipb.ac.rs (B. Stojadinović).

https://doi.org/10.1016/j.apsusc.2025.163753
Received 10 April 2025; Received in revised form 22 May 2025; Accepted 5 June 2025
Available online 4 July 2025

1. Introduction

Bismuth ferrite ($BiFeO_3$) is a notable room temperature multiferroic material, exhibiting both ferroelectricity and G-type antiferromagnetism, as well as, weak ferromagnetism and coupling between ferroelectricity and ferro/antiferromagnetism [1–3]. With high Curie and Néel temperatures ($T_C \approx 830$ °C and $T_N \approx 370$ °C), it is highly suitable for the applications in next generation of ferroelectric random access memory (FeRAMs) and magnetoresistive random-access memory (MRAM) devices, but can also be a promising material for spintronic devices such as novel types of magnetoelectric sensors and magnetoelectric random access memories (MERAM) [2–6].

However, the major issue for the practical application of $BiFeO_3$ is large leakage current density which mainly originates from Bi volatility and formation of oxygen vacancies or presence of impurity phases, responsible for the deterioration of multiferroic features of $BiFeO_3$ [7–9]. An effective way to suppress the high leakage current and improve the multifunctional properties of $BiFeO_3$ is the partial substitution of rare-earth ions at Bi sites. It is documented that rare-earth ion doping prevents the volatilization of Bi atoms and creation of oxygen vacancies and other impurity phases, enhancing the resistive properties of $BiFeO_3$ [9–15]. Nevertheless, some authors have shown that doping with rare earth elements more than 20% can deteriorate the electric properties of $BiFeO_3$ [16]. Among the rare-earth elements, terbium (Tb) doping has gained attention for its ability to suppress the formation of oxygen vacancies and impurity phases, thereby enhancing ferroelectric or ferromagnetic characteristics of $BiFeO_3$ thin films and nanostructures [8,17–20]. However, higher Tb doping (≥ 10%) causes structural phase transition, when improved ferroelectric characteristics weaken [20,21].

The conductivity properties of Tb-doped $BiFeO_3$ are controversial. Some authors stated that for $BiFeO_3$ nanowires [8] and thin films [20], leakage current continuously decreases with increasing of Tb content up to 15%. When the substitution exceeds 15% of Tb, the leakage current increases approaching the value of undoped $BiFeO_3$ [20]. The other authors claimed that only 5 or 10 (11)% of Tb doping of $BiFeO_3$ thin films led to the reduction of leakage current [19,22,23]. These findings suggest that Tb doping of $BiFeO_3$ can mitigate defect-related conduction, but the conductivity is strongly dependent on dopant concentration and structural modifications and therefore warrants further investigation.

Previous conductivity measurements were mostly performed on a macroscopic scale. However, these measurements often fail to reveal important local variations in conductivity. Such local conductivity measurements can be performed using conductive atomic force microscopy (C-AFM), but its application to $BiFeO_3$ films has been scant [24,25]. In above mentioned papers structural, electrical, magnetic and ferroelectric properties of Tb-doped $BiFeO_3$ have been widely studied, but to the best of our knowledge the density functional theory (DFT) calculations of Tb influence on electronic structure of $BiFeO_3$ have not been performed. These calculations are useful to predict the role of dopant and defects i.e. how their position within the crystal lattice and concentration will play on conductivity.

This study investigates the effect of Tb doping on structural, morphological and conductivity properties of $BiFeO_3$ thin films, combining several experimental techniques and DFT calculations of electronic structure. We discussed the relations between dopant and vacancy concentrations on one hand and electronic properties on the other hand, which gave us an in-depth understanding of our experimental results. By correlating the above-mentioned findings, we aim to clarify the mechanisms responsible for the significant improvement in electrical performance of the 10% Tb-doped $BiFeO_3$ film, in order to optimize $BiFeO_3$-based materials for advanced multiferroic applications.

2. Methods

2.1. Materials synthesis

$Bi_{1-x}Tb_xFeO_3$ thin films were prepared using the sol–gel spin coating process. Knowing from the literature that the solubility limit of Tb is between 15 and 20% [8,26], $BiFeO_3$ films were doped with 5, 10 and 20% of Tb. The following reagents were used: bismuth nitrate pentahydrate ($Bi(NO_3)_3{\cdot}5H_2O$, Sigma-Aldrich), terbium nitrate hexahydrate ($Tb(NO_3)_3{\cdot}6H_2O$, Sigma-Aldrich), iron nitrate nonahydrate ($Fe(NO_3)_3{\cdot}9H_2O$, Sigma-Aldrich), and glacial acetic acid (CH_3COOH, Merck Millipore). The reagents were dissolved in acetic acid and mixed under constant magnetic stirring for 30 min. Films were deposited onto FTO glass (Fluorine doped Tin Oxide coated glass slide). substrates from the prepared solution using sol–gel spin coating. Depositions were carried out at 1000 rpm for 30 seconds using a Laurell WS-650-23 Spin Coater. The films were dried for 40 min at 150 °C, followed by heat treatment at 550 °C for 2 h.

2.2. Structural and morphological characterization

The crystalline structure of $Bi_{1-x}Tb_xFeO_3$ thin films has been investigated using a Rigaku Ultima IV diffractometer, equipped with Cu $K\alpha_{1,2}$ radiations and operating at 40 kV and 40 mA in the 2θ range of 20° to 80° in a continuous scan mode with a scanning step size of 0.05° and a scan rate of 1°/min. Thin films were analyzed using X-ray diffraction at a grazing incidence angle of 0.5°, a technique known as Grazing Incidence X-ray Diffraction (GIXRD). This method was chosen to improve the signal quality. By using a small angle, we get better X-ray penetration into the film, which enhances the resolution of the diffraction pattern and gives us clearer details about the film's structure and crystallinity. The PDXL2 (Ver. 2.8.4.0) software was used to evaluate the phase composition and identification [27]. All obtained thin films were identified using the ICDD database [28] and the ICSD database [29]. GIXRD pattern analysis was performed using the software package Powder Cell [30,31]. The TCH pseudo-Voigt profile function gave the best fit to the experimental X-ray data. Crystallite sizes and microstrain were estimated from the GIXRD data using the Williamson-Hall method [32]. Micro-Raman spectra of thin films of $Bi_{1-x}Tb_xFeO_3$ were collected in a backscattering configuration using a Jobin Yvon T64000 triple spectrometer, with the spectral resolution of 2 cm^{-1}. The argon/krypton ion laser with an emitting line at $\lambda = 514.5$ nm was used as an excitation source, with the output laser power less than 2 mW to avoid the heating effects and/or sample degradation.

All atomic force microscopy measurements were done using Ntegra Prima system from NT-MDT. Topographic imaging of samples was done in tapping mode using SCOUT 350 RAI probes from NUNANO. Based on these images, we calculated surface roughness (from the images with 30 × 30 μm^2 scan size), and grain size distributions (from the images with 2 × 2 μm^2 scan size).

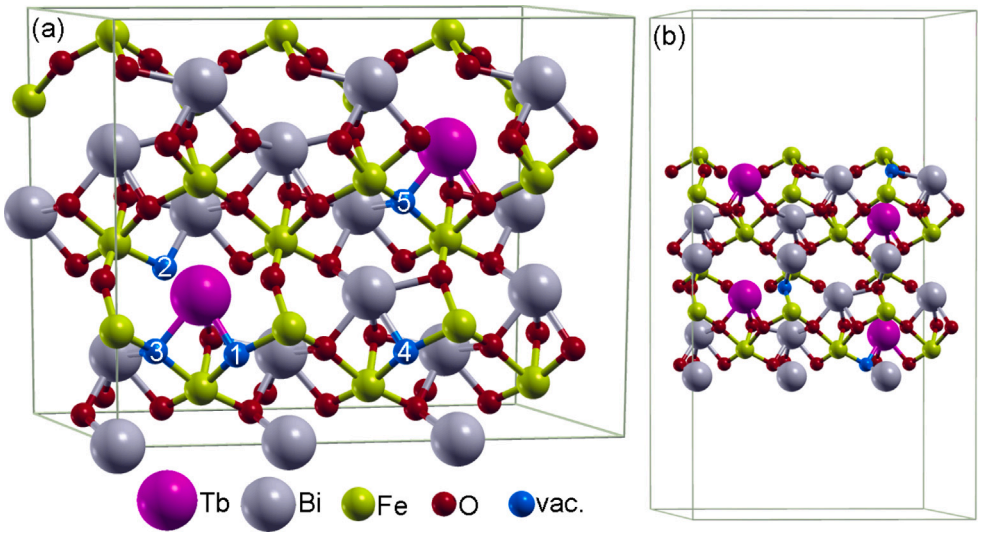

Fig. 1. (a) Perspective view of the conventional unit cell with considered positions of terbium dopants (pink spheres) and oxygen vacancies (blue spheres). (b) The surface supercell. Green lines indicate the boundaries of the bulk and surface supercells.

2.3. Macroscopic and microscopic leakage current measurements

The leakage current of $Bi_{1-x}Tb_xFeO_3$ films was measured by macroscopic, as well as microscopic electrical measurements. Macroscopic I–V curves were measured using a Keithley 2450 Source Meter, with the voltage varied from −3 V to 3 V, providing leakage current density as a function of voltage.

Local electrical currents (microscopic measurements) of investigated samples were measured using C-AFM and platinum coated AFM probes CSG10/Pt. The measurements were done by recording the electrical current through the conductive probes during scanning in contact mode, while a DC bias voltage was applied to the conductive FTO glass substrate (conductive AFM probe was virtually grounded). In order to get statistical information about conductivity from two dimensional current maps, we determined a conductive surface in percents in the following way. For each current map, we first calculated a bearing ratio curve which corresponds to the cumulative probability density function. Each point on this curve gives the percentage of points (y-axis) in the considered current map with a current below the value specified on the x-axis. The current map is taken as conductive if the current measured at this point is above the threshold defined as 10 pA or 50 pA. Therefore, the conductive surface in percents was obtained from bearing ratio curves by calculating percents of points with the current above the specified threshold current.

2.4. X-ray photoelectron spectroscopy

Chemical analysis of the $Bi_{1-x}Tb_xFeO_3$ thin films was performed by X-ray photoelectron spectroscopy (XPS). SPECS System with XP50M X-ray source for Focus 500 and PHOIBOS 100/150 analyzer was employed, operating at 12.5 kV and 250 W. Excitation of the spectra was performed with monochromatic Al Kα radiation (1486.7 eV). Survey spectra were recorded in the range of 800-0 eV, with constant pass energy of 40 eV, step size 0.5 eV and dwell time of 0.2 s in the fixed analyzer transmission (FAT) mode. High resolution spectra of Fe 2p, O 1s and C 1s peaks were recorded with constant pass energy of 20 eV, step size of 0.1 eV and dwell time of 2 s in the FAT mode. Instrument base pressure was ~10^{-9} mbar during the experiments. To minimize the effect of charging at samples, electron flood gun (SPECS FG15/40) was used for charge neutralization, and all peak positions were referenced to C 1s at 284.8 eV. The data was analyzed after Shirley-type background subtraction, and by using CasaXPS software package. The fitting of high-resolution spectra was conducted with a Gaussian/Lorentzian (70/30) product formula for peak shapes. For the Fe 2p spectra, area constraints were applied to ensure a 2:1 ratio between the 2p3/2 and 2p1/2 peaks.

2.5. Theoretical calculations

2.5.1. Parameters used in DFT calculations

Density functional theory calculations were performed using SIESTA software [33] with the Perdew–Burke–Ernzerhof (PBE) form of the generalized gradient approximation (GGA) of exchange–correlation functional [34], norm-conserving Troullier–Martins pseudopotentials [35], and a double-ζ basis including polarization orbitals. Since GGA does not always describe well transition metals and lanthanoids, we employed GGA+U functionals [36–38], which proved efficient in our previous studies [39,40]. We used a Hubbard parameter U_{eff} = 3.8 eV for the Fe 3d orbital, U_{eff} = 0.95 eV for the Fe 4s orbital, and U_{eff} = 2.5 eV for Tb 4f orbital. The reciprocal space was sampled with a 2 × 8 × 2 k-point mesh for geometry optimizations and refined to 10 × 16 × 10 for calculations of electronic properties. A real-space sampling cut-off energy of 350 Ry was used. To achieve atomic geometries where maximum atomic forces do not exceed 0.05 uniteV/Å, we integrated several optimization methods: conjugate gradient, FIRE [41], L-BFGS [42], and a modified Broyden algorithm [43]. Each method was allowed to proceed up to 600 steps; if convergence failed, the structure with minimal atomic forces served as the initial point for subsequent method. Due to difficulties to achieve convergence of atomic forces, we applied constrained optimization on some structures containing vacancies, allowing only atoms adjacent or second-nearest neighbors to vacancies and dopants to move while other atoms remained fixed. Moreover, since a lattice parameter change of 0.33% between crystals with 0% and 10% doping levels was experimentally observed, close to the accuracy limit of our DFT method with pseudopotentials, we fixed the lattice parameters in our calculations to their experimental values. We investigated the type G antiferromagnetic (AFMG) ordering, which is the most prevalent in $BiFeO_3$ crystal.

2.5.2. Model of atomic structure and structural relaxation

Studying both bulk and surface structures in materials like $BiFeO_3$ doped with terbium is essential for a comprehensive understanding of their properties and behavior. The bulk structure provides fundamental information about the intrinsic material properties. However, surfaces and interfaces can exhibit distinct behaviors due to altered coordination

environments. These effects are critical for understanding phenomena like charge transport, which is often dominated by surface states.

To simulate materials approximating experimental doping levels of 5%, 10%, and 20%, we used a supercell containing 18 Bi atoms, with one, two, or four Tb atoms substituted for Bi atoms at respective concentrations of 5.5%, 11.1%, and 22.2%. A larger supercell would more accurately match the desired doping levels but at the expense of significantly increased DFT computational time. The conventional unit cell of terbium-doped $BiFeO_3$ is depicted in Fig. 1(a). It was formed by $3 \times 1 \times 1$ replication of the hexagonal unit cell. The supercell has lattice parameters a = 16.65 Å, b = 5.55 Å, and c = 13.84 Å. For relatively small b lattice parameter, terbium dopants form chains; however, the dispersion of terbium electronic bands is minimal, as discussed later, indicating negligible Tb–Tb coupling in these chains.

In addition to terbium doping, we introduced oxygen vacancies in $BiFeO_3$. We analyzed combinations of 0.0%, 5.5% (1 Tb dopant per supercell), and 11.1% (2 Tb dopants per supercell) doping levels in conjunction with 0.0%, 1.9% (one vacancy per supercell), and 3.8% O vacancies (two vacancies per supercell). Bulk crystals with 20% doping level are not presented since structural relaxation could not drop atomic forces below the desired threshold of 0.05 eV/Å. Given the computational complexity, we could not calculate all possible combinations using an ab initio method. For instance, for 11.1% Tb doping and 3.7% vacancies, there are $\binom{54}{2} \times \binom{18}{2} = 218943$ possible arrangements to choose two Bi atoms from the supercell for substitution by two Tb atoms and two O atoms for vacancies. Therefore, we selected a representative subset of combinations. Particularly, we focused on positions of O vacancies, indicated as blue spheres in Fig. 1, that were either adjacent to or separated from Tb dopants by several intervening atoms. The locations of these Tb atoms are also shown in the same figure. Calculated configurations are labeled accordingly; for instance, v1 configuration is vacancy at position 1, whereas v12 is the configuration with two vacancies at positions 1 and 2. v4 is a vacancy separated from nearest Tb atom by several intervening atoms. Besides bulk we also considered a (0001) surface atomic structure, which model is shown in Fig. 1(b). It is constructed from the bulk supercell with lattice parameter c extended to 29 Å, which presents a 15 Å thick vacuum layer between the periodic replicas.

3. Results and discussions

3.1. Structural and morphological properties

Fig. 2 shows the diffraction patterns of $Bi_{1-x}Tb_xFeO_3$ thin films on FTO glass substrate. Based on the results of GIXRD analysis, it was determined that the rhombohedrally distorted *R3c* (S.G. N° 161) perovskite structure is present in all samples. The corresponding Miller indices of the *R3c* phase are indicated, whereas all other peaks can be indexed to tetragonal $P4_2/mnm$ (S.G. N° 136) cassiterite SnO_2 (ICSD # 56671) originating from the FTO glass substrate, without the presence of impurities.

The broad peaks of low intensity indicate the nanocrystalline nature of the thin films. With an increase of terbium content, a minimal changes of peak intensities are observed, but not their shift towards larger or smaller angles. Good agreement was obtained (based on data from the database, card number ICSD # 168740) between the experimental and calculated diffractograms.

The values of the lattice parameters and the unit cell volume are presented in Table 1, whereas the crystallite size and microstrain as a function of Tb doping are presented in the inset of Fig. 2. The lattice parameters *a* and *c* show a slight decrease up to 10% Tb doping, accompanied by a shrinkage of the unit cell volume. This behavior is consistent with the substitution of Bi^{3+} (~1.03 Å) by smaller Tb^{3+} ions (~0.92 Å) [19,20]. At 20% doping, a slight increase in both lattice parameters and unit cell volume is observed. The changes of the lattice parameters and unit cell volume correlate well with the evolution of crystalite size and microstrain with Tb doping, as shown in the inset of Fig. 2. As can be seen, the crystallite size increases with Tb doping, whereas the microstrain values decrease. The presence of higher microstrain in $Bi_{1-x}Tb_xFeO_3$ samples with smaller crystallite size can lead to the shrinkage of the unit cell, particularly along the c-axis [44]. The microstrain decreases as the crystallite size increases [45], causing the lattice to slightly expand, which is reflected in the moderate increase of the *a* and *c* parameters, as observed in the case of 20% Tb-doped sample.

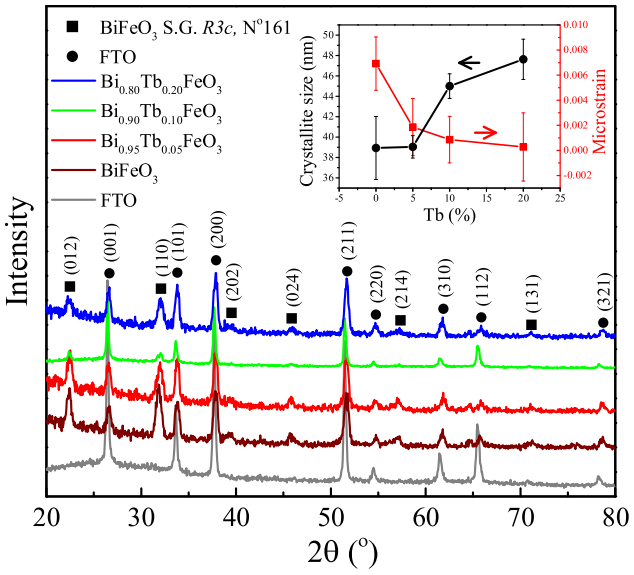

Fig. 2. GIXRD pattern of the $Bi_{1-x}Tb_xFeO_3$ thin films fabricated by the sol–gel spin coating process. The inset illustrates the average crystallite size and microstrain as a function of Tb doping.

In order to investigate the surface morphology and grain size distribution of the samples, AFM topographic images and corresponding height histograms are presented in Fig. 3. This figure includes 30 × 30 μm² and 2 × 2 μm² AFM images for $Bi_{1-x}Tb_xFeO_3$ samples at various doping levels (images (a), (d), (g), and (j) for 30 × 30 μm² and (b), (e), (h), and (k) for 2 × 2 μm²). The topographic images show that all films have a flat surface, without visible cracks and holes, and with a well defined grain structure. The histograms (images (c), (f), (i), and (l)) depict an average grain size, showing values of 180, 187, 200, and 224 nm for $BiFeO_3$, $Bi_{0.95}Tb_{0.05}FeO_3$, $Bi_{0.90}Tb_{0.10}FeO_3$ and $Bi_{0.80}Tb_{0.20}FeO_3$, respectively.

Using these topographic images, we calculated the surface roughness and the grain size distribution. The corresponding results are presented in Fig. 4. The grain size increases with Tb doping, in agreement with XRD crystallite size. The grain sizes are several times larger than the crystallites, indicating that each grain consists of multiple

Table 1
The lattice parameters and the volume of the unit cell.

Phase	$BiFeO_3$	$Bi_{0.95}Tb_{0.05}FeO_3$	$Bi_{0.90}Tb_{0.10}FeO_3$	$Bi_{0.80}Tb_{0.20}FeO_3$
$BiFeO_3$				
ICSD #168740	a = 5.58 Å	a = 5.57 Å	a = 5.56 Å	a = 5.57 Å
rhombohedral	c = 13.87 Å	c = 13.87 Å	c = 13.82 Å	c = 13.85 Å
S. G. *R3c* N°(161)	V = 374.25 Å³	V = 373.10 Å³	V = 371.07 Å³	V = 372.67 Å³

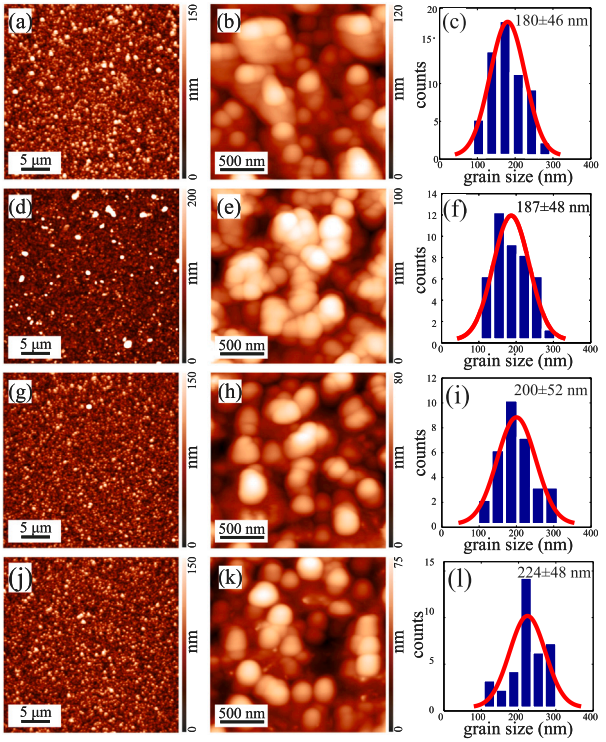

Fig. 3. The left column (images (a), (d), (g), (j)) presents 30 × 30 μm² AFM images, whereas the middle column (images (b), (e), (h), (k)) shows 2 × 2 μm² AFM images of $BiFeO_3$, $Bi_{0.95}Tb_{0.05}FeO_3$, $Bi_{0.90}Tb_{0.10}FeO_3$ and $Bi_{0.80}Tb_{0.20}FeO_3$ thin films, respectively. The right column (images (c), (f), (i), (l)) displays the corresponding histograms of average grain size derived from the 2 × 2 μm² AFM images. The red lines stand for Gaussian fits.

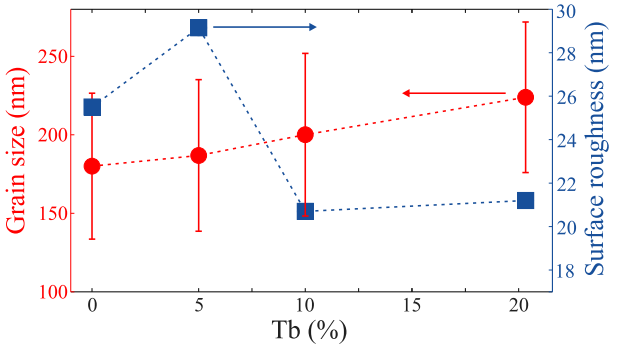

Fig. 4. Grain size (left axis) and surface roughness (right axis) data obtained from AFM measurements of $Bi_{1-x}Tb_xFeO_3$ thin films.

crystallites. The surface roughness of investigated films is low, in the range 20–30 nm.

Fig. 5(a) presents the room-temperature Raman spectra of $Bi_{1-x}Tb_xFeO_3$ thin films, deconvoluted using a Lorentzian type profiles. According to the factor group analysis, rhombohedral structure of $BiFeO_3$ exhibits 13 Raman-active modes, classified as 4 A_1 and 9E, all of which are observed in the spectrum of $BiFeO_3$ at room temperature and marked in Fig. 5(a). The low frequency, intense A_1 and E modes, are associated with Bi–O vibrations. The weaker E modes at higher frequencies, mainly correspond to Fe–O vibrations.

Tb doping induces noticeable changes in the Raman spectrum. At lower Tb concentrations, slight peak shifts to higher wavenumbers and a reduction of the intensity of low-frequency A_1 modes are observed. As the Tb content increases, the blueshift and broadening of the Raman modes become more pronounced [46]. These changes of the A_1 modes

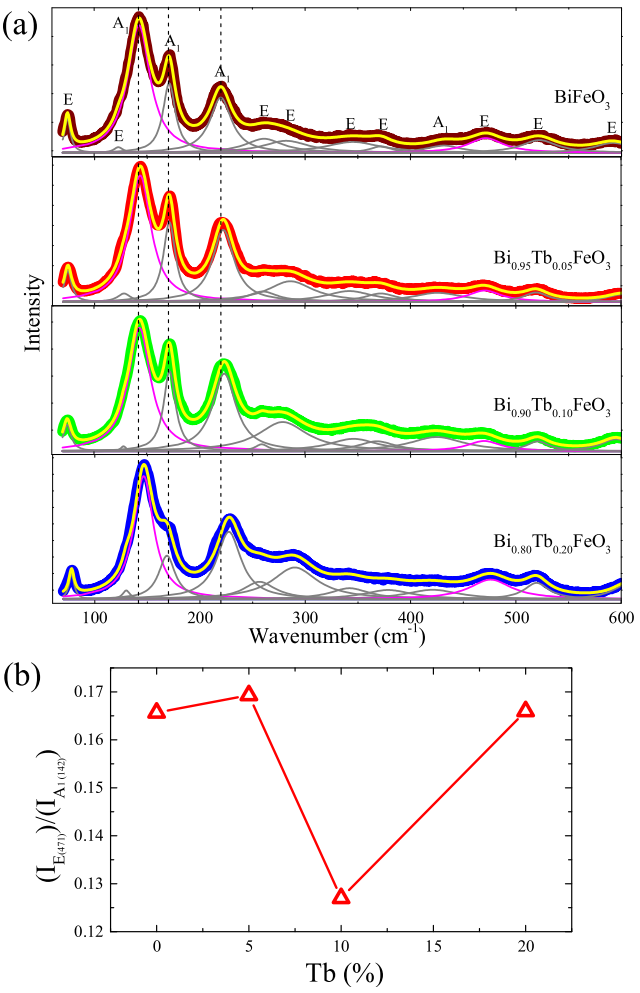

Fig. 5. (a) Raman spectra of $Bi_{1-x}Tb_xFeO_3$ thin films (thick colored lines), along with cumulative fits (yellow lines). Individual Lorentzian peaks are presented with thin lines. Vertical dashed lines represent the guide to the eye in tracking the shift of specific modes. (b) Intensity ratio of the $E_{(471)}$ and $A_{1(142)}$ Raman modes, as a function of Tb doping.

suggest structural distortion due to the substitution of Bi^{3+} ions with the smaller Tb^{3+} ones and higher electronegativity of the Tb–O bonds which strengthen the Bi(Tb)–O covalent bonds [23]. The rest of the E and A_1 modes at higher frequencies show minor shifts and intensity changes, except the E mode at 471 cm^{-1}. This mode undergoes a pronounced blue shift and intensity increase in all doped samples except for $Bi_{0.90}Tb_{0.10}FeO_3$, suggesting the modifications in Fe–O bonding interactions with Tb incorporation.

It is well known that the volatility of Bi^{3+} during synthesis process promotes the formation of oxygen vacancies, which significantly influence the structural and vibrational properties of $BiFeO_3$. These defects predominantly affect Fe–O bond dynamics within the FeO_6 octahedra, altering specific Raman modes. Notably, the E mode located around 471 cm^{-1}, associated with Fe–O–Fe bending vibrations, exhibits a distinct blue shift and intensity change with Tb doping.

As suggested by Gupta et al. [47], the E mod at 471 cm^{-1} is affected by oxygen vacancies. They found that relative intensity ratio of E and A_1 modes at 471 and 142 cm^{-1} ($E_{(471)}/A_{1(142)}$) increases with increased disorder, i.e increased concentration of oxygen vacancies. In Fig. 5(b) is presented the $E_{(471)}/A_{1(142)}$ ratio as a function of Tb doping. As can be seen, the lowest $E_{(471)}/A_{1(142)}$ ratio is found in 10% Tb-doped sample, indicating that this sample has the lowest oxygen vacancy concentration. In undoped, 5% and 20% Tb–doped samples

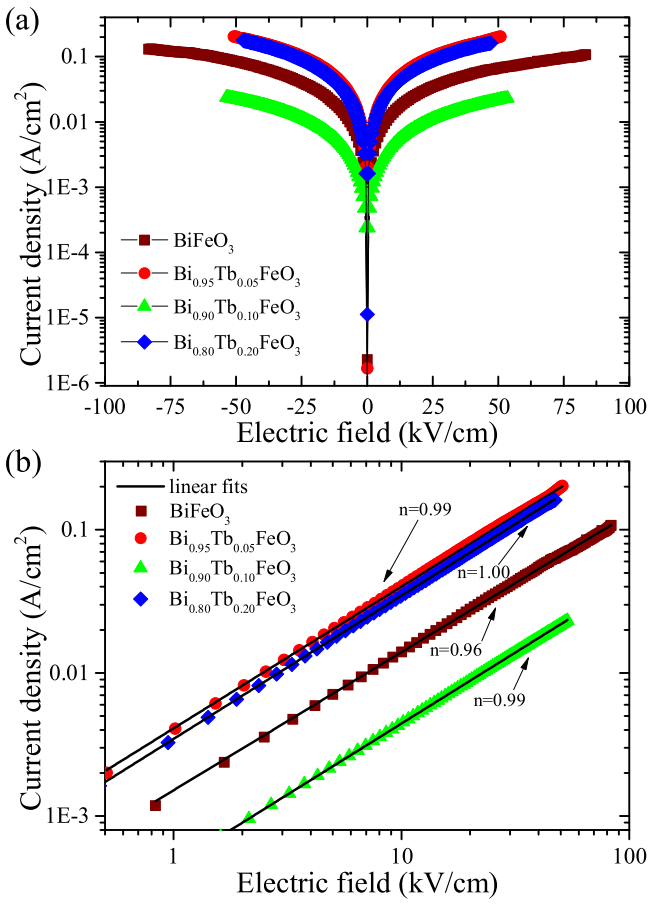

Fig. 6. (a) Semilogarithmic representation of current density (J) versus electric field (E) for $Bi_{1-x}Tb_xFeO_3$ thin films. (b) Log–log representation of current density versus electric field, including linear fits with corresponding slope coefficients.

this intensity ratio is higher implying that these samples have higher concentration of oxygen vacancies.

3.2. Leakage current

Fig. 6(a) presents the current density (J) versus electric field (E) curves for $Bi_{1-x}Tb_xFeO_3$ thin films, while Fig. 6(b) displays the same data in a logarithmic scale. The data in Fig. 6(a) show that the 10% Tb-doped sample exhibits a current density an order of magnitude lower compared to other doping levels. In Fig. 6(b), the measured data were fitted with linear functions, yielding slopes approximately equal to 1, indicating that the Ohmic conduction is dominant [23].

Our results indicate that the most significant reduction in leakage current occurs at 10% Tb doping. Further doping does not proportionally enhance resistive properties; instead, the $Bi_{0.80}Tb_{0.20}FeO_3$ sample becomes more conductive. A similar non-monotonic dependence of conductivity on Tb content has been observed in previous studies, where intermediate doping levels led to minimized leakage current, while higher doping concentrations resulted in increased conductivity [22].

Although the previous results of the macroscopic measurements revealed how electrical conductivity change with Tb-doing, we employed C-AFM in order to measure local currents at the micro-scale and to get further insights into conduction mechanisms. Typical current maps measured on the surface of the $Bi_{0.90}Tb_{0.10}FeO_3$ film using C-AFM at different bias voltages ((a) 1 V, (b) 2 V, (c) 3 V, and (d) 4 V) are displayed in Fig. 7. As can be seen, the maps exhibit very low currents for low bias voltages (1 V and 2 V, Figs. 7(a) and 7(b), respectively).

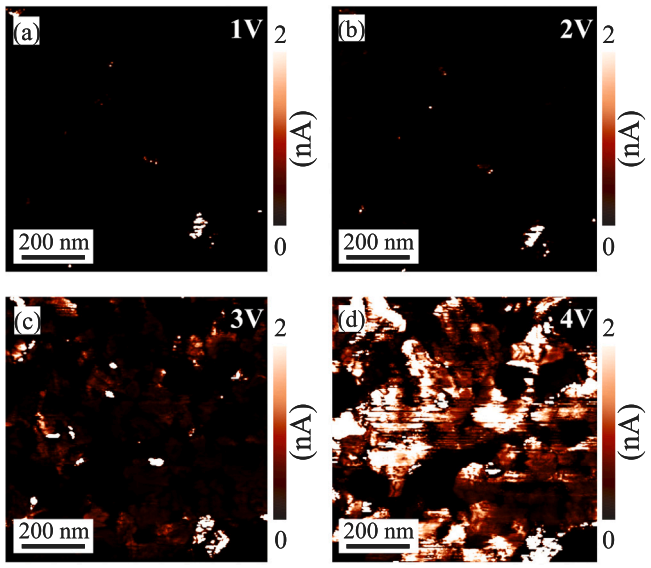

Fig. 7. Current maps of the $Bi_{0.90}Tb_{0.10}FeO_3$ sample measured by C-AFM at different bias voltages: (a) 1 V, (b) 2 V, (c) 3 V, and (d) 4 V. The color scales for all maps were adjusted to the same range 0-2 nA (they were saturated at 2 nA) in order to highlight lower (leakage) currents and at the same time, to facilitate the comparison of all current maps.

At the same time, conductive paths represented by a bright contrast and associated with a more pronounced current are very narrow and localized. On the other hand, at higher bias voltages (3 V and 4 V, Figs. 7(c) and 7(d), respectively), the current is significantly enhanced while conductive paths become extended. Therefore, one of the main features of the presented current maps is their spatial inhomogeneity. This implies that the film surface is associated with an analogous spatial inhomogeneity of the conductivity.

The current maps from Fig. 7 show that the conduction starts from very small and localized domains, which are spatially separated. With increasing bias voltage, these domains spatially extend. Finally, for high voltages they start to merge into large conductive domains.

As we have already demonstrated for similar $BiFeO_3$ samples, there is a significant difference in electrical properties among the grains and grain boundaries [24]. The most obvious difference is that the grain boundaries are much more conductive. Since the grain boundaries present a certain discontinuity in a crystal structure of single grain, they are always associated with an increased concentrations of various defects which facilitate conduction. Oxygen vacancies are the most frequent defects in $BiFeO_3$ films. Therefore, bright contrast in the current maps in Fig. 7 measured at lower voltages, most probably corresponds to a network of grain boundaries with enhanced concentration of oxygen vacancies resulting in increased conductivity. Current maps like in Fig. 7 (recorded at increasing bias voltage) were measured on all investigated films. The current maps of all samples, measured at 1 V, are presented in Figs. 8(a–d) for comparison. The color scales in all maps are saturated at 100 nA for better visibility and easier comparison. Since absolute current value is, in principle, not relevant for our study, the presented current maps exhibit a nearly black-and-white color contrast. They are practically binary images, where dark areas (zero current) indicate insulating domains, and bright areas represent conductive domains. As can be seen, the dark contrast dominates in all maps indicating a near-zero current, while bright spots mark narrow conductive paths. Based on the visual comparison, the area of the conductive paths is the smallest for the film with 10% Tb doping (Fig. 8(c)) implying the lowest conductivity. On the other hand, the film with 5% Tb doping (Fig. 8(b)) exhibits a dense network of bright domains indicating a pronounced leakage current.

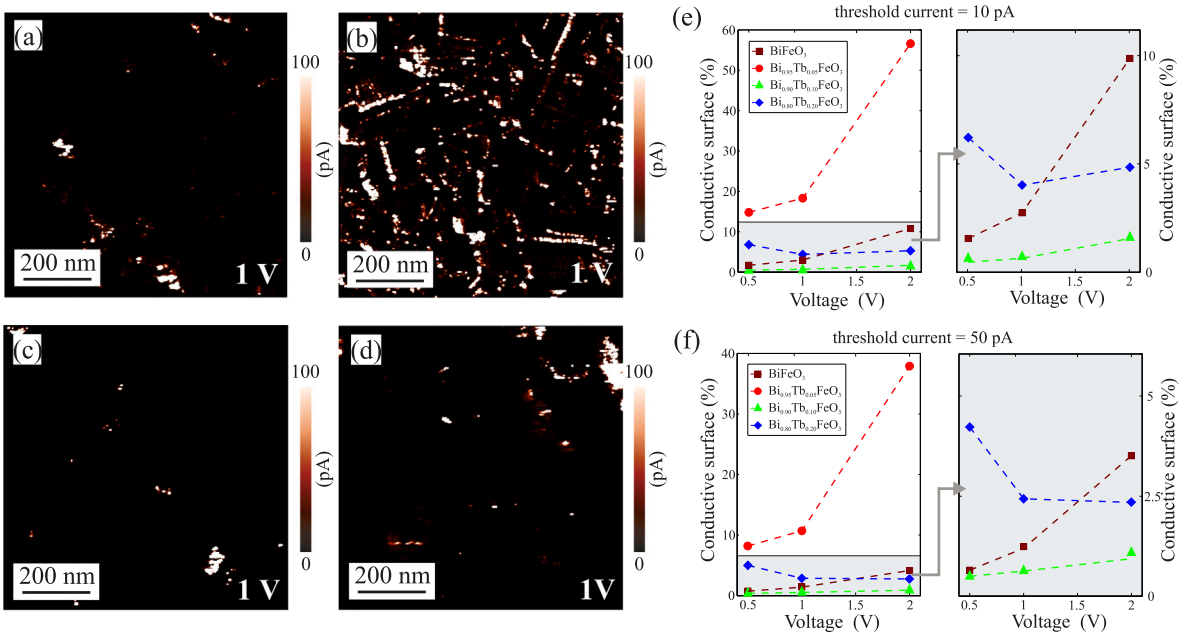

Fig. 8. Current maps measured at 1 V for (a) $BiFeO_3$, (b) $Bi_{0.95}Tb_{0.05}FeO_3$, (c) $Bi_{0.90}Tb_{0.10}FeO_3$ and (d) $Bi_{0.80}Tb_{0.20}FeO_3$ thin films. The color bar is saturated at 100 pA in all current maps in order to emphasize the contrast on conductive paths representing leakage currents. Conductive surface of investigated films expressed in percents as a function of applied voltage and for two current thresholds: (e) 10 pA and (f) 50 pA. To better illustrate the evolution of the conductive surface in the approximate range of 0%–10%, the gray regions marked on the main graphs are enlarged and shown on the right-hand side.

In order to compare the presented current maps, each of them was associated with a corresponding conductive surface expressed in percents. Briefly, each point on a measured current map (each map consists of 256 × 256 pixels) was counted as a conductive if the measured current at the considered point was larger than the predefined threshold current. The conductive surface in percents was then obtained as a ratio between a number of conductive and total number of points for one map. Two selected threshold currents were set at 10 pA and 50 pA. The comparison of conductive surfaces for all considered samples as a function of the applied bias voltage is given in Figs. 8(e) and 8(f). As can be seen, the $Bi_{0.90}Tb_{0.10}FeO_3$ film exhibits the smallest conductive surface for both threshold currents. This observation is in accordance with the results of the macroscopic I–V measurements and it confirms that the $Bi_{0.90}Tb_{0.10}FeO_3$ film has the smallest conductivity.

While moderate doping (around 10%) effectively reduces leakage current, higher doping levels (20%) lead to an increase in leakage current. Therefore, a delicate balance between Tb dopant concentration and defect control is essential to optimize the electrical performance of $BiFeO_3$ thin films.

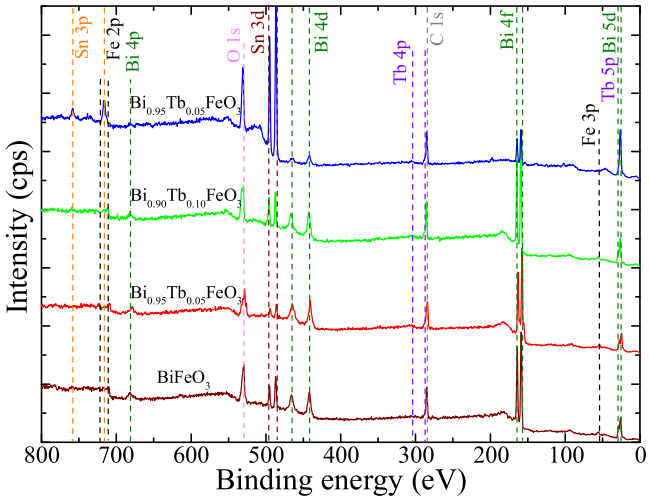

Fig. 9. XPS survey spectra of $Bi_{1-x}Tb_xFeO_3$ thin film.

3.3. X-ray photoelectron spectroscopy (XPS)

The survey XPS spectra of $Bi_{1-x}Tb_xFeO_3$ thin films, as shown in Fig. 9, provide insights into the chemical composition, oxidation states and the presence of defects.

These survey spectra confirm the presence of all major elements in the films: Fe, Bi, Tb, and O, whose most prominent lines are clearly marked. One can also see signals from the Sn substrate and adventitious carbon (C 1s) contamination at 284.8 eV, reflecting the sensitivity of the XPS technique in capturing both intrinsic and extrinsic elements. Furthermore, the changes in the O 1s and Fe 2p spectra can provide insight into defect structure of $Bi_{1-x}Tb_xFeO_3$ thin films.

The oxidation states of Fe in $Bi_{1-x}Tb_xFeO_3$ thin films, analyzed by XPS, are shown in Fig. 10 (right panel). The Fe $2p_{3/2}$ peak is deconvoluted into two components corresponding to Fe^{2+} at 709.6(2) eV and Fe^{3+} at 711.1(2) eV. Their coexistence indicates charge compensation mechanisms mediated by oxygen vacancies. The splitting between Fe $2p_{3/2}$ and Fe $2p_{1/2}$ components is consistently 13.6 eV for all samples, confirming the expected multiplet structure. Additionally, a noticeable Sn 3p contribution, present in all samples, overlaps with the Fe 2p region, preventing us to perform more precise quantitative estimation of Fe^{2+}/Fe^{3+} fraction. Since XPS only probes the surface to a few nanometers, the Sn signal is more prominent in the undoped sample and decreases with the increased thickness of the doped films. The presence of Sn in the spectra can also be attributed to thermal treatment, which has caused Sn to diffuse towards the film's surface.

The O 1s spectra of $Bi_{1-x}Tb_xFeO_3$ samples, presented in Fig. 10 (left panel), were deconvoluted into multiple peaks. The binding energies of lattice oxygen bonded to Fe and Sn are 529.4(1) eV and 530.5(1) eV, respectively, while the peak centered at 531.4(2) eV corresponds to oxygen vacancy-related species and hydroxides [48,49]. To quantitatively investigate the effect of Tb doping on oxygen vacancies, atomic percentages of oxygen vacancies (V_O) for each sample were extracted

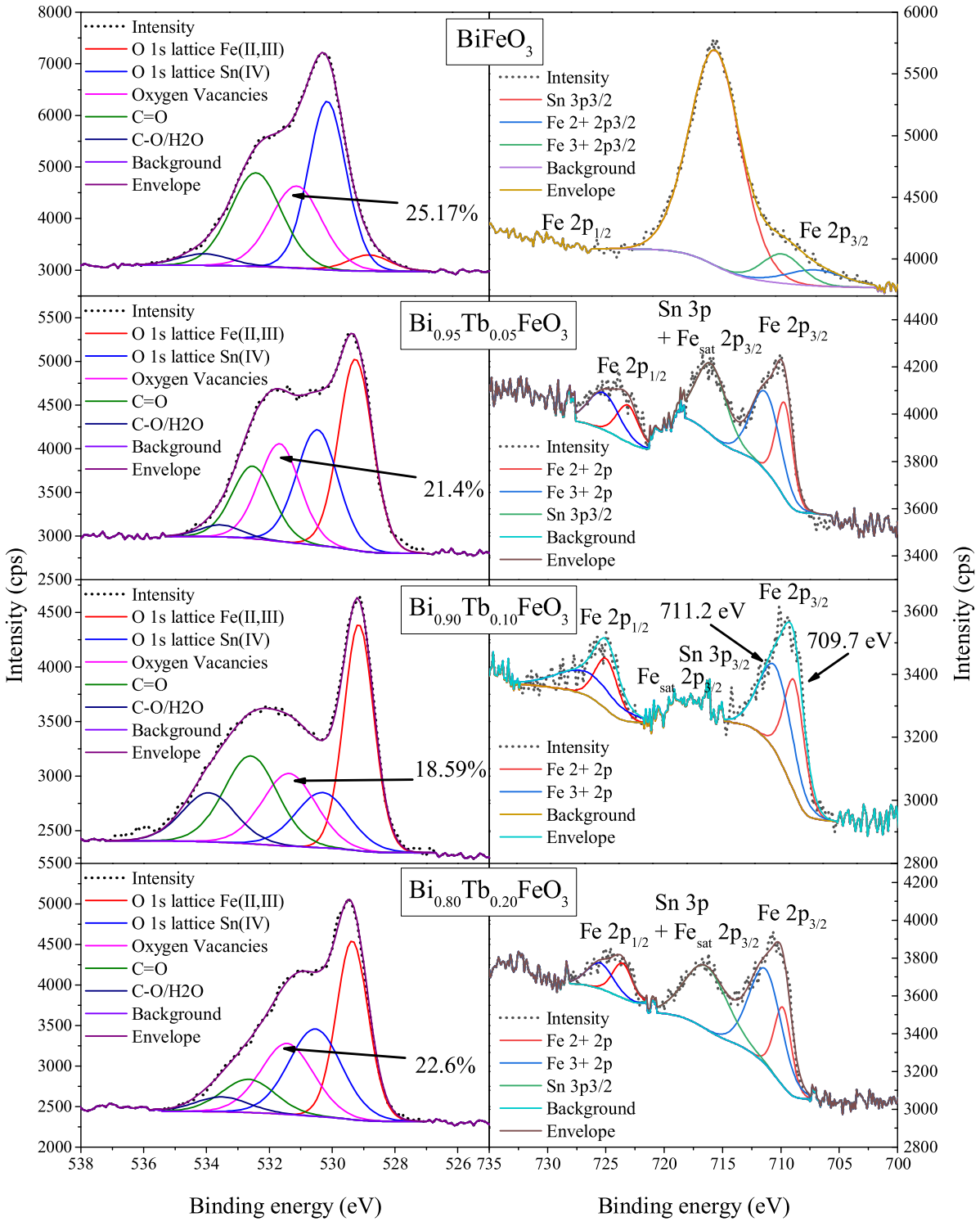

Fig. 10. High-resolution XPS spectra of O 1s (left) and Fe 2p (right) regions for $Bi_{1-x}Tb_xFeO_3$ thin films, including experimental data (dots) and fitted peaks (solid lines).

from deconvoluted high-resolution XPS spectra of O 1s spectrum and are summarized in Table 2.

The concentration of oxygen vacancies is the highest in the undoped $BiFeO_3$ film and decreases a bit for $Bi_{0.95}Tb_{0.05}FeO_3$ sample, reaching a minimum for the $Bi_{0.90}Tb_{0.10}FeO_3$ sample. However, at higher doping levels, a slight increase is observed, suggesting a complex relationship between defect concentration and dopant incorporation. The XPS results are in fairly good agreement with the conductivity measurements, showing that among all samples the $Bi_{0.90}Tb_{0.10}FeO_3$ has the lowest

Table 2
Atomic percentage of oxygen vacancies (V_O) for $Bi_{1-x}Tb_xFeO_3$ thin films.

Sample	V_O [at%]
$BiFeO_3$	25.2
$Bi_{0.95}Tb_{0.05}FeO_3$	21.4
$Bi_{0.90}Tb_{0.10}FeO_3$	18.6
$Bi_{0.80}Tb_{0.20}FeO_3$	22.6

Table 3
Relaxation energies and vacancy formation energies. Configuration labels correspond to the positions of vacancies marked in Fig. 1.

Configuration	E_{rel} (eV/atom)	E_{form} (eV/atom)
undoped		
no vac.	−0.020	
v1	−0.008	0.061
v2	−0.006	0.057
v12	−0.013	0.119
1 Tb (5.5%)		
no vac.	−0.015	
v4	−0.049	0.026
v5	−0.040	0.037
v1	−0.034	0.043
v2	−0.030	0.034
v45	−0.051	0.067
v13	−0.003	0.097
2 Tb (11.1%)		
no vac.	−0.024	
v4	−0.012	0.031
v1	−0.009	0.042
v13	−0.001	0.063
v14	−0.001	0.030

concentration of oxygen vacancies which makes this sample the least conductive.

3.4. Theoretical calculations

3.4.1. Bulk atomic structure and relaxation energies

The favorable vacancy concentration can typically be derived from the formation energy associated with specific chemical reactions used in sample fabrication. However, the fabrication conditions employed in this study introduce uncertainties that complicate precise theoretical calculations. For instance, the exact atomic structures of nitrates involved in the fabrication process cannot be definitively determined. To circumvent these limitations, we compared relaxation energies upon introducing vacancies into bulk structures for various atomic configurations and also evaluated vacancy formation energies. While this approach does not yield an exact vacancy concentration for our experimental samples, it provides qualitative insights into doping level versus vacancy concentration dependencies.

The relaxation energies from structural optimization are detailed in Table 3. When oxygen vacancies are introduced near the Tb dopant sites (designated as v1 and v2) within a 5.5%-doped crystal, the relaxation energies decrease to −0.034 eV and −0.030 eV from their respective values of −0.008 eV and −0.006 eV in undoped sample. This observation indicates a strong interaction between Tb doping and nearby oxygen vacancies, enhancing structural stability. Interestingly, when the vacancies are located farther away from the Tb dopant (designated as v4 and v5), their presence leads to even lower relaxation energies of −0.049 eV and −0.040 eV. This suggests that while local interactions between Tb doping and oxygen vacancies contribute significantly to stability, long-range effects also play an important role in lowering the overall energy of the doped system. For structures with two Tb dopants (11.1% doping concentration), the presence of vacancies results in relaxation energies higher than those without any vacancy. This indicates that at 11.1% doping level, the system is less prone to incorporating oxygen vacancies.

Vacancy formation energies are also presented in Table 3. These energies are defined as:

$$E_{\text{form}} = \frac{E_t\ (\text{vacant str.}) + N_{\text{O}}\frac{E_t(\text{O}_2)}{2} - E_t\ (\text{pristine})}{N},$$

where E_t (vacant str.) and E_t (pristine) are the total DFT energies of relaxed structures with vacants and pristine structures respectively, $E_t(\text{O}_2)$ is the energy of an oxygen molecule, N_{O} is the number of oxygen vacancies and N is the number of atoms in the structure. Similar to the trend observed for relaxation energies, vacancy formation energies are consistently lower in lattices with 5.5% doping compared to undoped structures. However, at an 11.1% doping concentration, these energies do not significantly differ from those at a 5.5% doping level.

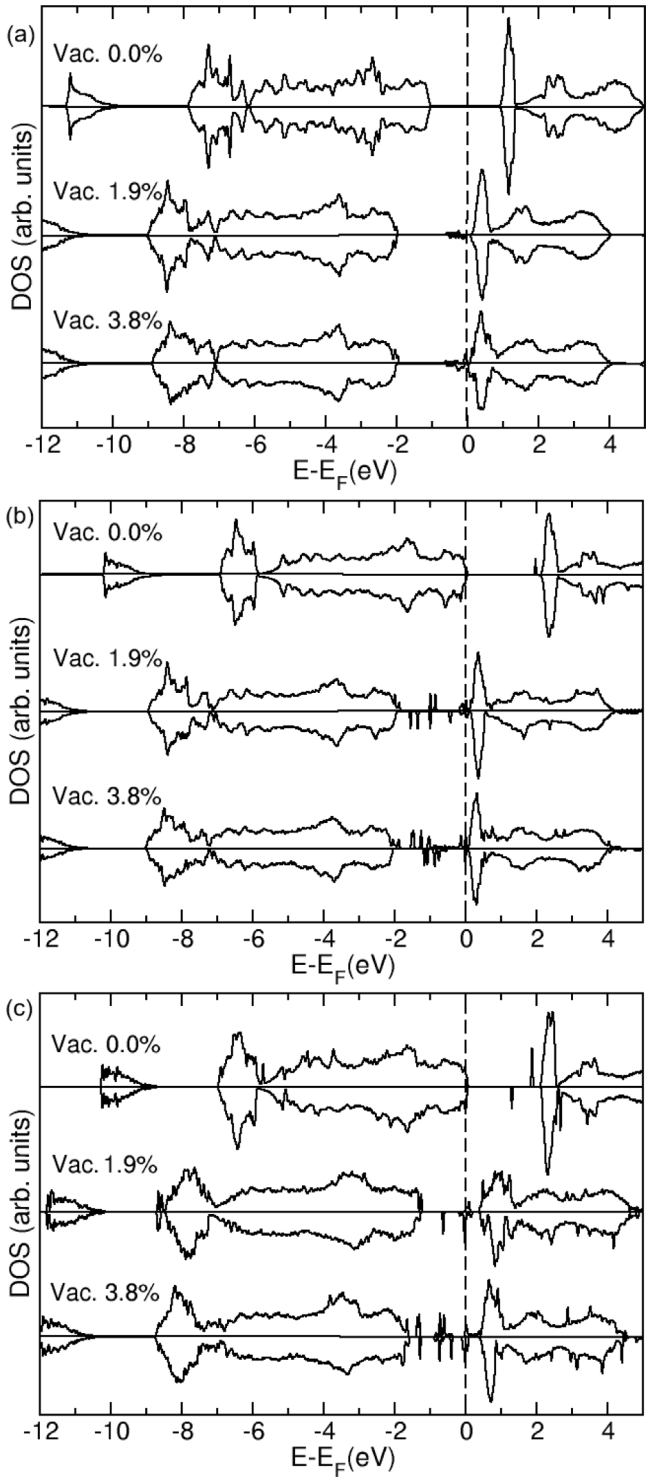

Fig. 11. DOS of (a) undoped, (b) 5.5% doped and (c) 11.1% Tb doped $BiFeO_3$. In each panel the top, middle and bottom graphs correspond to 0.0%, 1.9% and 3.8% oxygen vacancies. Each graph depicts DOS for majority/minority spins above/below local horizontal axes. Vertical dashed line marks the Fermi level.

3.4.2. Analysis of bulk electronic properties

In Fig. 11, we present a comparative analysis of the electronic density of states (DOS) of $BiFeO_3$ with varying concentrations of terbium dopants and oxygen vacancies. We examined three doping levels: 0%, 5.5%, and 11.1% terbium, alongside three vacancy concentrations: 0%, 1.9%, and 3.8%.

The Fermi level of the undoped vacant-free $BiFeO_3$ is positioned at the center of the band gap, as expected for the semiconducting pristine bismuth ferrite. Introducing the oxygen vacancies into an undoped crystal shifts the Fermi level towards the bottom of the conduction band due to excess electrons from vacant oxygen sites (Fig. 11(a)). In contrast, the Fermi level for 5.5% and 11.1% doped $BiFeO_3$ with no oxygen vacancies (0.0%) is positioned at the top of the valence band, evident from the top graphs in panels b and c of Fig. 11. In $BiFeO_3$ crystals doped at 5.5%of Tb (Fig. 11(b)), oxygen vacancies cause a significant upward shift in the Fermi level, placing it near or within the conduction band. At higher terbium doping levels (11.1%, Fig. 11(c)), an equilibrium between vacancy-induced n-type doping and dopant-induced p-type behavior results in the Fermi level returning to the bandgap. Our DFT calculations encountered convergence issues for terbium concentrations above 11.1% in bulk structures, preventing theoretical DOS graphs for these conditions. However, further doping would likely exacerbate p-type behavior, shifting the Fermi level towards or within the valence band. Both terbium doping and oxygen vacancies introduce states within the bandgap of $BiFeO_3$. In vacancy-free crystals, dopants at 5.5% and 11.1% concentrations generate one and two distinct bandgap states, respectively. Conversely, systems with oxygen vacancies exhibit a proliferation of bandgap states due to the presence of numerous dangling bonds. These additional states are characterized by minimal dispersion, indicating strong localization. The localized nature of these bandgap states plays a crucial role in modulating charge transport properties. In vacancy-free crystals, excess electrons would naturally fill the conduction band upon increasing vacancy concentration, potentially rendering the material conductive. However, the presence of localized bandgap states necessitates sequential filling according to Fermi-Dirac statistics and Pauli exclusion principle, thereby impeding easy movement of the Fermi level within the bandgap.

3.4.3. Local density of states

Local density of states (LDOS) integrated ±0.05 eV around the Fermi level is presented for three atomic configurations in Fig. 12: an undoped supercell with 2 vacancies (Fig. 12(a)), a supercell with 1 Tb atom and two neighboring vacancies (Fig. 12(b)), and a supercell with 2 Tb atoms, each with one neighboring vacancy (Fig. 12(c)). Graphical representation of LDOS can vary with isosurface values; from our careful analysis of LDOS for a range of isovalues we found that isovalue of 0.0003 states/eV/$Å^3$ captures the most important details of investigated supercells' electronic structures.

Fig. 12 reveals two key observations: 1. In the undoped configuration (a), significant LDOS contributions are not localized around both vacancies, contrary to expectations, but rather LDOS is relatively delocalized through the supercell. 2. For doped configurations (b) and (c), LDOS is concentrated around Tb dopants and their neighboring vacancies, with a decaying distribution further away. These findings suggest that in doped systems, electronic states become more localized near the dopant sites, potentially leading to delocalization at higher doping concentrations as the wavefunctions overlap increasingly with dopant concentration (conversely the Tb–Tb distance decreases). This could result in percolation effects and an increase in electrical conductivity as dopant concentration increases. The states around the Fermi level in undoped structure are delocalized, which is one of the key conditions for high electric conductivity.

Table 4
Vacancy formation energies.

Configuration	E_{form} (eV/atom)
undoped	
one vac. in bulk	0.039
one vac. on Bi surf.	0.034
one vac. on Fe surf.	0.036
1 Tb (5.5% doping)	
one vac. in bulk	0.016
one vac. on Bi surf.	0.003
one vac. on Fe surf.	0.055
2 Tb (11.1% doping)	
one vac. in bulk	0.042
one vac. on Bi surf.	0.210
one vac. on Fe surf.	0.060
4 Tb (22.2% doping)	
one vac. in bulk	0.102
one vac. on Bi surf.	0.049
one vac. on Fe surf.	0.121

3.4.4. Vacancy formation energies in surfaces

The infinite periodic structures we considered above are representative of doping and vacancy effects in bulk. However, experimental samples are rather polycrystalline in which surfaces and grain boundaries may affect the electronic and transport properties. The lower coordination of oxygen atoms at surfaces can significantly alter their binding energies and consequently affect the distribution of vacancies. To bridge this gap between theoretical models and experimental observations, we extended our investigation to incorporate surface phenomena. Specifically, we introduced a single vacancy into either the Bi or Fe layer at the surface or within deeper layers of the structure. We utilized the supercell from our bulk studies but modified it by extending the c lattice vector to 29 Å to ensure an adequate vacuum layer between periodic replicas, i.e. negligible interaction between them. While we aimed to optimize these surface structures, atomic forces could not be reduced below a tolerance level of 0.05 ev/Å for some structures. In order to have fair comparison among all configurations, we present data only for unoptimized structures. The Table 4 presents calculated values of vacancy formation energy for various configurations, including undoped and doped structures with one, two or four Tb atoms per supercell. These calculations are performed to determine the most favorable positions for oxygen vacancies within these structures. Undoped $BiFeO_3$ exhibits similar vacancy formation energies regardless of the surface type, indicating minimal intrinsic anisotropy in oxygen vacancies under pristine conditions. When one Tb atom is introduced per supercell (corresponding to 5.5% doping level), vacancy formation energies change significantly. The energy in bulk (0.016 eV/atom) and Fe surface (0.055 eV/atom) decrease compared to the undoped structure, suggesting that Tb doping facilitates oxygen vacancy formation in these configurations. However, the most striking change is observed at the Bi surface: 0.003 eV/atom. This suggests that Tb doping strongly facilitates vacancy formation on the Bi-terminated surface even at the room temperature. Introducing two Tb atoms per supercell (corresponding to 11.1% doping level) alters these trends. The vacancy energy increases for all studied configurations, indicating a less favorable environment for vacancies in these configurations. This is in agreement with our analysis of vacancies using XPS (Section 3.4), while the doping level also corresponds well to the doping level for which the reduced leakage current was observed (Section 3.2). Interestingly, the most significant increase of vacancy formation energy is for Bi-terminated surface, which is the most favorable place for less doped level. This implies that with two Tb atoms per supercell, oxygen vacancies are least favorable to form at either surfaces or in bulk. At four Tb atoms per supercell (corresponding to 22.2% doping level), vacancies become significantly least favorable in bulk and Fe-terminated surfaces. Vacancy formation energy on Bi-terminated surface decreases to 0.049 eV/atom from

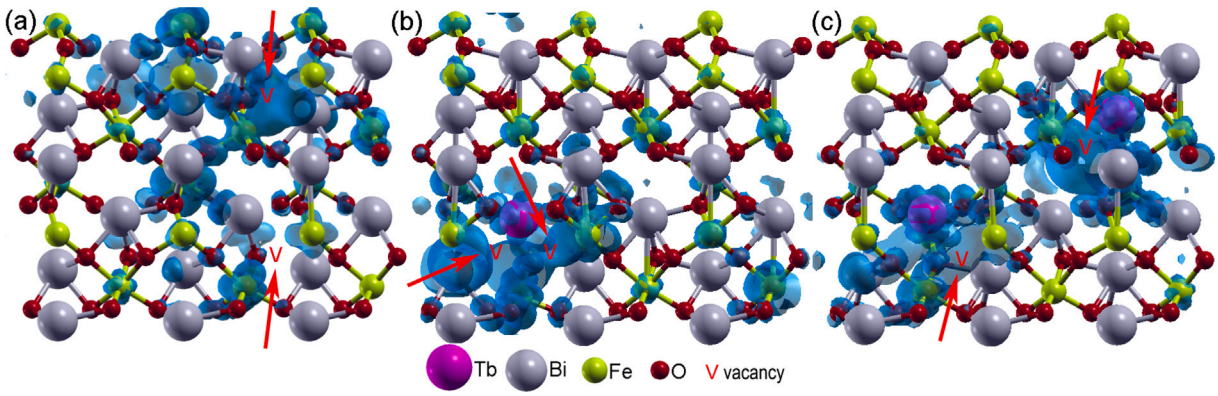

Fig. 12. Local density of states integrated within ±0.05 eV around the Fermi level for three different supercell configurations: (a) an undoped supercell with two vacancies, a supercell containing one Tb atom, (b) with two neighboring vacancies to the Tb atom, and (c) a supercell with two Tb atoms each having a neighboring vacancy. Elemental spheres are color-coded as indicated in the legend at the bottom. Vacancies are marked by red 'V' labels. An isosurface value of 0.0003 states/eVÅ^3 is depicted for all configurations.

0.210 eV/atom in structure with 2 Tb atoms per supercell; however this is still significantly larger than the values obtained for 5.5%-doped structures. Interesting, the trend of DFT-predicted change of vacancy concentrations corresponds to the dependence of grain sizes and surface roughness obtained with our AFM measurements. Particularly, DFT calculations indicate that vacancy concentration rises for undoped to 5.5%-doped structures, whereas the vacancy concentration decreases for 11.1% and 22.2% Tb doping levels. Less vacancies, i.e. defects can naturally result in larger grains and smoother surfaces, as observed experimentally. At room temperature, which corresponds to approximately 0.025 eV/atom, we can infer that vacancies would be most favorable in structures with a single Tb dopant per super cell and vacancy located on the Bi surface (formation energy 0.003 eV/atom). This is because this vacancy formation energy is well below the room temperature and represents the lowest activation barrier for vacancy formation. It is important to note that these energies are calculated for non-optimized structures. Optimization would likely decrease all vacancy formation energies, potentially bringing them closer to the room temperature value and enhancing the stability of vacancies at certain positions. Note that vacancy formation energies obtained for unrelaxed surfaces are consistently lower than those for relaxed bulk structures (Table 3), further signifying the possibility for vacancy formation in the former configurations.

3.4.5. Electronic structure of surfaces with vacancies

The DOS profiles for surface energetically favorable structures of $BiFeO_3$, doped with 0%, 5.5%, 11.1%, and 22.2% terbium, and containing vacancy concentrations of either 0% or 1.9%, are depicted in Fig. 13. Fig. 13(a) illustrates the DOS for energetically favorable atomic configurations of Tb-doped $BiFeO_3$ with and without oxygen vacancies. Notably, there are both qualitative and quantitative differences between undoped and 5.5% doped materials compared to those with higher doping concentrations (11.1% and 22.2%). The total DOS for these structures indicates electronic bandgaps of approximately 0.2 eV for the former two configurations and around 0.3 eV and 0.4 eV for the latter two.

A critical factor influencing electric conductivity is the position of the Fermi level relative to the available energy states. In undoped and 5.5% doped structures, the Fermi level resides at the bottom of dispersive bands, providing numerous accessible electronic states that enhance electrical conductivity. Conversely, in both 11.1% and 22.2% doped structures, the Fermi level is positioned at the top of filled bands separated from unfilled bands by a sizable bandgap. The similar DOS characteristics of 11.1% and 22.2% doped structures seemingly contradicts our experimental finding, which shows an increase in current when doping level increases from 10% to 20%. To address this disagreement we have to inspect the projected density-of-states (PDOS).

Fig. 13 (panels (b), (c) and (d)) provide PDOS for analyses of 5.5%, 11.1%, and 22.2% doping levels, respectively. These figures illustrate that the electronic states around the Fermi level predominantly originate from the first atomic surface layers, mainly Fe-terminated surfaces, with less influence from Bi-terminated surface and minor contributions from bulk Bi and Fe layers. In all cases, a narrow Tb state is present at the Fermi level. However, contribution to PDOS from Tb dopants varies with dopant concentration. In the energy range ±2 eV around Fermi level the Tb states are sparse and non-dispersive for 5.5% and 11.1% doping levels. Importantly, as the doping concentration increases from 11.1% to 22.2%, there is a significant increase in the number of available Tb states, as evidenced by comparing PDOS profiles for these concentrations. The physical origin of the experimentally observed variation in electric conductivity with Tb doping level can be summarized as follows:

1. Effects of doping and vacancies are mutually opposite; while vacancies shift Fermi level up towards the conduction band, doping pulls the Fermi level towards the valence band.
2. Undoped and weakly doped bismuth ferrites are conducting materials, with transport channels localized primarily on surfaces and eventually grain boundaries in experimental samples. The oxygen vacancies present at this doping level n-type doped material, bringing its Fermi level to the region with high density of dispersive well-conducting states.
3. Samples with the approximately 10% doping level lack states responsible for electronic transport; the Fermi level is shifted below a bandgap, making unoccupied states that provide conducting channels in undoped and lower-doped materials unreachable at low bias voltages in the intermediately doped structure. Additionally, dopant states around Fermi level are dispersionless, which do not contribute to efficient charge transport.
4. Increased conductivity in highly doped (approximately 20%) samples can be attributed to a significantly denser population of Tb states around the Fermi level. With a sufficient dopant concentration these states can overlap, delocalize and present dispersive, hence conducting states.

The results of DFT calculation are in accordance with our experimental findings. Undoped and weakly Tb-doped (~5%) $BiFeO_3$ thin films are conductive due to the formation of oxygen vacancies primarily on the surface and grain boundaries. For much higher Tb doping (~20%) DFT calculations indicate a significant increase of Tb conducting states around the Fermi level and less formation of oxygen vacancies. Therefore, experimentally obtained high conductivity of $Bi_{0.80}Tb_{0.20}FeO_3$ sample originates from the increased number of Tb conductive states. In the case of intermediate Tb doping (~10%) DFT calculations showed that the formation of oxygen vacancies is the

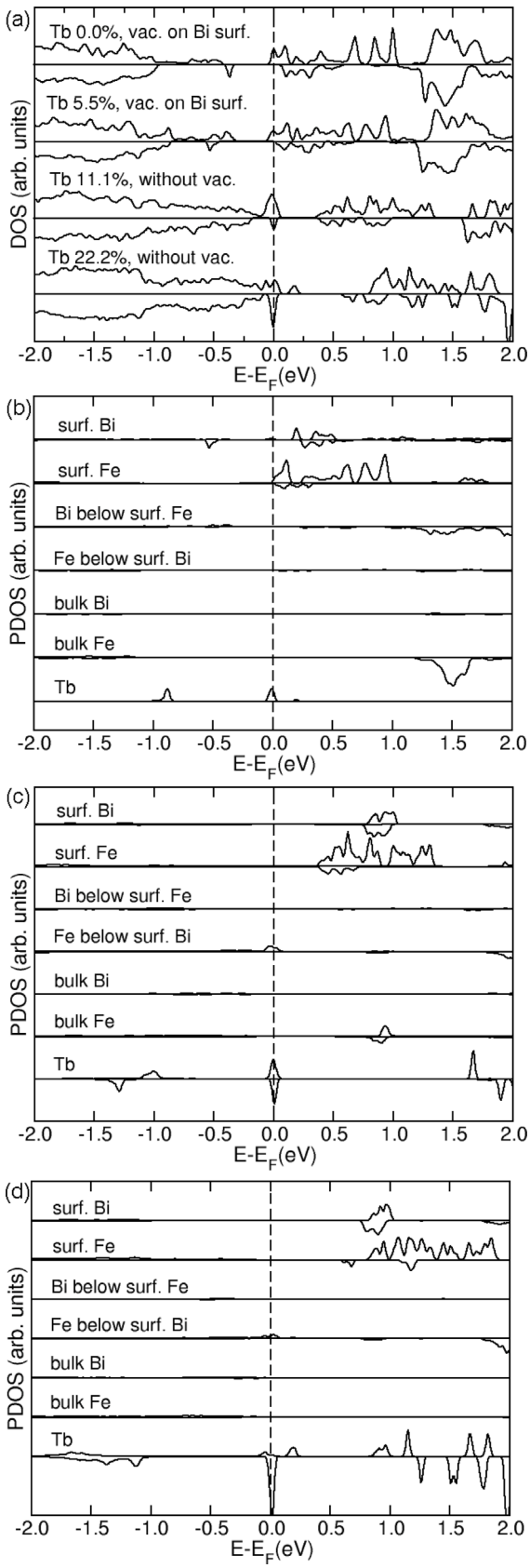

Fig. 13. Electronic structure of Tb-doped $BiFeO_3$ surfaces. (a) DOS of favorable vacancy configurations for different doping levels. Partial contributions to DOS from surface Bi layer, surface Fe layer, Bi layer below Fe surface, Fe layer below Bi surface, a bulk Bi layer, a bulk Fe layer and Tb dopants for (b) 5.5% doped structure with a vacancy on Bi surface, (c) 11.1% doped structure without vacancies, and (d) 22.2% doped vacant-free structure. Each graph shows DOS for majority/minority spins above/below local horizontal axes. Vertical dashed line marks the Fermi level.

least favorable, whereas sparse and non-dispersive Tb states do not contribute to efficient charge transport. It can be concluded that the balance between dopant concentration and defect formation is a key factor in achieving the much higher resistivity of the $Bi_{0.90}Tb_{0.10}FeO_3$ sample compared to the other samples. The findings presented above give a meaningful insight into how the Tb doping concentration influences the defect formation and thus the electrical properties of $BiFeO_3$ thin-films.

4. Concluding remarks

In summary, this study revealed that Tb doping has a great and non uniform influence on the formation of oxygen vacancy defects and electronic structure of $BiFeO_3$ thin films. The noticeable decrease of the intensity of 471 cm^{-1} Raman mode, seen in 10% Tb-doped film, indicates that 10% Tb doping leads to a decrease in the oxygen vacancy concentration. XPS analysis confirmed that 10% Tb-doped film has the lowest concentration of oxygen vacancies. Macroscopic I–V measurements showed that this sample has significantly reduced leakage current i.e the smallest conductivity. C-AFM measurements at the micro-scale provided additional insights into the conduction processes of Tb-doped $BiFeO_3$ thin films. These measurements confirmed that among all films, 10% Tb-doped film is the least conductive. At low voltages, the conduction is confined to localized, spatially inhomogeneous domains and takes place across grain boundaries with enhanced concentration of defects. As the voltage increases, the localized domains merge into larger conductive domains. From ab initio calculations, atomistic insight into such phenomena was gained. Undoped and ~5% doped samples are conductive due to high density of dispersive well-conducting oxygen vacancy states. For much higher Tb dopant concentration (~20%), DFT calculations indicate that less oxygen vacancies are formed, whereas the high conductivity originates from increased density of Tb conductive states near the Fermi level. An intermediate Tb doping concentration of ~10% causes a lack of states responsible for electronic transport, i.e. the concentration of oxygen vacancies is significantly lower, whereas the dopant non-dispersive states near the Fermi level are sparse and insufficient for the efficient charge transport. It is exactly this balance between the dopant and oxygen vacancy concentrations that ensures the best electrical performances of 10% Tb-doped film. These investigations pave the way for designing advanced multiferroic materials with thoroughly controlled structural and electrical properties.

CRediT authorship contribution statement

Bojan Stojadinović: Writing – original draft, Visualization, Investigation, Formal analysis, Data curation, Conceptualization. **Igor Popov:** Writing – original draft, Supervision, Methodology, Investigation, Formal analysis. **Borislav Vasić:** Writing – original draft, Methodology, Investigation, Formal analysis. **Dejan Pjević:** Writing – original draft, Methodology. **Milena Rosić:** Software, Methodology. **Nenad Tadić:** Investigation, Data curation. **Zorana Dohčević-Mitrović:** Writing – review & editing, Supervision, Formal analysis.

Declaration of competing interest

The authors declare that they have no known competing financial interests or personal relationships that could have appeared to influence the work reported in this paper.

Acknowledgments

B. S., B. V. and Z. D. M. acknowledge funding provided by the Institute of Physics Belgrade, through the grant by the Ministry of Science, Technological Development and Innovation of the Republic of Serbia. I. P. acknowledges financial support from the Ministry of Science, Technological Development and Innovation of the Republic of Serbia (Contract No. 451-03-66/2024-03/200053, Institute for Multidisciplinary Research, University of Belgrade), while M. R. and D. P. acknowledges financial support from the same ministry under Contract No. 451-03-136/2025-03/200017 (“Vinča” Institute of Nuclear Sciences–National Institute of the Republic of Serbia, University of Belgrade). DFT calculations were performed using computational resources at the Center of Surface and Nanoanalytics, Johannes Kepler University, Linz, Austria. We are grateful to Prof. Kurt Hingerl for providing the necessary computational resources at JKU.

Data availability

Data will be made available on request.

References

[1] T. Zhao, A. Scholl, F. Zavaliche, K. Lee, M. Barry, A. Doran, M.P. Cruz, Y.H. Chu, C. Ederer, N.A. Spaldin, R.R. Das, D.M. Kim, S.H. Baek, C.B. Eom, R. Ramesh, Electrical control of antiferromagnetic domains in multiferroic $BiFeO_3$ film at room temperature, Nat. Mater. 5 (2006) 823–829.

[2] C.H. Yang, D. Kan, I. Takeuchi, V. Nagarajan, J. Seidel, Doping $BiFeO_3$: Approaches and enhanced functionality, Phys. Chem. Chem. Phys. 14 (2012) 15953–15962.

[3] G. Catalan, J. Scott, Physics and applications of bismuth ferrite, Adv. Mater. 21 (2009) 2463–2485.

[4] R. Ramesh, N. Spaldin, Multiferroics: Progress and prospects in thin films, Nat. Mater. 6 (2007) 21–29.

[5] N. Spaldin, Multiferroics: Past, present, and future, Phys. Today 63 (2010) 38–43.

[6] J. Ma, J. Hu, Z. Li, C.W. Nan, Recent progress in multiferroic magnetoelectric composites: From bulk to thin films, Adv. Mater. 23 (2011) 1062–1087.

[7] S. Iakovlev, C.-H. Solterbeck, M. Kuhnke, M. Es-Souni, Multiferroic $BiFeO_3$ thin films processed via chemical solution deposition: Structural and electrical characterization, J. Appl. Phys. 97 (2005) 094901.

[8] G. Lotey, N. Verma, Multiferroic properties of Tb-doped $BiFeO_3$ nanowires, J. Nanopart. Res. 15 (2013) 1553.

[9] Y.-J. Kim, J.W. Kim, C.M. Raghavan, J.-J. Oak, H.J. Kim, W.-J. Kim, M.H. Kim, T.K. Song, S.S. Kim, Enhancement of electrical properties of (Gd, V) co-doped $BiFeO_3$ thin films prepared by chemical solution deposition, Ceram. Int. 39 (2013) S195–S199.

[10] S.K. Pradhan, B.K. Roul, Effect of gd doping on structural, electrical and magnetic properties of $BiFeO_3$ electroceramic, J. Phys. Chem. Solids 72 (2011) 1180–1187.

[11] B. Yu, M. Li, Z. Hu, L. Pei, D. Guo, X. Zhao, S. Dong, Enhanced multiferroic properties of the high-valence Pr doped $BiFeO_3$ thin film, Appl. Phys. Lett. 93 (2008) 182909.

[12] N. Kumar, N. Panwar, B. Gahtori, N. Singh, H. Kishan, V.P.S. Awana, Structural, dielectric and magnetic properties of Pr substituted $Bi_{1-x}Pr_xFeO_3$ ($0 \le x \le 0.15$) multiferroic compounds, J. Alloy. Compd. 501 (2010) L29–L32.

[13] Y. Wang, R.Y. Zheng, C.H. Sim, J. Wang, Charged defects and their effects on electrical behavior in $Bi_{1-x}La_xFeO_3$ thin films, J. Appl. Phys. 105 (2009) 016106.

[14] J. Liu, M. Li, L. Pei, J. Wang, B. Yu, X. Wang, X. Zhao, Structural and multiferroic properties of the Ce-doped $BiFeO_3$ thin films, J. Alloy. Compd. 493 (2010) 544–548.

[15] B. Stojadinović, Z. Dohčević-Mitrović, D. Stepanenko, M. Rosić, I. Petronijević, N. Tasić, N. Ilić, B. Matović B. Stojanović, Dielectric and ferroelectric properties of Ho-doped $BiFeO_3$ nanopowders across the structural phase transition, Ceram. Int. 43 (2017) 16531–16538.

[16] P. Sharma, D. Varshney, S. Satapathy, P.K. Gupta, Effect of Pr substitution on structural and electrical properties of $BiFeO_3$ ceramics, Mater. Chem. Phys. 143 (2014) 629–636.

[17] G. Dhir, G.S. Lotey, P. Uniyal, P.N.K. Verna, Size-dependent magnetic and dielectric properties of Tb-doped $BiFeO_3$ nanoparticles, J. Mater. Sci.: Mater. Electron. 24 (2013) 4386–4392.

[18] Q.X. Xing, Z. Han, S. Zhao, Crystal structure and magnetism of $BiFeO_3$ nanoparticles regulated by rare-earth Tb substitution, J. Mater. Sci.: Mater. Electron. 28 (2017) 295–303.

[19] M.L. Yi, C.B. Wang, L. Li, J.M. Wang, Q. Shen, L.M. Zhang, Influence of tb doping on structure and multiferroic properties of $BiFeO_3$ films prepared by pulsed laser deposition, Appl. Surf. Sci. 344 (2015) 47–51.

[20] Y. Wang, C.W. Nan, Effect of Tb doping on electric and magnetic behavior of $BiFeO_3$ thin films, J. Appl. Phys. 103 (2008) 024103.

[21] M. Muneeswaran, R. Dhanalakshmi, N. Giridharan, Effect of Tb substitution on structural, optical, electrical and magnetic properties of $BiFeO_3$, J. Mater. Sci.: Mater. Electron. 26 (2015) 3827–3839.

[22] G. Dong, G. Tan, W. Liu, A. Xia, H. Ren, Effect of Tb doping on structural and electrical properties of $BiFeO_3$ thin films prepared by Sol-Gel technique, J. Mater. Sci. Technol. 30 (2014) 365–370.

[23] G. Dong, G. Tan, Y. Luo, W. Liu, H. Ren, A. Xia, Investigation of Tb-doping on structural transition and multiferroic properties of $BiFeO_3$ thin films, Ceram. Int. 40 (2014) 6413–6419.

[24] B. Stojadinović, B. Vasić, D. Stepanenko, N. Tadić, R. Gajić, Z. Dohčević-Mitrović, Variation of electric properties across the grain boundaries in $BiFeO_3$ film, J. Phys. D Appl. Phys. 49 (2015) 045309.

[25] Y. Wang, P. Zhou, L. Fetisov, Y. Fetisov, Y. Qi, T. Zhang, Phase conductance of $BiFeO_3$ film, Sensors 23 (2023) 9123.

[26] S. Saxin, C.S. Knee, Crystal structure of $Bi_{1-x}Tb_xFeO_3$ from high-resolution neutron diffraction, J. Solid State Chem. 184 (2011) 1576–1579.

[27] Rigaku, PDXL Integrated X-Ray Powder Diffraction Software, Rigaku, Tokyo, Japan, 2011.

[28] PDF-2, International Crystallographical Database (ICDD). N.S. 12 Campus Blvd, PA 19073, USA, Editor. 2012: USA (2023).

[29] https://icsd.products.fiz-karlsruhe.de/.

[30] W. Kraus, G. Nolze, POWDER CELL — A program for the representation and manipulation of crystal structures and calculation of the resulting X-ray powder patterns, J. Appl. Crystallogr. 29 (1996) 301–303.

[31] PowderCell for Windows 2.4, software available at http://powdercell-for-windows.software.informer.com/2.4/. (Accessed 15 February 2019).

[32] G.K. Williamson, W.H. Hall, X-ray line broadening from filed aluminium and wolfram, Acta Metall. Mater. 1 (1) (1953) 22–31.

[33] E. Artacho, E. Anglada, O. Diéguez, J.D. Gale, A. García, J. Junquera, R.M. Martin, P. Ordejón, J.M. Pruneda, D. Sánchez-Portal, J.M. Soler, The SIESTA method; developments and applicability, J. Phys.: Condens. Matter. 20 (2008) 064208.

[34] J. Perdew, K. Burke, M. Ernzerhof, Generalized gradient approximation made simple, Phys. Rev. Lett. 77 (1996) 3865–3868.

[35] N. Troullier, J. Martins, Efficient pseudopotentials for plane-wave calculations, Phys. Rev. B 43 (1991) 1993–2006.

[36] A. Liechtenstein, V. Anisimov, J. Zaanen, Density-functional theory and strong interactions: Orbital ordering in Mott–Hubbard insulators, Phys. Rev. B 52 (1995) R5467–R5470.

[37] V. Anisimov, J. Zaanen, O. Andersen, Band theory and mott insulators: Hubbard U instead of stoner I, Phys. Rev. B 44 (1991) 943–954.

[38] V.I. Anisimov, F. Aryasetiawan, A.I. Lichtenstein, First-principles calculations of the electronic structure and spectra of strongly correlated systems: The LDA+ U method, J. Phys.: Condens. Matter. 9 (1997) 767.

[39] M. Čebela, D. Zagorac, K. Batalović, J. Radaković, B. Stojadinović, V. Spasojević, R. Hercigonja, $BiFeO_3$ perovskites: A multidisciplinary approach to multiferroics, Ceram. Int. 43 (2017) 1256–1264.

[40] M. Čebela, D. Zagorac, I. Popov, F. Torić, T. Klaser, Ž. Skoko, D. Pajić, Enhancement of weak ferromagnetism, exotic structure prediction and diverse electronic properties in holmium substituted multiferroic bismuth ferrite, Phys. Chem. Chem. Phys. 25 (2023) 22345–22358.

[41] E. Bitzek, P. Koskinen, F. Gähler, M. Moseler, P. Gumbsch, Structural relaxation made simple, Phys. Rev. Lett. 97 (2006) 170201.

[42] D. Liu, J. Nocedal, On the limited memory BFGS method for large scale optimization, Math. Program. 45 (1989) 503–528.

[43] D. Johnson, Modified Broyden’s method for accelerating convergence in self-consistent calculations, Phys. Rev. B 38 (1988) 12807–12813.

[44] S. Nandy, P. Mocherla, C. Sudakar, Temperature-dependent Raman spectral evidence of local structural changes in $BiFeO_3$ thin films: Influence of substrate and oxygen vacancies, J. Appl. Phys. 135 (2024) 024101.

[45] P. Mocherla, C. Karthik, R. Ubic, M. Rao, C. Sudakar, Effect of microstrain on the magnetic properties of $BiFeO_3$ nanoparticles, Appl. Phys. Lett. 105 (2014) 132409.

[46] J. Zhang, Y.J. Wu, X.K. Chen, X.J. Chen, Structural evolution and magnetization enhancement of $Bi_{1-x}Tb_xFeO_3$, J. Phys. Chem. Solids 74 (2013) 849–853.

[47] S. Gupta, M. Tomar, V. Gupta, A. James, M. Pal, R. Guo, A. Bhalla, Optimization of excess Bi doping to enhance ferroic orders of spin casted $BiFeO_3$ thin film, J. Appl. Phys. 115 (23) (2014) 234105.

[48] G. Gomez-Iriarte, A. Pentón-Madrigal, L. Oliveira, J. Sinnecker, XPS study in $BiFeO_3$ surface modified by argon etching, Materials 15 (2022) 4285(1–13).

[49] Y. Zhang, Y. Wang, J. Qi, Y. Tian, J. Zhang, M. Wei, Y. Liu, J. Yang, Structural, magnetic and impedance spectroscopy properties of Ho^{3+} modified $BiFeO_3$ multiferroic thin film, J. Mater. Sci.: Mater. Electron. 30 (2019) 2942–2952.

Nanoscale

PAPER

View Article Online
View Journal | View Issue

Cite this: *Nanoscale*, 2017, **9**, 19337

Fortune teller fermions in two-dimensional materials†

Vladimir Damljanović, *[a] Igor Popov [a,b] and Radoš Gajić[c]

Received 18th October 2017,
Accepted 15th November 2017

DOI: 10.1039/c7nr07763g

rsc.li/nanoscale

Dirac-like electronic states are the main engines powering tremendous advancements in the research of graphene, topological insulators and other materials with these states. Zero effective mass, high carrier mobility and numerous applications are some consequences of linear dispersion that distinguishes Dirac states. Here we report a new class of linear electronic bands in two-dimensional materials with zero electron effective mass and sharp band edges, and predict stable materials with such electronic structures utilizing symmetry group analysis and an *ab initio* approach. We make a full classification of completely linear bands in two-dimensional materials and find that only two classes exist: Dirac fermions on the one hand and fortune teller-like states on the other hand. The new class supports zero effective mass similar to that of graphene and anisotropic electronic properties like that of phosphorene.

1. Introduction

Electrons can move in certain materials as if they have no mass. Massless fermions in solid state materials have played an increasingly important role since the discovery of graphene,[1] a material where zero electron effective mass is caused by linear Dirac-like dispersion. While the first mapping of the electronic structure of graphene to the Dirac equation was an interesting theoretical curiosity,[2] the true significance of the Dirac-like states in solid state systems became apparent upon identification of many physical, measurable consequences of the linear dispersion.[3] For instance, the existence of massless fermions in graphene yields extraordinarily high electron and hole mobilities[4] with revolutionary implications in electronics. Other implications include, and are not limited to, Klein tunneling in single- and bi-layer graphene,[5] and the quantum Hall[6] and fractional quantum Hall[7] effects at room temperature. The two-dimensional (2D) nature of graphene and related materials brings numerous additional advantages including mechanical flexibility, optical transparency,[8] and possibilities for engineering heterostructures with the desired properties by stacking of two or more 2D materials.[9] There is a whole plethora of various 2D materials beyond graphene with a linear dispersion in their band structure,[10] including topological insulators[11] and semimetals.[12]

Although the behavior of electrons in the vicinity of K and K' points of graphene's 2D Brillouin zone (BZ) is actually described by the Weyl equation, such points are, for historical reasons, called 2D Dirac points (occasionally, 2D Weyl points).[13] Their generalizations to 3D bulk single crystals are called (spin-1/2) Weyl points. According to the fermion doubling theorem, Weyl points (fermions) must appear in pairs of opposite chirality in the BZ. Two such Weyl fermions appearing at the same point in the BZ are called a 3D Dirac point,[14] while a pair of 3D Dirac points at the same k-vector forms a double Dirac point.[15] Note that at a band crossing, a Weyl point (3D Dirac point, double Dirac point) is two-fold (four-fold, eight-fold) degenerate. Generalizations for higher pseudo-spins are possible. Recent *ab initio* calculations show spin-1 Weyl and spin-3/2 Rarita–Schwinger–Weyl fermions in transition metal silicides,[16] such as RhSi.[17] An additional type of Dirac point appears in antiferromagnetic (AFM) 2D layers.[18,19] Here the crossing point is four-fold degenerate, the corresponding Chern number of each band is zero and such crossings can appear as a single point in the BZ. Quasiparticles in solids can even go beyond their Weyl and Dirac counterparts as shown by the classification of linear and quadratic three-, six- and eight-band crossings in 3D crystals with a strong spin–orbit coupling (SOC).[20] Other studies also discuss three-,[16] six-,[16,17] and eight-fold[15] degenerate fermions. Different types of electronic dispersions are intricately linked to symmetry, as also exemplified with cone engineering by symmetry manipulation,[21] whereas new 2D Dirac cones have been generated in graphene under an external periodic potential.[22] Mañes has used space group representations to find sufficient

[a]*Institute of Physics Belgrade, University of Belgrade, Pregrevica 118, 11080 Belgrade, Serbia. E-mail: damlja@ipb.ac.rs; Fax: +381 11 3162 190; Tel: +381 11 3713 060*

[b]*Institute for Multidisciplinary Research, University of Belgrade, Kneza Višeslava 1, 11030 Belgrade, Serbia*

[c]*Graphene Laboratory (GLAB) of Center for Solid State Physics and New Materials, Institute of Physics Belgrade, University of Belgrade, Pregrevica 118, 11080 Belgrade, Serbia*

†Electronic supplementary information (ESI) available: Group-theoretical derivations, the effective mass and density of states calculation as well as the outline of the algorithm used in *ab initio* calculations. See DOI: 10.1039/C7NR07763G

conditions for the existence of spin-1/2 Weyl points in the BZ of 3D single crystals, and enumerated the possible *T*-symmetric corepresentations of such points for spinless systems (single groups).[23] Recently, a set of symmetry conditions that guarantees 2D Dirac-like dispersion in the vicinity of high symmetry points in the BZ of any non-magnetic 2D material with negligible SOC has been reported.[24,25] Also, the existence of 2D Dirac fermions in bilayer non-honeycomb crystals using symmetry analysis has been indicated.[26] It has recently been shown that certain non-symmorphic symmetries induce new band hourglass-like dispersion at the surface of some 3D single crystals.[27] Non-symmorphic symmetries also cause a similar dispersion in 2D (layer) systems with SOC.[28,29] Topologically protected band touchings (TPBT) were found on the BZ surface of a SnTe 3D material class[30] and the A_2B_3 family of materials.[31] Note that such band touchings[27,30,31] are located away from the high-symmetry points of the BZ, and that they *can be moved but cannot be removed* by the change of model parameters used to calculate the band structure. Surprisingly, the existence of classes of massless fermions other than 2D Dirac-like, in 2D non-magnetic, time-reversal symmetric (TRS), materials with negligible SOC has not been addressed yet.

Here we report that combined TRS and certain crystal non-symmorphic symmetries of 2D materials lead to the emergence of peculiar massless linearly dispersive bands which we call fortune teller (FT) states. The geometries of these FT states in reciprocal space are pyramidal and paper fortune teller-like, unnoticed in solid state matter before. Our analysis indicates that these states and the Dirac cones are the unique possibilities for essential linear dispersive bands in all diperiodic directions of non-magnetic 2D materials without SOC. Our results are based on the analysis of all eighty layer single groups, which are all possible symmetries of non-magnetic 2D materials with negligible SOC. Inclusion of SOC would require an analysis of eighty layer double groups. These are distinct mathematical entities, and the results for the SOC-case do not apply to the non-SOC-case or *vice versa*. For this reason we treat here the non-SOC-case and leave analogous analysis for the SOC-case for future research. Similar search for Dirac-like and other (unconventional) quasiparticles has already been performed in the SOC-case.[15,20,28,29] Finally, we predict stable 2D materials with our new massless fermions using DFT and our own-developed software. The *ab initio* calculations have confirmed the existence of the predicted electronic dispersion and quantitatively determined structural and electronic properties, which can be utilized in further experimental realizations of the new class of 2D materials.

2. Classification of linear states in 2D materials

We consider all possible symmetry groups of non-magnetic crystals with negligible SOC, which are periodic in two spatial directions and finite in the perpendicular direction. These are the so-called layer single groups (or diperiodic groups). This implies that spinful degeneracy of a band is twice the spinless (orbital) degeneracy. Representation-protected band spinless degeneracy at the wave vector $\mathbf{k}_0$ in the 2D BZ, for bands belonging to the allowed[32] (relevant,[33] small[34]) irreducible representation (irrep) R of the group of the wave vector (little group) $G(\mathbf{k}_0)$, is given by the dimension of R. For all eighty layer single groups irreps R are either one- or two-dimensional.[32,35] TRS either doubles spinless band-degeneracy at given $\mathbf{k}_0$ or leaves it unchanged.[36] Therefore, possible essential spinless band-degeneracies are one, two or four.

Since the orbitally (spinless) non-degenerate band is smooth, its second derivative is finite and the effective mass, being inversely proportional to the second derivative,[37] is nonzero. Therefore, the bands carrying zero effective mass are possible only in the vicinity of points in the BZ where the electron energy is orbitally (spinless) degenerate. We show in the ESI† that in the vicinity of a spinless double degenerate point, 2D Dirac bands are the only possible massless bands.

The behavior of the bands near four-fold orbitally (spinless) degenerate points in non-magnetic 2D materials with no SOC has not been examined thus far and we perform this task as described in the next section. Before that, we comment on why we think that four-fold spinless degeneracies can only be caused by combined TRS and crystal symmetry. It is well-known that some crystal non-symmorphic symmetries combined with certain topological properties can lead to touching of two bands somewhere on high symmetry lines in the BZ. We call this topologically protected band touchings (TPBT). In such TPBT, band degeneracy is larger than required by dimensionality of irreps of the corresponding little group. Such an approach started with Zak's introduction of elementary band representations[38] (EBR) and culminated with the recent classification of all possible 10 403 band structures in double space groups.[39] Essentially, the presence of TPBT can be established by investigation of compatibility relationships of irreps along certain closed loops in the BZ.[40] Alternative formulation is in terms of non-symmorphic symmetry eigenvalues.[28,29] It sometimes happens that a band belongs to different irreps at two end points in the symmetry line and consequently must have touched another band an odd number of times (most probably once). The method cannot determine where exactly in the symmetry line two bands touch. Such a position depends on the model used to calculate the band structure. In layer single groups irreps of little groups for symmetry lines are one-dimensional inside BZ. BZ edges have either several one-dimensional irreps or only one two-dimensional irrep or two one-dimensional irreps related by TRS.[32] Corresponding three-fold (four-fold *etc.*) spinless degeneracy would require TPBT of three (four *etc.*) bands *at the same point in the BZ* which we assume is unlikely. In addition, all these three (four *etc.*) bands would have to belong to different irreps of the little group, which at some point becomes impossible. On the other hand, two double-degenerate bands at the edge of the BZ belong to the same irrep and therefore cannot touch.[41] For these reasons, we assume that TPBT can lead at most to double spinless degeneracy and to Dirac-like dispersion. The

same assumption holds even for band touchings that are not protected by topology but are model-dependent (accidental band touchings). Note that above arguments do not apply to the SOC case. For example, TPBT of two two-fold spinful degenerate bands exist in some layer double groups.[28]

3. Fortune teller states

In the following, the functional form of the new linear dispersion relation that corresponds to the vicinity of four-fold spinless degeneracy will be presented and compared to 2D Dirac-like dispersion. As before, we assume that $\mathbf{q}$ is a wave vector of small modulus, $\mathbf{t}$ a real 2D vector, u_1, u_2 positive quantities and q_1, q_2 projections of $\mathbf{q}$ along certain, mutually orthogonal directions. If $\mathbf{k}_0$ is a point that hosts a pair of 2D Dirac cones, then the Taylor expansion of the electron energy around this point reads:

$$E_{1,2}(\mathbf{k}_0+\mathbf{q}) \approx E_0 + \mathbf{t}\cdot\mathbf{q} \pm \sqrt{u_1 {q_1}^2 + u_2 {q_2}^2}. \quad (1)$$

For $u_1 = u_2$, 2D Dirac cones are isotropic and for $\mathbf{t} \neq 0$, the cones are tilted.[42,43] The new electronic dispersion presented in this paper is:

$$E_{1,2,3,4}(\mathbf{k}_0+\mathbf{q}) \approx E_0 \ \pm\ |u_1|q_1|\ \pm\ u_2|q_2||. \quad (2)$$

While the 2D Dirac band has the geometric form of a simple cone with a circular or elliptical cross section, the geometry of dispersion (2) consists of two different geometric forms. The plus sign under the absolute value yields the geometry of a four-sided pyramid, whereas the minus sign corresponds to a more complex geometry, which looks like the paper origami called paper fortune tellers [Fig. 2(b)]. Since both forms always appear together, we label dispersion (2) using one name – the fortune teller (FT) dispersion.

Next, we state the conditions that lead to four-fold essential spinless degeneracy. According to Herring,[36] there are, in principle, two possibilities for achieving this. The first one is:

O_1: $\mathbf{k}_0$ is equivalent to its inverse $-\mathbf{k}_0$,

O_2: R is two-dimensional,

O_3: R is pseudo-real or complex.

The second one is: $\mathbf{k}_0$ is not equivalent to $-\mathbf{k}_0$, $-\mathbf{k}_0$ is in the star of $\mathbf{k}_0$, R is two-dimensional, $R_{\text{in}} = R{\uparrow}G$ is pseudo-real or complex (R_{in} is the representation of the whole layer single group G, obtained by induction from R). Detailed case-by-case study of representations of layer single groups[32] shows, by exhaustion, that the second possibility never occurs in 2D non-magnetic materials with negligible SOC. A more detailed discussion on the conditions for four-fold spinless degeneracy and the classification of all massless bands in non-magnetic 2D materials with weak SOC is given in the ESI.† Therefore conditions O_1–O_3 are the only essential four-fold spinless degeneracies in such systems.

Now we show how the linear dispersion (2) is connected to TRS and crystal symmetry. A general matrix form of the Taylor expansion of a four-component Hamiltonian around a given $\mathbf{k}_0$ point of BZ is:

$$\hat{H}(\mathbf{k}_0+\mathbf{q}) \approx E_0\hat{I}_4 + \hat{H}', \quad (3)$$

where

$$\hat{H}' = \hat{W}(\hat{I}_4 \otimes |\vec{q}\rangle), \quad (4)$$

and

$$\hat{W} = \left[\left\langle \frac{\partial}{\partial \mathbf{q}}\right| \hat{H}(\mathbf{k}_0+\mathbf{q})\right]_{\mathbf{q}=0}. \quad (5)$$

$\hat{I}_4$ is a four-dimensional unit matrix, $\otimes$ denotes the Kronecker product, $\langle\partial/\partial\mathbf{q}|$ is the transposed gradient at $\mathbf{q} = 0$, hence $\hat{W}$ is a four-by-eight matrix. We can combine the representation R and its complex conjugate R^* to obtain one four-dimensional, physically irreducible, real representation D in the following way: $D = R\oplus R^*$. It follows that we can choose the basis functions $\{\varphi_1, \ldots, \varphi_4\}$ for D to be real at $\mathbf{k}_0$ so that TRS imposes the following (* denotes complex conjugation):[23]

$$\hat{H}^*(\mathbf{k}_0+\mathbf{q}) = \hat{H}(\mathbf{k}_0-\mathbf{q}). \quad (6)$$

Taking the first order derivative of this equation with respect to $\mathbf{q}$, at $\mathbf{q}$= 0 gives the following condition for $\hat{W}$:

$$\hat{W}^* = -\hat{W}. \quad (7)$$

Taking into account in addition the hermicity of the Hamiltonian, we obtain for $\hat{H}'$ the following:

$$\hat{H}' = \mathrm{i}\begin{pmatrix} 0 & \mathbf{v}_1\cdot\mathbf{q} & \mathbf{v}_2\cdot\mathbf{q} & \mathbf{v}_3\cdot\mathbf{q} \\ -\mathbf{v}_1\cdot\mathbf{q} & 0 & \mathbf{v}_4\cdot\mathbf{q} & \mathbf{v}_5\cdot\mathbf{q} \\ -\mathbf{v}_2\cdot\mathbf{q} & -\mathbf{v}_4\cdot\mathbf{q} & 0 & \mathbf{v}_6\cdot\mathbf{q} \\ -\mathbf{v}_3\cdot\mathbf{q} & -\mathbf{v}_5\cdot\mathbf{q} & -\mathbf{v}_6\cdot\mathbf{q} & 0 \end{pmatrix}, \quad (8)$$

where $\mathbf{v}_j$ are real 2D vectors. Since $\hat{H}'$ is purely imaginary, for every eigenstate ψ_n corresponding to energy E_j, there exists an eigenstate ψ_n^* that corresponds to the energy $-E_j$. Therefore, eigenvalues of $\hat{H}'$ come in pairs (E_j, $-E_j$) and the Hamiltonian $\hat{H}'$ obeys the particle-hole symmetry. The eigenvalues of $\hat{H}(\mathbf{k}_0)$ + $\hat{H}'$ given by eqn (9) confirm our statement:

$$E_{1,2,3,4} = E_0 \pm \frac{1}{\sqrt{2}}\sqrt{\sum_{j=1}^{6}(\mathbf{v}_j\cdot\mathbf{q})^2 \pm \sqrt{\left[\sum_{j=1}^{6}(\mathbf{v}_j\cdot\mathbf{q})^2\right]^2 - 4[(\mathbf{v}_1\cdot\mathbf{q})(\mathbf{v}_6\cdot\mathbf{q}) - (\mathbf{v}_2\cdot\mathbf{q})(\mathbf{v}_5\cdot\mathbf{q}) + (\mathbf{v}_3\cdot\mathbf{q})(\mathbf{v}_4\cdot\mathbf{q})]^2}}. \quad (9)$$

Note that particle-hole symmetry is not accidental, but it is a consequence of the fact that complex conjugation is a symmetry operation. More precisely, in our case the combination of TRS, reality of representation D and the fact that $\mathbf{k}_0$ is time-reversal invariant momentum leads to purely imaginary $\hat{H}'$, and to particle-hole symmetry with respect to E_0.

To further simplify eqn (9) we use the following identity[23] valid for every element (in Seitz notation) $(\hat{h}|\tau_{\hat{h}} + \mathbf{R})$ of the little group $G(\mathbf{k}_0)$:

$$\hat{H}(\mathbf{k}_0 + \mathbf{q}) = \hat{D}^{+}((\hat{h}|\tau_{\hat{h}} + \mathbf{R}))\hat{H}(\mathbf{k}_0 + \hat{h}'\mathbf{q})\hat{D}((\hat{h}|\tau_{\hat{h}} + \mathbf{R})), \quad (10)$$

where $\hat{D}((\hat{h}|\tau_{\hat{h}} + \mathbf{R}))$ is the matrix of the representation D that corresponds to the element $(\hat{h}|\tau_{\hat{h}} + \mathbf{R})$ and $\hat{h}'$ is the reduction (as an operator) of $\hat{h}$ to two-dimensional $\mathbf{k}$-space. After differentiating (10) with respect to $\mathbf{q}$, at $\mathbf{q} = 0$ we obtain (T denotes transposition):

$$\hat{W} = \hat{D}((\hat{h}|\tau_{\hat{h}} + \mathbf{R}))\hat{W}[\hat{D}((\hat{h}|\tau_{\hat{h}} + \mathbf{R})) \otimes \hat{h}']^{\mathrm{T}}. \quad (11)$$

Eqn (11) is a consequence of crystal symmetry. If we write the matrix $\hat{W}$ as a column-vector $|\hat{W}\rangle$, eqn (11) becomes:

$$[\hat{D}((\hat{h}|\tau_{\hat{h}} + \mathbf{R})) \otimes \hat{D}((\hat{h}|\tau_{\hat{h}} + \mathbf{R})) \otimes \hat{h}']|\hat{W}\rangle = |\hat{W}\rangle. \quad (12)$$

It follows that the matrix $\hat{W}$ belongs to the totally symmetric part of the representation $D \otimes D \otimes \Gamma_{\mathrm{2DPV}}$, where Γ_{2DPV} is a two-dimensional polar-vector representation. For all groups that satisfy conditions O_1–O_3 we have, using Wigner's method of group projectors, found the form that symmetry imposes on the matrix $\hat{W}$ and consequently on vectors $\mathbf{v}_j$, and inserted the result in eqn (9). In all cases, the equation for eigenvalues (9) reduces to the dispersion (2). More details on the application of group projectors are given in the ESI.†

It turns out that only three out of eighty layer single groups have allowed representations satisfying the conditions O_1–O_3. Groups allowing the dispersion (2) are listed in Table 1. All three groups are non-symmorphic and belong to the rectangular system. The component q_1 can be chosen as projection of $\mathbf{q}$ along a direction that is parallel to any screw axis 2_1, q_2 is a projection along the perpendicular direction. The points $\mathbf{k}_0$ hosting the dispersion (2) are located at the corners $(\pm\pi/a, \pm\pi/b)$ of the rectangle that presents the BZ border. The corresponding space group from Table 1 denotes the space group that is obtained by periodic repetition of layer groups' elements along the axis perpendicular to the diperiodic plane. The diperiodic plane in Table 1 denotes the position of the layer single group plane within the corresponding 3D space group. The effective mass of both dispersions (1) and (2) is zero, as shown in the ESI† using the usual formula for $\hat{m}_{\mathrm{eff}}$.[37]

Analogous four-fold degeneracies are present in bulk 3D systems,[16,17] on the surface of 3D systems[31] or in 2D AFM crystals.[18,19] These are all spinful degeneracies in the presence of SOC. Dispersion of Rarita–Schwinger–Weyl fermions[16] is proportional to $S_z\sqrt{q_x^2 + q_y^2 + q_z^2}$, where S_z is a projection of pseudo-spin $S = 3/2$ along the z-axis, while the unconventional fermion at the BZ center of RhSi is a combination of two $S = 1/2$ and two $S = 3/2$ states with a similar dispersion.[17] In 2D AFM systems the dispersion $\pm\sqrt{q_x^2 + q_y^2}$ is double degenerate,[18,19] and the same holds for surface Dirac fermions.[31] The dispersion (2) differs from these Dirac-like dispersions, it is a property specific to 2D materials and consequently falls into the range of nanophysics.

Orbital wave functions must belong to an allowed irrep at a given point in the BZ. This statement is valid irrespective of strength of electronic correlations, since the Coulomb repulsion between electrons has the same transformation properties as the rest of the Hamiltonian. The allowed irreps of the groups listed in Table 1 are the only ones at these points of the BZ, hence the electronic correlations cannot change the form of the dispersion (2) *as long as TRS and crystal symmetries are preserved*. Even if the band picture fails the energy of all electrons in the crystal has dispersion (2). If one acts simultaneously by a space group element to radius vector of every electron in the crystal the many-body wave function has the same symmetry as the single-particle wave function of the corresponding non-interacting model. On the other hand, a combination of SOC and Hubbard interaction can result in an AFM order, which then breaks TRS.[46,47] The same effect might occur even without SOC.[48] Our analysis does not refer to such cases so a detailed *ab initio* investigation of particular material should show whether transition to the AFM order occurs.

Symmetry of the crystal lattice is responsible for (an)isotropy of single crystals.[49] For example, isotropy of the electric susceptibility tensor in silicon is caused by the cubic symmetry, while the in-plane isotropy of graphene is caused by the hexagonal symmetry. In our cases, crystal axes are maximally of the second order, the irreps of the corresponding point groups are all one-dimensional and the materials belonging to layer groups listed in Table 1 are expected to be *anisotropic*.

From the analysis of irreps of layer double groups[50] we conclude that in the presence of SOC, originally eight-fold, spinful degeneracy splits into four doubly spinful degenerate levels for Dg33 and two four-fold spinful degenerate levels for Dg43 and Dg45. Since Dg43 and Dg45 contain inversion, bands are at least spinful double-degenerate, so the four-fold spinful degenerate level cannot split into four non-degenerate ones along *e.g.* the BZ-diagonal. On the other hand, layer double group

Table 1 Layer single groups hosting the dispersion (2) in the vicinity of the BZ corners: $\mathbf{k}_0 = (\pm\pi/a, \pm\pi/b)$. The notation for layer- and space-groups are according to Kopsky and Litvin[44] and Hahn,[45] respectively. The x-, y- and z-axes are along a-, b- and c-directions of the orthorhombic 3D unit cell, respectively. The notation for allowed representation in the last column is according to the Bilbao Crystallographic Server.[32] Symbol ⇔ denotes equivalence between representations. In all three cases the little group $G(\mathbf{k}_0)$ is the whole layer single group

Layer single group		Corresponding space group			Diperiodic plane	irreps R at $\mathbf{k}_0$
Dg33	$pb2_1a$	29	$Pca2_1$	C_{2v}^{5}	$y = 0$	$U_1 \Leftrightarrow U_1^*$
Dg43	$p2/b2_1/a2/a$	54	$P2_1/c2/c2/a$	D_{2h}^{8}	$y = 0$	$U_1, U_2 \Leftrightarrow U_1^*$
Dg45	$p2_1/b2_1/m2/a$	57	$P2/b2_1/c2_1/m$	D_{2h}^{11}	$x = 0$	$T_1, T_2 \Leftrightarrow T_1^*$

Dg33 does not support four-fold degeneracy at the BZ corners, which is necessary for FT dispersion. We conclude that SOC destroys FT dispersion at BZ corners of layer groups from Table 1. This result is valid irrespective of the strength of SOC. The four-fold orbital, and therefore eight-fold spinful degeneracy in layer single groups from Table 1 leads to electron band filling of $8n$ (n = 1, 2, 3, ...), as a necessary condition for bands to be either completely filled or completely empty.[51,52] This requirement remains even in the SOC case.[28] In fact Dg33, Dg43 and Dg45 are the only layer double groups with band filling $8n$ necessary for insulating systems.[28] In contrast to layer single groups from Table 1, essential eight-fold spinful degeneracy does not exist in their double group counterparts.[50] Instead, four spinful double-degenerate bands are tangled together in an hourglass manner in double-Dg43 and Dg45, while in non-centrosymmetric double-Dg33, eight non-degenerate bands form a "cat's cradle" structure.[28] Analysis of band connectivity[28] for double-Dg33, Dg43 and Dg45 confirms our prediction of SOC splitting for bands at the corners of the BZ for groups from Table 1.

Since there is only one FT dispersion in the first BZ of each group from Table 1, it is interesting to investigate if band topology requires appearance of additional dispersions somewhere else in the first BZ. According to Chern, the following integral must be an integer C_n:

$$C_n = \frac{\mathrm{i}}{2\pi}\int\int_{1^{\mathrm{st}}\,\mathrm{BZ}} \nabla_{\mathbf{q}} \times \langle \psi_n(\mathbf{q})|\nabla_{\mathbf{q}}\psi_n(\mathbf{q})\rangle \cdot \mathrm{d}^2\mathbf{S}, \qquad (13)$$

where ψ_n is the eigenstate of n^{th} level, C_n is the Chern number, while $\mathrm{i}\nabla_{\mathbf{q}} \times \langle \psi_n(\mathbf{q})|\nabla_{\mathbf{q}}\psi_n(\mathbf{q})\rangle$ is the Berry curvature.[11,53] In the case of graphene, each Dirac point gives contribution of 1/2 to the C_n and consequently, the number of Dirac points in the first BZ must be even. This is a 2D version of the Fermion doubling theorem. In contrast to graphene, our dispersion leads to zero Berry curvature for each of four states in each of the three groups. Consequently, the Berry phase is zero along any closed contour in the BZ, which gives $C_n = 0$ for all n = 1, 2, 3, 4. It follows that topology does not forbid FT to be the only dispersion at the Fermi level. Similar conclusion holds for *e.g.* AFM Dirac cone, where the contact point is also four-fold degenerate.[18]

Next we discuss the behavior of FT dispersion under strain. Application of strain that deforms the rectangular primitive cell into an oblique one, lowers the symmetry from a Dg33 to a Dg5 layer group, *i.e.* from Dg43 and Dg45 to Dg7. Since both Dg5 and Dg7 necessarily host the semi-Dirac dispersion,[54] FT dispersion splits into two pairs of semi-Dirac cones. The Chern number of semi-Dirac dispersion is zero, so such bands are topologically trivial. It follows that any linear combination of single band Chern numbers, such as mirror Chern number or spin Chern number, is also zero in this case. For strain that does not deform the rectangular primitive cell, the behavior of FT dispersion is determined by *translationengleiche* subgroups of Dg33, Dg43 and Dg45. As detailed analysis of band degeneracies in all layer single groups shows, breaking of horizontal glide plane symmetry of Dg33, splits an FT point into two spinless double-degenerate points, both belonging to double spinless degenerate lines. Such splitting occurs also in Dg43 and Dg45, when one breaks any symmetry element of their subgroup Dg33. On the other hand, breaking of any element belonging to Dg43 or Dg45 but not to Dg33 gives the final group Dg33 and FT states are robust against such deformations.

Density of states (DOS) per unit area/volume for the n^{th} energy band is given by the following formula: $\rho_n(\varepsilon) = (1/2\pi)^{D_{\mathrm{im}}}\int\int_{1^{\mathrm{st}}\,\mathrm{BZ}} \delta(\varepsilon - \varepsilon_n(\mathbf{q}))\mathrm{d}^{D_{\mathrm{im}}}\mathbf{q}$. Here, the dimensionality D_{im} is equal to three (two) for 3D (2D) systems. For Dirac dispersion $\pm v|\mathbf{q}|$ in 3D (in 2D), it is convenient to change to spherical (polar) coordinates. DOS is proportional to $\int_0^{\mathrm{bzb}} q^{D_{\mathrm{im}}-1}\delta(\varepsilon - vq)\mathrm{d}q$, where the BZ border bzb depends on the azimuthal and polar angles. For a sufficiently small energy ε measured from the bands contact point, we obtain, after including the particle-hole symmetry, $\rho_n(\varepsilon) \sim |\varepsilon|$ for 2D, *i.e.* $\rho_n(\varepsilon) \sim \varepsilon^2$ for 3D Dirac dispersion. In both cases, DOS becomes vanishingly small in the vicinity of contact points of the cones. This result refers, among other cases, also to four-fold spinful degenerate fermions in 3D.[16,17] On the other hand, change to polar coordinates does not help in calculating DOS for dispersion (2). It is more convenient to introduce linear transformations of q_1 and q_2 such that expression under the Dirac delta function contains only one variable of integration. Details of calculations are given in the ESI,† while the final result is:

$$\rho(\varepsilon) \approx \frac{3}{\pi\hbar}\left[\frac{1}{av_b} + \frac{1}{bv_a}\right], \qquad (14)$$

with degeneracy due to the spin included. Here a and b are lattice constants while v_a and v_b are Fermi velocities along a and b. It is worth noting that DOS of FT is constant around E_{F} in contrast to DOS of Dirac states in graphene. This unique coexistence of zero electron effective mass and non-zero DOS at E_0 might have consequences on *e.g.* charge transport properties. For example, a smaller sensitivity of conductance is expected when charged impurities are introduced in materials with FT states.

4. *Ab initio* search for realistic materials

Next we report examples of (meta)stable 2D materials with the desired layer groups predicted using *ab initio* calculations. We have developed and utilized software that automatically searches for materials with a given group, analyzes their stability and band structure. The outline of the algorithm is listed in the ESI.† Since the atomic SOC strength increases as the fourth power of the atomic number,[13] we limited our search only to light elements of the periodic table. For the sake of demonstration of the new electronic dispersion in real materials, we have searched for stable crystals with the above

stated symmetry groups among a few light elements, including B, C, Si and P. These are known to build stable 2D materials of various crystal symmetries and have negligible SOC. Note that the materials presented here are for demonstration purposes only, without intent to be a complete list. More elemental crystals with given symmetries are possible, while the list exponentially grows when compounds of two or more elements per unit cell are considered. Our symmetry arguments do not determine the position of FT states on the energy scale, so it is not guaranteed that the Fermi level will cross the energy near E_0. We have applied band filling theory[28,51,52] to our groups and found that the number of valence electrons per primitive cell must be an odd multiple of four, for FT states to touch exactly at E_F and that no other bands cross the Fermi level. The simplest structures satisfying these necessary (but non-sufficient) conditions have four identical nuclei in the primitive cell and belong to Dg45. The structures are listed in Table 2.

Note that we mean the *structural stability* here when we write about stability. Our DFT calculations have been conducted for the materials in an absolute vacuum. This has been a common approach in related papers.[15–18,20,27,30,31] Here we propose a new class of materials which may include dozens of materials. Their chemical stability, *i.e.* stability in the atmosphere and reactivity with oxygen and other chemicals depend on the particular material's chemical composition, hence the chemical stability varies among materials in the class. For instance, phosphorene (double layer) has a Dg45 symmetry group (hence it belongs to the new class), while its reactivity with hydrogen, oxygen and fluorine has been analyzed in detail.[55] Questions of chemical stability of other found and yet to be found materials in the new class are to be answered in future research.

A stable structure with FT contact points positioned exactly at the Fermi level [P(Dg45), marked with bold letters in Table 2] is shown in Fig. 1(a). It consists of zig-zag chains of P atoms placed alternately at two parallel planes. The potential energy surface (PES) of elemental phosphorus has multiple local minima, *i.e.* many allotropes have been recently predicted,[56] hence there are numerous (meta)stable phases of phosphorus with different symmetries. P(Dg45) is a new one, placed at the distinct local minimum of PES in the configuration subspace with the Dg45 group and 4-fold multiplicity of Wyckoff positions [Fig. 1(b)]. Its stability is further confirmed by molecular dynamics simulations at 100 K.

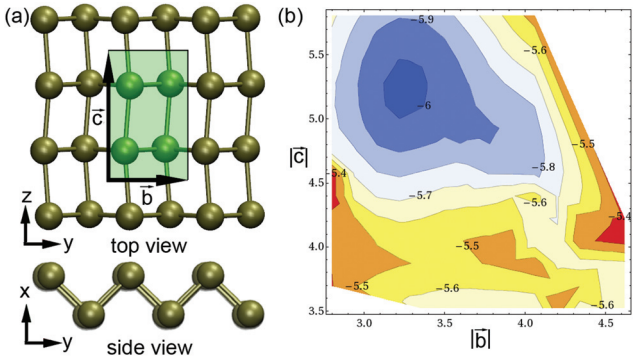

Fig. 1 Example of a stable structure with FT states at E_F. Top and side views of the optimized geometry of P(Dg45) is shown in panel (a). An elementary unit cell is marked with a green rectangle together with lattice vectors. Potential energy surface (atomization energy is given in eV per atom) in the configuration space constrained by the Dg45 group and 4-fold multiplicity of Wyckoff positions is shown in (b). The lattice parameters are given in Angstroms. Calculations are not done in the white region of panel (b) since the search algorithm predetermined instability of the crystal in this region.

The band structure of P(Dg45) along lines between high symmetry points is shown in Fig. 2(a). At *Y*–*R*–*Z* section of the BZ, four states touch at E_F (both upper and lower states are doubly spinless degenerate), yielding 4-fold spinless degeneracy at the point of contact (E_F). Constant and non-zero DOS in the vicinity of E_F confirms our prediction given by eqn (14). The bands around *R* point obey the electron–hole symmetry, in agreement with our discussion related to eqn (9). The Fermi velocities of these states in the *Y*–*R* and *R*–*Z* directions are 1.08×10^6 m s^{-1} and 0.46×10^6 m s^{-1}, which are in the range of the Fermi velocity of graphene.

The Fermi velocity of P(Dg45) is highly anisotropic. Therefore anisotropic electronic properties are expected to be similar to those of doped phosphorene.[57] The 2-fold spinless degeneracy of both lower and upper bands at *R* is lifted along the diagonal direction (*Γ*–*R*). Note another set of bands between *Z* and *Γ*, with 2-fold spinless degeneracy below E_F. More geometry details of the states around *R* are visible in Fig. 2(b). These states look exactly the same as the symmetry analysis predicted above: the FT states consisting of two pyramid-like and two paper fortune teller-like bands that touch at their tips and two lines, respectively. Sharp edges of the dispersion are unique among the electronic structure of

Table 2 Examples of stable 2D crystals with the Dg45 group. Mult. is multiplicity of Wyckoff position. E_{at} is atomization energy, *b* and *c* are lattice parameters. Coordinates of only one atom are given for each element. Other coordinates can be obtained from Wyckoff positions. $\Delta E_F = E_{FT} - E_F$ – energy difference between the Fermi level and nearest FT states. Group velocities v_b and v_c are calculated using $v_j = \frac{1}{\hbar}\frac{\partial E(k_1,k_2)}{\partial k_j}$ where index *j* corresponds to *b* or *c* lattice directions. A corresponding stable structure for carbon was not found

Element	E_{at} [eV per atom]	*b* [Å]	*c* [Å]	Coordinates [Å]	ΔE_F [eV]	v_b [10^6 m s^{-1}]	v_c [10^6 m s^{-1}]
B	−6.51	3.12	2.97	(0.390 0.387 0.743)	−0.65	1.22	1.52
Si	−5.56	3.74	4.64	(0.765 0.583 1.160)	−2.30	0.91	0.79
P	**−6.03**	**3.22**	**5.24**	**(0.780 0.708 1.310)**	**0.00**	**1.08**	**0.40**

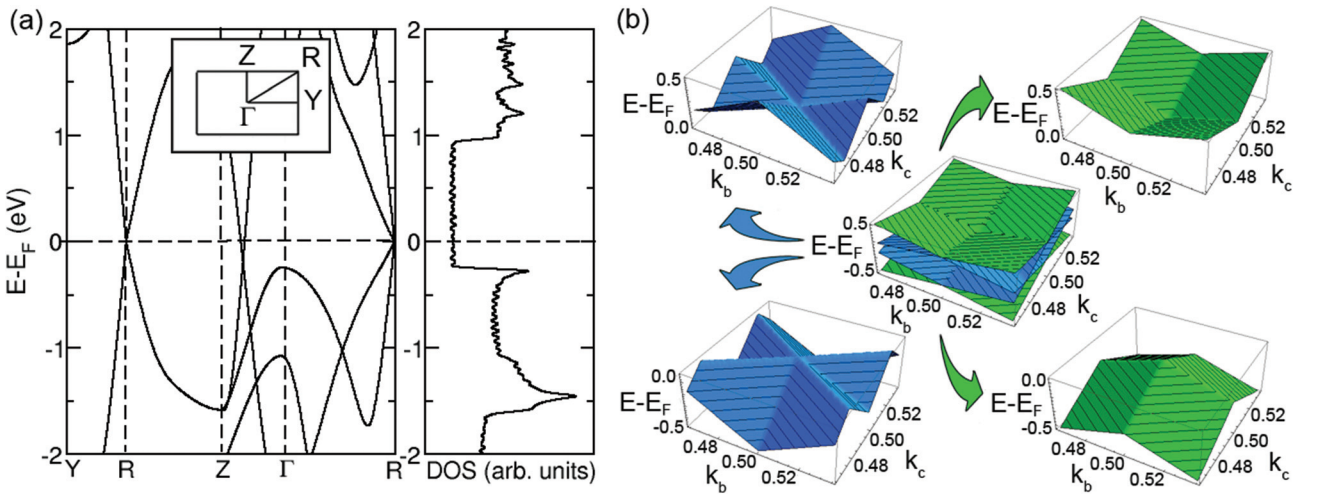

Fig. 2 The band structure of P(Dg45). (a) Electronic band structure along the lines between high-symmetry k-points (left panel) and the corresponding density of states (right panel). (b) FT states consisting of pyramidal (green) and paper fortune teller-like (blue) bands at point R. Energies are in units of eV relative to E_F, k-points are in units of $2\pi/|\mathbf{b}|$ and $2\pi/|\mathbf{c}|$. Coordinates of the R-point are (0.5, 0.5), while the $R-Z$ direction ($R-Y$ direction) is parallel to the $\mathbf{k_b}$ ($\mathbf{k_c}$) axis.

any known crystal, and particularly in contrast to the smooth features of Dirac cones.

In order to image experimentally the sharp edges as the unique signature of the FT state, angle-resolved photoemission spectroscopy (ARPES)[58] can be utilized. ARPES can probe the momentum-dependent electronic band structure of 2D materials providing detailed information on the band dispersion and Fermi surface. Importantly for the fine structural feature of edges, recent progress of this technique allows ARPES measurements with a precision of roughly 1 meV energy resolution and 0.1 degree angular resolution. Prior to application of ARPES the material should be doped to move the Fermi level from the contact point and reach a doped Fermi surface with edges. Doping can be achieved by electron transfer between the target material and a substrate which acts as a donor or an acceptor of electrons. In order to preserve the symmetry, the donor/acceptor should be sputtered to both surfaces of the target material. The contact between the substrate and only one face of the sample would reduce the symmetry of the system and open a gap. The same holds for gating, when an electric field is applied perpendicularly to the sample. These symmetry arguments explain *e.g.* the gap opening in bilayer graphene under gating.[59] On the other hand, adding dopant elements to the target material in a way that preserves the original symmetry does not affect the FT dispersion. Even though preserving symmetry in highly doped systems is a formidable task, a light doping, in percent or even ppm ranges, would be sufficient for shifting of the Fermi level from the contact points, depending on a particular material. Light doping is still negligible for breaking of crystal symmetry. Other than ARPES, inverse photoemission spectroscopy can be used to probe the unoccupied states in the electronic band structure. In addition to the edges as a very unique feature of the novel FT state, transport measurements would address the anisotropic electronic nature of the states.

5. Conclusions

In conclusion, we have established a full classification of states with linear dispersions in non-magnetic, time-reversal symmetric 2D materials with a negligible spin–orbit coupling, based on group theory analysis, and found that only one additional massless state to the Dirac one is possible. These states have not only unique and interesting geometric forms, but they also can open new horizons for both fundamental research and applications. For instance, these fermions in 2D materials do not have a counterpart in elementary particle physics, in analogy to some new fermions predicted for the 3D space groups.[15–17,20] The sharp edges in the electronic bands have been neither predicted nor measured before, so their existence in the FT states may spawn new phenomena in solid state materials. Materials with FT bands can be competitive to the popular phosphorene due to the importance of anisotropy of its electronic structure.[57] Our unified classification of linearly dispersive bands paves the way to engineer new materials with Dirac and FT states. We hope that findings presented here will be of great motivation for experimental groups to bring these materials into existence.

Author contributions

VD performed the symmetry group analysis, discovered FT dispersion, analytically calculated the effective mass, density of states and the Berry curvature, and wrote the corresponding

parts of the manuscript. IP developed and used the software for *ab initio* search, conceptualized and wrote the larger part of the manuscript. RG initiated the research with the idea that Dirac dispersion can be a consequence of symmetry.

Conflicts of interest

There are no conflicts to declare.

Acknowledgements

We are thankful to Jelena Pešić, Marko Spasenović and Andrea Damascelli for discussions and suggestions related to this work. DFT calculations were performed using computational resources at the Center of Surface and Nanoanalytics, Johannes Kepler University, Linz, Austria. We are grateful to Prof. Kurt Hingerl for providing the necessary computational resources at JKU. This work was supported by the Serbian Ministry of Education, Science and Technological Development under project numbers OI 171005 and III 45016.

References

1 K. S. Novoselov, A. K. Geim, S. V. Morozov, D. Jiang, Y. Zhang, S. V. Dubonos, I. V. Grigorieva and A. A. Firsov, *Science*, 2004, **306**, 666–669.
2 G. W. Semenoff, *Phys. Rev. Lett.*, 1984, **53**, 2449–2452.
3 A. H. Castro Neto, F. Guinea, N. M. R. Peres, K. S. Novoselov and A. K. Geim, *Rev. Mod. Phys.*, 2009, **81**, 109–162.
4 K. Bolotin, K. Sikes, Z. Jiang, M. Klima, G. Fudenberg, J. Hone, P. Kim and H. Stormer, *Solid State Commun.*, 2008, **146**, 351–355.
5 M. I. Katsnelson, K. S. Novoselov and A. K. Geim, *Nat. Phys.*, 2006, **2**, 620–625.
6 Y. Zhang, Y.-W. Tan, H. L. Stormer and P. Kim, *Nature*, 2005, **438**, 201–204.
7 X. Du, I. Skachko, F. Duerr, A. Luican and E. Y. Andrei, *Nature*, 2009, **462**, 192–195.
8 D. Akinwande, N. Petrone and J. Hone, *Nat. Commun.*, 2014, **5**, 5678.
9 A. K. Geim and I. V. Grigorieva, *Nature*, 2013, **499**, 419–425.
10 J. Wang, S. Deng, Z. Liu and Z. Liu, *Natl. Sci. Rev.*, 2015, **2**, 22–39.
11 M. Z. Hasan and C. L. Kane, *Rev. Mod. Phys.*, 2010, **82**, 3045–3067.
12 Z. K. Liu, B. Zhou, Y. Zhang, Z. J. Wang, H. M. Weng, D. Prabhakaran, S.-K. Mo, Z. X. Shen, Z. Fang, X. Dai, Z. Hussain and Y. L. Chen, *Science*, 2014, **343**, 864–867.
13 S. A. Yang, *SPIN*, 2016, **06**, 1640003.
14 S. M. Young, S. Zaheer, J. C. Y. Teo, C. L. Kane, E. J. Mele and A. M. Rappe, *Phys. Rev. Lett.*, 2012, **108**, 140405.
15 B. J. Wieder, Y. Kim, A. M. Rappe and C. L. Kane, *Phys. Rev. Lett.*, 2016, **116**, 186402.
16 P. Tang, Q. Zhou and S.-C. Zhang, *Phys. Rev. Lett.*, 2017, **119**, 206402.
17 G. Chang, S.-Y. Xu, B. J. Wieder, D. S. Sanchez, S.-M. Huang, I. Belopolski, T.-R. Chang, S. Zhang, A. Bansil, H. Lin and Z. M. Hasan, *Phys. Rev. Lett.*, 2017, **119**, 206401.
18 S. M. Young and B. J. Wieder, *Phys. Rev. Lett.*, 2017, **118**, 186401.
19 J. Wang, *Phys. Rev. B: Condens. Matter Mater. Phys.*, 2017, **95**, 115138.
20 B. Bradlyn, J. Cano, Z. Wang, M. G. Vergniory, C. Felser, R. J. Cava and B. A. Bernevig, *Science*, 2016, **353**, aaf5037.
21 L. A. Ponomarenko, R. V. Gorbachev, G. L. Yu, D. C. Elias, R. Jalil, A. A. Patel, A. Mishchenko, A. S. Mayorov, C. R. Woods, J. R. Wallbank, M. Mucha-Kruczynski, B. A. Piot, M. Potemski, I. V. Grigorieva, K. S. Novoselov, F. Guinea, V. I. Fal'ko and A. K. Geim, *Nature*, 2013, **497**, 594–597.
22 C.-H. Park, L. Yang, Y.-W. Son, M. L. Cohen and S. G. Louie, *Phys. Rev. Lett.*, 2008, **101**, 126804.
23 J. L. Mañes, *Phys. Rev. B: Condens. Matter Mater. Phys.*, 2012, **85**, 155118.
24 V. Damljanović and R. Gajić, *J. Phys.: Condens. Matter*, 2016, **28**, 085502.
25 V. Damljanović and R. Gajić, *J. Phys.: Condens. Matter*, 2016, **28**, 439401.
26 G. van Miert and C. M. Smith, *Phys. Rev. B: Condens. Matter Mater. Phys.*, 2016, **93**, 035401.
27 Z. Wang, A. Alexandradinata, R. J. Cava and B. A. Bernevig, *Nature*, 2016, **532**, 189–194.
28 B. J. Wieder and C. L. Kane, *Phys. Rev. B: Condens. Matter Mater. Phys.*, 2016, **94**, 155108.
29 S. M. Young and C. L. Kane, *Phys. Rev. Lett.*, 2015, **115**, 126803.
30 T. H. Hsieh, H. Lin, J. Liu, W. Duan, A. Bansil and L. Fu, *Nat. Commun.*, 2012, **3**, 982.
31 B. J. Wieder, B. Bradlyn, Z. Wang, J. Cano, Y. Kim, H.-S. Kim, A. M. Rappe, C. L. Kane and A. B. Bernevig, arXiv:1705.01617, 2017.
32 M. I. Aroyo, A. Kirov, C. Capillas, J. M. Perez-Mato and H. Wondratschek, *Acta Crystallogr., Sect. A: Found. Crystallogr.*, 2006, **62**, 115–128.
33 J. F. Cornwell, *Group Theory in Physics, Volume I*, Academic Press, 1984.
34 C. J. Bradley and A. P. Cracknell, *The Mathematical Theory of Symmetry in Solids*, Clarendon, 2010.
35 I. Milošević, B. Nikolić, M. Damnjanović and M. Krčmar, *J. Phys. A: Math. Gen.*, 1998, **31**, 3625.
36 C. Herring, *Phys. Rev.*, 1937, **52**, 361–365.
37 N. W. Aschroft and N. D. Mermin, *Solid State Physics*, Saunders College Publishing, 1972.
38 J. Zak, *Phys. Rev. B: Condens. Matter Mater. Phys.*, 1982, **26**, 3010–3023.
39 B. Bradlyn, L. Elcoro, J. Cano, M. G. Vergniory, Z. Wangl, C. Felser, M. I. Aroyo and A. B. Bernevig, *Nature*, 2017, **547**, 298–305.

40 L. Michel and J. Zak, *Phys. Rep.*, 2001, **341**, 377–395.
41 L. D. Landau and L. M. Lifshitz, *Quantum Mechanics: Non-Relativistic Theory*, Butterworth-Heinemann, 1981.
42 S. Katayama, A. Kobayashi and Y. Suzumura, *J. Phys. Soc. Jpn.*, 2006, **75**, 054705.
43 M. O. Goerbig, J.-N. Fuchs, G. Montambaux and F. Piéchon, *Phys. Rev. B: Condens. Matter Mater. Phys.*, 2008, **78**, 045415.
44 V. Kopsky and D. B. Litvin, *International Tables of Crystallography Volume E: Subperiodic Groups*, Kluwer Academic Publishers, 2002.
45 T. Hahn, *International Tables of Crystallography Volume A: Space-Group Symmetry*, Springer, 2005.
46 J.-M. Carter, V. V. Shankar, M. A. Zeb and H.-Y. Kee, *Phys. Rev. B: Condens. Matter Mater. Phys.*, 2012, **85**, 115105.
47 G. Sharma, Z. Zhao, P. Sarker, B. A. Nail, J. Wang, M. N. Huda and F. E. Osterloh, *J. Mater. Chem. A*, 2016, **4**, 2936–2942.
48 D. Di Sante, A. Hausoel, P. Barone, J. M. Tomczak, G. Sangiovanni and R. Thomale, *Phys. Rev. B: Condens. Matter Mater. Phys.*, 2017, **96**, 121106.
49 A. S. Nowick, *Crystal Properties Via Group Theory*, Cambridge University Press, 2005.
50 L. Elcoro, B. Bradlyn, Z. Wang, M. G. Vergniory, J. Cano, C. Felser, B. A. Bernevig, D. Orobengoa, G. de la Flor and M. I. Aroyo, *J. Appl. Crystallogr.*, 2017, **50**, 1457–1477.
51 H. Watanabe, H. C. Po, M. P. Zaletel and A. Vishwanath, *Phys. Rev. Lett.*, 2016, **117**, 096404.
52 H. Watanabe, H. C. Po, A. Vishwanath and M. Zaletel, *Proc. Natl. Acad. Sci. U. S. A.*, 2015, **112**, 14551–14556.
53 M. V. Berry, *Proc. R. Soc. London, Ser. A*, 1984, **392**, 45–57.
54 V. Damljanović and R. Gajić, *J. Phys.: Condens. Matter*, 2017, **29**, 185503.
55 D. W. Boukhvalov, A. N. Rudenko, D. A. Prishchenko, V. G. Mazurenko and M. I. Katsnelson, *Phys. Chem. Chem. Phys.*, 2015, **17**, 15209–15217.
56 J. Guan, Z. Zhu and D. Tománek, *Phys. Rev. Lett.*, 2014, **113**, 046804.
57 J. Kim, S. S. Baik, S. H. Ryu, Y. Sohn, S. Park, B.-G. Park, J. Denlinger, Y. Yi, H. J. Choi and K. S. Kim, *Science*, 2015, **349**, 723–726.
58 A. Damascelli, *Phys. Scr.*, 2004, **T109**, 61–74.
59 K. F. Mak, C. H. Lui, J. Shan and T. F. Heinz, *Phys. Rev. Lett.*, 2009, **102**, 256405.

Carbon 162 (2020) 497–501

Contents lists available at ScienceDirect

Carbon

journal homepage: www.elsevier.com/locate/carbon

Superior hardness and stiffness of diamond nanoparticles

Alexander Quandt [a], Igor Popov [b], David Tománek [c, *]

[a] Mandelstam Institute for Theoretical Physics and School of Physics, University of the Witwatersrand, 2050, Johannesburg, South Africa
[b] Institute of Physics Belgrade and Institute for Multidisciplinary Research, University of Belgrade, Belgrade, Serbia
[c] Physics and Astronomy Department, Michigan State University, East Lansing, MI, 48824, USA

ARTICLE INFO

Article history:
Received 14 January 2020
Received in revised form
20 February 2020
Accepted 25 February 2020
Available online 29 February 2020

Keywords:
ab initio
Calculation
Stability
Hardness
Nanoparticle
DFT

ABSTRACT

We introduce a computational approach to estimate the hardness and stiffness of diamond surfaces and nanoparticles by studying their elastic response to atomic nanoindentation. Results of our *ab initio* density functional calculations explain the observed hardness differences between different diamond surfaces and suggest bond stiffening in bare and hydrogenated fragments of cubic diamond and lonsdaleite. The increase in hardness and stiffness can be traced back to bond length reduction especially in bare nanoscale diamond clusters, a result of compression that is driven by the dominant role of the surface tension.

1. Introduction

In the field of ultrahard materials, the role of diamond as the hardest material on Earth seems to be well established. Not long ago, this fact has been disputed by reports that compressed fullerenes [1,2], nanotubes [3] and graphite [4–6], which occur as highly disordered and twinned nanocrystalline structures, may be still harder. Also crystalline C_3N_4 was initially believed to be harder than diamond due to its high bulk modulus [7], but ultimately turned out to be softer due to its inferior shear modulus [8,9]. On the macro-scale, mechanical hardness is commonly associated with plastic deformations introduced by an external force, whereas mechanical stiffness is associated with resistance to compression and shear in the elastic regime. This distinction becomes blurred on the nanometer scale, where the energy cost of introducing plastic deformations exceeds that of fracture [10]. There, a scratch test appears to be a more suitable measure of hardness, since the harder system need not undergo irreversible plastic deformations.

So far, theoretical attempts to correlate mechanical hardness with a particular bulk crystal structure have been mostly disappointing [11–18]. More recently, theoretical and experimental studies have established a correlation between hardness, stiffness, and linear elastic constants in covalently bounded materials [19–21]. A new interesting evidence suggests that indentation hardness may be proportional to the gravimetric density in carbon materials [22]. Progress in computational materials science suggests that *ab initio* calculations should be a valuable approach to determine the stiffness and hardness of systems beyond the reach of common experimental techniques. Observations in polycrystalline materials including cubic boron nitride indicate an increasing hardness with decreasing size of the nanocrystallites [23,24]. We find it conceivable that also diamond nanoparticles [25] should be harder than their macroscopic counterparts due to the dominant role of the surface tension, which compresses the nanoparticles and stiffens the interatomic interactions in the anharmonic regime. In the macro-scale counterpart, stiffening of diamond under pressure is evidenced in the non-vanishing third-order elastic constants [26].

At this point, we must emphasize that dislocation defects are absent in nanosized particles due to the associated large energy penalty. Consequently, Hall-Petch strengthening [27,28] associated with dislocation motion does not occur in nanoparticles. This fact sets nanostructures apart from their bulk counterparts.

Here we introduce a computational approach to estimate and compare the hardness and stiffness of diamond surfaces and nanoparticles, independent of size, by studying their elastic

* Corresponding author.
E-mail address: tomanek@msu.edu (D. Tománek).

https://doi.org/10.1016/j.carbon.2020.02.076
0008-6223/

response to atomic nanoindentation. Results of our *ab initio* density functional calculations explain the observed stiffness differences between different diamond surfaces and indicate the occurrence of bond stiffening in bare and hydrogenated fragments of cubic diamond and of lonsdaleite. The increase in stiffness, especially in bare diamond fragments, can be traced back to bond length reduction that is driven by compression and caused by the surface tension. In absence of plastic deformations on the nanometer scale, increased stiffness corresponds to an increase in hardness.

2. Results

The relaxed geometries of hydrogen-terminated C_nH_m diamondoid nanoparticles with $10 \leq n \leq 136$ carbon atoms, obtained as fragments of cubic diamond and lonsdaleite, also called hexagonal diamond, are shown in Fig. 1. Since all carbon atoms are sp^3- hybridized in these hydrogen terminated systems, the equilibrium atomic arrangement is very close to that in the bulk structure. The situation is very different in bare carbon nanoparticles, where a significant fraction of surface atoms with unsaturated bonds causes large-scale reconstruction of the structures. The equilibrium structure of C_n nanoparticles [29] comprises sp^1- bonded chains and rings for $n < 20$ and sp^2- bonded fullerenes for $n \geq 20$. Some small nanoparticles, including the C_{10} adamantane and C_{14} diamantane, maintain their strained diamond-like morphology as metastable structures. We found all larger nanoparticles in this study, with diameters up to ≈7 Å, to be unstable with respect to surface graphitization due to the dominant role of unsaturated bonds at the surface. This is true even in very large nanoparticles such as C_{136}, where half the atoms change their hybridization from sp^3 to sp^2.

As mentioned in the Introduction, mechanical hardness H is commonly associated with resilience to plastic deformations introduced by an external force. In macroscopic structures, H is measured by nanoindentation and defined by the ratio of the load acting on a sharp nanoindenter and the resulting indentation depth, as indicated schematically in Fig. 2 (a). It is an integral characteristic of a solid that reflects resistance to compression and shear and depends on quantities such as ductility, elastic stiffness, plasticity, strength, toughness, and viscosity. Since this complex response is hard to reproduce by *ab initio* techniques, a number of empirical approaches have been developed in recent years to estimate this quantity [31]. Model calculations [32,33], which have relied on simplified expressions based on a combination of valence charges, bond ionicities and interatomic distances, have so far failed to describe the dependence of hardness on the surface orientation in extended solids. Due to their dependence on a suitable choice of parameters, such model approaches are typically limited to a specific class of systems.

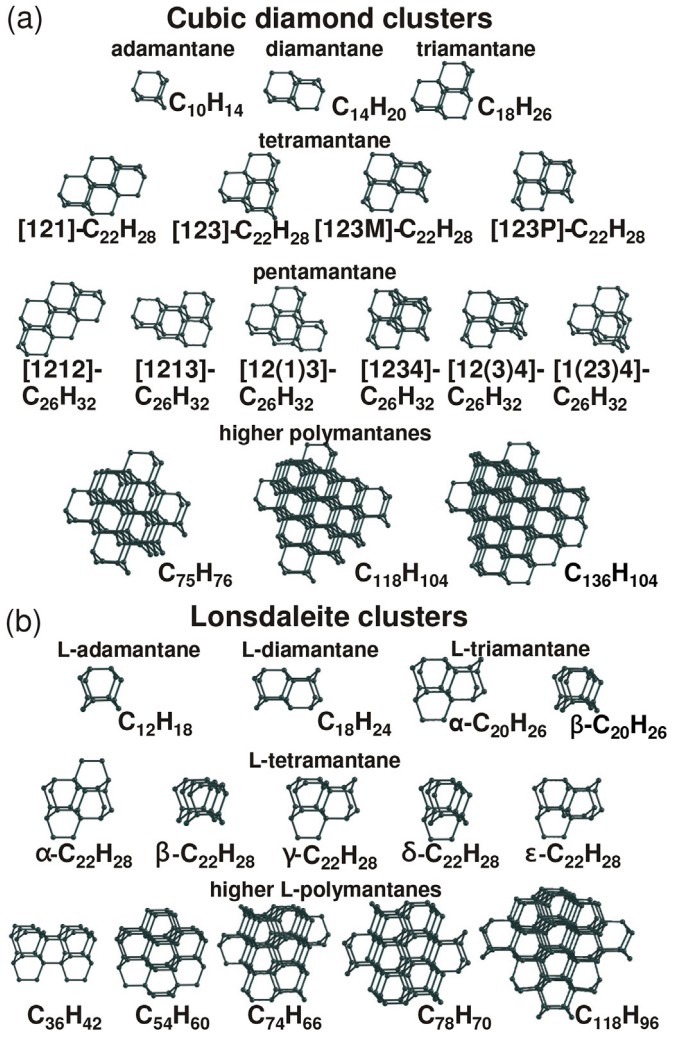

Fig. 1. Ball-and-stick models of (a) cubic diamond and (b) lonsdaleite nanoparticles. Terminating hydrogen atoms have been omitted for clarity. (A colour version of this figure can be viewed online.)

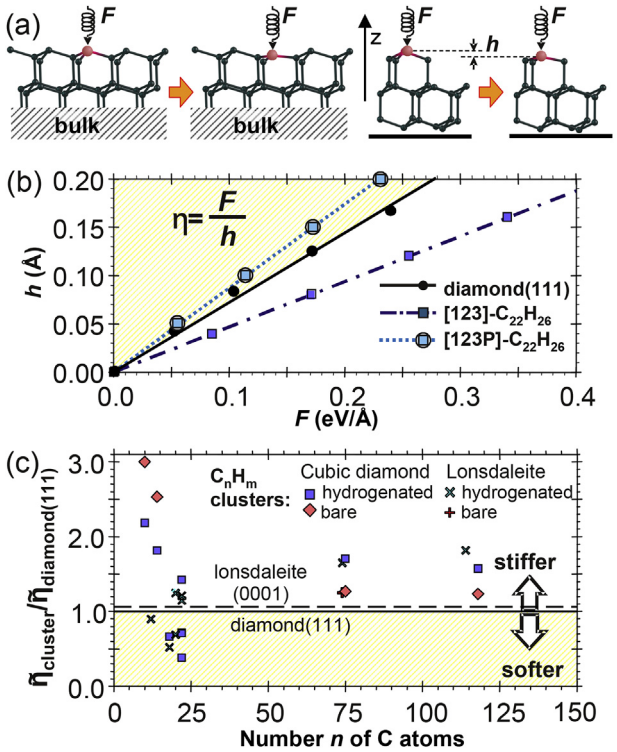

Fig. 2. (a) Schematic of an atomic nanoindenter. The displacement h of a surface atom, highlighted in red, after being subject to force F, serves as a local probe of hardness and stiffness of crystal surfaces and nanoparticles. Bulk atoms far underneath the extended surface and at the bottom of nanoparticles are constrained in the direction of the force. (b) Calculated $F - h$ relationship at the (111) cubic diamond surface and in two tetramantane isomers. (c) Normalized hardness $\bar{\eta}$ in bare and hydrogen terminated nanoparticles of cubic diamond and lonsdaleite compared to the corresponding quantity for the (111) surface of cubic diamond. Shaded regions in (b) and (c) represent response in systems softer than diamond. (A colour version of this figure can be viewed online.)

In principle, direct calculations of indentation [30] should be able to describe hardness anisotropy. Such studies would, however, necessitate very large unit cells that currently exceed the scope of accurate *ab initio* calculations. Here we introduce an alternative way to predict differences in hardness based on the elastic response to particular deformations that is based on *ab initio* total energy calculations. We have considered specifically the Rockwell nanoindentation technique [34], which relates hardness to the indentation depth caused by a conical nanoindenter that is rammed into a surface by a given force. To extend our results to nanoparticles, which are much smaller than any nanoindenter, we have identified an individual surface atom as a nanoindenter. Then, we relate the local hardness and stiffness to the $\eta = F/h$ ratio of the normal force F to the atomic displacement h.

This approach naturally describes the response to compression and shear on the atomic scale and allows us to discriminate between different surface orientations. The atomic nanoindenter is shown schematically in Fig. 2(a) for semiinfinite surfaces and nanoparticles. Our calculations determine directly the chemical stiffness of interatomic bonds at the diamond surface. This quantity is related to the earlier-defined chemical hardness [34], which measures the resistance to a change in chemical bonding. As demonstrated earlier [35], the indentation hardness is a monotonic function of the chemical hardness density.

In our computational nanoindentation study, with a setup depicted in Fig. 2(a), we displace a particular atom by the distance h normal to the surface, relax the system, and determine the force acting on the nanoindenter atom from $F = -\partial E_{total}/\partial h$. This approach requires specific structural constraints, which we specify in Section 5 on Computational Techniques.

For indentation depths h not exceeding a fraction of the carbon-carbon bond length d_{CC}, we find a linear relationship between h and F, as seen in our results for the (111) surface of cubic diamond and two tetramantane isomers in Fig. 2(b). Our results indicate that the force constant η of the [123] diamond isomer is larger and that of the [123*P*] isomer is lower than that of the (111) surface of cubic diamond. We conclude that the hardness of these particular diamond fragments is close to, and may even exceed that of the bulk crystalline diamond structure.

To compare the hardness of different crystal surfaces, we introduce the normalized hardness $\tilde{\eta}$, which we define by

$$\tilde{\eta} = \frac{\eta}{A} = \frac{F}{h \cdot A}\,, \qquad (1)$$

where A is the area per atom at a particular surface. We have combined observed hardness values H with our calculated values of the related quantity $\tilde{\eta}$ for different surfaces of cubic diamond and lonsdaleite in Table 1. Experimental data indicate that the (111) surface is the hardest surface of cubic diamond and that the (100) surface is 18% softer. Even though our computational approach does not provide absolute hardness values, the calculated ratio $\tilde{\eta}(100)/\tilde{\eta}(111) = 0.88$ agrees well with the ratio of the observed hardness values $H(100)/H(111) = 0.82$ in cubic diamond [1]. There are no experimental observations for the lonsdaleite structure, which occurs only as inclusions in cubic diamond and is believed to be somewhat harder. Based on our calculated values of $\tilde{\eta}$ listed in Table 1, we believe that the (0001) surface of lonsdaleite may be 2% harder than the (111) surface of cubic diamond.

Table 1
Observed hardness H and calculated normalized hardness $\tilde{\eta}$ at the (111) and (100) surfaces of cubic diamond and the (0001) surface of lonsdaleite, as well as ratios of these quantities.

	Diamond		$\frac{(100)}{(111)}$	Lonsdaleite	$\frac{(0001)}{(111)}$
	(111)	(100)		(0001)	
H (GPa)	167±5[a] 117[b]	137±6[a] 95[b]	0.82±0.06 0.81	–	–
$\tilde{\eta}$ (eV/Å^3)	0.72	0.64	0.88	0.74	1.02

[a] Ref. [1].
[b] Ref. [30].

Results in Table 1 indicate that presence of lonsdaleite alone may not explain reported hardness values that are significantly higher than those of cubic diamond [1-6]. Therefore, we determine the normalized hardness $\tilde{\eta}$ also for hydrogen-terminated and bare diamond nanoparticles. For a reasonable comparison, we have aligned each nanoparticle so that the topmost atom of the unrelaxed structure, which will be subject to force F, belongs to the (111) surface of cubic diamond or to the corresponding (0001) surface of lonsdaleite. Since the area per atom is affected by the net contraction of the nanoparticle, we estimated its surface area S from that of a polyhedron spanned by the nuclei of the outermost atoms. We then used $A = A_i \times (S_f/S_i)$ for the atom area in Eq. (1), where A_i is the area per atom at the corresponding infinite surface and S_f/S_i is the ratio of total nanoparticle surface areas in the final (f) and the initial (i) structures.

We present our results for $\tilde{\eta}$ in hydrogen covered and bare nanoparticles of cubic diamond as well as lonsdaleite in Fig. 2(c) and compare them to those for the (111) surface of cubic diamond. Our results indicate that a significant fraction of diamond nanoparticles appears to be significantly harder than the hardest diamond surface. We find large differences in the calculated values of $\tilde{\eta}$ even between different isomers of the same nanostructure, such as the [123] and [123*P*] isomers of tetramantane. Their different elastic response, depicted in Fig. 2(b), reflects the simple fact that particular structures may expand more or less easily in the plane normal to the applied force. This flexibility is partly suppressed in polycrystalline bulk assemblies of nanoparticles and also in larger free-standing structures, which, however, approach bulk diamond values with increasing nanoparticle size.

3. Discussion

There is an intuitive explanation for our finding that the apparent hardness increases with decreasing size of diamond nanoparticles. We need to note at this point that hardness enhancement in nanoparticles of diamond and other solids is fundamentally different from the behavior observed in macrostructures, often described as the Hall-Petch effect, which is associated with the nucleation and motion of dislocations [27,28]. As mentioned earlier, plastic deformations do not occur in nanoparticles due to the associated high energy cost.

In nanoparticles with a significant portion of surface atoms, surface tension reduces significantly the surface area and thus the interatomic bond length d_{CC}. We have determined the bond length distribution in all nanoparticles presented in Fig. 1 and plot this quantity separately for bare and for hydrogenated nanoparticles in Fig. 3(a). Termination by hydrogen reduces the surface energy and provides a bulk-like bonding environment even for carbon atoms at the surface. Therefore, bond lengths in hydrogenated nanoparticles are all close to the 1.54 Å value found in sp^3- hybridized diamond. On the other hand, we observe a significant bond length contraction in bare diamond nanoparticles. Under-coordinated atoms at the surface, which dominate in small nanoparticles, reconstruct to form a “net” that contains and compresses the “bulk” of the structure in a “snug fit”. Most surface atoms relax to a more favorable sp^2- like graphitic bonding geometry with $d_{CC} \approx 1.42$ Å. Only a small fraction of two-fold coordinated surface atoms is bonded in an sp^1- like carbyne environment with $d_{CC} \approx 1.28$ Å. The

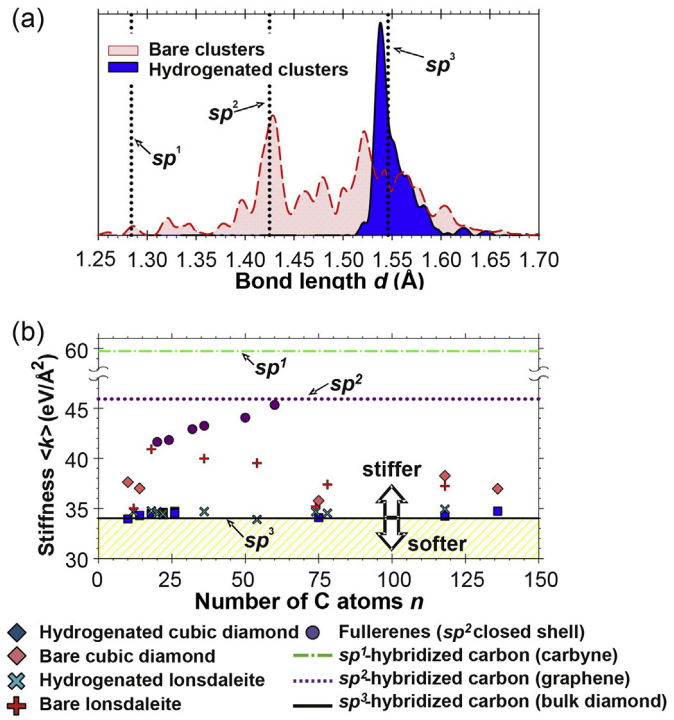

Fig. 3. (a) Bond length distribution in C_nH_m diamond nanoparticles of Fig. 1. The light (red) shaded area below the dashed line represents bare C_n nanoparticles, and the dark (blue) shaded area below the solid line represents hydrogenated nanoparticles. (b) Comparison between the average bond stiffness $\langle k \rangle$, defined in Eq. (2), in the nanoparticles of panel (a) and in sp^1, sp^2 and sp^3 bonded bulk systems. (A colour version of this figure can be viewed online.)

degree of bond contraction we find in nano-diamond agrees with estimates for nanometer-sized diamond particles based on elastic constants and surface energy. Due to the anharmonicity in the interatomic bonds, the net bond contraction should cause a stiffening in particular of bare nanoparticles. This reasoning is consistent with the recent observation [22] that indentation hardness increases at higher densities caused by bond contraction and reconstruction in nanostructures.

To validate our interpretation, we estimated the bond stiffness in nanoparticles considered in our study. In each optimized nanoparticle, we first determined the average bond length $\langle d_{CC,0} \rangle$ and the bond energy $E_{b,0} = E_{coh,0}/N_b$ by dividing the cohesive energy E_{coh} by the number of nearest-neighbor bonds N_b. We then uniformly expanded or contracted the nanoparticle and determined the corresponding average bond length $\langle d_{CC,0} \rangle$ and bond energy E_b. Finally, we determined the average bond stiffness $\langle k \rangle$ in a given particle using

$$|E_b - E_{b,0}| = \frac{1}{2}\langle k \rangle \left(\langle d_{CC} \rangle - \langle d_{CC,0} \rangle \right)^2 . \qquad (2)$$

We plot the quantity $\langle k \rangle$ for C_nH_m nanoparticles and compare it to that of sp^3, sp^2 and sp^1 hybridized systems in Fig. 3(b). Our results indicate that the bond stiffness in hydrogenated nanoparticles is comparable to that in sp^3- hybridized diamond and is typically much higher in bare nanoparticles, approaching the higher bond stiffness of sp^2- hybridized graphene. For the sake of fair comparison, we also present bond stiffness values of fullerenes in Fig. 3(b). These hollow graphitic nanoparticles display sp^2 bonding with a small sp^3 admixture, and their bond stiffness values are in the expected range. We conclude that the enhanced bond stiffness in bare nanoparticles is caused by surface reconstruction from dominant sp^3 to at least partial sp^2- type bonding. We may expect that diamond nanoparticles with a graphitized outer surface, which are often observed experimentally [36], may have stiffer bonds than diamond.

At this point we should re-emphasize that the connection between bond stiffness, reflecting elastic response, and hardness, which describes irreversible plastic deformations, is only indirect. Bond stiffness describes the resistance of bonds to stretching and compression, which we model by uniformly compressing the entire structure. On the other hand, hardness characterizes the resistance of a structure to indentation, which we model by displacing one single surface atom. The hardest nanoparticles in our study were bare and hydrogen-terminated $C_{10}H_x$ adamantane and $C_{14}H_x$ diamantane nanoparticles. With the exception of these two systems, hydrogenated nanoparticles were found to be harder than bare nanoparticles. The significant increase in nominal hardness, which we found in ultra-small nanoparticles, diminishes rapidly in systems containing hundreds of carbon atoms and approach rapidly well-established bulk values.

4. Summary and conclusions

In conclusion, we have introduced a computational approach to estimate and compare the hardness and stiffness of both single-crystal surfaces and nanoparticles of diamond, which are too small for indentation experiments, by studying their elastic response to atomic nanoindentation. Results of our *ab initio* density functional calculations of this nanoindentation process correlated well with the observed differences in hardness between different diamond surfaces. More important, we find bond stiffening in bare and hydrogenated fragments of both cubic diamond and lonsdaleite. The increase in stiffness, especially in bare nano-diamond particles, can be traced back to bond length reduction. The net average bond compression is driven by the dominant role of the surface tension and leads to surface reconstruction. Since plastic deformations do not occur on the nanometer scale, increased stiffness indicates an increase in hardness. It is likely that the scratch hardness of diamond nanoparticles, which are used to cover drill heads, may exceed that of monocrystalline diamond.

5. Computational Techniques

5.1. Representation of nanoindentation

We represent a periodic infinite surface, shown in the left panels of Fig. 2(a), by a unit cell with a finite surface area, which contains infinitely many atoms below the surface. In principle, the displacement of the atomic nanoindenter along the $-z$ direction into the surface may cause all atoms within the unit cell to move, but the shape of the unit cell will not change. In our study, we only allow atomic displacement within a thick surface region above a frozen bulk structure that balances the force caused by the nanoindenter. E_{total} is determined for the optimized geometry.

In finite nanoparticles, depicted in the right panels of Fig. 2(a), there are no symmetry restrictions on atomic displacements or global shape deformations. To provide a realistic description of nanoindentation in a previously relaxed nanoparticle, we first displace the atomic nanoindenter along the $-z$ direction. Next, we fix the z-coordinates, but not the x- and y-coordinates, of all bottom atoms of the nanoparticle to balance the force caused by the nanoindenter. Finally, we relax all remaining atomic degrees of freedom and determine E_{total}. For both infinite surfaces and finite nanoparticles, we obtain the force that caused the deformation from $F = -\partial E_{total}/\partial h$.

5.2. Total energy formalism

Our calculations of the optimum atomic structure, stability and elastic properties of diamond surfaces and nanoparticles are based on the density functional theory (DFT) [37,38]. We used the PBE-PAW approximation [39] to DFT, as implemented in the VASP [40–42] code. All systems have been represented using periodic boundary conditions and a plane-wave energy cutoff of 520 eV. Spurious interaction between neighboring particles has been suppressed by requiring the closest-approach distance between adjacent surfaces to exceed [43] 6 Å. All structures have been relaxed until all forces acting on atoms were less than 0.01 eV/Å.

Declaration of competing interest

The authors declare that they have no known competing financial interests or personal relationships that could have appeared to influence the work reported in this paper.

CRediT authorship contribution statement

Alexander Quandt: Methodology, Validation, Writing - original draft. **Igor Popov:** Investigation, Visualization, Writing - original draft. **David Tománek:** Conceptualization, Methodology, Visualization, Validation, Writing - original draft.

Acknowledgments

We thank Mikhail Yu. Popov and Arthur G. Every for useful discussions. This study was supported by the NSF/AFOSR EFRI 2-DARE grant number EFMA-1433459. Computations have been performed by Liubov Yu. Antipina and Pavel B. Sorokin while visiting Michigan State University in 2013–2014. Computational resources have been provided by the Michigan State University High Performance Computing Center and the Moscow State University Supercomputer. AQ thanks the Materials for Energy Research Group (MERG) and the DST-NRF Centre of Excellence in Strong Materials (CoE-SM) at the University of the Witwatersrand for support. AQ and DT also thank the Mandelstam Institute for Theoretical Physics (MITP) and the Simons Foundation, award number 509116, for support.

References

[1] V. Blank, M. Popov, G. Pivovarov, N. Lvova, K. Gogolinsky, V. Reshetov, Ultrahard and superhard phases of fullerite C_{60}: comparison with diamond on hardness and wear, Diam. Relat. Mater. 7 (2–5) (1998) 427–431.
[2] L. Wang, B. Liu, H. Li, W. Yang, Y. Ding, S.V. Sinogeikin, Y. Meng, Z. Liu, X.C. Zeng, W.L. Mao, Long-range ordered carbon clusters: a crystalline material with amorphous building blocks, Science 337 (6096) (2012) 825–828.
[3] M. Popov, M. Kyotani, Y. Koga, Superhard phase of single-wall carbon nanotube, Phys. B Condens. Matter 323 (1–4) (2002) 262–264.
[4] W.L. Mao, H. Mao, P.J. Eng, T.P. Trainor, M. Newville, C. Kao, D.L. Heinz, J. Shu, Y. Meng, R.J. Hemley, Bonding changes in compressed superhard graphite, Science 302 (5644) (2003) 425–427.
[5] T. Irifune, A. Kurio, S. Sakamoto, T. Inoue, H. Sumiya, Ultrahard polycrystalline diamond from graphite, Nature 421 (2003) 599–600.
[6] K. Tanigaki, H. Ogi, H. Sumiya, K. Kusakabe, N. Nakamura, M. Hirao, H. Ledbetter, Observation of higher stiffness in nanopolycrystal diamond than monocrystal diamond, Nat. Commun. 4 (2013) 2343.
[7] A.Y. Liu, M.L. Cohen, Prediction of new low compressibility solids, Science 245 (4920) (1989) 841–842.
[8] D.M. Teter, R.J. Hemley, Low-compressibility carbon nitrides, Science 271 (5245) (1996) 53–55.
[9] G.S. Manyali, R. Warmbier, A. Quandt, J.E. Lowther, *Ab initio* study of elastic properties of super hard and graphitic structures of C_3N_4, Comput. Mater. Sci. 69 (2013) 299–303.
[10] A. Griffith, VI. The phenomena of rupture and flow in solids, Phil. Trans. Roy. Soc. Lond. A221 (1920) 163–198.
[11] L. Chernozatonskii, N. Serebryanaya, B. Mavrin, The superhard crystalline three-dimensional polymerized C_{60} phase, Chem. Phys. Lett. 316 (3–4) (2000) 199.
[12] S. Berber, E. Osawa, D. Tomanek, Rigid crystalline phases of polymerized fullerenes, Phys. Rev. B 70 (8) (2004), 085417.
[13] Q. Li, Y. Ma, A.R. Oganov, H. Wang, H. Wang, Y. Xu, T. Cui, H.-K. Mao, G. Zou, Superhard monoclinic polymorph of carbon, Phys. Rev. Lett. 102 (17) (2009) 175506.
[14] K. Umemoto, R.M. Wentzcovitch, S. Saito, T. Miyake, Body-centered tetragonal C^4: sp^3carbon allotrope, Phys. Rev. Lett. 104 (12) (2010) 125504.
[15] J.-T. Wang, C. Chen, Y. Kawazoe, Low-temperature phase transformation from graphite to sp^3orthorhombic carbon, Phys. Rev. Lett. 106 (7) (2011), 075501.
[16] D. Selli, I.A. Baburin, R. Martoňák, S. Leoni, Superhard sp^3carbon allotropes with odd and even ring topologies, Phys. Rev. B 84 (2011) 161411.
[17] M. Amsler, J.A. Flores-Livas, L. Lehtovaara, F. Balima, S.A. Ghasemi, D. Machon, S. Pailhès, A. Willand, D. Caliste, S. Botti, A. San Miguel, S. Goedecker, M.A.L. Marques, Crystal structure of cold compressed graphite, Phys. Rev. Lett. 108 (2012), 065501.
[18] Y.A. Kvashnina, A.G. Kvashnin, P.B. Sorokin, Investigation of new superhard carbon allotropes with promising electronic properties, J. Appl. Phys. 114 (18) (2013) 183708.
[19] X.-Q. Chen, H. Niu, D. Li, Y. Li, Modeling hardness of polycrystalline materials and bulk metallic glasses, Intermetallics 19 (9) (2011) 1275–1281.
[20] V.A. Mukhanov, O.O. Kurakevych, V.L. Solozhenko, Thermodynamic aspects of materials' hardness: prediction of novel superhard high-pressure phases, High Pres. Res. 28 (4) (2008) 531–537.
[21] X. Jiang, J. Zhao, X. Jiang, Correlation between hardness and elastic moduli of the covalent crystals, Comput. Mater. Sci. 50 (7) (2011) 2287–2290.
[22] S. Kang, Z. Xiang, H. Mu, Y. Cai, Mechanical properties, lattice thermal conductivity, infrared and Raman spectrum of the fullerite C_{24}, Phys. Lett. A 384 (1) (2020) 126035.
[23] N. Dubrovinskaia, V.L. Solozhenko, N. Miyajima, V. Dmitriev, O.O. Kurakevych, L. Dubrovinsky, Superhard nanocomposite of dense polymorphs of boron nitride: noncarbon material has reached diamond hardness, Appl. Phys. Lett. 90 (10) (2007) 101912.
[24] V.L. Solozhenko, O.O. Kurakevych, Y.L. Godec, Creation of nanostuctures by extreme conditions high-pressure synthesis of ultrahard nanocrystalline cubic boron nitride, Adv. Mater. 24 (12) (2012) 1540–1544.
[25] J.E. Dahl, J.M. Moldowan, K.E. Peters, G.E. Claypool, M.A. Rooney, G.E. Michael, M.R. Mello, M.L. Kohnen, Diamonxdoid hydrocarbons as indicators of natural oil cracking, Nature 399 (7) (1999) 54–57.
[26] M.H. Grimsditch, E. Anastassakis, M. Cardona, Effect of uniaxial stress on the zone-center optical phonon of diamond, Phys. Rev. B 18 (1978) 901–904.
[27] H. Van Swygenhoven, Grain boundaries and dislocations, Science 296 (5565) (2002) 66–67.
[28] Y. Mo, D. Stone, I. Szlufarska, Strength of ultrananocrystalline diamond controlled by friction of buried interfaces, J. Phys. D Appl. Phys. 44 (40) (2011) 405401, and 45, 069501 (2012) (E).
[29] D. Tomanek, M.A. Schluter, Growth regimes of carbon clusters, Phys. Rev. Lett. 67 (17) (1991) 2331–2334.
[30] A. Richter, R. Ries, R. Smith, M. Henkel, B. Wolf, Nanoindentation of diamond, graphite and fullerene films, Diam. Relat. Mater. 9 (2) (2000) 170–184.
[31] Y. Tian, B. Xu, Z. Zhao, Microscopic theory of hardness and design of novel superhard crystals, Int. J. Refract. Metals Hard Mater. 33 (2012) 93–106.
[32] A. Šimůnek, Anisotropy of hardness from first principles: the cases of ReB_2 and OsB_2, Phys. Rev. B 80 (2009), 060103.
[33] F. Gao, Theoretical model of hardness anisotropy in brittle materials, J. Appl. Phys. 112 (2) (2012), 023506.
[34] J. Gilman, Chemistry and Physics of Mechanical Hardness, John Wiley & Sons, 2009.
[35] W. Yang, R.G. Parr, L. Uytterhoeven, New relation between hardness and compressibility of minerals, Phys. Chem. Miner. 15 (2) (1987) 191–195.
[36] S. Welz, Y. Gogotsi, M.J. McNallan, Nucleation, growth, and graphitization of diamond nanocrystals during chlorination of carbides, J. Appl. Phys. 93 (7) (2003) 4207.
[37] P. Hohenberg, W. Kohn, Inhomogeneous electron gas, Phys. Rev. 136 (3B) (1964) 864–871.
[38] W. Kohn, L.J. Sham, Self-consistent equations including exchange and correlation effects, Phys. Rev. 140 (4A) (1965) 1133–1138.
[39] J.P. Perdew, K. Burke, M. Ernzerhof, Generalized gradient approximation made simple, Phys. Rev. Lett. 77 (18) (1996) 3865–3868.
[40] G. Kresse, J. Hafner, Ab initio molecular dynamics for liquid metals, Phys. Rev. B 47 (1) (1993) 558–561.
[41] G. Kresse, J. Hafner, Ab initio molecular-dynamics simulation of the liquid-metal-amorphous-semiconductor transition in germanium, Phys. Rev. B 49 (20) (1994) 14251–14269.
[42] G. Kresse, J. Furthmüller, Efficient iterative schemes for ab initio total-energy calculations using a plane-wave basis set, Phys. Rev. B 54 (1996) 11169–11186.
[43] On a per-surface-atom basis, the interaction energy between diamond surfaces separated by 6 Å differs by less than 0.02 meV from that for surfaces separated by 10 Å.

PAPER

Designing topological defects in 2D materials using scanning probe microscopy and a self-healing mechanism: a density functional-based molecular dynamics study

To cite this article: Igor Popov *et al* 2017 *Nanotechnology* **28** 495706

IOP Publishing Nanotechnology
Nanotechnology **28** (2017) 495706 (8pp) https://doi.org/10.1088/1361-6528/aa9679

Designing topological defects in 2D materials using scanning probe microscopy and a self-healing mechanism: a density functional-based molecular dynamics study

Igor Popov[1,2], **Ivana Đurišić**[2] **and Milivoj R Belić**[3]

[1] Institute for Multidisciplinary Research, University of Belgrade, Kneza Višeslava 1, 11030 Belgrade, Serbia
[2] Institute of Physics Belgrade, University of Belgrade, Pregrevica 118, 11080 Belgrade, Serbia
[3] Science Program, Texas A & M University at Qatar, P.O. Box 23874, Qatar

E-mail: popov@ipb.ac.rs

Received 23 August 2017, revised 25 October 2017
Accepted for publication 27 October 2017
Published 15 November 2017

Abstract

Engineering of materials at the atomic level is one of the most important aims of nanotechnology. The unprecedented ability of scanning probe microscopy to address individual atoms opened up the possibilities for nanomanipulation and nanolitography of surfaces and later on of two-dimensional materials. While the state-of-the-art scanning probe lithographic methods include, primarily, adsorption, desorption and repositioning of adatoms and molecules on substrates or tailoring nanoribbons by etching of trenches, the precise modification of the intrinsic atomic structure of materials is yet to be advanced. Here we introduce a new concept, scanning probe microscopy with a rotating tip, for engineering of the atomic structure of membranes based on two-dimensional materials. In order to indicate the viability of the concept, we present our theoretical research, which includes atomistic modeling, molecular dynamics simulations, Fourier analysis and electronic transport calculations. While stretching can be employed for fabrication of atomic chains only, our comprehensive molecular dynamics simulations indicate that nanomanipulation by scanning probe microscopy with a rotating tip is capable of assembling a wide range of topological defects in two-dimensional materials in a rather controllable and reproducible manner. We analyze two possibilities. In the first case the probe tip is retracted from the membrane while in the second case the tip is released beneath the membrane allowing graphene to freely relax and self-heal the pore made by the tip. The former approach with the tip rotation can be achieved experimentally by rotation of the sample, which is equivalent to rotation of the tip, whereas irradiation of the membrane by nanoclusters can be utilized for the latter approach. The latter one has the potential to yield a yet richer diversity of topological defects on account of a lesser determinacy. If successfully realized experimentally the concept proposed here could be an important step toward controllable nanostructuring of two-dimensional materials.

Keywords: graphene membrane, atomic structure, nanostructuring, topological defects, molecular dynamics, scanning probe methods

(Some figures may appear in colour only in the online journal)

1. Introduction

Precise, accurate and predictable nanostructuring is an ultimate goal of nanophysics and nanotechnology. Scanning probe microscopy (SPM) including scanning tunneling microscopy (STM) [1] and atomic force microscopy (AFM) [2] have proven records of their capabilities for nanostructuring (i.e. scanning probe nanostructuring—SPN) at the nanometer level. Impressive precision has already been demonstrated by Eigler in 1989 who manipulated 35 individual xenon atoms on a nickel substrate [3]. The first nanostructuring demonstration was followed by nanoscale patterning of a H-passivated Si(100) surface by STM [4], which paved the way for using STM as a tool in lithography processes [5]. The focus of research in SPN techniques has been mainly on adsorption, desorption and manipulation of adatomic and molecular decorations of substrates [6–11]. Local anodic oxidation [12, 13] is also often utilized, which can provide a spatially controlled modification of various materials including graphene sheets [14]. Complex structures with lithographic resolutions down to 25 nm have been demonstrated using the AFM method [15, 16], whereas much higher spatial resolutions down to 2.5 nm have been achieved by STM in the fabrication of graphene nanoribbons with the desired crystallographic orientations [17]. The thermochemical nanolithography technique has also been presented as a promising SPN–AFM method [18].

Here we introduce a conceptually new approach to SPN: utilization of SPM with a rotating tip as an additional degree of freedom. Using atomistic modeling, density functional-based molecular dynamics simulations, and Fourier analysis we demonstrate this concept with the engineering of topological defects in a suspended graphene membrane, whereas the method is transferable to the larger class of two-dimensional (2D) materials. Defects have important roles in the properties of graphene and other 2D materials [19, 20] hence large effort has been invested in understanding their effects, detection, elimination or utilization in the engineering of the desired material properties [21, 22]. Our simulations indicate that a choice of a material for the scanning probe tip, which does not strongly chemically interact with the graphene, allows rebinding of carbon atoms based primarily on positions of the atoms relative to the nearest atomic neighbors of the tip. Rotation of the tip presents an additional degree of freedom to the standard SPM, which can provide a finer precision necessary to achieve the desired relative positioning of the tip and carbon neighbors. Note that one can rotate the membrane rather than the tip to achieve the same effect, since only relative positions matter. Application of STM on a rotating sample has already been experimentally demonstrated [23]. In the second part of the manuscript we analyze the possibility of engineering topological defects by the self-healing mechanism upon instant removal of the tip from the graphene membrane after the tip has penetrated the membrane up to certain depths. This approach can also be realized in an equivalent experiment with a similar effect, for example by irradiation of the graphene membrane by energetic nanoscale clusters. The experimental feasibility of generating defects in graphene by this method but with supersonic microclusters has been recently demonstrated [24].

2. Method

We employed the density functional-based tight binding (DFTB) method [25, 26] as implemented in DFTB+ code [27]. The method has a proven record in the research of plastic deformations of graphene, including our reports on the breaking of graphene nanoribbons under extreme uniaxial stresses [28–30]. We performed geometry optimizations, molecular dynamics (MD) simulations and electronic transport calculations within a Γ-point approximation. The initial geometries prior to MD simulations were fully relaxed by conjugate gradient optimization where the maximal force on atoms was smaller than 0.04 eV $Å^{-1}$. Van der Waals interaction was included in calculations. Conductance of the systems was obtained by DFTB augmented by Green's functions [31], whereas the Landauer–Buttiker [32] formula was utilized for calculations of electronic current.

We investigated the mechanism of piercing of suspended graphene using an atomically sharp STM tip within the supercell approach. The length of the supercell was 4.92 nm along the armchair direction of graphene and 5.11 nm along its zig-zag direction. The whole supercell contained 960 carbon (C) atoms and 120 gold (Au) atoms (figure 1(a)). The tip consisted of face-centered cubic Au crystal with a pyramidal geometry. The tip apex was made of a single Au atom. The sides of the pyramid corresponded to the stable Au(111) surfaces, as shown in figure 1(a). The existence of pyramidal golden nanoclusters has been reported before [33]. We chose gold for the tip material since, as a noble metal, it does not strongly chemically interact with other materials, including graphene. In order to isolate the effects of the tip on graphene from eventual changes of tip geometry we did not allow Au atoms to relax during the simulations, essentially simulating an ideally rigid tip. The approximation was adequate for proving the concept while other weakly reactive tips, stronger than the target 2D material, should be utilized in real experiment.

3. Results and discussion

The drilling started with the tip apex initially positioned above one of the three high-symmetry sites of graphene: the center of a phenyl ring (*hollow site*), on the top of a carbon atom (*top site*) or at the middle of a C–C bond (*bridge site*). The suspension of graphene is simulated by fixing C atoms that encompass two rows of phenyl rings at each edge of the simulated membrane. The starting position of the tip apex is 2 Å above the graphene. We optimized all initial geometries prior to MD simulations using the conjugate gradient method. The tip–graphene repulsion caused a shallow sag in the graphene with maximal departure of C atoms by 1.01 Å from the basal graphene plane (i.e. fixed C atoms).

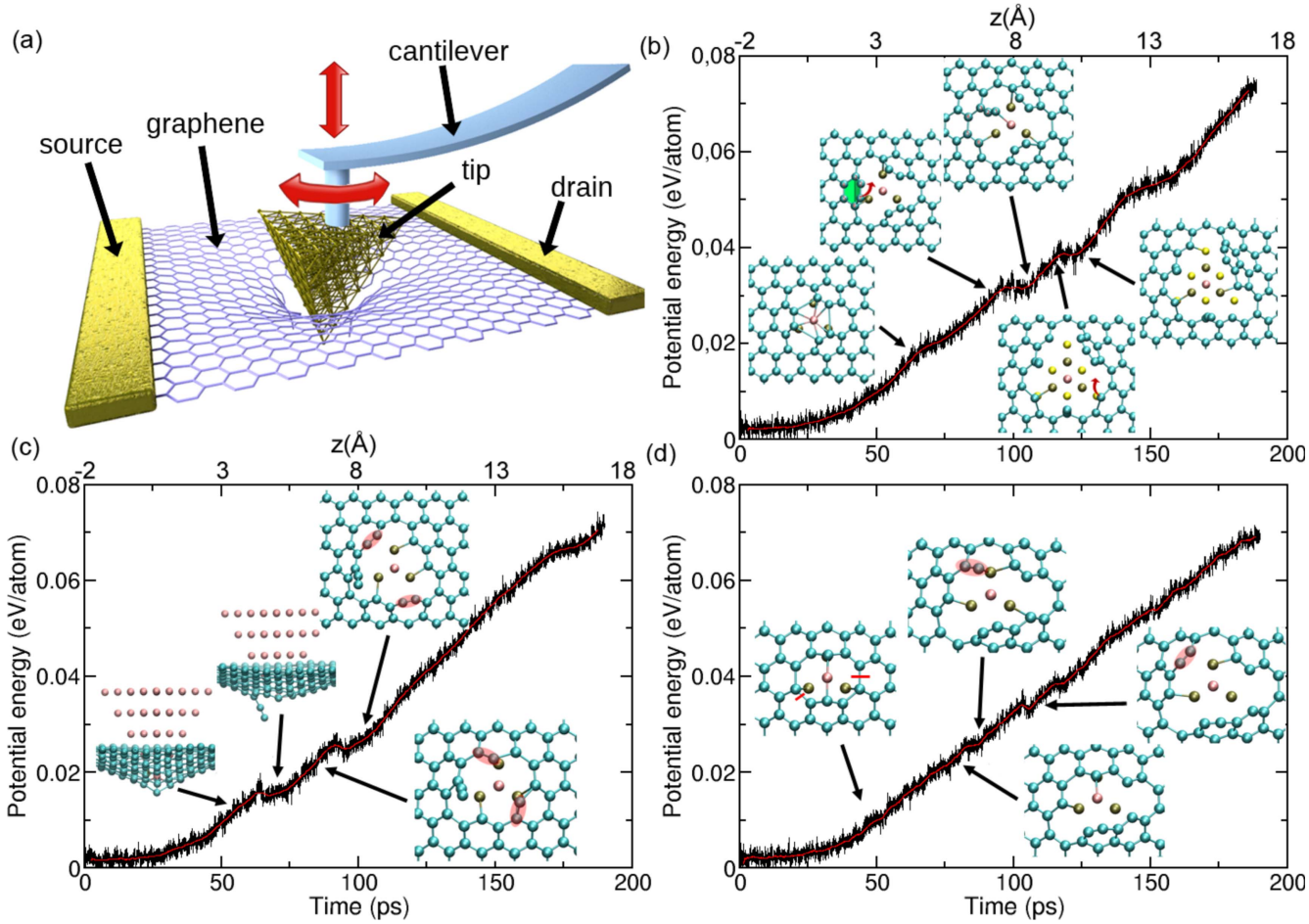

Figure 1. An illustration of the scanning probe nanomanipulator with a rotating pyramidal golden tip is shown in panel (a). The surface area of the graphene membrane is around 5 × 5 nm. The suspension of graphene is realized in the MD simulations by fixing C atoms that encompass two rows of phenyl rings at each edge of the simulated membrane. Red arrows indicate translational and rotational degrees of freedom for the STM tip. Potential energy curves with respect to time of the tip progression (equivalently the depth z (Å) of the tip apex relative to the basal graphene plane) are shown for the *hollow, top* and *bridge* sites in panels (b), (c) and (d), respectively. These sites correspond to initial (i.e. at the first MD step) lateral positions of the tip apex above the center of a carbon hexagon (*hollow* site), above a carbon atom (*top* site) and above the middle of a C–C bond (*bridge* site). The lateral positions are fixed at the beginning of the MD simulations and do not change as they progress. The structures in the panels (b), (c) and (d) are snapshots of MD simulations as viewed from a position below membranes. Red, golden and yellow spheres represent gold atoms of the tip apex, the second and third Au layers. Red lines and ellipses are a guide for the eye for bond breaking and bond rotations.

After the initial geometry optimizations we proceeded with MD simulations. The movement of the tip was realized by alternating its translational motion inward graphene by 0.1 Å and MD simulation with a duration of 1 ps at the temperature of 300 K using a Nosé Hoover thermostat [34, 35]. This corresponds to a speed of 10 m s^{-1}, which is much smaller than the speed of atoms due to their thermal motion. Hence the effects of the tip kinematics can be neglected and the results of simulations are expected to be the same for much smaller tip velocities, as the ones in real experiments. The depth z of the tip apex relative to the graphene basal plane corresponds to the time t of MD simulations according to expression $z(t) = -2$ (Å) + 0.1 (Å ps^{-1}) t. We analyzed the piercing mechanism for the three lateral tip positions. Two main regimes can be distinguished. After the initial elastic regime characterized by the parabolic-like dependence of potential energy with respect to time (equivalently the strain) the drilled graphene transits to the plastic regime with approximately linear dependence with abrupt discontinuities (figures 1(b)–(d)). The transitions from the elastic to the plastic regimes are triggered by the first breaking of chemical bonds in graphene during the piercing process. In the case of the *hollow site* three alternative bonds of the phenyl ring under the tip apex break simultaneously (figure 1(b)). The system stabilization is two-fold: (i) C atoms of the ring move away from the repulsive tip apex effectively lowering their mutual repulsion and (ii) three double bonds form, which gain energy relative to the conjugated state of the stretched phenyl ring that existed prior the breakage of bonds. At the moment of breaking the angle between the planes of that phenyl ring and neighboring rings is nearly 30°. When the tip apex is at the *top site*, the underneath C atom shifts faster than its three neighboring C atoms with the progress of tip (figure 1(c)). The corresponding three C–C bonds elongate until the threshold of 2 Å is reached when two of the C–C bonds break simultaneously. The third bond contracts forming a shorter and stronger double or triple

C–C bond. This rebinding releases energy, which transforms into the kinetic energy of the two C atoms. The energy is sufficient to tear off a C atom from the neighboring hexagon and a two-atom chain (i.e. a dimer) emerges (figure 1(c)). In the case of the *bridge site* the bridge elongates with the penetration of the tip apex and breaks at the threshold bond length of 2 Å (figure 1(d)). Breaking of the bond is not sufficient to transfer the released energy to a secondary relaxation as in the previous case. Interestingly, the initial change of the bonding in graphene, even so minor as that in the *bridge* case, changes the potential energy slope from the parabolic/elastic to the nearly linear/plastic. The potential energy has discontinuities in the plastic regime, each corresponding to certain stabilization mechanism and transformation of topology. Relative orientation of C atoms with their nearest Au neighbors and current local atomic structure of graphene primarily determine the mechanism of its structural reconfiguration. For example, around the 100th picosecond the tip apex in the *hollow site* case has already passed through the graphene sheet, whereas three Au atoms from the second tip layer are positioned next to certain C atoms (figure 1(b)). A phenyl ring bends (shown with green color in figure 1(b)) due to the proximity of the repulsive force of a neighboring Au atom. This causes the planar sp^2 hybridization to become unfavorable. One C–C bond of the ring breaks at the threshold bending angle of the ring of around 30° and a two-atom chain forms, as indicated by the red arrow in figure 1(b). Due to the same atomic coordination, two additional C dimers form next to two other Au atoms from the second tip layer. In the *top site* case Au atoms from the second tip layer are nearly on top of two C atoms. A pair of C–C bonds, marked with the red ellipses in figure 1(c), rotate and form two heptagons. It is possible for a hexagon to accommodate an additional atom when the local strain is large enough such that more space is available for the atom. We observe the same process in the *bridge* case where the relative positions of Au and C atoms are close to those in the *top* case and a heptagonal ring also forms. The same interaction and reconfiguration mechanisms repeat when the third Au layer arrives at the level of pores. For instance, in the *hollow site* case around the 125th ps the third atomic layer of the tip approaches the graphene (represented by yellow spheres in figure 1(b)). When one of the Au atoms positions above a C atom in a zigzag edge of the pore, the C atom moves into an empty space indicated by the red arrow, forming a pentagonal ring (figure 1(b)). In order to verify the consistency of the obtained results we have repeated segments of MD simulations starting 1 ps before the simulation times when structural reconfigurations take over. In the repeated MD runs we shifted the STM tip in random directions in the basal plane of graphene by up to 0.5 Å, prior to continuation of the tip indentation. We performed these simulations at 300 K for each C–C rebonding ten times. Surprisingly, the same atomic structure reconfigurations were reproduced for all the cases. This indicates a comfortable margin for deterministic realization of real experiments at this and lower temperatures. We expect lower reproducibility for higher temperatures. However, STM experiments can routinely be carried out even at much lower temperatures nowadays.

These findings of rather reproducible mechanisms for the creation of atomic chains, pentagonal and heptagonal rings may be utilized for the controllable design and fabrication of topological defects in graphene. Since the reconfiguration of atomic bonds was determined by the positions of Au atoms relative only to neighboring C atoms, rotation of the STM tip (red arrow in figure 1(a)) about the axis perpendicular to the basal plane of graphene, alternating with progression of the tip through the membrane can position Au atoms at a designated place for a desired reconfiguration to take over. The same mechanism continues in the consequent retraction of the tip from the membrane. Finally the membrane with aimed modification of atomic structure remains. Note that the intended relative positioning of the tip and sample can be also achieved by rotating the sample instead of the tip, as experimentally demonstrated in [23].

Next we analyze a relaxation mechanism of graphene membrane when the STM tip is not retracted from the graphene upon penetration but rather released beneath it. This was realized by the simple removal of the tip at a given moment of MD simulation. The membrane starts to relax freely at that moment. We removed the tip at the 100th, 150th or 190th picosecond after the beginning of tip penetration. The corresponding initial sizes of the pores are designated as large, mid and small in the following text. The actual surface areas of the pores, difficult to precisely define due to their irregular nonplanar forms, range roughly from 40 $Å^2$ to 140 $Å^2$, which is from about 8 to 27 times larger than the surface of a phenyl ring in an unperturbed graphene membrane. We conducted MD simulations for a range of temperatures between 50 and 2000 K. These simulations were inspired by a recently reported experiment where graphene was penetrated by supersonic micrometer-sized atomic clusters [24]. This paper demonstrates the possibility of generating delocalized defects using this method. In contrast to the experiment our system was smaller by three orders of magnitude and the cluster (i.e. tip) was significantly slower. The same method reported in the paper but with smaller and slower nanoclusters may be utilized for engineering of localized topological defects in graphene membranes.

Graphene self-heals within the first 1 ps of tip removal. The pores patch with new atomic structures presenting a variety of topological defects (see figure 2). Table 1 summarizes the fabricated structures for a range of temperatures, initial size of the pore and three initial puncturing sites, *hollow*, *top* and *bridge*, defined above. In contrast to controllable penetration and retraction of the STM tip, atomic structures generated by the self-healing process are more nondeterministic. However some regularities are indicative of the MD simulations. The final atomic structure of the membrane is determined primarily by three factors:

- defects present in the system before the relaxation stage,
- breaking of bonds during relaxation, and
- temperature.

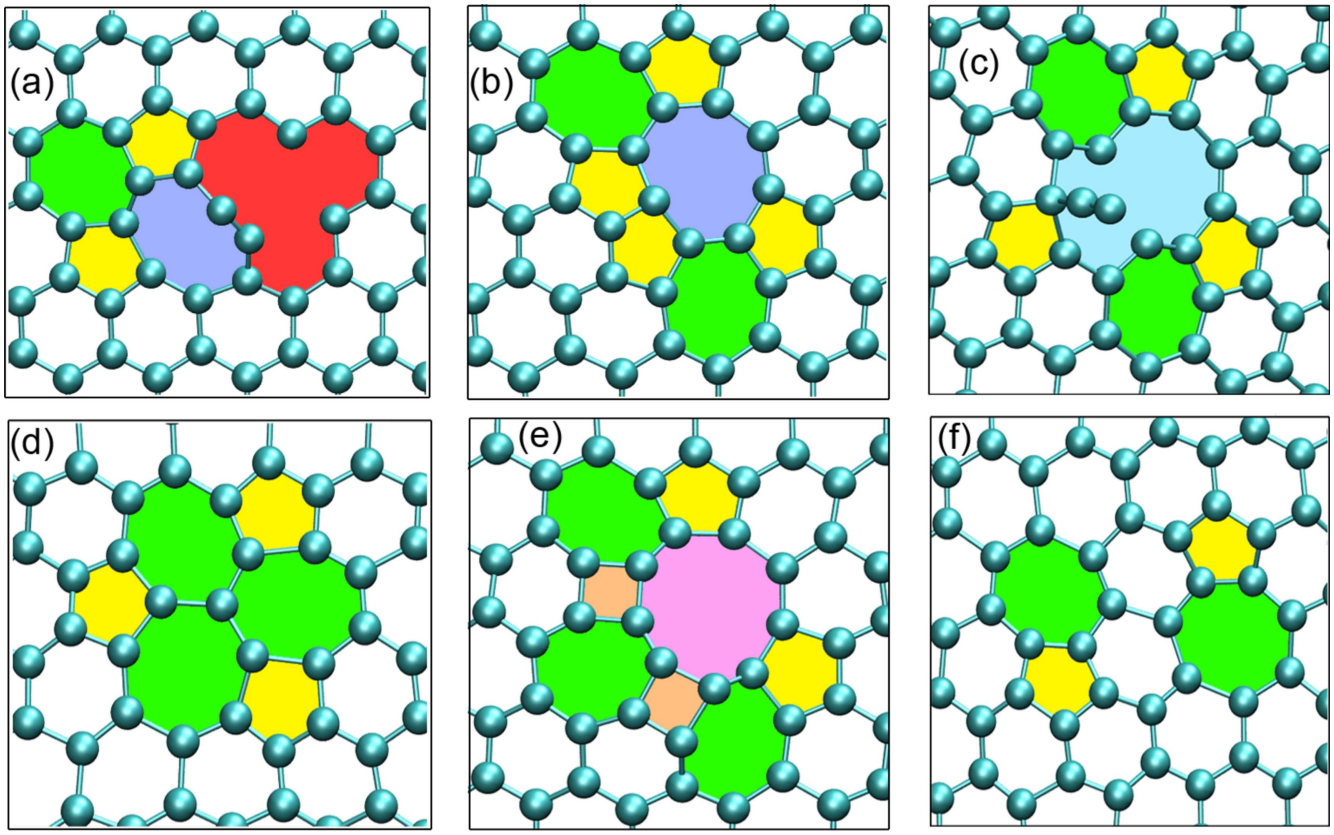

Figure 2. Topological point defects obtained in the self-healing stage. The panels are referenced in table 1. Geometric figures (squares, pentagons, hexagons, etc.) are painted with different colors as a guide for the eye.

Table 1. Topological defects generated in the self-healing process.

	Hollow			Top			Bridge		
T (K)	Large	Mid	Small	Large	Mid	Small	Large	Mid	Small
50	(a)	(c)[a]	6-gon	(c)	(c)	(c)	S–W	S–W	6-gon
300	(a)	(c)	6-gon	(c)	(b)	(c)	S–W	S–W	6-gon
600	S–W[b]	(c)	6-gon	6-gon	(b)	S–W	S–W	6-gon	6-gon
900	S–W	S–W	6-gon	S–W	(b)	(c)	S–W	S–W	6-gon
1200	6-gon[c]	S–W	6-gon	(e)[d]	(d)	S–W	6-gon	S–W	6-gon
1500	S–W	6-gon	6-gon	6-gon	6-gon	6-gon	6-gon	(f)	6-gon
2000	S–W	(c)	6-gon	(d)	S–W	6-gon	6-gon	S–W	6-gon

*Large, mid and small indicate the size of initial pore before the relaxation stage; these correspond to removal of tip when tip apex is at depths of 17 Å, 13 Å and 8 Å, respectively.
**Letters in parentheses correspond to panels in figure 2:
[a] Carbon chain such as that in figure 2(c) but with possible different configuration of surrounding atoms.
[b] Stone–Wales (S–W) defect.
[c] Pristine hexagonal graphene.
[d] A complex geometry with two C atoms driven out of graphene.

The pristine hexagonal graphene is recovered for small initial pores in the *hollow* and *bridge* cases, whereas short carbon chains emerge for the *top* case, which reflect their atomic structures before the self-healing stage. Elastic energy of small pores accumulated in the puncturing phase is not sufficient to break a C– bond during the self-healing process when edges of pores collide with each other. In contrast, a wide variety of defects emerges when pores are large (see table 1). Chemical bonds elongate with elevating temperatures, making 2D materials more flexible and their atoms more motile, essentially covering a larger part of phase space and possible number of atomic reconfigurations. Relatively high temperatures and large pores with pre-existing carbon chains is an optimal combination of conditions for fabrication of complex topological defects like the one in figure 2(e).

After the self-healing relaxation stage the accumulated strain energy localized around the pore transfers across the whole system via mechanical waves. We gained the

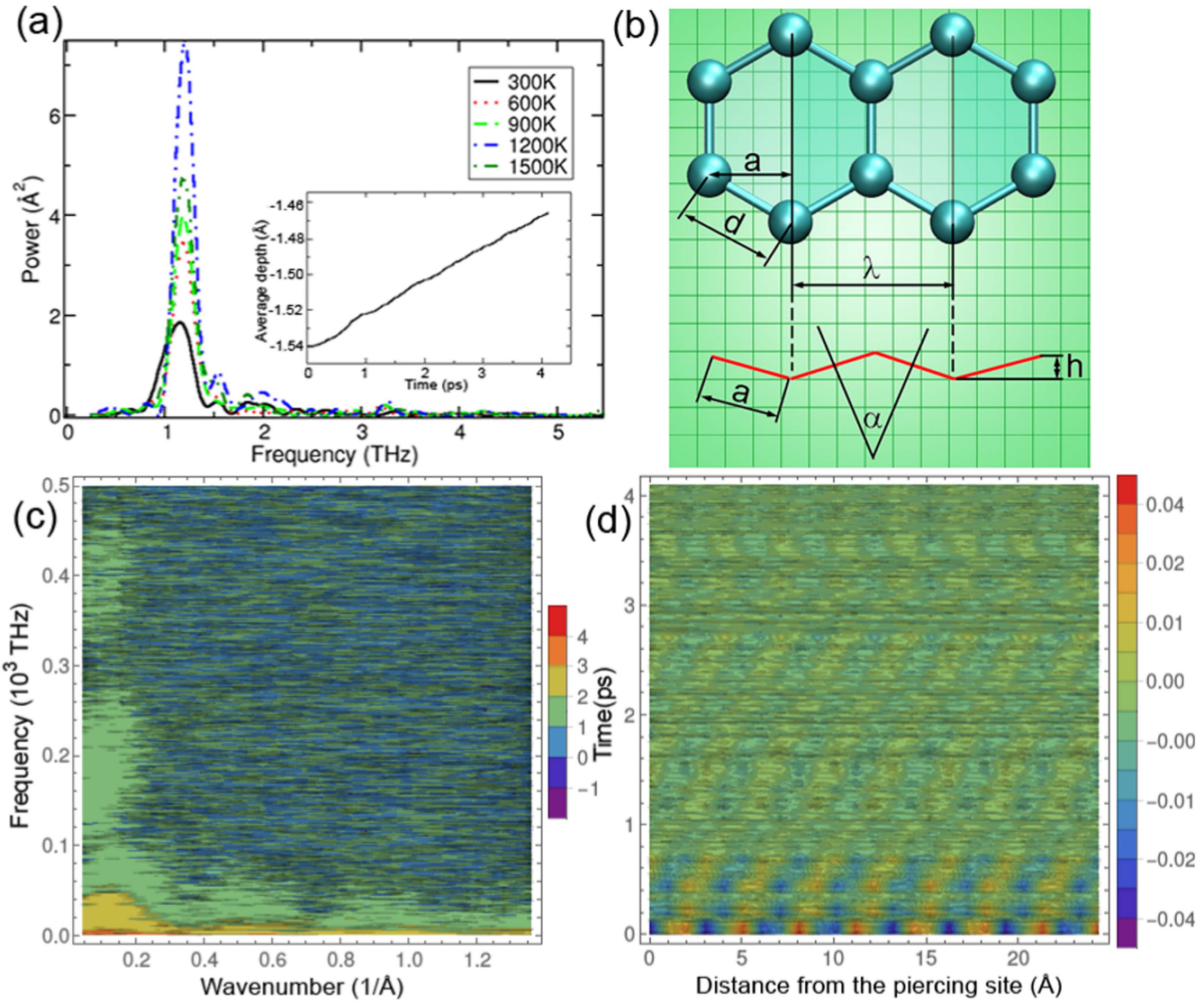

Figure 3. (a) FT of the average depth of graphene (average distance of C atoms from the basal plane of graphene) versus time (average depth dependence on time is shown in the inset). (b) Illustration of a mechanical wave with wavelength λ in graphene. The red line shows the side view where C atoms are alternatively shifted up and down. α is the angle between the planes shaded by dark and light green colors and h is twice the amplitude of the wave. (c) 2D FT from the space–time to wavenumber–frequency domain. The legend scale is in dB. (d) Inverse 2D FT obtained from (c) for the optimal wavenumber 0.28 Å^{-1} and all frequencies above 2.5 THz. The legend scale is given in Å.

information about the waves using Fourier transform (FT) analysis. We obtained the power spectrum (figure 3(a)) of the average depth of graphene for the *hexagonal site* case in the relaxation stage with respect to time (inset in figure 3(a)). The spectrum has the most pronounced peaks around 1.2 THz. The varying of heights of the peaks with temperature indicate damped waves with the characteristic attenuation time increasing with temperature. However, the dependence is not monotonically increasing, as the highest peak is obtained for 1200 K rather than 1500 K. The origin of this anomaly is the defect-dependency of attenuation, in addition to the temperature dependency; while Stone–Wales defects emerge at 600, 900 and 1500 K the pristine defect-free graphene self-heals in simulation at 1200 K.

Now we analyze a possibility for secondary rupturing of graphene and eventual delocalization of defects due to the induced waves. We observed above that carbon bonds break only under extreme dihedral angles and bond lengths. In order to achieve such conditions with a wave, optimally its wavelength has to be $\lambda = d\sqrt{3} = 3.46$ Å for $d = 2$ Å (bond length at which the C–C bond breaks), which corresponds to the wavenumber $k = 0.29$ Å^{-1} (figure 3(b)). The angle α between planes (marked with light and dark green shades) has to exceed 30°. It follows that the amplitude $h/2$ of the wave has to be around 0.27 Å. We obtained amplitudes of induced waves from the space–time FT (STFT, figure 3(c)) and the inverse FT (figure 3(d)) for the optimal wavenumber $k = 0.29$ Å^{-1} after filtering out frequencies below 2.5 THz. Periods of the filtered waves are significantly large compared to the simulation time. The FTs are obtained for positions of atoms in a 1 Å wide stripe from the center of the membrane to the extreme right position of the simulation box. Using this setup

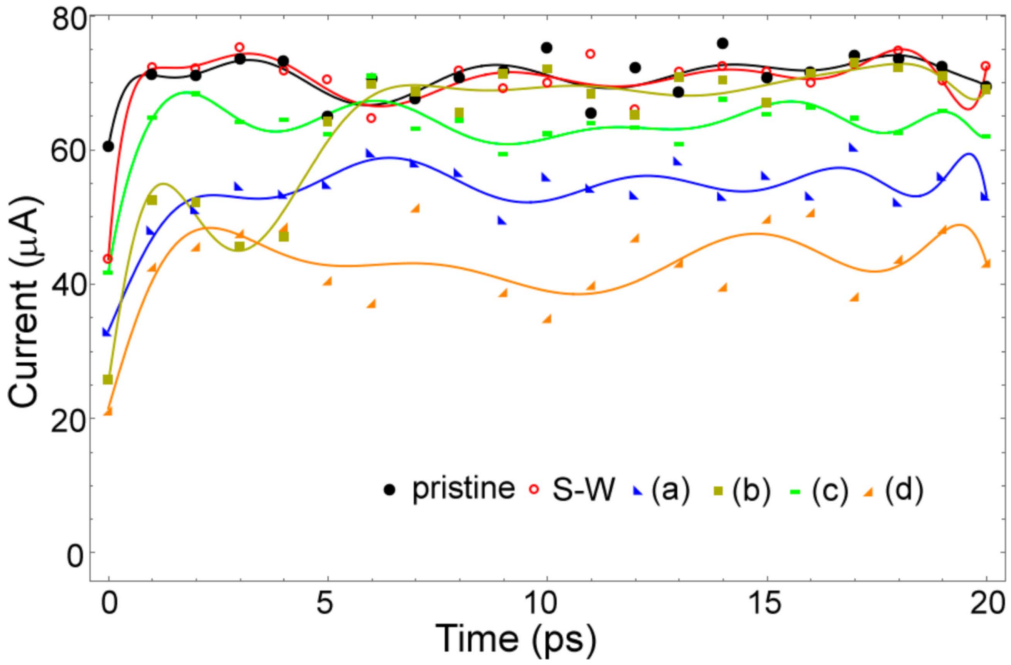

Figure 4. Dependence of electronic current on time for systems with different defects. Zero time is at the beginning of the self-healing process after removal of the SPM tip. Letters (a)–(d) in the legend correspond to defects in figures 2(b)–(d), and S–W to a single Stone–Wales defect. Pristine corresponds to self-healing to the ideal graphene. Various symbols designate actual values of calculated current, whereas curves are polynomial fits to these values. The current is calculated for the bias voltage of 1V.

the STFT includes only one space coordinate along the stripe. We interpolated the position of atoms prior to application of STFT. The power spectrum is the most prominent for small frequencies below $0.05 \cdot 10^3$ THz with relatively large fluctuations for higher frequencies. Note a propagating wave in figure 3(d) with the phase speed of around 280 m s^{-1}. The amplitude of the wave attenuates from 0.47 Å to below 0.05 Å in only 0.7 ps. After that time the amplitude remains constant. Importantly, the amplitude of the wave in the steady state is significantly smaller than the threshold of 0.27 Å for the secondary breaking of carbon bonds. We obtained the same conclusion for every considered temperature, puncturing site and initial size of pores. Therefore the topological defects remain localized around the penetration site since secondary defects cannot emerge due to induced traveling waves. This finding may not be true for other 2D materials, in which stiffness is smaller than that of graphene as an extreme example.

Electronic transport of 2D materials sensitively depends on the nature of their defects. Figure 4 shows the evolution of electronic current with time at a bias voltage of 1V for investigated systems in the self-healing stage. Note that defects (a) to (d) in this section correspond to defects (a) to (d) in figure 2. Electrodes are placed at the opposite ends of membranes and consist of ideal graphene. All currents are calculated at 300 K except for the case of defect (d), which is obtained at 1200 K. The higher temperature causes a larger amplitude of oscillations of the membrane and correspondingly of electronic current. Defect (d) causes maximal degradation of conductance among the investigated defects, by around 45% relative to the case of ideal graphene. It is followed by defects (a) and (c). A general feature is that currents are minimal at the beginning of the relaxation stage, when pores are still present in membranes. Electronic currents rapidly grow within the first 1 ps when the pores become closed and the final binding topology is reached for the all defects. Current saturates to specific values depending on the obtained defect, i.e. topology, while oscillating due to induced mechanical waves analyzed above in detail. While saturated currents are different for various defects ((a), (c) and (d)), our calculations also predict an unexpected overlapping of saturated currents in the case of pristine graphene, a single S–W and the (b) defect. The initial time dependence of current for these cases is still different, especially for the (b) defect. Therefore transport measurements of a defective graphene membrane during its self-healing process can provide information on the specific topological defect fabricated in the membrane.

In conclusion, we introduced a concept of SPM with a rotating tip as an additional degree of freedom. Our comprehensive MD simulations of puncturing of a suspended graphene membrane indicate a new possibility for engineering atomic structure of 2D materials in a controllable and reproducible manner with the novel SPM method. Another approach is releasing the SPM tip after piercing of the membrane and its subsequent self-healing. The alternative to the latter method is shooting of membrane by a nanocluster. Although SPN loses a bit of determinacy when the latter approach is used, fabrication of a variety of individual topological defects is accessible. Additionally, Fourier analysis of oscillations induced by STM puncturing of the graphene membrane indicates that the generated defects remain local, i.e. they do not permeate off the puncturing site. The proposal for the new SPM method presented here and simulated on a suspended graphene membrane is a proof of concept, which can be applied to a wider range of two-dimensional materials. Manipulation of the intrinsic atomic

structure can be a qualitative step beyond the state-of-the-art of nanomanipulation today. The prior knowledge of tip geometry, details of its interaction with a 2D material and precise tip rotation by desired angles are the main challenges for successful experimental realization of the concepts presented here. All three challenges can be successfully addressed with present technologies or the sustained development of the technologies can reach the necessary level of sophistication. Controlled fabrication of atomically sharp STM tips has been in steady progress over the years [36–38]. Atomistic simulations like these shown here can assist in gaining the details of the tip–sample interaction. The technique for controlling the rotational degree of freedom in SPM has already been demonstrated in [23], where the desired orientation of the tip relative to the sample was achieved by the rotation of the sample instead of the tip. These two approaches are equivalent, since only relative tip–sample orientation matters for the fabrication of the topological defects analyzed in our proposal. However, a further improvement of the method is still necessary. Namely, the circular scanning pattern shown in [23] has to be reduced to a rotation of the sample with a fixed rotational axis that penetrates the tip apex. The rotation axis should also be perpendicular to the membrane's basal plane for the sake of simplicity and better control of the tip-membrane interactions at the atomistic level. Hence, there are no physical obstacles that could principally forbid the realization of real experiments. The engineering issues that make real differences between the somewhat idealized simulation conditions used here and realistic experiments will be resolved in the sustained progress of the field that we witness nowadays. Until then our concept and results can serve as a 'thought experiment' without complete overlap with current experimental possibilities, but as a guideline for their future development. In the meantime we can expect a realization of the second proposal here, engineering of the wide variety of the localized topological defects by nanocluster irradiation (the tip removal equivalence), for which the experimental techniques already exist. We hope the concept that we have presented will ignite sufficient interest in the experimental community for an SPM with a rotating tip as a new tool for nanomanipulation, one of the ultimate goals in nanophysics and nanotechnology.

Acknowledgments

We would like to thank Borislav Vasić for helpful discussions on SPM methods and Sanja Andrić for English proofreading. This work was supported by the Serbian Ministry of Education, Science and Technological Development under project numbers OI 171005. This research is also supported by Qatar National Research Fund, cycle seven, (QNRF) under grant number NPRP 7-665-1-125.

ORCID iDs

Igor Popov https://orcid.org/0000-0002-2030-3530

References

[1] Binnig G, Rohrer H, Gerber C and Weibel E 1982 *Appl. Phys. Lett.* **40** 178
[2] Binnig G, Quate C and Gerber C 1986 *Phys. Rev. Lett.* **56** 930
[3] Eigler D and Schweizer E 1990 *Nature* **344** 524
[4] Lyding J, Shen T-C, Hubacek J, Tucker J and Abeln G 1994 *Appl. Phys. Lett.* **64** 2010
[5] Walsh M and Hersam M 2009 *Ann. Rev. Phys. Chem.* **60** 193
[6] Sessi P, Guest J, Bode M and Guisinger N 2009 *Nano Lett.* **9** 4343
[7] Greenwood J *et al* 2015 *ACS Nano* **9** 5520
[8] Alaboson J *et al* 2013 *Nano Lett.* **13** 5763
[9] Johns J E and Hersam M 2013 *Acc. Chem. Res.* **46** 77
[10] Mali K, Greenwood J, Adisoejoso J, Phillipson R and Feyter D 2015 *Nanoscale* **7** 1566
[11] Liu G-Y, Xu S and Qian Y 2000 *Acc. Chem. Res.* **33** 457
[12] Dagata J, Schneir J, Harary H, Evans C, Postek M and Bennett J 1990 *Appl. Phys. Lett.* **56** 2001
[13] Garcia R, Martinez R and Martinez J 2006 *Chem. Soc. Rev.* **35** 29
[14] Giesbers A, Zeitler U, Neubeck S, Freitag F, Novoselov K and Maan J 2008 *Solid State Commun.* **147** 366
[15] Weng L, Zhang L, Chen Y and Rokhinson L 2008 *Appl. Phys. Lett.* **93** 093107
[16] Masubuchi S, Ono M, Yoshida K, Hirakawa K and Machida T 2009 *Appl. Phys. Lett.* **94** 082107
[17] Tapasztó L, Dobrik G, Lambin P and Biró L P 2008 *Nature Nanotechnol.* **3** 397
[18] Wei Z *et al* 2010 *Science* **328** 1373
[19] Liu L, Qing M, Wang Y and Chen S 2015 *J. Mater. Sci. Tech.* **31** 599
[20] Banhart F, Kotakoski J and Krasheninnikov A 2011 *ACS Nano* **5** 26
[21] Vicarelli L, Heerema S, Dekker C and Zandbergen H 2015 *ACS Nano* **9** 3428
[22] Berger D and Ratsch C 2016 *Phys. Rev.* B **93** 235441
[23] Nasrallah H, Mazeran P-E and Noël O 2011 *Rev. Sci. Instrum.* **82** 113703
[24] Lee J-H, Loya P E, Lou J and Thomas E L 2014 *Science* **346** 1092
[25] Porezag D, Frauenheim T, Kohler T, Seifert G and Kaschner R 1995 *Phys. Rev.* B **51** 12947
[26] Seifert G, Porezag D and Frauenheim T 1996 *Int. J. Quantum Chem.* **58** 185
[27] Aradi B, Hourahine B and Frauenheim T 2007 *J. Phys. Chem.* **111** 5678
[28] Erdogan E, Popov I, Rocha C G, Cuniberti G, Roche S and Seifert G 2011a *Phys. Rev.* B **83** 041401
[29] Erdogan E, Popov I and Seifert G 2011b *Phys. Rev.* B **83** 245417
[30] Kawai T, Poetschke M, Miyamoto Y, Rocha C, Roche S and Cuniberti G 2011 *Phys. Rev.* B **83** 241405
[31] Ivanovskaya V, Ranjan N, Heine T, Merino G and Seifert G 2005 *Small* **1** 399
[32] Datta S 1997 *Electronic Transport in Mesoscopic Systems* (Cambridge: Cambridge University Press)
[33] Huang W, Bulusu S, Pal R, Zeng X and Wang L 2009 *ACS Nano* **3** 1225
[34] Hoover W and Holian B 1996 *Phys. Lett.* A **211** 253
[35] Nosé S 1984 *J. Chem. Phys.* **81** 511
[36] Chaika A *et al* 2014 *Sci. Rep.* **4** 3742
[37] Yu Z, Wang C, Du Y, Thevuthasan S and Lyubinetsky I 2008 *Ultramicroscopy* **108** 873
[38] Song J, Pryds N, Glejbøl K, Mørch K, Thølén A and Christensen L 1993 *Rev. Sci. Instrum.* **64** 900

Self-assembly of rylene-decorated guanine ribbons on graphene surface for optoelectronic applications: a theoretical study

IOP Publishing Nanotechnology
Nanotechnology 32 (2021) 435405 (15pp) https://doi.org/10.1088/1361-6528/ac162c

Self-assembly of rylene-decorated guanine ribbons on graphene surface for optoelectronic applications: a theoretical study

Branislav Milovanović[1], Mihajlo Etinski[1] and Igor Popov[2,3,*]

[1] University of Belgrade, Faculty of Physical Chemistry, Studentski trg 12-16, Belgrade, Serbia
[2] Institute for Multidisciplinary Research, University of Belgrade, Kneza Višeslava 1, Belgrade, Serbia
[3] Institut of Physics, University of Belgrade, Pregrevica 118, Belgrade, Serbia

E-mail: popov@ipb.ac.rs

Received 7 April 2021, revised 3 June 2021
Accepted for publication 20 July 2021
Published 6 August 2021

Abstract

We are witnessing a change of paradigm from the conventional top-down to the bottom-up fabrication of nanodevices and particularly optoelectronic devices. A promising example of the bottom-up approach is self-assembling of molecules into layers with predictable and reproducible structural, electronic and optical properties. Nucleobases possess extraordinary ability to self-assembly into one-, two-, and three-dimensional structures. Optical properties of nucleotides are not suitable for wider application to optoelectronics and photovoltaics due to their large optical band gap, which is in contrast to rylene-based dyes that have been intensively investigated in organic optoelectronics. However, these lack the self-assembly capability of nucleobases. Combinations of covalently decorated guanine molecules with rylene type chromophores present 'the best of the both worlds'. Due to the large size of such compounds and its flexible nature their self-assemblies have not been fully understood yet. Here, we use a theoretical approach to study the structural, energetic and optical properties of rylene-based dye decorated guanine (GPDI), as self-assembled on a graphene sheet. Particularly we utilize the density-functional based tight-binding method to study atomic structure of these systems including the potential energy surface of GPDI and stability and organization of single- and multilayered GPDIs on graphene sheet. Using density-functional theory (DFT) we employ the energy decomposition analysis to gain a deeper insight into the contributions of different moieties to stability of GPDI films. Using time dependent DFT we analyze optical properties of these systems. We find that atomically thin films consisting of only a few molecular layers with large surface areas are more favorable than isolated thick islands. Our study of excited states indicates existence of charge separated states similar to ones found in the well-studied hydrogen bonded organic frameworks. The self-assembly characterized with a large homogeneous coverage and long-living charge-separated states provide the great potential for optoelectronic applications.

Supplementary material for this article is available online

Keywords: DFT, DFTB, guanine, rylene, self-assembly, stability, electronics

(Some figures may appear in colour only in the online journal)

* Author to whom any correspondence should be addressed.

1. Introduction

Complexity and difficulties in fabrication of optoelectronic nanodevices, including photovoltaics, rapidly rise as their minimal structural features decrease. Consequently the conventional top-down solutions are increasingly getting substituted by bottom-up fabrication methods. The self-assembly process provides a highly promising bottom-up approach toward the fabrication of novel functional materials and nanodevices. Nucleobases are the representative example of microscopic building blocks ideally suited for self-assembling into nanostructures. Non-covalent bonding between nucleobases is the key feature that enables nucleobases to build the complex nanostructures including the deoxyribonucleic acid (DNA). In recent years several groups have demonstrated novel nucleotide-based nanostructures beyond the usual helical ones [1–13]. Unfortunately, materials based exclusively on nucleobases are not well suited for optoelectronic and photovoltaic applications due to their photo-activity only to the ultra-violet part of the solar spectrum. To this end a range of organic dyes are considered [14–20], however they usually lack the self-assembly ability of nucleobases. Hydrogen bonded organic frameworks (HOFs) present a prominent 'best of the both worlds' solution [21–25]. The so far experimentally realized nucleobase based HOFs are built up from covalently decorated guanine molecules (G) with rylene type chromophore as a linker. In particular, naphthalene-1,4:5,8-bis(dicarboximide) (NDI) and 2,5,8,11-tetrahexylperylene-3,4:9,10-bis(dicarboximide) (PDI) linkers have been studied [26, 27], where tasks of self-assembly and desired optical properties are assigned to guanine and the dye molecules, respectively. The important advantage of HOFs is a wide choice of molecules to assemble with guanine, which provides a great potential to finely tune materials for desired optical properties. It is demonstrated that G-quadruplexes can serve as effective conduits for photogenerated positive charge in ordered columnar architectures—covalently linked electron rich core (G-quarduplex) and rylene dye based electron acceptors [22–28].This unique hole-trapping ability of guanines within the central quadruplex channel could be exploited for range of applications in optoelectronic devices. Chromophore organization within these systems ensure presence of the long-lived charge-separated (CS) states. Upon photoexcitation to the bright excitonic $\pi\pi^*$ state localized on the rylene dyes, system undergoes charge separation to form CS state ($G^{\bullet+}$-$dye^{\bullet-}$) that later encounter ground state through charge recombination. Such CS states are found for guanine-PDI (GPDI) folded quadruplexes and decays to the ground state within 1.2 ± 0.2 ns [22]. Such long decay is attributed to the electron delocalization over adjacent PDI chromophores. Another, shorter decay time constant is also observed (98 ± 12 ps) and it is associated with PDIs localized excimer-like state decay towards CS state [22]. Fast photoinitiated hole transport within quadruplexes suggest potential utilization for conductive nanodevices. Mechanism of such hole transport is still speculated [28, 29]. Another interesting type of long-lived CS state is observed for guanine coupled to the terrylenediimide (TDI) to form units which build GTDI-quadruplex [24, 25]. High degree of stacking between adjacent TDIs ensures that upon photoexcitation system efficiently populates symmetry-breaking CS (SB-CS) state, i.e. ion pair excited state ($TDI^{\bullet+}$-$TDI^{\bullet-}$) which has undivided attention for the organic photovoltaics application [30]. Similar excited states characteristics are found for G-quadruplex-based organic frameworks [26, 27] and GTDI thin films on the glass substrate [25]. Alternative structures to HOFs with the same guanine-(dye molecule) building blocks and potentially the task sharing capability are quasi-one-dimensional nanoribbons and two-dimensional layered materials based on them. Beside rylene diimide substituted guanine, i.e. NDI and PDI, in literature we find several more compounds of interest for the optoelectronic applications as a guanine/guanosine substituent: oligothiophenes [9, 31–33], oligo(p-phenylene-vinylene) [34], boron-dipyrromethene [35] and butylphyneyl [36]. From the experimental aspect, synthesis of these compounds is complex and time-consuming [22–27]. For instance, synthesis of the GPDI takes place in the solution with total preparation time of ≈116 h (see Synthesis details from the [22]). Particularly in case of GPDI, synthesis is a three-step process: (1) guanine is functionalized at C8 position using ethynyl group (see figure 2(a)); (2) PDI rylene dye is functionalized using 4-iodophenyl (arene linker) at N position of one of the PDI imide groups; (3) GPDI conjugate is prepared in the mixture of organic solvents (dimethylformamide and triethylamine). Likewise, characterization of these compounds requires several complex experimental techniques.

Importantly, having structure of atomically thin films, these materials can be considered for flexible photovoltaic and optoelectronic applications when deposited on a transparent electrode. Graphene has gained the increased interest as transparent electrode. Crystalline semiconductor—graphene heterojunctions, where semiconductor has optical properties tuned for application of interest, have been intensively investigated recently [37–39]. Besides these systems, self-assembled systems of various rylene diimides adsorbed on highly oriented pyrolytic graphite (HOPG) have been reported [40] as well as the covalently decorated guanine/guanosine molecules with oligothiophene derivates [9, 31–34]. However, understanding interfaces of the relatively large flexible molecules and graphene is challenging primarily from the computational aspect, hence details of their structural, energetic, electronic and optical properties remain scarce.

In this paper, we use a theoretical approach, which includes density functional theory (DFT) and density-functional based tight-binding (DFTB) method, to analyze properties of the self-assembled GPDI molecules at the atomic level. This combination of methods provides a very good balance between accuracy and speed necessary to investigate in detail the large systems of interest. We find that GPDI molecules tend to self-assemble in homogeneous atomically thin films, which, as in the case of above mentioned crystalline semiconductor—graphene heterojunction, is important for applications in optical devices. Despite having different structures than HOFs, we show that optical absorption

properties of investigated layered ribbons are very similar to those of HOFs. These optical properties of atomically thin self-assembled layered homogeneous anisotropic graphene-GPDI heterojunctions provide an alternative solid ground for their applications in flexible photovoltaics and optoelectronic devices.

The paper is organized in the following order: after introduction of investigated systems, stability of self-assembled structures will be discussed based on binding energy, energy decomposition analysis (EDA) and electronic density of states (DOS). Optical properties of these systems will be analyzed in detail, and conclusions given at the end.

2. Theoretical methodology

We used DFTB+ program [41] to perform DFTB calculations. DFTB SCC-Hamiltonian is constructed within a framework of the third order density functional tight-binding model (DFTB3) along with D3 correction for disperion interactions [42, 43] in conjuction with 3ob third-order parametrization for organic and biological systems [44]. During DFTB3 optimizations and molecular dynamics runs we also enabled additional corrections for dispersion interactions and hydrogen bonds [45, 46] denoted with H5. Accuracy of DFTB3 method along with other popular semiempirical methods is recently found to have a good accuracy for complex non-covalently glued molecular systems [47–49]. DFTB method has also been tested for a range of organic molecules including nucleobases and its molecular complexes (stacked guanine trimer, guanine-cytosine dimers) [47] and reasonable agreement (structural and energetic) with the reference structures is found. Furthermore, results are not much different from those obtained using more sophisticated DFT functionals such as M06-2X in combination with modest basis sets. Another study conducted comprehensive investigation of the performance of DFTB-D3 method along with various H-bond corrections. [48] In general, non-covalent interactions (binding energies) between π conjugated biomolecules (including nucleobases) are slightly overestimated, while dispersion interactions with graphene-like substrate are slightly underestimated. Another fact is that different H-bonding parametrization can lead to drastic changes from geometry and/or energetic aspects. Transferability of parameters of semiempirical methods among different classes of molecules/interactions is a well-known issue, and therefore evaluation of the parameters on a model system is required. For the benchmark purposes we used G-quartet as a model system. G-quartet is a representative of finely tuned non-covalently glued molecular system. Also, G-quartet is a key motif responsible for the assembly of the HOFs used for the comparison in this work and it exhibit same types of hydrogen bonds which are encountered in studied GPDI ribbons. Various available DFTB general purpose parameter sets are used for the benchmark and the results are reported in the SI. DFTB3-D3H5 in conjunction with 3ob parameter set for bio and organic molecules outperform other tested methods/parameters. In addition, we slightly changed default H5 parameters to even better reproduce results obtained with hybrid functionals (benchmark is also provided in the SI). The DFTB3-D3H5/3ob geometry optimizations were followed by single point (SP) energy calculation at DFTB3-D3/3ob level of theory, i.e. without H5 correction since in this case binding energies are much closer to the DFT results as discussed in the following section. Geometry optimizations are performed using conjugate gradient method and maximal force component threshold of 1×10^{-4} a.u.. All periodic calculations are performed at the Γ-point.

Siesta code [50] was used to perform periodic DFT calculations. These calculations were employed to benchmark binding energies obtained using DFTB methodology. 4770 eV is used for the plane wave cutoff in the real space grid and the Perdew–Burke–Ernzerhof form of the generalized gradient approximation [51], while the core electrons are described by norm-conserving pseudopotentials with partial core corrections [52].

Two-dimensional nature of the material is simulated by setting the lattice vector c (which is perpendicular to the materials plane) to 30 Å, which provides vacuum of around 20 Å between a unit cell and its periodic replica for the largest, multilayared ribbons. Two types of ribbons were investigated. Type I ribbons are simulated using cell vectors of 22.29, 47.30 and 30.00 Å along x, y and z axes, respectively. This resulted in a super-cell containing 660 atoms for single layered type I ribbon in which four GPDI molecules were hydrogen bonded and adsorbed on a graphene surface. Type II ribbons (also four hydrogen bonded GPDIs adsorbed on graphene) are simulated using somewhat smaller cell vectors of 22.29, 43.00 and 30.00 Å along x, y and z axes, respectively, which resulted in a super-cell accommodating 624 atoms in total. We also simulated multilayered ribbons (up to three layers) where each additional stacked ribbon layer contained 264 atoms. For comparison with the ribbons we also investigated previously experimentally realized HOF structures [26]. These are prepared using *in silico* procedure described in the [26]. In HOF structures PDI molecule serves as a covalent linker between two guanines which is denoted with G_2PDI. Hydrogen at N^9 position of guanine is substituted with soluble octyl group as in the case of the experimentally realized HOF [26, 27]. Structure and arrangement of G_2PDI in HOFs require only two G_2PDI per unit cell where both ends of the G_2PDI participate in the hydrogen bonding to form HOF. Cell vectors of such system amount to 43.00, 42.12 and 30.00 Å along x, y and z axes, respectively, which results in a super-cell that contain 960 atoms. Multilayered HOFs (up to three additional layers) are constructed analogously to the multilayered ribbons with additional 280 atoms per layer. Beside structures adsorbed on graphene, we simulate infinite layers of ribbons and HOF by reducing z axis cell vector to 5.97, 6.09 and 6.87 Å for type I, type II ribbon and HOF, respectively. These values correspond to the double value of average interlayer separation since we used two layers and periodic boundary conditions to construct an infinite layer. Parameters characterizing supercells of studied systems are compiled in the table 1.

Table 1. Parameters for constructing super-cells for type I ribbons, type II ribbons and HOFs. Note that *z*-axis is always perpendicular to the molecular frameworks plane. In case of ribbons *x*-axis is positioned in the direction of the H-bonds, while in case of the HOFs *x*-axis is positioned perpendicular to the N–H···O H-bond formed between two G_2PDI in the unit cell. Initial single-layered HOF is prepared following *in silico* procedure described in the [26].

Molecular framework name	Number of layers	Super-cell vectors (*x*, *y*, *z*)	Number GPDI/G_2PDI molecules in the super-cell	Total number of atoms in the super-cell	Atoms per layer
Type I ribbon	1	22.29, 47.30, 30.00	4	660	264
	2	22.29, 47.30, 30.00	8	924	
	3	22.29, 47.30, 30.00	12	1188	
	∞	22.29, 47.30, 5.97	8	528	
Type II ribbon	1	22.29, 43.00, 30.00	4	624	264
	2	22.29, 43.00, 30.00	8	888	
	3	22.29, 43.00, 30.00	12	1152	
	∞	22.29, 43.00, 6.09	8	528	
HOF	1	43.00, 42.12, 30.00	2	960	140
	2	43.00, 42.12, 30.00	4	1240	
	∞	43.00, 42.12, 6.87	4	560	

Total interaction energy between GPDI units adsorbed on graphene is decomposed using EDA [53] implemented in Turbomole program package [54]. In order to make study computationally feasible for EDA purposes we used non-periodic DFT with B-LYP functional [55, 56] and Grimmes' D3 dispersion correction [57] in conjuction with def2-TZVPP basis set [58, 59]. Electronic Coulomb interactions were calculated using multipole accelerated resolution-of-identity.

Electronic absorption spectrum for two layered ribbons and HOF structures is obtained for geometries optimized at DFTB3-D3H5/3ob level of theory. Each system contained 8 GPDI/G_2PDI units without absorbent (graphene) which is mostly transparent within studied excitation window. This amounted to 528 and 736 atoms for the most stable two layered type I/II ribbons and HOF structures, respectively. Excitations were computed using linear response time-dependent density functional theory (LR-TDDFT) and the long-range corrected CAM-B3LYP functional [60] in conjunction with def2-SV(P) basis set [58, 59]. LR-TDDFT calculations were carried out using Gaussian09 software [61]. For each system 64 lowest lying singlet excited states (N_s) were calculated. Vertical electronic transitions are broadened using Gaussian shaped function and electronic absorption spectrum is obtained as:

$$A(E) \sim \sum_{i=1}^{N_s} \frac{f_i}{\sqrt{2\pi}\,\gamma} exp\left(-\frac{(E-E_i)^2}{2\gamma^2}\right), \qquad (1)$$

where f_i and E_i is oscillator strength and energy of the ith electronic excited state, respectively. γ is the broadening parameter set to 0.2 eV in order to better visually resolve spectrum. The density of transition (DOT) is also obtained using equation (1) with f_i values set to 1. Benchmark calculation for the employed method i.e. absorption profile calculation and comparison to the experimental spectrum is available in the SI. Excited states character is analyzed using TheoDORE program package [62–66] which relies on the analysis of the one-electron transition density matrix (1eTDE) and it is useful to resolve types of excitations in the systems of interacting chromophores. Excited states character is determined using two descriptors based on decomposition of the 1eTDE. First descriptor denoted with PR is calculated as arithmetic mean of the participation ratios of hole and electron, i.e. number of fragments on which they are delocalized. Second descriptor denoted with CT is describing charge transfer character of the excited state, with the range of values from zero (locally excited state) to one (completely charge separated state (CS)). PR and CT descriptors are useful for distinction between localized, excimer and charge separation transitions in our case. In addition, we used another descriptor denoted with CT_{nt} which represents amount of charge transferred between the defined fragments. Detailed derivation of used descriptors from the 1eTDM could be found elsewhere [63]. Fragmentation of the system is important for this type of analysis and it is described in the section *The Excited States Densities of Transitions*.

3. Results and discussion

3.1. GPDI organization on graphene

In order to estimate quality of our DFTB structural and energy calculations firstly we optimized GPDI molecule on graphene using orthogonal super-cell that is large enough (34.64 Å × 34.28 Å × 30.00 Å), such that GPDI molecules' replicas could not interact with each other. Afterwards we refined the DFTB structures of GPDI on graphene at PBE/DZP+PP level of theory. We found excellent agreement for the adsorption energy. PBE adsorption energy is 10.147 eV (19.5 meV/atom) while DFTB value is 10.044 eV (19.3 meV/atom). Therefore, the computationally feasible DFTB method still gives us valuable structural and energetic data concerning these large supramolecular assemblies which has been so far treated only with molecular mechanics models on this scale [26].

To examine the orientation of GPDI interaction with graphene we calculated the adsorption energy of GPDI on graphene with respect to the orientation angle and average GPDI-graphene separation (see figure 1).

In total 2400 SP energy calculations were done to explore configurational space by varying the orientation angle in steps of 3° and GPDI-graphene separation in steps of 0.1 Å. The GDPI adsorption interaction with the graphene surface is nearly isoenergetic with respect to the defined orientation angle coordinate. Therefore, there is no preferential angle for GPDI adsorption on graphene. Beside SP calculations, we also performed optimization for different starting GPDI conformations on graphene which introduced multiple minima on the potential energy surface. Adsorption energies for these structures are compiled in the table 2.

Adsorption energies for the optimized structures do not differ much from the SP calculated energies, which indicates that deformation energy of the graphene layer and GPDI molecule due to their mutual interaction is small, amounting to 0.13 meV/atom and 1.14 meV/atom, respectively. The energy released upon GPDI deposition on graphene is sufficient to compensate the deformation penalty. Adsorption energies for optimized structures span in energy range from −18.1 to −19.3 meV/atom. Similar to the case of SP calculations, there is not a preferential orientational angle for adsorption while average separation of GPDI and graphene amounts to 3.08 Å. All attempts to find possible stable side-adsorbed structures (sideways adsorption) failed, since geometry optimization always reorients the GPDI molecule to be parallel to the graphene sheet. Several SP calculations imply that side-adsorption energy amounts to around -4 meV/atom, which is significantly smaller than adsorption energy of parallel conformations.

Various almost isoenergetic GPDI conformations on graphene allows different starting grounds to build up G-ribbons. In the following paragraph we investigate stability and organization of two types of G-ribbons and G_2PDI based HOF structures in mono- and multilayer organizations.

Free-standing guanine-based ribbons have been previously studied in detail [1, 3, 4, 6, 9, 67–71]. Since hydrogen

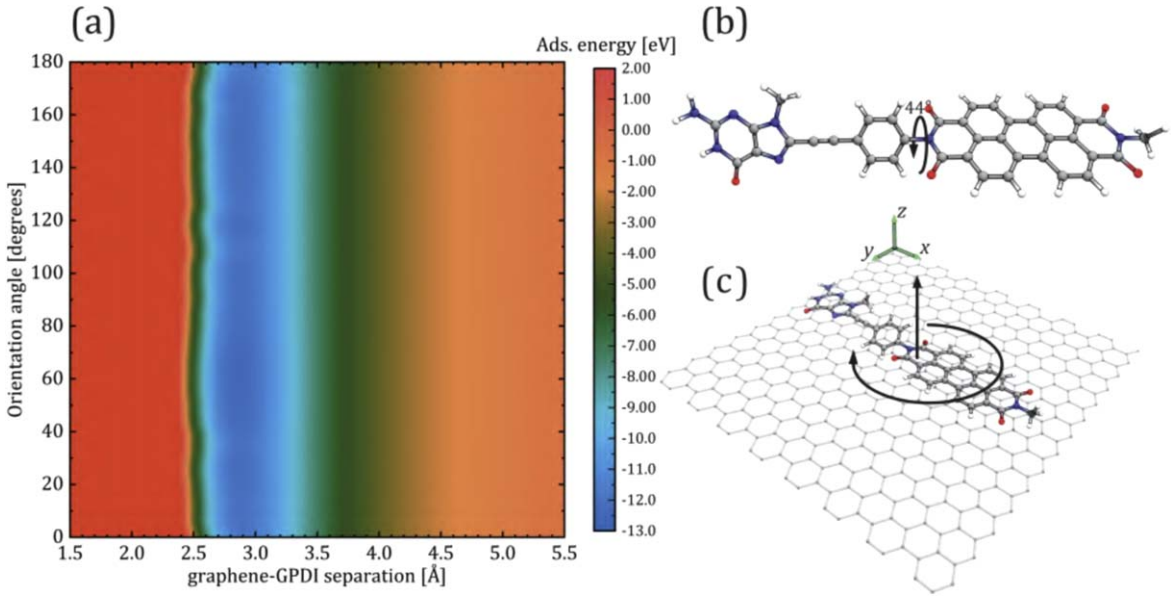

Figure 1. (a) Adsorption energy for single GPDI molecule on the graphene monolayer. (b) GPDI structure optimized at the DFTB3-D3H5/3ob level of theory. Torsion angle between arene and PDI moiety is indicated. (c) Structure of the single GPDI molecule adsorbed on the graphene monolayer. Arrows depicts two coordinates used for molecule positioning on the graphene: orientation angle—angle between longest intramolecular rotational axis and *x*-axis. Graphene—GPDI separation—all atom average separation of GPDI molecule from the graphene at DFTB3-D3H5/3ob level of theory.

Table 2. Adsorption energies for the optimized GPDI structures on the graphene. GPDI molecule positions are characterized with graphene-GPDI separation and orientation angle (see figure 1 for the coordinates definition).

Graphene-GPDI separation [Å]	Orientation angle [degrees]	Adsorption energy [meV/atom]	Graphene—GPDI separation [Å]	Orientation angle [degrees]	Adsorption energy [meV/atom]
3.00	−1.0	−19.3	3.08	100.7	−18.7
3.08	9.0	−18.8	3.08	110.5	−19.1
3.07	20.0	−18.5	3.08	118.3	−19.3
3.09	24.3	−18.6	3.11	123.3	−19.2
3.09	50.6	−18.6	3.06	153.4	−18.9
3.12	60.4	−18.1	3.08	161.8	−18.7
3.09	68.6	−18.7	3.08	169.3	−18.4
3.09	80.2	−19.0	3.05	177.2	−19.1
3.07	89.6	−18.8			

bonds between neighboring guanine molecules are responsible for stability of ribbons, only two ribbon configurations are possible. Following the same spatial reasoning and considering positions of H-bond accepting O6 and N3 and H-bond donating N1 and N2 atoms of guanine moiety (for atom numbering see figure 2), we determine only two possibilities for arranging of GPDI into ribbons on a graphene sheet. The same H-bonding pattern as in type B ribbon of the [12] is employed in GPDI-based ribbon, which we denoted here as type I ribbon. In contrast, H-bonding pattern of type A ribbon of the [12] cannot be realized for GPDI ribbons, since the PDI decoration of guanine at C8 position would encounter steric hindrance between neighboring ribbon units. Same hindrance problem is encountered when considering type III ribbon of the [4]. However, we derived another possible GPDI ribbon geometry from the type I ribbon by rotating one of the GPDI units by 180° around its longest intramolecular axis and than rotating it again by 90° perpendicular to the longest intramolecular axis. We denoted this ribbon as type II ribbon. Both studied ribbon types are presented in the figure 2. To best of our effort we recognized only these two ribbon types.

For both ribbons type, we identified four hydrogen bonds in which guanine moieties participate—two on each non Watson–Crick side of the guanine. For type I ribbon we identified two pairs of two opposite N2–H2⋯N3 and N1–H1⋯O6 H-bonds where N1–H1⋯O6 are slightly shorter (see figure 2). Single type of H-bond is found on each of the non Watson–Crick side of the guanine. For type II ribbon we also identified two types of H-bond, N2–H2⋯O6 and N1–H1⋯N3. In this case both H-bond types are found on both non Watson–Crick sides of guanine also in the opposite arrangement. Type II ribbons have more pronounced geometrical differences in H-bonding pattern between guanines

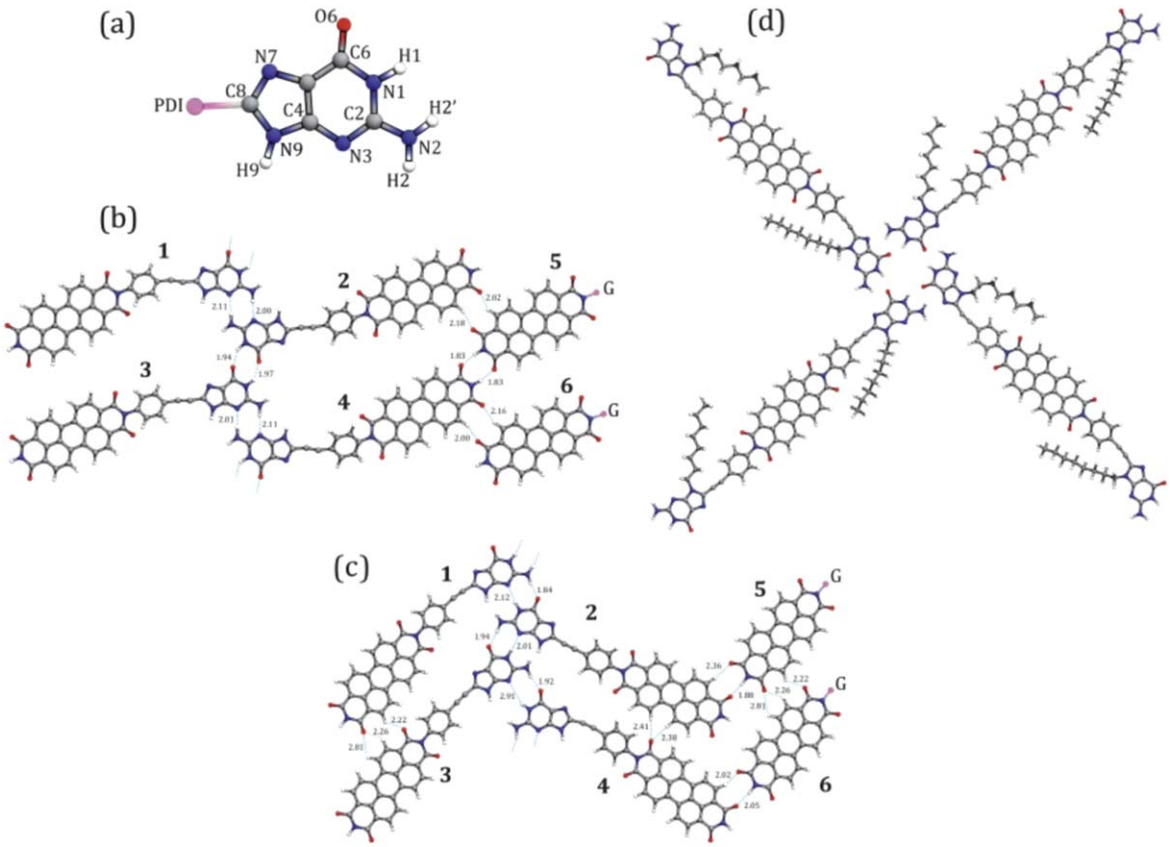

Figure 2. (a) Guanine molecule with its atoms numbering. (b) type I ribbon, (c) type II ribbon and (d) HOF structures. GPDI molecule numbering is indicated with numbers from 1 to 5. PDI moieties on the right-hand side of the ribbons present part of the periodic replicas to illustrate H-bonding between PDI moieties. Blue dotted lines represent H-bonds with their lengths indicated in Å units. Pink atoms show places where rest of the molecule is bound to. Graphene layer underneath structures is excluded due to clarity.

compared to type I ribbons. This is probably due PDI–PDI moieties interactions, i.e. geometrical arrangement of the GPDI units. When analyzing contacts between PDI moieties, i.e. ribbons periodic replicas we find that they establish H-bonds via imide functional groups. Two imide groups are present, front and terminal, i.e. closer and further from the arene moiety linker, respectively. Imide groups oxygen atoms are H-bond acceptor in this case interacting with hydrogens bound to nitrogen and carbon atoms of the PDI. This yields two types of hydrogen bonds: N–H···O and C–H···O. In case of the type I ribbon PDI moieties interact only via terminal imide group forming in total four hydrogen bonds per PDI—two N–H···O and two C–H···O in the opposite directions. Somewhat more complex situation is found for the type II ribbon where front imide group participate in the H-bonding as well. Different geometrical arrangement of the GPDI molecules allow that front imide group oxygens' now interact with neighboring PDI's side C–H groups and form one bifurcated H-bond. As it will be qualitatively described later with EDA analysis, these H-bonds are not strong as ones established between guanines, but their contribution in the total stability of the ribbon cannot be neglected.

To gain a deeper insight into the multilayer GPDI ribbons formation on graphene we analyze the binding energy in figure 3. The binding energy is calculated as difference of the energies of optimized periodical supramolecular assembly and separately optimized geometries of GPDI and graphene under the same periodic conditions. The binding energies without graphene are calculated as a difference of the SP energy of the adsorbed GPDI geometries and separately optimized geometries of GPDI. Ratio of following energies indicates the formation mechanisms of investigated systems: *formation of ribbon in plane parallel to graphene, vertical stacking of molecules, and their interaction with graphene*. GPDI-graphene interaction has a crucial role in the initial steps of ribbon formation. In the formation of type I ribbon the binding energy is lowered by 32 meV/atom when second GPDI is added to initial molecule placed on graphene, whereas the energy is nearly constant when graphene is absent. Addition of second pair of GPDI molecules in the ribbon lowers the energy by about 5 meV/atom. Two pairs of GPDI in the type II arrangement has even larger energy difference of 59 meV/atom when graphene is or is not present. This can be attributed to the local polar nature of the type II ribbon, which will be better understood later in text after the EDA analysis. Introduction of the second layer in the stack significantly stabilizes the system by around 12–18 meV/atom (for type I ribbon, depending on stacking dislocations and mutual layers orientation) and about 23 meV/atom (for type II ribbon, the range of energies is smaller for this ribbon type). We analyzed three types of stacking geometries as illustrated in figures 3(a) and (b): face-to-back (F2B), and two

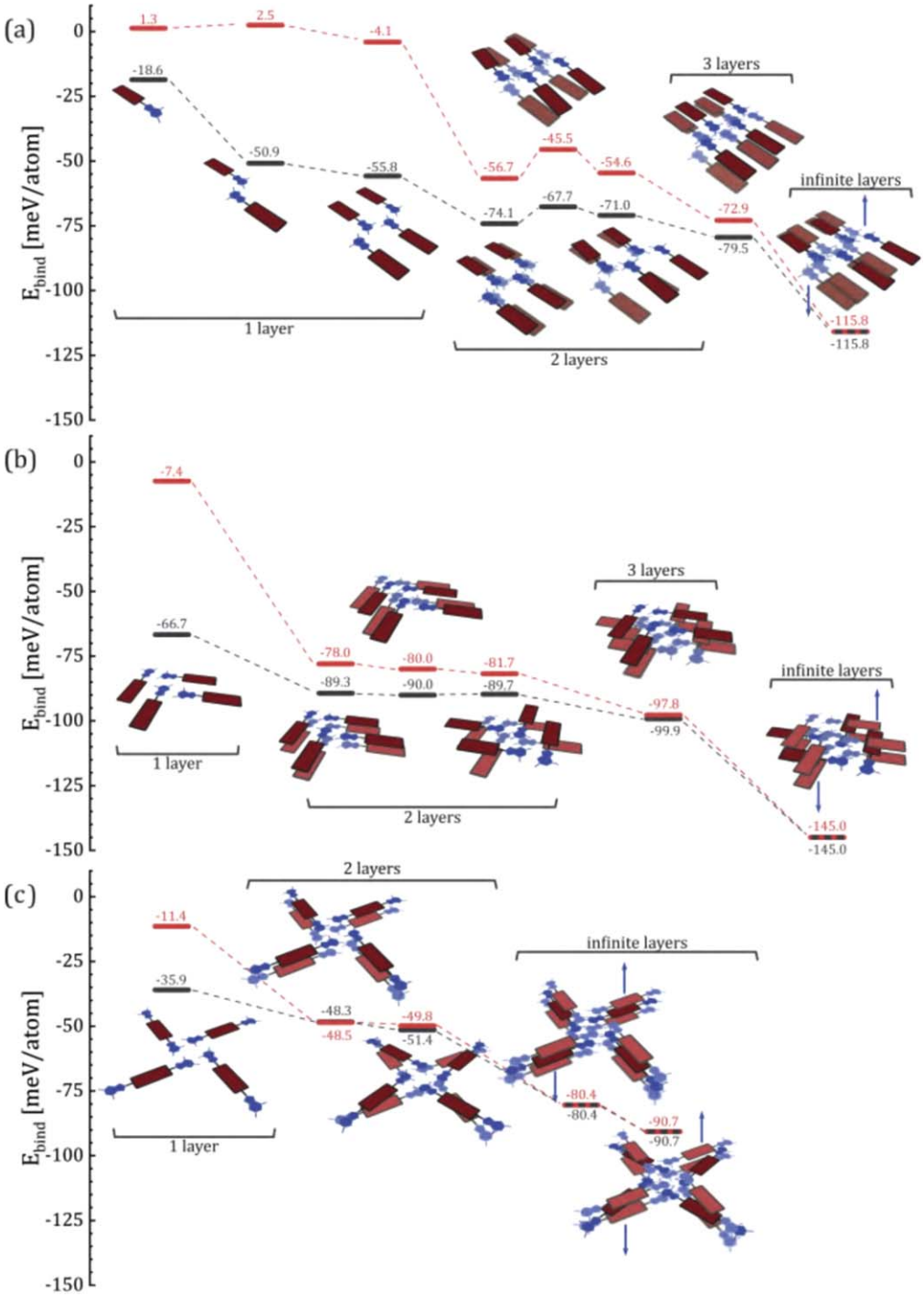

Figure 3. Stability and organization of GPDI and HOF structures on graphene. Binding energy for the system with and without graphene is shown respectively in black and red colors, respectively for type I (panel (a)), type II (panel (b)) ribbons and HOFs (panel (c)). Progressing from left to right are shown structures and binding energies for monolayer, bilayer, trilayer and infinitely thick structures (GPDI/HOF stacks). For each thickness systems the energy and geometries for one, two and more GPDI molecules in ribbon assemblies are presented. Shades of brown rectangles illustrate the PDI moiety in different levels of stacked ribbons. Graphene layer underneath ribbons and HOF structures is omitted for clarity.

face-to-face (F2F) configurations. F2B geometries were derived by adding one ribbon on the top of the another in the same arrangement. One type of the F2F geometries is constructed by rotating upper ribbon layer by 180° with the respect to the central guanine units (i.e. H-bonds directions) whereas subsequent rotation perpendicular to the central guanine units yielded another F2F arrangement. All multilayered ribbon types showed tendency towards interlayer slippage with respect of the directions of guanine-guanine H-bonds. Interlayer slippage between ribbons occures in order to minimize steric hindrance between arene linker moieties (see figure 1(b)). The antiparallel electric dipoles

Table 3. EDA for type I and type II ribbons. See figure 2 for fragments (GPDI molecules) layout. All energies are given in kcal mol^{-1}.

Type I ribbon								
	1–2	**2–3**	**2–4**	**1–3**	**2–5**	**4–6**	**2–6**	**4–5**
ΔE_{tot}	−12.7	−14.7	−1.2	−1.2	−6.3	−5.9	0.0	−14.0
ΔE_{ele}	−15.9	−22.6	−0.5	−0.4	−10.0	−9.6	0.0	−21.7
ΔE_{ex}	−3.7	−5.2	0.1	0.1	−1.8	−1.8	0.0	−5.5
ΔE_{rep}	27.6	34.6	0.0	0.0	19.5	18.8	0.0	37.1
ΔE_{pol}	−10.4	−10.9	−0.2	−0.2	−4.7	−4.6	0.0	−13.0
ΔE_{disp}	−10.3	−10.5	−0.6	−0.6	−9.2	−8.7	0.0	−10.9
Type II ribbon								
	1–2	**2–3**	**2–4**	**1–3**	**2–5**	**4–6**	**2–6**	**4–5**
ΔE_{tot}	−16.7	−18.0	−11.0	−8.8	−9.2	−8.8	−0.5	0.0
ΔE_{ele}	−18.6	−22.2	−7.1	−8.1	−11.0	−12.3	0.5	0.0
ΔE_{ex}	−4.0	−4.8	1.2	−0.2	−1.5	−2.2	0.3	0.0
ΔE_{rep}	31.8	38.0	15.8	19.7	16.9	20.4	0.1	0.0
ΔE_{pol}	−13.7	−14.5	−4.8	−5.1	−5.8	−6.0	−0.4	0.0
ΔE_{disp}	−12.3	−14.4	−16.0	−15.0	−7.9	−8.7	−1.1	0.0

(antiferroelectric-like) in the bilayer stack of the polar type II ribbons is more stable than the parallel orientation by around 4 meV/atom due to the dipole–dipole interaction. Initial stacking from mono to bilayer ribbon (when it is still small containing two pairs of GPDI molecules) has a significantly larger energy change for free-standing ribbons than in the case of the stack growth on graphene. As well, the initial stabilization due to vertical growth is more energy remarkable than the in-plane development of the ribbons. Importantly, these differences rapidly decay already with triplelayer. The effect of graphene-GPDI interaction is crucial at the initial stage of structural growth, while the interaction is becoming irrelevant for thick stacks. Energy difference between infinitely thick stack and a monolayer is 60 meV/atom and 78 meV/atom for type I and type II ribbons, respectively. Importantly, these binding energies have type I/II monolayer ribbons that contain 30/32 GPDI molecules (equivalent 15/32 unit cells) in one layer, which can be estimated from energy decrease of 5 meV/atom with in-plane growth of ribbon by a pair of GPDI molecules (one unit cell). Considering that energy difference in stacking process is relatively large in mono- to bi-layer ribbon of graphene transition (around 18 meV/atom for type I ribbon and 23 meV/atom for type II ribbon) very short ribbons with only 10 GPDI molecules in a monolayer (5 unit cell) are more energy favorable than bilayer ribbons. Therefore, in-plane growth is more likely than stacking and consequently very thin films of GPDI molecules covering large surface areas of graphene are expected, as indicated by the sample energy difference analysis. We also calculated binding energy of reported hydrogen bonded organic frameworks based on GPDI molecules (figure 3(c)) reported in the literature [26, 27]. Due to large systems it was not feasible to calculate energies of their in-plane growth, but only a columnar phase. Similarly to ribbons, the energy difference of free-standing HOFs and HOFs on graphene rapidly decreases by stacking thickness, reaching zero already for a bilayer HOF. Here, we also investigated F2B and F2F arrangements of HOFs. The energy loss in mono- to bi-layer transition of HOF on graphene is only about 13 meV/atom. If we assume that in-plane growth decreases energy close to that value of ribbons (a reasonable assumption since similar types of H-bonds are also responsible for growth of HOFs) then in-plane growth on graphene is also a more preferable than stacking.

It has been experimentally demonstrated that alkylated guanosine derivates can form supramolecular nanoribbons on the solid(HOPG)-solution interface [72]. Role of the solvent and solubilizing alkyl or glycol tails is important in order to effectively furnish these kinds of supramolecular architectures. However, we do not tackle this issue as it would dramatically increase number of atoms in the system and consequently the computational time. Yet, due to the very flexible nature of studied molecules and ribbons and their high mobility when deposited on graphene there can be sufficient space for long alkyl or glycol solubilizing tails with whom GPDI can be functionalized at different positions. Therefore, solubility of GPDI in different organic solvents would be ensured. Assuming a fine balance between solubility and the molecular association on the graphene and according to results from this section (similar binding energies for single-layered ribbons and HOFs with four units, i.e. 55.8 and 35.9 meV/atom, respectively) it is very likely that ribbon-like in-plane organization of GPDI molecules would indeed occur.

3.2. Energy decomposition analysis

In order to gain a deeper insight into guanine-guanine and PDI–PDI moieties interactions, i.e. driving force for GPDI ribbons assemblies, we performed EDA by decomposing total interaction energy (ΔE_{tot}) between GPDI molecules into electrostatic (ΔE_{ele}), exchange (ΔE_{ex}), repulsion (ΔE_{rep}),

polarization (ΔE_{pol}) and dispersion (ΔE_{disp}) energy terms EDA results for type I and type II ribbons are compiled in the table 3. H-bonding patterns for type I and type II ribbons are previously discussed in the text and here we present its energetic aspects.

Most stabilizing interaction for type I ribbon is found between GPDI molecules 2 and 3 (see figure 2 for molecule numbering). Molecules 2 and 3 are glued through guanine moieties with two N1–H1⋯O6 H-bonds in the opposite direction with similar bond lengths of 1.94 and 1.97 Å. Main and only destabilizing term for interaction(s) between these two (any other) molecules is ΔE_{rep} amounting to 34.6 kcal mol^{-1}. This contribution is easily overcomed by all other stabilizing interactions and mainly with ΔE_{ele} (-22.6 kcal mol^{-1}) whereas ΔE_{pol} and ΔE_{disp} terms are of equal importance and amount to -10.9 kcal mol^{-1} and -10.5 kcal mol^{-1}, respectively. The relatively large ΔE_{pol} indicate significant change in the orbital shape and partially covalent character of this H-bond which is expected since O6 of guanine moiety is strong H-bond acceptor. Second strongest interaction for type I ribbon is found between PDI moieties, i.e. molecules 4 and 5. This interaction has almost the same stabilizing effect as H-bonding between molecules 2 and 3. This is expected since same type and number of the H-bonds mediate this interaction, particularly two N-H⋯O with the opposite direction. However, their bond length of 1.83 Å is shorter than those of N1–H1⋯O6 of guanine moieties (1.94 and 1.97 Å) but with less favorable angle between H-bond donor and acceptor–143 and 168°, respectively. Third strongest intermolecular interaction is found between molecules 1 and 2. This interaction is mediated through two N2–H2⋯N3 H-bonds arranged in the opposite direction and its total interaction amounts to -12.7 kcal mol^{-1}. This is somewhat weaker interaction when compared to the total interaction between molecules 2 and 3 or 4 and 5. Weaker affinity of N3 as H-bond acceptor compared to O6 of guanine moiety is responsible for this effect. Non-negligible interactions are also found between molecules 2–5 and 4–6, i.e. neighboring PDI moieties. Total interaction between these molecules amount to -6.3 and -5.9 kcal mol^{-1}, respectively. Similar interplay of the energy terms is found for 2–5 and 4–6 as for the strongest ones except for ΔE_{disp} which now plays even more important role and it amounts to -9.2 and -8.7 kcal mol^{-1}.

More diverse contacts between GPDIs are found for type II ribbon. Strongest interactions are again found between guanine moieties, i.e. molecules 1–2 and 2–3 and ΔE_{tot} for them amount to -16.7 and -18.0 kcal mol^{-1}, respectively. Two H-bonds in the opposite direction are stabilizing guanine moieties—N2–H2⋯N3 and N1–H1⋯O6. Increased stabilization compared to the type I ribbon originate from the favorable locale dipole arrangement of the guanine moieties. Another distinguishable feature for type II ribbons is non-negligible interactions between molecules 1–3 and 2–4 that amounts to -8.8 and -11.0 kcal mol^{-1}. Bifurcated H-bonds are responsible for stabilization between these molecules with pronounced ΔE_{disp} term. PDI–PDI interaction between neighboring molecules (2–5 and 4–6) is also noticeable (-9.2 and -8.8 kcal mol^{-1}) for type II ribbons.

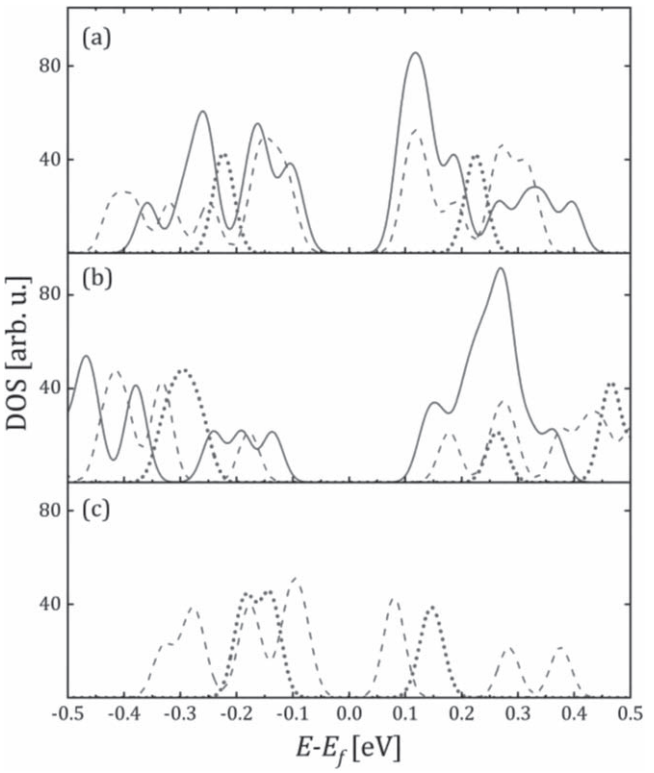

Figure 4. Density of states (DOS) for (a) type I ribbon, (b) type II ribbon and (c) HOF systems. Dotted, dashed and solid lines correspond to the one-, two- and three-layered structures' DOS. Gaussian broadening function is used with broadening parameter set to 0.025 eV.

Overall higher stability (lower binding energy, see figure 3 and accompanying text) of the type II ribbon compared to the type I ribbon is attributed to additional favorable dispersion driven contacts between PDI moieties and dipole enhanced H-bonding within guanine moieties.

Many-body effects are not investigated within this EDA scheme. ΔE_{ele} and ΔE_{ex} terms are pairwise additive, while ΔE_{pol}, ΔE_{rep} and ΔE_{disp} are not and all many-body effects in non-covalenty glued systems like this should originate from the polarization energy [53]. One can also inspect to which extent H-bonding cooperativity is increasing stabilization in these systems since H-bonding cooperativity is a fingerprint property of self-assembled free standing G-quartets and G-ribbons on the surfaces [4] and it is beyond the scope of this paper.

3.3. Electronic DOS

In section 3.1. we showed that in-plane parallel to graphene growth is more likely to occur than the vertical stacking of the molecules. To investigate electronic properties of the proposed structures we calculated DOS for the most stable one-, two- and three-layered ribbon structures as well as for one- and two-layered HOF structures (see figure 3). DOS profiles are calculated with DFTB3-D3/3ob method, i.e. using the same level of theory as for the single-point energy calculations in the section 3.1. DOS diagrams in the vicinity of the

HOMO-LUMO gaps are presented in the figure 4. Complete DOS profiles are reported in the SI.

DOS for all studied structures exhibit characteristic molecular DOS profiles. Type I and type II ribbons' DOS profiles are very similar in the vicinity of the HOMO and LUMO energies. Addition of second layer to these systems leads to broadening of the DOS profile and consequently a reduction of the HOMO-LUMO gap from 0.44 to 0.22 eV and from 0.53 to 0.36 eV for type I and type II ribbons, respectively. On the other hand, adding the third layer does not dramatically influence DOS profiles for the ribbons. Somewhat more pronounced influence of the third layer is observed for type II ribbon due to the antiparallel orientation of the electric dipoles in the three-layered stack. This additional layer slightly reduces the HOMO-LUMO gap for both systems by 0.03 and 0.08 eV for type I and type II ribbons, respectivelly. HOF system's DOS profile initially have smaller HOMO-LUMO separation (0.28 eV) compared to those of ribbons. Addition of a second layer to the HOF structure also reduces the HOMO-LUMO gap by 0.12 eV, i.e. from 0.28 to 0.16 eV. Although, GPDI and G_2PDI molecules that build ribbons and HOF structures, respectively, are not equivalent, their DOS profiles and the HOMO-LUMO separations are found to be similar. This indicates similar electronic properties of these supramolecular architectures.

3.4. The excited states densities of transitions

Faith of rylene dye covalently decorated G-quadruplex long-lived CS states' lifetimes and quantum yields is highly affected via spatial and orbital overlap between stacked dye units, i.e. its structural properties [23, 25, 26]. Solvent polarity plays minor to almost no role in the CS states dynamics due to shielding of aromatic GTDI quadruplex core with aliphatic shell [25] which again can be considered as a structural constraint. Results in the following section are gas phase results. Including implicit solvent model in the calculations would probably lead to the stabilization of the CS states. More polar solvents would lead to the greater stabilization of the CS states than the less polar ones. On the other hand, solvents with a strong H-bond accepting properties could lead to disruption of self-assemblies, like in the case of pyridine and GTDI assemblies. [25] However, we expect this effect to be similar for all of the studied structures and therefore does not affect conclusions withdrawn from the gas phase results.

Structural similarities to those of G-quadruplex based organic frameworks and columnar supramolecular architectures are encountered in multilayered G-ribbons studied here. High-degree of π stacking between PDIs in multilayered G-ribbons could imprint similar CS states properties to those of HOFs and columnar G-quadruplex based donor-acceptor systems. Accurate computational study of the exciton formation, evolution and decay for large molecules' systems such GPDI quadruplexes and ribbons is not yet feasible. Therefore, we are only limited to study excited states' properties in the Frank–Condone region and compare it to their HOFs counterparts.

Types of excitations encountered in the multilayered GPDI ribbons and GPDI based HOFs are presented in the figure 5. In order to distinguish between localized, excimer and CS states we divided system into the fragments in the way that each PDI moiety and each guanine together with arene linker build one fragment. Descriptors obtained within this fragmentation scheme are denoted with CT_1 and PR_1. Thresholds for descriptors are chosen somewhat arbitrary. In that sense excitations with $CT_1 < 0.2$ are considered to be localized, while $CT_1 > 0.8$ are considered as pure CS states. If CT values are between these two threshold values ($0.2 < CT_1 < 0.8$) excimer character is attributed to the given excited state. Furthermore, considering PR_1 descriptor value to be lower or greater than 1.25 we could distinguish between PDI localized and PDI excitonic states, respectively. $PR_1 > 1.25$ means that $1/4$ of the total electron density is delocalized over more than one fragment in the system. Inspection of the natural transition orbitals (NTOs) suggests that only PDIs are involved in the localized transitions within this energy window. Combination of $0.2 < CT_1 < 0.8$ and $PR_1 > 1.25$ characterizes excimer states. States with $0.2 < CT_1 < 0.8$ and $PR_1 < 1.25$ are not encountered in none of these systems. To further distinguish between different types of excimer and CS states different fragmentation of the system is required. CT_4 descriptor is obtained when system is described with two fragments only, one consisting of all PDI moieties and another of all guanine moieties in the system. PDI and G-PDI excimer states are then sorted with $CT_4 < 0.2$ and $0.2 < CT_4 < 0.8$ conditions, respectively. Various types of CS states are also identified and could be divided into two groups, i.e. $G^{\bullet+}$- $PDI^{\bullet-}$ and $PDI^{\bullet+}$-$PDI^{\bullet-}$ CS states which are previously experimentaly identified [22, 30]. Another two fragmentation schemes are required to classify them in more detailed fashion. CT_2 descriptor is acquired when single GPDI/G_2PDI molecule is considered as a separate fragment while CT_3 descriptor is obtained when whole ribbon/HOF layer consisting of four molecules is considered as a fragment. CT_2 would suggest if CS state is monomolecular (occurring withing single GPDI/G_2PDI molecule) while CT_3 would describe inter or intralayer CS. Different combinations of CT_1, CT_2, CT_3 and CT_4 as presented on the figure 5 helps us identify CS $G^{\bullet+}$-$PDI^{\bullet-}$ monomolecular, CS $G^{\bullet+}$-$PDI^{\bullet-}$ intralayer, CS $G^{\bullet+}$-$PDI^{\bullet-}$ interlayer, CS $PDI^{\bullet+}$-$PDI^{\bullet-}$ intralayer and CS $PDI^{\bullet+}$-$PDI^{\bullet-}$ interlayer states. All of the CS states can be considered as almost pure ion-pair excited states since they exhibit high CT_{nt} descriptor value ranging from 0.90 for $G^{\bullet+}$-$PDI^{\bullet-}$ monomolecular CS state to 0.95 for inter- and intralayer CS states in all systems. Localized and CS states involving guanine moieties only are not found within this energy window nor PDI localized states due to high overlap of PDI moieties which favours PDI exciton formation.

Absorption profiles, DOT and its decompositions are given in the figure 6. Absorption spectra (figure 6(a)) of type I ribbon has one pronounced peak located at 2.65 eV originating from transition to the bright PDI excimeric states. Two shoulders to this peak are encountered on the high and low energy part of the spectrum arising from PDI excimeric and

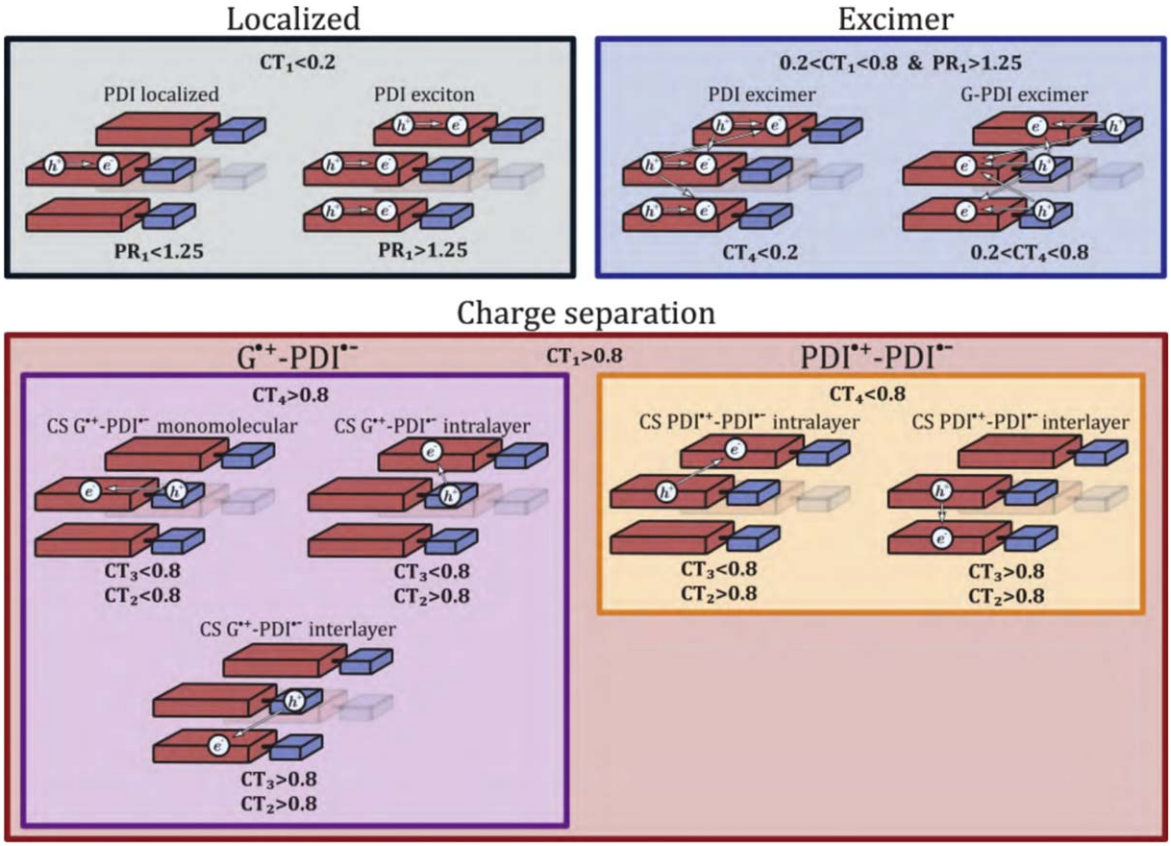

Figure 5. Schematic representation of types of the excited states in multilayered GPDI ribbons. Red and blue rectangular cuboids represent PDI and guanine moieties, respectively. Thresholds for descriptors (PR and CT) are given. h^+ and e^- depicts electron-hole and excited-electron, respectively. Note that same types of excitations are present within HOF absorption profile.

localized PDI excitonic transitions, respectively. Negligible contribution of CS states to the absorption is also observed. Distinctive red tail absorption feature at 2.08 eV for type I is found and attributed to populating four closely lying PDI excimer states. Absorption profile of type II ribbon also has pronounced peak at 2.65 eV. However, in this case localized transitions are not contributing to the absorption spectra but at higher energies (peak at around 2.98 eV) there is non-negligible absorption attributed to the CS $G^{\bullet+}$-$PDI^{\bullet-}$. Two shoulders to the main absorption peak coincide to those of HOF structure making type II ribbon more alike HOFs absorption profile than type I ribbon. Electronic absorption for optimized two layered HOF is found in the almost same energy range (2.15–3.10 eV) as for type I and type II ribbons 2.00–3.15 eV and 2.15–3.15 eV, respectively. However, HOF absorption profile is characterized with two distinct peaks located at 2.42 and 2.82 eV, both originating from the electron promotion to the mixture of PDI and G-PDI excimer states. We also observed that peak located at 2.82 eV has considerable participation of the CS $G^{\bullet+}$-$PDI^{\bullet-}$ which suggest that these CS states could be populated directly upon photon absorption. Same characteristic garnish type II ribbon absorption but in this case different type of CS $G^{\bullet+}$-$PDI^{\bullet-}$ are enrolled. The band gap between the frontier molecular orbitals (HOMO and LUMO) is determined for all three systems (see section 3.3.). It is clear that these energies do not correlate with any of the corresponding absorption maximum energies since the HOMO → LUMO transition is not represented in any of these absorption bands. For example, two most dominant contributions to the absorption band for the type I ribbon located at 2.65 eV are: HOMO-11 → LUMO+4 and HOMO-12 → LUMO+2.

Compared to absorption profiles, DOT profiles appear in the wider energy range, especially for the ribbon arrangements. When analyzing global DOT composition (figure 6(b)) we notice that amount of CS $G^{\bullet+}$-$PDI^{\bullet-}$ states are similar between all the systems and equal for type I ribbon and HOF arrangement (65.6%). Although CS $G^{\bullet+}$-$PDI^{\bullet-}$ states appear in the similar energy range with ribbons' CS contribution blueshifted by around 0.3 eV, their distribution across DOT is not equal. Low energy part of the DOT for type I ribbons lacks of CS $G^{\bullet+}$-$PDI^{\bullet-}$ states but they are supplant by other type CS $PDI^{\bullet+}$-$PDI^{\bullet-}$ states, i.e. 15.6% compared to 4.7% in HOF structure. This is not the case for type II ribbon where CS content is high for for both types of CS excited states, 54.7% and 20.3% for CS $G^{\bullet+}$-$PDI^{\bullet-}$ and CS $PDI^{\bullet+}$-$PDI^{\bullet-}$, respectively. Another interesting feature is greater presence of localized transitions for type I ribbon (7.9%) compared to type II and HOF (1.6%) structures. On the other hand, HOF structure has highest participation of excimeric states, 28.1% compared to 10.9% and 23.4% for ribbons. Most of these excited state characteristics can be explained by different spatial organization of HOF and ribbon structures. Greater $\pi\pi$ overlap between both PDI and guanine moieties in HOF

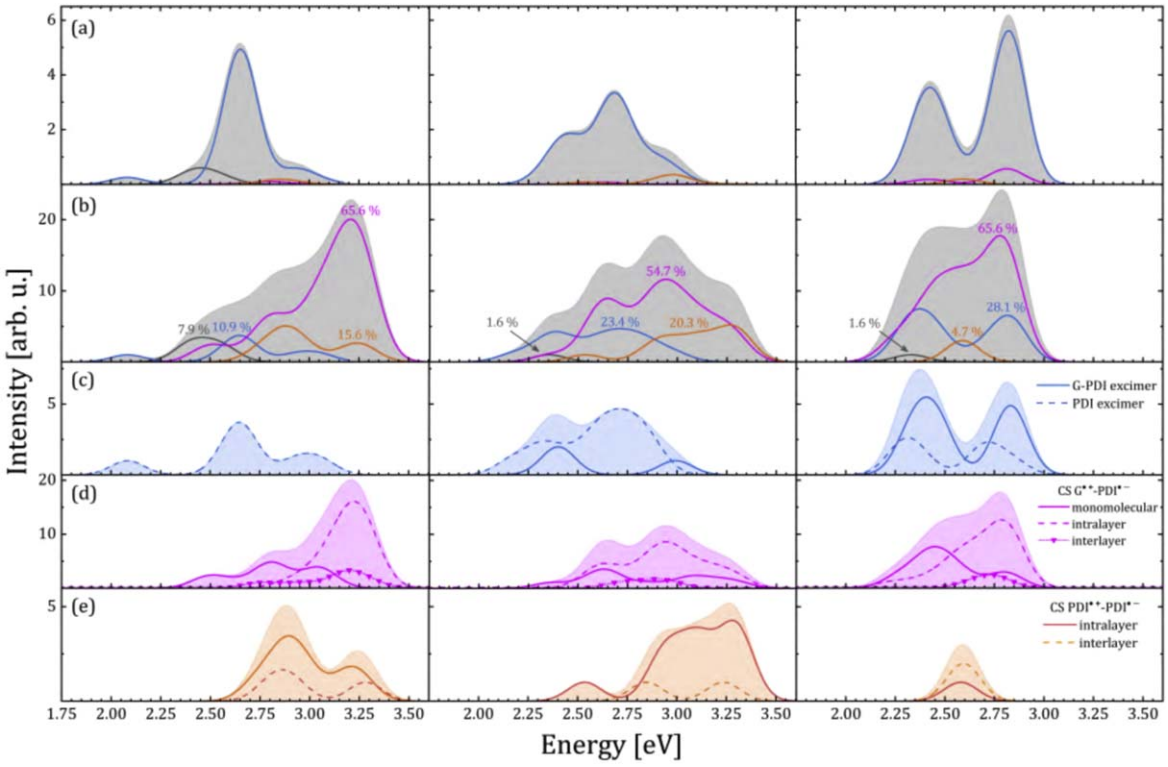

Figure 6. Decomposition of (a) absorption spectrum (shaded area) and (b) density of transitions (DOT) (shaded area) into the localized (black lines), excimeric (blue lines), CS $G^{\bullet+}$-$PDI^{\bullet-}$ (magenta) and CS $PDI^{\bullet+}$-$PDI^{\bullet-}$ (orange) excited states contributions. Percentage of each contribution in DOT is indicated. Type I ribbon absorption profile is presented on the far left, type II ribbon in the middle and HOF absorption profile on the far right panel. Panels (c), (d) and (e) represent more detailed decomposition of excimeric, CS $G^{\bullet+}$-$PDI^{\bullet-}$ and CS $PDI^{\bullet+}$-$PDI^{\bullet-}$ contributions to the DOT, respectively. For excited states types description see figure 5 and corresponding text.

structures compared to ribbons enhances electronic coupling and therefore promotes excimer formation. This can be rationalized via further decomposition of excimeric contribution to the DOT (figure 6(c)) and noticeable absence of G-PDI excimers for type I ribbons. Type II ribbon arrangement is characterized with higher overlap PDIs (comparable to those of HOF) and therefore can accommodate both G-PDI and PDI excimers just like HOF. Due to higher number of identical guanine chromophores within the HOF, G-PDI excimer participation is reasonably higher. Higher degree of chromophore $\pi\pi$ overlap also leaves different imprint to the CS $PDI^{\bullet+}$-$PDI^{\bullet-}$ states (Figure 6(e)), while relative arrangement of CS $G^{\bullet+}$-$PDI^{\bullet-}$ states (figure 6(d)) is relatively similar. Content of intralayer CS $PDI^{\bullet+}$-$PDI^{\bullet-}$ states is significantly higher for the ribbons arrangements due to proximity of adjacent PDI units. Stronger electronic interaction between adjacent PDI moieties is pronounced for type II ribbon where intralayer CS $PDI^{\bullet+}$-$PDI^{\bullet-}$ clearly dominates. This type of excitations would require more energy in the case of HOF arrangement. Relative amount and ordering of CS $G^{\bullet+}$-$PDI^{\bullet-}$ states within DOT profiles is maintained for all three systems. Monomolecular contributions are lowest in energy followed by interlayer and intralayer contributions. It is important to note that characteristics of both types of CS states could be exploited for optoelectronic applications as well as there are not huge differences between type II ribbon and HOF structures absorption and DOT profiles at Frank–Condone region. In fact, in total both types of ribbons exhibit higher amount of total CS withing this energy region compared to HOF, 81.2% and 75% compared to 70.3%, respectively. Furthermore, we believe that these differences would become even less pronounced if we used ensemble average of absorption and DOT profiles and/or model consisting of more GPDI molecules. Overall, surprising similarities of DOT composition are encountered for these systems making ribbons worthwhile for further investigation of exciton dynamics.

4. Conclusions

While HOFs based on GPDI molecules have been studied in detail for application in optoelectronics, layered ribbons made of these molecules supported on graphene have not been studied in such details yet. This is primarily due to complexity of the interfaces of flexible molecules and graphene and relatively large systems that are difficult to study with demanding *ab initio* methods. Our theoretical approach has proved as an excellent choice to overcome this obstacle. We theoretically analyzed favorable growth mechanism and structure of deposits using DFTB method and optical properties by the LR-TDDFT. We found that growth is rather homogeneous and thin few-layers ribbon structures cover large surface area of graphene. Absorption spectra and especially DOT profiles are very similar to those in HOFs in

the investigated energy window. We showed that CS $G^{\bullet+}$-$PDI^{\bullet-}$ states can be directly populated upon photo-excitation in the HOF and type II ribbon structures. Increased presence of CS $PDI^{\bullet+}$-$PDI^{\bullet-}$ states in the ribbons arrangements is encountered and this excited state feature is ascribed to the favorable geometrical organization. Existence of CS states between layers of the stacked structures promises potential application of these atomically thin graphene-GPDI heterostructures in photovoltaics and other optoelectronic devices.

Acknowledgments

The research leading to these results has been co-funded by the European Commission under the H2020 Research Infrastructures contract no. 675 121 (project VI-SEEM). Authors acknowledge the financial support by Ministry of Education, Science and Technological Development of Republic of Serbia through the institutional funding of Faculty of Physical Chemistry, University of Belgrade and Institute for Multidisciplinary Research, University of Belgrade. I.P. acknowledges the financial support of the Ministry for Education, Science and Technological development of the Republic of Serbia, contract with the Institute for Multidisciplinary Research, University of Belgrade 451-03-68/2020-14/200053. I.P. also acknowledges Qatar National Research Fund, cycle eleven, the grant number NPRP11S-1126-170033.

Data availability statement

All data that support the findings of this study are included within the article (and any supplementary files).

ORCID iDs

Branislav Milovanović https://orcid.org/0000-0001-7106-9353
Mihajlo Etinski https://orcid.org/0000-0003-0342-7045
Igor Popov https://orcid.org/0000-0002-2030-3530

References

[1] Li W, Jin J, Liu X and Wang L 2018 *Langmuir* **34** 8092–8
[2] Davis J T and Spada G P 2007 *Chem. Soc. Rev.* **36** 296–313
[3] Bald I, Wang Y G, Dong M, Rosen C B, Ravnsbæk J B, Zhuang G L, Gothelf K V, Wang J G and Besenbacher F 2011 *Small* **7** 939–49
[4] Paragi G and Fonseca Guerra C 2017 *Chem. Eur. J.* **23** 3042–50
[5] Jissy A K and Datta A 2014 *J. Phys. Chem. Lett.* **5** 154–66
[6] Livshits A I and Kantorovich L 2013 *J. Phys. Chem.* C **117** 5684–92
[7] Otero R, Schöck M, Molina L M, Lægsgaard E, Stensgaard I, Hammer B and Besenbacher F 2005 *Angew. Chem. Int. Ed.* **44** 2270–5
[8] Lena S, Masiero S, Pieraccini S and Spada G P 2009 *Chem. Eur. J.* **15** 7792–806
[9] Garah M E, Perone R C, Bonilla A S, Haar S, Campitiello M, Gutierrez R, Cuniberti G, Masiero S, Ciesielski A and Samorì P 2015 *Chem. Commun.* **51** 11677–80
[10] Saikia N, Waters K, Karna S P and Pandey R 2017 *ACS Omega* **2** 3457–66
[11] Rinaldi R, Maruccio G, Biasco A, Arima V, Cingolani R, Giorgi T, Masiero S, Spada G P and Gottarelli G 2002 *Nanotechnology* **13** 398–403
[12] Ciesielski A, El Garah M, Masiero S and Samorì P 2016 *Small* **12** 83–95
[13] Milovanović B, Stanković I M, Petković M and Etinski M 2020 *J. Phys. Chem.* A **124** 8101–11
[14] Jiang W, Li Y and Wang Z 2014 *Acc. Chem. Res.* **47** 3135–47
[15] Ostroverkhova O 2016 *Chem. Rev.* **116** 13279–412
[16] Prakash Neupane G, Ma W, Yildirim T, Tang Y, Zhang L and Lu Y 2019 *Nano Mater. Sci.* **1** 246–59
[17] Murad R, Iraqi A, Aziz A, Abdullah N S and Brza M A 2020 *Polymers* **12** 2073–4360
[18] Schmidt-Mende L, Fechtenkötter A, Müllen K, Moons E, Friend R H and MacKenzie J D 2001 *Science* **293** 1119–22
[19] Zhan X, Facchetti A, Barlow S, Marks T J, Ratner M A, Wasielewski M R and Marder S R 2011 *Adv. Mater.* **23** 268–84
[20] Huang C, Barlow S and Marder S R 2011 *J. Org. Chem.* **76** 2386–407
[21] del Prado A, González-Rodríguez D and Wu Y L 2020 *ChemistryOpen* **9** 409–30
[22] Wu Y L, Brown K E and Wasielewski M R 2013 *J. Am. Chem. Soc.* **135** 13322–5
[23] Wu Y L, Brown K E, Gardner D M, Dyar S M and Wasielewski M R 2015 *J. Am. Chem. Soc.* **137** 3981–90
[24] Powers-Riggs N E, Zuo X, Young R M and Wasielewski M R 2019 *J. Am. Chem. Soc.* **141** 17512–6
[25] Powers-Riggs N E, Zuo X, Young R M and Wasielewski M R 2020 *J. Chem. Phys.* **153** 204302
[26] Wu Y L *et al* 2017 *Nat. Chem.* **9** 466–72
[27] Wu Y L *et al* 2018 *Angew. Chem. Int. Ed.* **57** 3985–9
[28] Thazhathveetil A K, Harris M A, Young R M, Wasielewski M R and Lewis F D 2017 JACS **139** 1730–3
[29] Lech C J, Phan A T, Michel-Beyerle M E and Voityuk A A 2013 *J. Phys. Chem.* B **117** 9851–6
[30] Bartynski A N *et al* 2015 *J. Am. Chem. Soc.* **137** 5397–405
[31] Sabury S, Adams T J, Kocherga M, Kilbey S M and Walter M G 2020 *Polym. Chem.* **11** 5735–49
[32] Pieraccini S, Bonacchi S, Lena S, Masiero S, Montalti M, Zaccheroni N and Spada G P 2010 *Org. Biomol. Chem.* **8** 774–81
[33] Bou Zerdan R, Cohn P, Puodziukynaite E, Baker M B, Voisin M, Sarun C and Castellano R K 2015 *J. Org. Chem.* **80** 1828–40
[34] González-Rodríguez D, Janssen P G A, Martín-Rapún R, Cat I D, Feyter S D, Schenning A P H J and Meijer E W 2010 *J. Am. Chem. Soc.* **132** 4710–9
[35] Li F, Zhang Y, Zhou L, Zhang X and Chen Z 2018 *J. Porphyrins Phthalocyanines* **22** 944–52
[36] Liu X, Kwan I C M, Wang S and Wu G 2006 *Org. Lett.* **8** 3685–8
[37] Britnell L *et al* 2013 *Science* **340** 1311–4
[38] Wong J, Jariwala D, Tagliabue G, Tat K, Davoyan A R, Sherrott M C and Atwater H A 2017 *ACS Nano* **11** 7230–40
[39] Jariwala D, Davoyan A R, Wong J and Atwater H A 2017 *ACS Photon.* **4** 2962–70
[40] Yuan Z, Lee S L, Chen L, Li C, Mali K S, De Feyter S and Müllen K 2013 *Chem. Eur. J.* **19** 11842–6

[41] Hourahine B *et al* 2020 *J. Chem. Phys.* **152** 124101
[42] Grimme S, Antony J, Ehrlich S and Krieg H 2010 *J. Chem. Phys.* **132** 154104
[43] Grimme S, Ehrlich S and Goerigk L 2011 *J. Comput. Chem.* **32** 1456–65
[44] Gaus M, Goez A and Elstner M 2013 *J. Chem. Theory Comput.* **9** 338–54
[45] Řezáč J 2017 *J. Chem. Theory Comput.* **13** 4804–17
[46] Řezáč J and Hobza P 2012 *J. Chem. Theory Comput.* **8** 141–51
[47] Sedlak R, Janowski T, Pitoňák M, Řezáč J, Pulay P and Hobza P 2013 *J. Chem. Theory Comput.* **9** 3364–74
[48] Christensen A S, Kubař T, Cui Q and Elstner M 2016 *Chem. Rev.* **116** 5301–37
[49] Cui Q and Elstner M 2014 *Phys. Chem. Chem. Phys.* **16** 14368–77
[50] Artacho E *et al* 2008 *J. Phys. Condens. Matter* **20** 064208
[51] Perdew J P, Burke K and Ernzerhof M 1996 *Phys. Rev. Lett.* **77** 3865–8
[52] Troullier N and Martins J L 1991 *Phys. Rev.* B **43** 1993–2006
[53] Su P and Li H 2009 *J. Chem. Phys.* **131** 014102
[54] Balasubramani S G *et al* 2020 *J. Chem. Phys.* **152** 184107
[55] Becke A D 1988 *Phys. Rev.* A **38** 3098–100
[56] Lee C, Yang W and Parr R G 1988 *Phys. Rev.* B **37** 785–9
[57] Grimme S, Antony J, Ehrlich S and Krieg H 2010 *J. Chem. Phys.* **132** 154104
[58] Weigend F and Ahlrichs R 2005 *Phys. Chem. Chem. Phys.* **7** 3297–305
[59] Weigend F 2006 *Phys. Chem. Chem. Phys.* **8** 1057–65
[60] Yanai T, Tew D P and Handy N C 2004 *Chem. Phys. Lett.* **393** 51–7
[61] Frisch M J *et al* 2009 *Gaussian Inc 09 Revision D.01* (Wallingford CT: Gaussian Inc)
[62] Plasser F 2020 *J. Chem. Phys.* **152** 084108
[63] Plasser F and Lischka H 2012 *J. Chem. Theory Comput.* **8** 2777–89
[64] Plasser F, Wormit M and Dreuw A 2014 *J. Chem. Phys.* **141** 024106
[65] Mai S, Plasser F, Dorn J, Fumanal M, Daniel C and González L 2018 *Coord. Chem. Rev.* **361** 74–97
[66] Plasser F 2016 *J. Chem. Phys.* **144** 194107
[67] Thornton N J and van Mourik T 2020 *Int. J. Mol. Sci.* **21** 6571
[68] Giorgi T, Grepioni F, Manet I, Mariani P, Masiero S, Mezzina E, Pieraccini S, Saturni L, Spada G P and Gottarelli G 2002 *Chem. Eur. J.* **8** 2143–52
[69] Calzolari A, Di Felice R, Molinari E and Garbesi A 2002 *Physica* E **13** 1236–9
[70] Meng L, Liu K, Mo S, Mao Y and Yi T 2013 *Org. Biomol. Chem.* **11** 1525–32
[71] Kwan I C, Mo X and Wu G 2007 *J. Am. Chem. Soc.* **129** 2398–407
[72] Lena S *et al* 2007 *Chem. Eur. J.* **13** 3757–64

PCCP

ROYAL SOCIETY OF CHEMISTRY

PAPER

View Article Online
View Journal

Cite this: DOI: 10.1039/d3cp03259k

Enhancement of weak ferromagnetism, exotic structure prediction and diverse electronic properties in holmium substituted multiferroic bismuth ferrite†

Maria Čebela,*[abc] Dejan Zagorac,*[bc] Igor Popov,*[de] Filip Torić,[a] Teodoro Klaser,[f] Željko Skoko[a] and Damir Pajić*[a]

Bismuth ferrite (BFO, $BiFeO_3$), exhibiting both ferromagnetic and ferroelectric properties at room temperature, is one of the most researched multiferroic materials with a growing number of technological applications. In the present study, using a combined theoretical–experimental approach, we have investigated the influence of Ho-doping on the structural, electronic and magnetic properties of BFO. Synthesis and structural XRD characterization of $Bi_{1-x}Ho_xFeO_3$ (x = 0.02, 0.05, and 0.10) nanopowders have been completed. After structure prediction of Ho-doped $BiFeO_3$ using bond valence calculations (BVC), six most favorable candidates were found: α-, β-, γ-, R-, T1, and T2. Furthermore, all structure candidates have been examined for different magnetic ordering using DFT calculations. The magnetic behavior of the synthesized materials was investigated using a SQUID magnetometer equipped with an oven. The plethora of magnetic and electronic properties of the Ho-doped BFO that our theoretical research predicted can open up rich possibilities for further investigation and eventual applications.

Received 11th July 2023,
Accepted 30th July 2023

DOI: 10.1039/d3cp03259k

rsc.li/pccp

1. Introduction

Multiferroic materials are materials that occur in more than one ferroic order.[1] Among these materials, the most interesting ones are those which possess magnetic and electric order simultaneously. Materials in which magnetic and electric properties are coupled are referred to as magnetoelectrics.[1] Simultaneous control and tuning of the magnetic properties by an electric field and *vice versa* opens a vast scope of potential applications such as magnetic memories and spintronics.[2,3]

Among these magnetoelectric materials, $BiFeO_3$ stands as a role model for research potential applications as it shows multiferroic properties at room temperature with the antiferromagnetic transition at 640 K and ferroelectric transition at 1100 K. $BiFeO_3$ also stands as a building model for investigating different doping approaches for enhancing its multiferroic properties.[4] In $BiFeO_3$, the competition between various exchange interactions manifests itself as a non-collinear spin order, *i.e.*, an incommensurate spin cycloid with a period of 64 nm.[5]

The experimentally known modification of bismuth ferrite crystallizes in the perovskite structure type (α) under standard conditions, with rhombohedral space group *R3c* (no. 161).[6–9] The residual porosity location, microstructure, size, grain growth habit and grain boundary geometry of the sintered specimen are very important factors in determining the electrical as well as magnetic properties of $BiFeO_3$.[10–13] Especially interesting are doped $BiFeO_3$ materials which can strongly affect the structure and properties of bismuth ferrite. In particular, various morphologies of Ho-substituted $BiFeO_3$ were recently fabricated including thin films,[14–17] nanofilms,[18] nanoparticles,[19,20] nanopowders,[21,22] nanocrystalline BFO,[23] bulk and polycrystalline ceramics.[24–27]

In this work, we investigated the influence of doping $BiFeO_3$ with Ho. Holmium serves as an interesting choice as it has the

[a] University of Zagreb, Faculty of Science, Department of Physics, Bijenička cesta 32, 10000, Zagreb, Croatia. E-mail: mcebela@vinca.rs, dpajic@phy.hr
[b] Materials Science Laboratory, Institute of Nuclear Sciences Vinča, University of Belgrade, National Institute of the Republic of Serbia, Mike Petrovića Alasa 12-14, Belgrade, Serbia. E-mail: dzagorac@vinca.rs
[c] Center of Excellence "CextremeLab", Institute of Nuclear Sciences Vinča, University of Belgrade, National Institute of the Republic of Serbia, Mike Petrovića Alasa 12-14, Belgrade, Serbia
[d] Institute for Multidisciplinary Research, University of Belgrade, Kneza Višeslava 1, 11030, Belgrade, Serbia. E-mail: popov@ipb.ac.rs
[e] Institute of Physics, University of Belgrade, Pregrevica 118, 11080, Belgrade, Serbia
[f] Ruđer Bošković Institute, Bijenička cesta 54, 10000, Zagreb, Croatia

† Electronic supplementary information (ESI) available. See DOI: https://doi.org/10.1039/d3cp03259k

highest magnetic moment among the lanthanides series. In contrast to the so far investigated $BiFeO_3$ compounds doped with Ho, we have performed a detailed magnetic study which includes zero field cooled (ZFC) and field cooled (FC) curves above the Néel T_N temperature of the antiferromagnetic transition. Along with the magnetization measurements, we performed *ab initio* theoretical calculations. For utilizing the multiferroic properties of $BiFeO_3$ it is necessary to understand and control the spin cycloid in $BiFeO_3$.[28] Furthermore, the structure–property relationship has been investigated in great detail with respect to Ho doping in $BiFeO_3$ and additional perovskite structures have been predicted as well as their electronic and magnetic properties. This complete picture of synthesis, XRD and magnetic measurements combined with structure prediction and *ab initio* theoretical calculations gives valuable information about the influence of Ho substitution on magnetic behavior including the development of weak ferromagnetism and magnetic irreversibility.

2. Materials and methods

2.1. Synthesis and structural characterization of $Bi_{1-x}Ho_xFeO_3$ (x = 0.02, 0.05, and 0.10) nanopowders

Nanocrystalline powders of $BiFeO_3$ and $Bi_{1-x}Ho_xFeO_3$ (x = 0.02, 0.05, and 0.10) were made according to the hydrothermal method.[29,30] The simple, low-cost and energy-saving hydrothermal method has advantages over the conventional methods. The chemical compounds used in this work were bismuth nitrate ($Bi(NO_3)_3 \times 5H_2O$), holmium nitrate ($Ho(NO_3)_3 \times 5H_2O$), iron nitrate ($Fe(NO_3)_3 \times 9H_2O$), and potassium hydroxide (KOH); all the chemicals were of analytical grade. The mixtures of ($Bi(NO_3)_3 \times 5H_2O$), ($Ho(NO_3)_3 \times 5H_2O$) and ($Fe(NO_3)_3 \times 9H_2O$) were dissolved in 40 mL of 8 M KOH. The mixture was stirred vigorously for 30 min and transferred into an autoclave. The hydrothermal treatments were conducted under autogenous pressure at a temperature of 200 °C for 6 h. The produced powders were collected at the bottom of the autoclave after cooling to room temperature. The products were washed at least five times by repeated cycles of centrifugation in distilled water and dispersed in ethanol by sonicating for 60 min. The powders were obtained by evaporating ethanol in a mortar heated at 60 °C.

Structural characterization of the obtained powders was carried out using a Philips X-ray diffractometer (XRD) using a graphite monochromator with Cu-Kα radiation (wavelength λ = 1.54 Å). The data for structural refinement were taken in the 2θ range of 10–90°, with a step width of 0.02° 2θ and 5 s per step. Refinement was performed using the X Pert HighScore Plus[31] computer program adopting the Rietveld calculation method.

2.2. Magnetic measurements

The magnetic behavior of the synthesized materials in the form of sintered pellets was investigated using a SQUID magnetometer equipped with an oven option. In this way, the temperature dependence of magnetization in a wide temperature interval (2–800 K) is obtained. Moreover, the combination of a standard sample environment (2–400 K) and an oven (300–800 K) is used especially in order to measure the true zero-field cooled (ZFC) and field-cooled (FC) magnetization curves. First, the sample is cooled down to 2 K in zero field and measured in a field of 1000 Oe during heating up to 350 K. Then the sample is moved from the standard plastic straw into the quartz tube oriented in the same direction and inserted into the oven installed within the sample space in the same magnetic field. Measurement is quickly continued from almost the same magnetic state at room temperature up to 800 K. In this way, the full temperature range ZFC curve is obtained. Thereafter the measurement is continued in the same field of 1000 Oe from 800 K down to 350 K. Finally, the oven is uninstalled and the sample is transferred from the quartz tube into the plastic straw preserving direction to continue measurement from the same magnetic state. As the last step, the sample is measured down to 2 K in the same field. Only in such a way, which is rarely found in the literature, the true and complete ZFC–FC curves are obtained, which is very important in order to correctly characterize the magnetic irreversibility in case of high-temperature magnetic transition. Additionally, isothermal magnetic hysteresis curves at low temperatures (4 K) and room temperature (300 K) were measured.

2.3. Structure prediction and bond valence calculations

The main principles and methods of the crystal structure prediction and identification of structure candidates, especially including rare earth elements, have been given in detail elsewhere,[32–35] as well as the details about previous successful applications of these methods on perovskites.[36–38] In order to generate new structure candidates of Ho-doped $BiFeO_3$ perovskites we have used the Structure Prediction Diagnostic Software (SPuDS).[39] The SPuDS program is based on bond valence calculations and is used to predict the crystal structures of perovskites, including those distorted by tilting of symmetric octahedra or caused by Jahn–Teller distortions.[36,37,39,40] The SPuDS software requires a minimum amount of input data: the composition ($Bi_{1-x}Ho_xFeO_3$, x = 0.02, 0.05, and 0.10) and the oxidation state of each ion (Bi^{+3}, Ho^{+3}, Fe^{+3}, O^{-2}). Afterwards, structure optimization has been performed by restricting the octahedra to remain rigid during calculation, with six equivalent BX distances and all X–B–X angles equal to 90°. In this way, a full crystal structure can be generated from the size of the octahedron and the magnitude of the octahedral tilting distortion. Furthermore, SPuDS calculates the fractional position of each atom at each tilt angle step over a wide range of octahedral tilt angles.[39,40]

The size of the octahedron and magnitude of the octahedral tilting distortion is calculated by using the bond valence model, S_{ij},

$$S_{ij} = e^{[(R_{ij}-d_{ij})/B]} \quad (1)$$

where d_{ij} is the cation–anion distance, the B parameter is empirically determined as a universal constant with a value of

0.37, and R_{ij} is empirically determined for each cation–anion pair, based on bond distance measurements.[39,40]

The stability of the novel predicted perovskite structures is determined by comparing the calculated bond valence sums and the ideal formal valences. This quantity is known as the global instability index (GII) and it is calculated according to the Ho quantity in $BiFeO_3$ corresponding to the different Glazer tilt systems. The Goldschmidt tolerance factor[41] is another important value for investigating perovskite-related structures and is defined as a measure of the fit of the A-site cation to the cubic corner-sharing octahedral network.[39] The SPuDS program uses both the ionic radii defined by Shannon[42] and the bond-valence parameters separately to calculate the tolerance factor (whenever possible). Theoretical determination and identification of the predicted structures were performed using the KPLOT program.[43] The symmetry of the predicted structures was analyzed with the algorithms SFND[44] and RGS,[45] while duplicate structures were removed using the CMPZ algorithm.[46] The investigated structures were visualized using the VESTA code.[47]

2.4. *Ab initio* structure and property calculations

Calculations of the structural, electronic and magnetic properties have been performed using density functional theory (DFT) as implemented in the SIESTA code.[48] Periodic boundary conditions have been used throughout the study. Calculation cells contain 30 atoms for the alpha phase, 40 atoms for beta, gamma, T1 and T2 crystals, while the crystal with R symmetry contains 60 atoms. One Ho atom is considered in each cell. We used the Perdew–Burke Ernzerhof (PBE)[49] exchange–correlation functional, norm-conserving Troullier–Martins pseudopotentials with partial core corrections,[50] and a double-ζ basis including polarization orbitals. The reciprocal space has been sampled by a fine Monkhorst–Pack mesh[51] of $8 \times 8 \times 4$, $8 \times 10 \times 12$, $12 \times 12 \times 12$, $8 \times 8 \times 8$, $8 \times 12 \times 12$, and $8 \times 12 \times 12$ k-points in the Brillouin zone (BZ) of the alpha, beta, gamma, R, T1 and T2 structures, respectively.

A high mesh cut-off energy of 700 Ry was used to determine the self-consistent density matrix. Geometries have been optimized using the conjugate gradient method[52] until none of the residual Hellmann–Feynman forces exceeded 0.04 eV $Å^{-1}$. Prior to the optimization of Ho-doped structures, bare Ho-free crystals were optimized. Lattice vectors were kept fixed since atomic forces and frequently density matrix could not converge in optimizations with varying lattice vectors. Since local functionals do not describe well some transition metals, including Fe, we utilized the DFT+U method and particularly its GGA+U flavor.[53–55] In all calculations, we fixed the Hubbard U_{eff} = 3.8 eV for the Fe 3d orbital and U_{eff} = 0.95 for the Fe 4s orbital, which was successfully used in our previous calculations.[38]

3. Results and discussion

3.1. X-Ray powder diffraction (XRPD) and Rietveld refinement of $Bi_{1-x}Ho_xFeO_3$ (x = 0.02, 0.05, and 0.10)

Samples doped with 2, 5 and 10 at% of Ho, $Bi_{1-x}Ho_xFeO_3$ with x = 0.02, 0.05, and 0.10, were studied by powder X-ray diffraction and the data were refined by the Rietveld method. The rhombohedral $R3cH$ structure[38] was taken as the starting structural model for the refinement. Ho atoms were introduced into the structural model assuming the substitution at the Bi atom site. For each sample, the occupancy of the site shared by Bi and Ho was fixed according to the starting synthesis conditions and was not refined. Refined patterns are shown in Fig. 1(a)–(c), while refined parameters are given in Table S1 (see the ESI†).

Fig. 1(d) show the evolution of the diffraction maxima (104) and (110) with the increase of the Ho content. These two maxima are shifting towards higher Bragg angles indicating that the lattice parameters decrease as the doping level of Ho increases. Furthermore, a slight change in the distance between the two maxima is observed, with the peaks getting closer to each other with the increase of the Ho content. This agrees with previous reports,[26,56–61] which state that the resulting lattice distortion eventually suppresses the rhombohedral phase, transforming into the lower symmetric orthorhombic phase. This happens for x(Ho) larger than 10%.[20,26]

The dependence of lattice parameters on the Ho content is shown in Fig. 2, while numerical values of the lattice parameters are given in Table 1. It can be seen from the data above that the lattice parameters decrease with the introduction of the Ho atoms into the crystal lattice of $BiFeO_3$. This is to be fully expected as the ionic radius of Ho^{3+} (1.015 Å) is smaller than the ionic radius of Bi^{3+} (1.14 Å). An increase of the Ho content from 2% to 10% decreases lattice parameter a by 0.5% and lattice parameter c by 0.4%. Fig. 3 shows the refined α-$BiFeO_3$ structure doped with holmium showing the rhombohedral $R3cH$ (no. 161) space group.

3.2. Structure prediction of Ho-doped $BiFeO_3$ perovskites

Structure prediction in Ho-doped BFO was performed using bond valence calculations (BVC) and SPuDS code in order to find possible additional structure candidates besides the experimentally observed α-$BiFeO_3$ perovskite structure. As a result, we have predicted 15 additional perovskite-related structure candidates in various chemical systems, depending on holmium doping in $BiFeO_3$. Table 2 shows calculated values of the global instability index (GII) and tilt system of the most promising predicted modifications in the $Bi_{0.98}Ho_{0.02}FeO_3$, $Bi_{0.95}Ho_{0.05}FeO_3$ and $Bi_{0.9}Ho_{0.1}FeO_3$ compound.

The most stable $BiFeO_3$ perovskite structure with Ho-doping based on the GII criterion (Table 2), is the β-type in the space group $Pnma$, with GII ranging from 0.03816 to 0.08023 depending on the Ho content. This is in agreement with previous experimental and theoretical observations where the beta orthorhombic structure was found as a secondary phase in Ho-doped BFO.[20,21,26,58–61] Predicted beta phase in the $Bi_{0.9}Ho_{0.1}FeO_3$ system (corresponding to 10% Ho-doping) is shown in Fig. 4a.

The next most stable predicted Ho-doped structure according to the GII index appears as R-type in the rhombohedral $R\bar{3}c$ space group. The GII index of the R-type modification is close to the beta phase regardless of holmium content (Table 2). Moreover, R-type appears in the rhombohedral $R\bar{3}c$ (no. 167) space

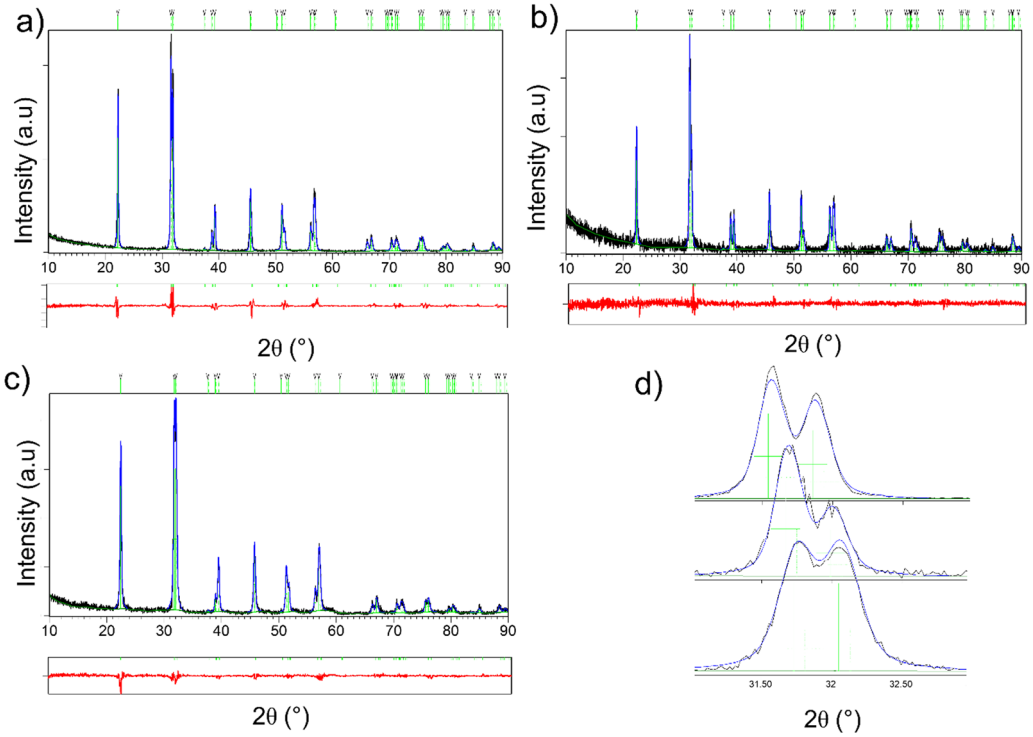

Fig. 1 Rietveld refinement of the samples (a) BHFO-2, (b) BHFO-5 and (c) BHFO-10, having 2%, 5% and 10% of Ho in BFO, respectively. The experimental curve is colored black whereas the refined one is colored blue. The difference between intensities is given at the bottom in red color. (d) The enlarged area between 31° and 33° 2θ with diffraction lines (104) and (110).

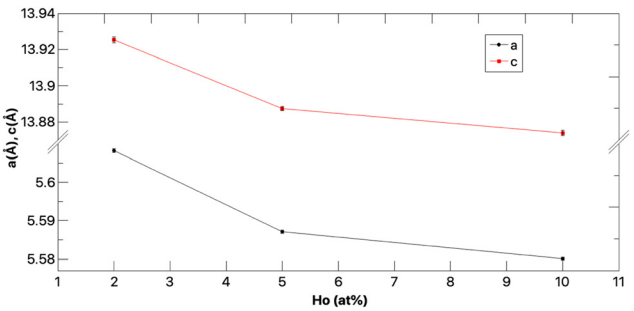

Fig. 2 Lattice parameters *a* and *c* dependent on the Ho content in the alpha $BiFeO_3$.

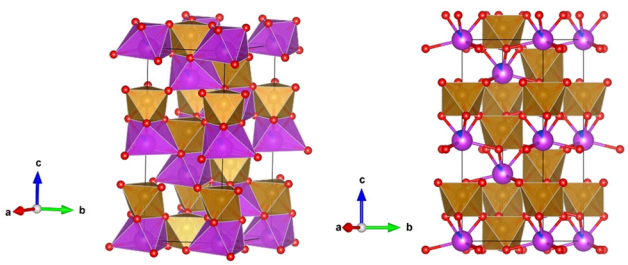

Fig. 3 The refined α-$BiFeO_3$ structure doped with holmium in rhombohedral *R*3*cH* (no. 161) space group: (a) polyhedra with sixfold coordination (CN = 6) of the Bi/Ho atom by O atom and Fe by O are shown; (b) *e.g.* 10% of Ho doping on Bi atomic positions in the alpha phase.

group, structurally related to the experimentally observed alpha phase appearing in the rhombohedral *R*3*c* (no. 161) space group, making the R-phase a strong structure candidate in Ho-doped BFO. In addition, previous experimental and theoretical data on pure $BiFeO_3$ show a high-temperature rhombohedral modification of $BiFeO_3$,[62–64] as our predicted R-phase. The predicted R-type in the $Bi_{0.9}Ho_{0.1}FeO_3$ system is shown in Fig. 4b.

Table 1 Lattice parameters of the samples with: 2% Ho (BHFO-2), 5% Ho (BHFO-5) and 10% Ho (BHFO-10) doping of $BiFeO_3$

Sample	*a* (Å)	*c* (Å)
BHFO-2	5.6082(5)	13.9253(2)
BHFO-5	5.5870(4)	13.8873(1)
BHFO-10	5.5800(4)	13.8739(2)

Structure prediction using BVC calculations and the GII index resulted in two additional tetragonal candidates, T1- and T2-type, which show the same value of GII index regardless of the Ho concentration in $BiFeO_3$ (Table 2). Both tetragonal T1 and T2 modifications are closely structurally related to T2 appearing as a polytype[32,65] of T1 along the *c*-direction (Fig. 5a and b). However, they are easily distinguishable by symmetry, where the T1 type appears in the *P*4/*mbm* (no. 127) space group, and the T2 phase appears in the *I*4/*mcm* (no. 140) space group. Alternative tetragonal phases have been previously reported in pristine $BiFeO_3$ at high temperatures,[66–68] as well as

Table 2 Calculated values of the global instability index (GII) and tilt system of the most promising predicted modifications in the (a) $Bi_{0.98}Ho_{0.02}FeO_3$; (b) $Bi_{0.95}Ho_{0.05}FeO_3$; and (c) $Bi_{0.9}Ho_{0.1}FeO_3$ compounds. Calculations were performed using the bond valence (BVC) method

Composition	$Bi_{0.98}Ho_{0.02}FeO_3$		
Modification	Space group	Tilt system	GII
β-type	*Pnma*	$a^-b^+a^-$	0.03816
R-type	$R\bar{3}c$	$a^-a^-a^-$	0.04284
T_1-type	*P4/mbm*	$a^0a^0c^-$	0.08938
T_2-type	*I4/mcm*	$a^0a^0c^-$	0.08938
γ-type	$Pm\bar{3}m$	$a^0a^0a^0$	0.72910
	$Bi_{0.95}Ho_{0.05}FeO_3$		
β-type	*Pnma*	$a^-b^+a^-$	0.05815
R-type	$R\bar{3}c$	$a^-a^-a^-$	0.06113
T_1-type	*P4/mbm*	$a^0a^0c^-$	0.09992
T_2-type	*I4/mcm*	$a^0a^0c^-$	0.09992
γ-type	$Pm\bar{3}m$	$a^0a^0a^0$	0.73225
	$Bi_{0.9}Ho_{0.1}FeO_3$		
β-type	*Pnma*	$a^-b^+a^-$	0.08023
R-type	$R\bar{3}c$	$a^-a^-a^-$	0.08226
T_1-type	*P4/mbm*	$a^0a^0c^-$	0.11480
T_2-type	*I4/mcm*	$a^0a^0c^-$	0.11480
γ-type	$Pm\bar{3}m$	$a^0a^0a^0$	0.73746

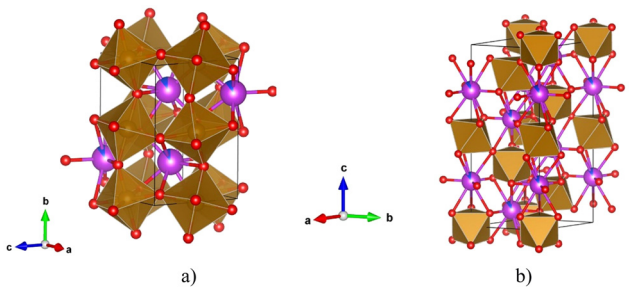

Fig. 4 Visualization of the predicted: (a) β-type of structure in the space group *Pnma* (no. 62) (b) R-type in the rhombohedral $R\bar{3}c$ (167) space group, in the $Bi_{0.9}Ho_{0.1}FeO_3$ system, corresponding to 10% of Ho doping in bismuth ferrite. Purple and blue balls correspond to Bi and Ho atoms, red atoms correspond to oxygen, while yellow atoms correspond to iron, represented by Fe–O octahedra in yellow color.

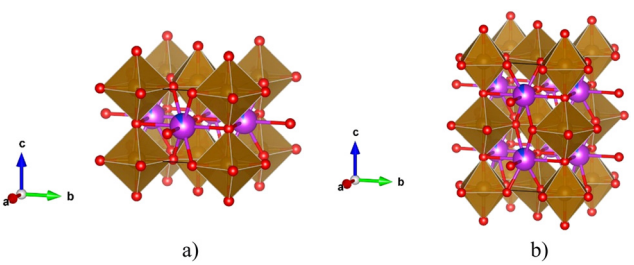

Fig. 5 Visualization of the predicted: (a) T1-type structure appearing in the space group *P4/mbm* (no. 127); (b) T2-type appearing in the *I4/mcm* (no. 140) space group, in the $Bi_{0.9}Ho_{0.1}FeO_3$ system. For colors see Fig. 4.

in our previous study,[38] supporting T1- and T2-types as very good structure candidates in Ho-doped BFO.

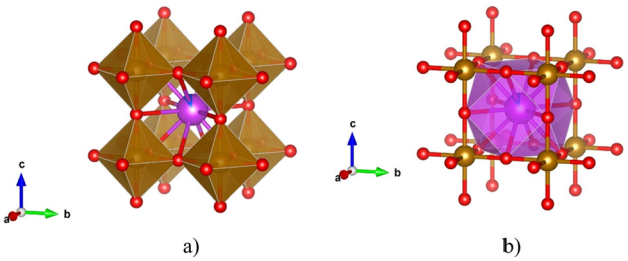

Fig. 6 Visualization of the predicted gamma phase in the $Bi_{0.9}Ho_{0.1}FeO_3$ system, corresponding to 10% of Ho doping in bismuth ferrite: (a) six-fold coordination (CN = 6) of the Fe atom by O forming perfect octahedra in cubic symmetry; (b) twelve-fold coordination (CN = 12) of the Bi/Ho atoms by O atom. For colors see Fig. 4.

Finally, the γ-type modification is the structure candidate with the highest level of the GII index regardless of Ho concentration in bismuth ferrite (Table 2), but it also shows the highest cubic symmetry ($Pm\bar{3}m$ (no. 221) space group). The Fe atoms are coordinated by six O atoms (CN = 6), forming a perfect octahedron (Fig. 6a), while Bi/Ho atoms are coordinated by twelve (CN = 12) oxygen atoms, different from eight-fold coordination in previous tetragonal phases (Fig. 5 and 6). Similarly, as in previous cases, the gamma type has been found in the experiments and theoretical studies in pure $BiFeO_3$ at high temperatures,[63,66,69] and was found in our previous work on BFO,[38] indicating the possible existence of the gamma phase in the Ho-doped $BiFeO_3$. To further check for the structural stability of the predicted phases, and investigate their properties, we have performed *ab initio* structure optimization.

3.3. *Ab initio* structure optimization

Each of the predicted structure candidates generated using BVC calculations and the SPuDs code, as well as equilibrium structures from experimental synthesis, were submitted to the *ab initio* local optimization using the conjugate gradient method. Hence, all calculations were carried out at absolute zero. In addition, all structures have been investigated for different magnetic ordering, ferromagnetic (FM) order and two antiferromagnetic orders (AFM1, AFM2). Since local functionals do not describe well some transition metals, including Fe, we utilized the DFT+*U* method and particularly its GGA+*U* flavor for local optimizations.[53–55] In all calculations we fixed the Hubbard U_{eff} = 3.8 eV for the Fe 3d orbital and U_{eff} = 0.95 for the Fe 4s orbital, which were successfully used in our previous calculations.[38] Since in this reference, other software was utilized rather than the one in the present study, before the production work we found that these U_{eff} parameters produce a band structure and DOS of bare $BiFeO_3$ very similar to those reported in the reference. We varied the U_{eff} of Ho 4f states (U_{eff} = 0.0, 2.5, 5.0, 7.5, and 9.0) electronvolts in order to investigate the influence of U_{eff} on the electronic structure of the doped $BiFeO_3$ crystals.

To compare the stabilities of the investigated structural types we present the substitutional formation energies of all optimized structures in Table 3. The substitutional

Table 3 Calculated substitutional formation energies (eV atom^{-1}) of the alpha, beta, gamma, R, T1, and T2 type structures for the ferromagnetic (FM) and two antiferromagnetic orders (AFM1 and AFM2). For the definition of × see in the text the considered chemical reaction. The energies are obtained using the DFT GGA+U method with fixed U_{eff} = 7.5 eV for Ho 4f states. N/A means that data are not available as calculations could not converge

	FM	AFM1	AFM2
Alpha (x = 1/6)	−0.257	−0.263	−0.248
Beta (x = 1/8)	−0.196	−0.199	−0.196
Gamma (x = 1/8)	−0.271	−0.255	−0.159
R (x = 1/12)	N/A	−0.180	−0.186
T1 (x = 1/8)	−0.258	−0.259	−0.241
T2 (x = 1/8)	−0.228	−0.218	−0.198

energies were calculated using the following formula: $1/N_{at}$ [$E_{tot}(Bi_{1-x}Ho_xFeO_3)$ + $x/2$ $E_{tot}(Bi_2O_3)$ − $E_{tot}(BiFeO_3)$ − $x/2$ $E_{tot}(Ho_2O_3)$], where E_{tot}(Y) is the total energy of structure Y, x is the number of Bi atoms substituted by Ho atoms given per one Bi atom, N_{at} is the number of atoms per conventional unit cell for which DFT calculations were performed. Note that substitutional energies account for the difference in the Bi : Fe : O : Ho stoichiometry of the investigated doped phases, *i.e.* the energies can be directly compared to obtain the relative plausibility of particular phases after Ho-doping. We considered the chemical reaction $BiFeO_3$ + $x/2$ Ho_2O_3 → $Bi_{1-x}Ho_xFeO_3$ + $x/2$ Bi_2O_3 for the calculations of substitutional formation energies which is simple and computationally inexpensive compared to the reaction that was essentially present in our experiments. Besides, the exact atomic structures of nitrates involved in the experiments are not exactly known, whereas the exact atomic structures are necessary for DFT calculations. In order to have compatible and comparable values of the substitutional formation energies for different investigated structure types we fixed U_{eff} at 7.5 eV in GGA+U calculations also for Ho 4f states (as is the case for Fe states) since the total energies for most phases are minimized for this U_{eff} value. The data in Table 3 suggest that the ferromagnetic gamma phase is the most plausible Ho-doped phase, with a substitutional formation energy of −0.271 eV atom^{-1}. However, it is only 8 meV atom^{-1} smaller than the substitutional energy of the AFM1 alpha phase. Note that the alpha phase was observed in our experiments. Substitutional energies of the T1 phase in ferromagnetic and AFM1 magnetic orders are by only 5 meV atom^{-1} s and 4 meV atom^{-1}, respectively, larger than the substitutional energy of the AFM1 alpha phase. Hence, the T1 type structure is also relatively prospective among Ho-doped $BiFeO_3$ crystals, in contrast to other investigated phases in which substitutional energies deviate significantly more from the mentioned structures. Note that the beta phase found in experiments is a less stable phase according to our DFT study. This may be attributed to the different chemical reactions used in the experiment and the one used for the calculation of substitutional energy from DFT calculations. Finite dimensions of the crystals in experiments with associated surface tension, which is not accounted for in DFT calculations, can also play an important role in the stability ladder of the investigated systems.

A summary of the calculated structural parameters of the most favorable $BiFeO_3$ perovskite structures in the $Bi_{0.9}Ho_{0.1}FeO_3$ system (corresponding to 10% of Ho doping in bismuth ferrite) compared to the experimental data (when available) is presented in Table 4. Our theoretical results on the alpha phase correspond to a = 5.55 Å and c = 13.84 Å, which is in good agreement with our experimental results from the synthesis and Rietveld refinement (a = 5.5800(4), c = 13.8739(2), Table 4), and with previously reported data.[56–58] Similarly, our calculated beta type of the structure concurs with experimentally observed modification for 10% of Ho-doping in $BiFeO_3$.[70] Other predicted structures are not yet synthesized in the Ho-doped BFO; however, structural data concur with the *ab initio* calculations from the pure $BiFeO_3$.[38] Full structural details of all predicted structures with 2%, 5% and 10% Ho doping can be found in the ESI.†

3.4. Magnetization study

Temperature dependence of magnetization measured as described in Subsection 2.2 is shown in Fig. 7a. The transition temperature for magnetic order does not change with the substitution, and amounts between 620 and 625 K (Fig. 7b). The transition temperature of pure $BiFeO_3$ is also around

Table 4 Theoretical structural data of the $BiFeO_3$ perovskite modifications doped with 10% of Ho compared to experimental data when available

Modification and space group	Cell parameters (Å) and unit-cell volume (Å^3) in experiments	Theoretical cell parameters (Å) and unit-cell volume (Å^3)
α-type	a = 5.5800(4), c = 13.8739(2)	a = 5.55, c = 13.84
*R*3*c* (no. 161)	V = 374.11	V = 369.19
β-$Bi_{0.9}Ho_{0.1}FeO_3$	a = 5.588, b = 7.816, c = 5.377	a = 5.60, b = 7.76, c = 5.39
Pnma (no. 62)	V = 234.84[a]	V = 233.93
R-$Bi_{0.9}Ho_{0.1}FeO_3$	N/A	a = 5.43, c = 13.96
R$\bar{3}$*c* (no. 167)		V = 357.05
T_1-$Bi_{0.9}Ho_{0.1}FeO_3$	N/A	a = 5.35, c = 4.03
*P*4/*mbm* (no. 127)		V = 115.45
T_2-$Bi_{0.9}Ho_{0.1}FeO_3$	N/A	a = 5.35, c = 8.06
*I*4/*mcm* (no. 140)		V = 230.91
γ-$Bi_{0.9}Ho_{0.1}FeO_3$	N/A	a = 4.03
Pm$\bar{3}$*m* (no. 221)		V = 65.50

[a] Ref. 70.

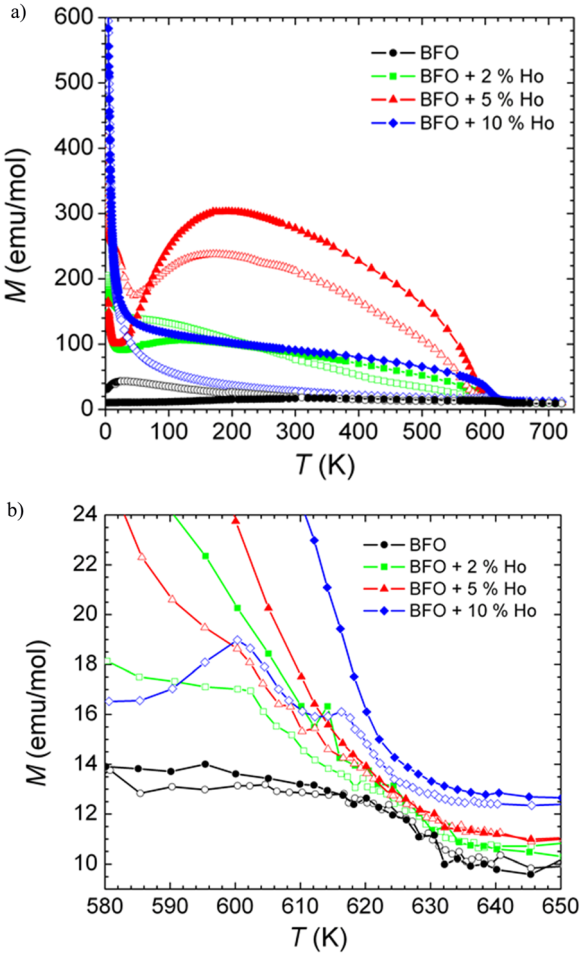

Fig. 7 (a) Temperature dependence of magnetization of pure $BiFeO_3$ and those substituted with 2, 5 and 10% of Ho measured in a field of 1000 Oe. Splitting between the zero-field-cooled (ZFC) and field-cooled (FC) magnetization curves becomes more pronounced as the Ho concentration is increased, pointing to the development of a weak ferromagnetic moment, which is usually connected with uncompensated spins or spin canting. (b) The transition temperature region for magnetic order at around 620–625 K.

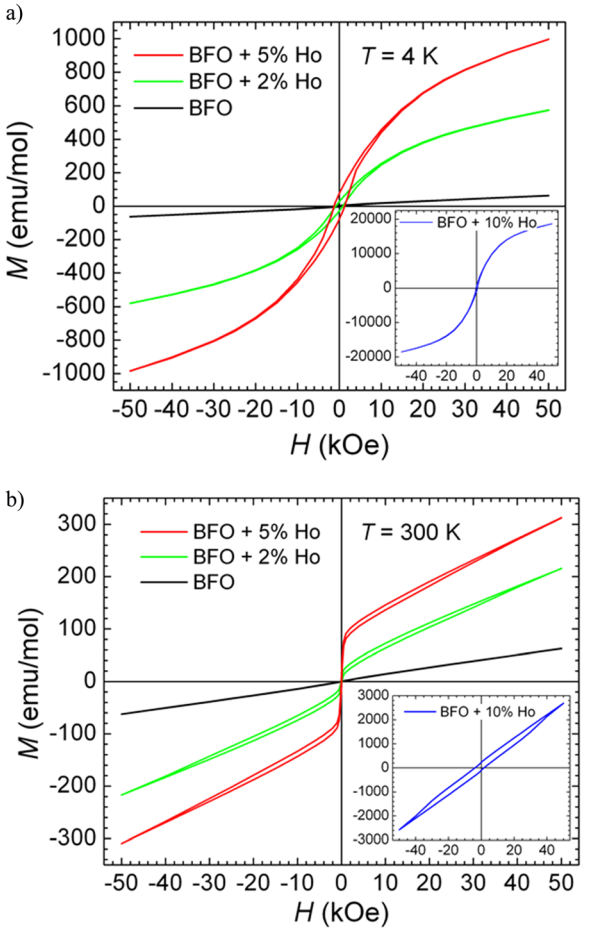

Fig. 8 Magnetic hysteresis of pure $BiFeO_3$ and those substituted with 2, 5 and 10% of Ho at: (a) 4 K and (b) 300 K.

620 K,[10,71] and the same transition temperature was observed with other substitutions, like with Gd, Nb, La, *etc.*[72–74]

The difference between the transition temperatures among these cases can be understood with chemical pressure induced with substitutions,[75] where it was found that the magnetic transition temperature increases at a rate of 0.66 K per 1% of Ca substitution. Performed substitution with Ho produces an influence of the same order. The absence of some larger change of magnetic transition temperature shows that the magnetic lattice of BFO is persistent to perturbations with substituted atoms and that the interactions which determine ordering temperature cannot be perturbed by any of the mentioned substitutions. The robustness of transition temperature might have a reason in a very long period of magnetic cycloid which is known to be more than a hundred times that of a crystal lattice unit and hence insensitive to the introduced substitutes.[76]

It is known that the nature of magnetic transition at $T_N \sim$ 620–625 K is antiferromagnetic. A well-observed peak at this temperature on ZFC $M(T)$ confirms the antiferromagnetic nature of the magnetic order for pure BFO. However, the FC $M(T)$ curve below T_N is clearly separated from the ZFC one and increases with cooling below T_N, which is not a sign of the pure antiferromagnet. Instead, it can be concluded that the order is of a weak ferromagnetic kind. Indeed, weak ferromagnetism was obtained in theoretical calculations appearing as a result of Dzyaloshinskii–Moriya interactions.[77] Substituted samples actually do not have a peak in magnetization at the transition temperature, but both ZFC and FC curves increase with cooling below the ordering temperature, which is also a sign of weak ferromagnetic order. Both the ZFC–FC splitting and magnetization considerably increase with an increased amount of substitution, showing that a weak ferromagnetic moment grows with the introduced defects, originating from the non-compensated magnetic moments due to the distortions of both the spin-cycloid order and the super-exchange bridges. Both distortions promote the additional spin-canting and increase the magnetization.

Another interesting phenomenon is the crossing of ZFC and FC curves. Generally, this crossing comes from the competition

of the complex interactions between the magnetic sublattices as well as within the sublattices. A similar effect was demonstrated in holmium-iron garnets.[78] This phenomenon was closely related to the magnetic structure of the Ho sublattice which has transitioned from collinear to noncollinear spin-order and the development of a so-called magnetic umbrella structure.[79] This exotic magnetic structure was studied in detail in holmium-substituted YIG.[80] The Ho^{3+} ions with unquenched orbital angular momentum behave differently in different non-collinear sublattices, and the underlying mechanism is not understood in detail. However, it is worth noticing the similarity of the complex magnetic behavior in our case of substitution with holmium having an unquenched orbital momentum into BFO having a non-collinear spin structure. This might be the reason for the observed ZFC–FC crossing, but it is far from understood. It is interesting to note that the crossing temperature goes down with the increase of the substitution amount, which points to the interplay between complex interactions and thermal energy, which is not surprising in such cases. All of this is motivating for further experimental studies with microscopic magnetic probes (nuclear magnetic resonance, muon spin rotation, *etc.*) and with theoretical hard-work thermodynamic simulations embedded with non-collinear DFT.

The evolution of magnetic response to the magnetic field is further presented in the form of hysteresis loops in Fig. 8. At low temperatures (4 K) the moment in the maximal field increases with the amount of substitution (Fig. 8a). The loops are not saturated in a high field, but their tails seem paramagnetic-like, as was also observed previously with Gd substitution. The uncompensated moments are the main contributor to this magnetization value, since the pure BFO has very low magnetization, and they contribute to the $M(T)$ at low temperatures in a paramagnetic-like manner.[72] A coercive field of the order of 1000 Oe is usual for substituted BFO being always a weak ferromagnet, but it is hard to compare exactly to other literature data, because of differences in the microstructure which often determines magnetic hardness.

For the applicative side of these materials, it is more useful to look at the room-temperature hysteresis loops (Fig. 8b). They also look typically as in weak ferromagnets: small hysteresis around zero and long straight lines for higher fields. The loop of the 10%Ho sample is surprisingly wide and with strong irreversibility up to the maximal measured field of 5T. Higher substitution (15%) is tried, but this amount leads to the appearance of the secondary phases of metal oxides. The sample with 10%Ho is the highest achievable substitution which shows no presence of secondary phases as obtained by XRD analysis, but the observed wide hysteresis loop could suggest that some microscopic precipitates are formed being not visible in XRD patterns, which cause pinning of the domain walls and make this material magnetically hard. Even the magnetization at 5T is comparable to some ordinary ferromagnets. This part of the study shows that it is possible to get some large magnetization from the weak ferromagnetic state, by 10% substitution with Ho.

3.5. DFT calculations of electronic and magnetic properties

As shown in Table 5, DFT predicts a rich variety of electronic structures among the investigated Ho-doped BFO crystals, including half-metals, semiconductors, semimetals, and

Table 5 Summary of calculated electronic and magnetic properties of the Ho-doped BFO modifications using DFT. FM-ferromagnet, AFM1-antiferromagnet (A type), AFM2-antiferromagnet (G type). Data are derived from figures of electronic band structure and element-resolved density of states for all investigated phases, which are provided in the ESI

Modification	Magnetic ordering	Type of el. str.	Gap (eV)	Gap character	Dispersion of val. band (eV)
Alpha	FM	Half-metal	0.80	Direct	1.70
	AFM1	Half-metal	1.30	Direct	1.60
	AFM2	Semiconductor	1.95	Indirect	0.30
Beta	FM	Half-metal	0.50	Direct	1.20
	AFM1	Semiconductor	0.2–1.7 (2)	Direct	1.70
	AFM2	Semiconductor	2.0	Direct	0.15
Gamma	FM	Semimetal	0.0		4.60
	AFM1	Semimetal	0.0		1.70
	AFM2	Semimetal	0.0		1.20
R	FM	[a]	[a]	[a]	[a]
	AFM1	Semiconductor	2.0	Indirect	0.15
	AFM2	Semiconductor	2.0	Indirect	0.30
T1	FM	Half-metal	0.15	Direct	1.20
	AFM1	Semiconductor	1.50	Indirect	0.30
	AFM2	Semiconductor	1.0–1.4[b]	Direct	0.40
T2	FM	Half-metal (valence)	0.20	Direct	>0.2[c]
	AFM1	Semicon. (U = 0) metal (U = 9)	0.0–0.7[b]	Indirect	1.30
	AFM2	Semiconductor	0.90	Indirect	1.40

[a] Data are not available. DFT did not converge. [b] Gap changes with variation of Hubbard U_{eff} (used values 0.0, 2.5, 5.0, 7.5, and 9.0 eV). [c] Below E_F −2 eV hybridization with other states is too large hence the valence band is not distinguishable anymore.

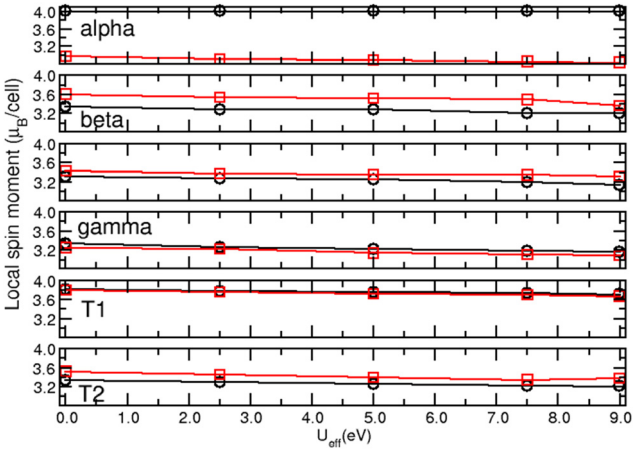

Fig. 9 The local magnetic moment for AFM spin configurations. Black lines show data for AFM1 and red lines for AFM2.

metals. This diversity eventually provides many possibilities for applications of these materials and further fundamental studies. In the ferromagnetic (FM) order in the calculation cells, all spins of Fe and Ho atoms are parallel. Two antiferromagnetic orders of the Fe sublattice are considered: type A (AFM1) and type G (AFM2), which are determined by the spin texture of the Fe sublattice. In the table, data obtained for U_{eff} = 0 are shown. U_{eff} does not affect considerably these values except for T2 AFM1 for which it is a semiconductor for U_{eff} = 0 eV and metal for U_{eff} = 9 eV. We neglected the presence of dopant states in the qualitative characterization of electronic structure type and determination of gap value. For example, in the alpha phase, we consider only electronic bands from Bi, Fe and O, which are all with spin-up character down to the energy E_F −0.8 eV, making the phase half-metallic. Fermi energy in all crystals is placed in the valence band (close to its top), which can eventually be shifted into the gap with further doping or electrostatic gating.

The local magnetic moment in the AFM order originates primarily from the Ho dopant. In order to obtain macroscopic magnetization calculations with larger cells are necessary, which would give a possibility to investigate spin textures also on the Ho sublattice. However, since these larger calculations are very difficult to converge, we present here only the local magnetic moment of the cells with a single Ho atom. With such a setup the Ho sublattice has an FM order. In the following figures, the atomic structure with spin texture, band structure and projected DOS are shown for selected crystals. Black and red lines represent spin-up and spin-down states, respectively. As seen in Fig. 9, Hubbard U_{eff} does not affect considerably the local magnetic moment. The effect of Hubbard U_{eff} in most cases is the shifting of Ho 4f states, except for T2 AFM1 where other states are affected a bit too. Ho states around the Fermi level have small dispersion for all crystals, whereas dispersion enlarges a bit at larger binding energies, which indicates the chemical bonding between Ho and surrounding O atoms at these energies.

The electronic structure and element-resolved density of state for Ho-doped BFO phases with the three smallest substitutional energies are shown in Fig. 10. The Fermi level for these and all other investigated phases is always positioned in valence bands. The valence bands have Bi, Fe and O contributions in all investigated crystals. Some crystals have a very dispersive valence band with a dispersion larger than 1 eV, with the extreme of 4.6 eV in the band structure of gamma FM (Fig. 10c and d). The gamma FM type structure appears as a semimetal, as is shown also for gamma AFM1 and AFM2 (Fig. S8 and S9, ESI†). The Gamma FM phase may have a topological crossing of spin-up bands at the S *k*-point around 0.5 eV below the Fermi energy. However, this should be further investigated in future research. The large band dispersions in all of the calculated Ho-doped BFO modifications indicate the large conductance of these structures. The T1 FM has a relatively small gap with a large dispersion of valence and small dispersion of conduction bands (Fig. 10e and f). This eventually opens a possibility to use these materials in electronic switches, where the conductive state may be switched on or off, for example, by shifting the Fermi level *via* electrostatic gating from the highly conductive valence band to/from the gap or the weakly conductive conduction band.

The alpha AFM1 (Fig. 10a and b) has relatively flat both valence and conduction bands with a band gap of about 1 eV, indicating low electric conductance of the alpha AFM1 phase. The top of its valence band has a dominantly spin-up character, however, the spin-down character emerges already 0.25 eV below the Fermi energy. More interesting for applications in spintronics are half-metals. Among other investigated phases half-metallic band structures are indicated for alpha FM, beta FM, T1 FM, and T2 FM (see Fig. S1, S4, S11 and S14, ESI†). Especially interesting are phases in which an electronic gap separates exclusively spin-up characterized valence and spin-down conduction bands, which are often considered for various spintronics applications. A typical example is the T1 FM phase, as shown in Fig. 10e and f. Further electronic and magnetic properties of the alpha, beta, gamma, R-, T1- and T2- type structures, with their calculated band structures and DOS in the FM, AFM1 and AFM2 magnetic ordering are presented in the ESI.†

4. Conclusions

A multidisciplinary study has been performed to investigate the influence of Bi/Ho substitution in $BiFeO_3$. Nanocrystalline powders of $Bi_{1-x}Ho_xFeO_3$ with x = 0.02, 0.05, and 0.10 were synthesized using the hydrothermal method. Structure prediction in Ho-doped BFO was performed using bond valence calculations to find possible additional structure candidates besides the experimentally observed α-$BiFeO_3$ perovskite structure. As a result, we have predicted the α-, β-,γ-, R-, T1, and T2 structure types in various Ho-doped BFO systems. Each of the predicted structure candidates generated using BVC calculations, as well as equilibrium structures from experimental

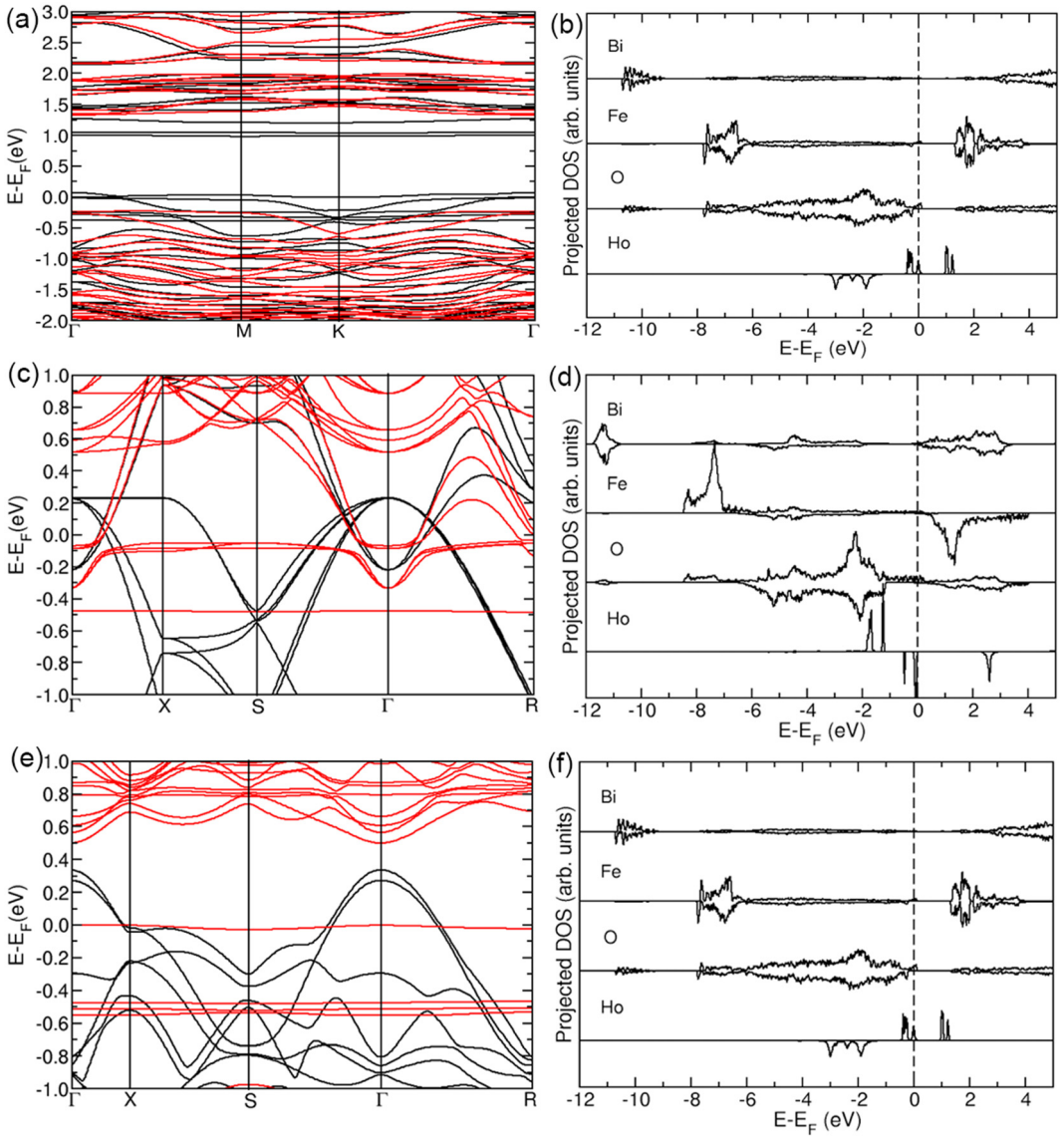

Fig. 10 Electronic band structure of alpha AFM1 (a), gamma FM (c), T1 FM (e) and element-resolved density of states of alpha AFM1 (b), gamma FM (d) and T1 FM (f) phases. Black lines present spin-up and red lines spin-down bands. Mirrored graphs of the density of states correspond to spin-up and spin-down states.

synthesis, were submitted to the *ab initio* local optimization. In addition, all structure candidates have been investigated for different magnetic ordering, ferromagnetic (FM) and two antiferromagnetic orders (AFM1 and AFM2). The DFT optimizations show that the most likely phases of BFO upon Ho-doping are gamma FM, alpha AFM1 and T1 FM and AFM1. Moreover, present DFT results are in good agreement with our experimental results from the synthesis and with previously reported data when existing.

The electronic and magnetic properties of synthesized and predicted perovskite structures have been studied as a function of Ho-substitution. The magnetic behavior of the synthesized materials was investigated using a SQUID magnetometer equipped with an oven option that gave the temperature dependence of magnetization in a wide temperature range of 2–800 K. This full temperature range measurement was exceptionally important because only in this way the true zero-field cooled (ZFC) and field-cooled (FC) curves were obtained, with the correct picture of thermal irreversibility. The transition temperature for magnetic order does not change with the substitution considerably, staying between 620 and 625 K. The observed behavior of the temperature dependence of magnetization confirmed the weak ferromagnetic state of the substituted $BiFeO_3$ and showed the enhancement of the weak ferromagnetic moment with increased substitution. Also, the magnetic hysteresis loops of pure $BiFeO_3$ and those substituted with 2, 5 and 10% of Ho at both 4 K and 300 K exhibited a higher magnetic response with increased substitution, with the origin in the higher magnetic moment of holmium ions, and more important in the influence of substitution on the

interactions and local magnetic order around the substituents. Furthermore, the widening of the hysteresis loops with substitution has its origin in increased thermal irreversibility coming also from the influence of holmium onto the magnetic lattice distortions. For the applicative side of these materials, the room-temperature hysteresis loops also look typically as in weak ferromagnets, and with increased substitution, they develop considerable magnetic hardness.

Present *ab initio* calculations based on DFT predict a rich variety of electronic structures among investigated Ho-doped BFO perovskite modifications, including half-metals, semiconductors, semimetals, and metals, and this diversity eventually provides many possibilities for applications and further fundamental studies. Alpha FM, beta AFM1, T1 FM and T2 FM have relatively small gaps with large dispersions of valence and small dispersion of conduction bands. This eventually opens the possibility to use these materials in electronic switches. Even more interesting for application in spintronics are half-metals, alpha FM and AFM1, beta FM, T1 FM, and T2 FM. Semimetals, which include the gamma structure with any spin texture, provide further opportunities to investigate possible nontrivial topologies in their band structures. In most of the investigated structures, a flat Ho state is positioned at the Fermi level, which originates a large DOS. A large DOS at the Fermi level may cause many instabilities and corresponding physical phenomena, like (spin) charge density waves and superconductivity. The prosperous diversity of electronic and magnetic properties and more importantly the possibility of their tuning by doping inspire us and hopefully the community for deeper research into individual phases and their properties.

Author contributions

M. C., D. Z., I. P. and D. P. conceived the idea; M. C. performed the synthesis of the $Bi_{1-x}Ho_xFeO_3$ (x = 0.02, 0.05, and 0.10) nanopowders; XRD characterization, analysis, and Rietveld refinement have been performed by T. K. and Z. S.; SQUID measurements and magnetization study were carried out by F. T. and D. P.; structure prediction and BVC calculations were carried out by D. Z.; the *ab initio* structure optimizations and DFT calculations were performed by I. P.; all authors contributed to the discussion and writing of the paper. All authors have read and agreed to the published version of the manuscript.

Conflicts of interest

The authors declare that they have no known competing financial interests or personal relationships that could have appeared to influence the work reported in this paper.

Acknowledgements

This work was supported by the Croatian Science Foundation, Zagreb, Croatia [project UIP-2014-09-8276]; and by the Ministry of Science, Technological Development and Innovation of the Republic of Serbia, Belgrade, Serbia [grant no. 451-03-68/2022-14/200017, 1702313 and 0402311]. M. Č. acknowledges the support from the European Research Council (ERC Consolidator grant no. 725521) and Bilateral Project Between Serbia and Austria (OeAD-GmbH-Project no. RS 24/2022) 337-00-577/2021-09/6. We acknowledge the support from the COST Action CA17123-Ultrafast opto-magneto-electronics for non-dissipative information technology (MAGNETOFON). M. Č., F. T., T. K., Ž. S. and D. P. acknowledge the support from project CeNIKS, co-financed by the Croatian Government and the EU through the European Regional Development Fund: Competitiveness and Cohesion Operational Programme (grant KK.01.1.1.02.0013). I. Popov acknowledges the financial support from the Ministry of Science, Technological Development and Innovation of the Republic of Serbia, contract with the Institute for Multidisciplinary Research, University of Belgrade 451-03-68/2022-14/200053. DFT calculations were performed using computational resources at the Center of Surface and Nanoanalytics, Johannes Kepler University, Linz, Austria. We are grateful to Prof. Kurt Hingerl for providing the necessary computational resources at JKU. We are grateful to Andrey Enyashin from the Institute of Mathematics and Computer Science, Ural Federal University, Yekaterinburg, Russia, for enlightening discussions.

References

1 N. A. Spaldin and R. Ramesh, Advances in magnetoelectric multiferroics, *Nat. Mater.*, 2019, **18**, 203–212.
2 M. Bibes and A. Barthélémy, Towards a magnetoelectric memory, *Nat. Mater.*, 2008, **7**, 425–426.
3 H. Béa, M. Gajek, M. Bibes and A. Barthélémy, Spintronics with multiferroics, *J. Phys.: Condens. Matter*, 2008, **20**, 434221.
4 J. Liu, M. Niu, L. Wang, C. Peng and D. Xu, Effect of tuning A/B substitutions on multiferroic characteristics of BiFeO3-based ternary system ceramics, *J. Magn. Magn. Mater.*, 2020, **510**, 166928.
5 S. R. Burns, D. Sando, B. Xu, B. Dupé, L. Russell, G. Deng, R. Clements, O. H. C. Paull, J. Seidel, L. Bellaiche, N. Valanoor and C. Ulrich, Expansion of the spin cycloid in multiferroic BiFeO3 thin films, npj Quantum, *Materials*, 2019, **4**, 18.
6 J. M. Moreau, C. Michel, R. Gerson and W. J. James, Ferroelectric BiFeO3 X-ray and neutron diffraction study, *J. Phys. Chem. Solids*, 1971, **32**, 1315–1320.
7 F. Kubel and H. Schmid, Structure of a ferroelectric and ferroelastic monodomain crystal of the perovskite BiFeO3, *Acta Crystallogr., Sect. B: Struct. Sci.*, 1990, **46**, 698–702.
8 J. Wang, J. B. Neaton, H. Zheng, V. Nagarajan, S. B. Ogale, B. Liu, D. Viehland, V. Vaithyanathan, D. G. Schlom, U. V. Waghmare, N. A. Spaldin, K. M. Rabe, M. Wuttig and R. Ramesh, Epitaxial BiFeO3 Multiferroic Thin Film Heterostructures, *Science*, 2003, **299**, 1719–1722.

9 H. Feng, Magnetism and electronic properties of BiFeO3 under lower pressure, *J. Magn. Magn. Mater.*, 2010, **322**, 3755–3759.
10 G. Catalan and J. F. Scott, Physics and Applications of Bismuth Ferrite, *Adv. Mater.*, 2009, **21**, 2463–2485.
11 L. W. Martin, S. P. Crane, Y. H. Chu, M. B. Holcomb, M. Gajek, M. Huijben, C. H. Yang, N. Balke and R. Ramesh, Multiferroics and magnetoelectrics: thin films and nanostructures, *J. Phys.: Condens. Matter*, 2008, **20**, 434220.
12 J. Wu, Z. Fan, D. Xiao, J. Zhu and J. Wang, Multiferroic bismuth ferrite-based materials for multifunctional applications: Ceramic bulks, thin films and nanostructures, *Prog. Mater. Sci.*, 2016, **84**, 335–402.
13 J.-G. Park, M. D. Le, J. Jeong and S. Lee, Structure and spin dynamics of multiferroic BiFeO3, *J. Phys.: Condens. Matter*, 2014, **26**, 433202.
14 Y. Wang, Y. Wang, M. Wei, J. Zhang and Y. Zhang, Role of Ho Doping in Magnetization Mechanism of BiFeO3 Thin Films, *J. Supercond. Novel Magn.*, 2019, **32**, 3495–3501.
15 Y. Q. Liu, Y. J. Wang, J. Zhang, M. Gao, Y. J. Zhang, M. B. Wei and J. H. Yang, Effect of Ho substitution on structure and magnetic property of BiFeO3 prepared by sol–gel method, *Mater. Sci. Semicond. Process.*, 2015, **40**, 787–795.
16 S. Sharif, G. Murtaza, T. Meydan, P. I. Williams, J. Cuenca, S. H. Hashimdeen, F. Shaheen and R. Ahmad, Structural, surface morphology, dielectric and magnetic properties of holmium doped BiFeO3 thin films prepared by pulsed laser deposition, *Thin Solid Films*, 2018, **662**, 83–89.
17 P. Hou, B. Liu, Z. Guo, P. Zhou, B. Wang and L. Zhao, Effect of Ho doping on the crystal structure, surface morphology and magnetic property of BiFeO3 thin films prepared *via* the sol-gel technology, *J. Alloys Compd.*, 2019, **775**, 59–62.
18 Q. Yun, A. Bai and S. Zhao, Lattice distortion of holmium doped bismuth ferrite nanofilms, *J. Rare Earths*, 2014, **32**, 884–889.
19 M. R. Islam, M. A. Zubair, R. H. Galib, M. S. B. Hoque, J. A. Tomko, K. Aryana, A. K. Basak and P. E. Hopkins, Vacancy-Induced Temperature-Dependent Thermal and Magnetic Properties of Holmium-Substituted Bismuth Ferrite Nanoparticle Compacts, *ACS Appl. Mater. Interfaces*, 2022, **14**, 25886–25897.
20 S. Chaturvedi, R. Bag, V. Sathe, S. Kulkarni and S. Singh, Holmium induced enhanced functionality at room temperature and structural phase transition at high temperature in bismuth ferrite nanoparticles, *J. Mater. Chem. C*, 2016, **4**, 780–792.
21 B. Stojadinović, Z. Dohčević-Mitrović, D. Stepanenko, M. Rosić, I. Petronijević, N. Tasić, N. Ilić, B. Matović and B. Stojanović, Dielectric and ferroelectric properties of Ho-doped BiFeO3 nanopowders across the structural phase transition, *Ceram. Int.*, 2017, **43**, 16531–16538.
22 D. Kuang, F. Yang, W. Wang and Z. Yang, Effects of Ho3+ and transition metal ion doping on optical and magnetic properties of BiFeO3 nanopowders, *J. Mater. Sci.: Mater. Electron.*, 2018, **29**, 4041–4047.
23 P. Thakuria and P. A. Joy, High room temperature ferromagnetic moment of Ho substituted nanocrystalline BiFeO3, *Appl. Phys. Lett.*, 2010, **97**, 162504.
24 N. Jeon, D. Rout, I. W. Kim and S.-J. L. Kang, Enhanced multiferroic properties of single-phase BiFeO3 bulk ceramics by Ho doping, *Appl. Phys. Lett.*, 2011, **98**, 072901.
25 S. K. Pradhan, J. Das, P. P. Rout, V. R. Mohanta, S. K. Das, S. Samantray, D. R. Sahu, J. L. Huang, S. Verma and B. K. Roul, Effect of holmium substitution for the improvement of multiferroic properties of BiFeO3, *J. Phys. Chem. Solids*, 2010, **71**, 1557–1564.
26 N. Van Minh and N. G. Quan, Structural, optical and electromagnetic properties of $Bi1_{-x}Ho_xFeO_3$ multiferroic materials, *J. Alloys Compd.*, 2011, **509**, 2663–2666.
27 M. Muneeswaran, S. H. Lee, D. H. Kim, B. S. Jung, S. H. Chang, J.-W. Jang, B. C. Choi, J. H. Jeong, N. V. Giridharan and C. Venkateswaran, Structural, vibrational, and enhanced magneto-electric coupling in Ho-substituted BiFeO3, *J. Alloys Compd.*, 2018, **750**, 276–285.
28 A. Haykal, J. Fischer, W. Akhtar, J. Y. Chauleau, D. Sando, A. Finco, F. Godel, Y. A. Birkhölzer, C. Carrétéro, N. Jaouen, M. Bibes, M. Viret, S. Fusil, V. Jacques and V. Garcia, Antiferromagnetic textures in BiFeO3 controlled by strain and electric field, *Nat. Commun.*, 2020, **11**, 1704.
29 J. Maletaškić, M. Čebela, M. P. Đorđević, D. Kozlenko, S. Kichanov, M. Mitrić and B. Matović, Combined magnetic and structural characterization of hidrothermal bismuth ferrite (Bifeo3) nanoparticles, *Sci. Sintering*, 2019, **51**, 71–79.
30 M. Cebela, B. Jankovic, R. Hercigonja, M. J. Lukic, Z. Dohcevic-Mitrovic, D. Milivojevic and B. Matovic, Comprehensive characterization of BiFeO3 powder synthesized by the hydrothermal procedure, *Process. Appl. Ceram.*, 2016, **10**, 201–208.
31 T. Degen, M. Sadki, E. Bron, U. König and G. Nénert, The HighScore suite, *Powder Diffr.*, 2014, **29**, S13–S18.
32 D. Zagorac and J. C. Schön, Energy landscapes of pure and doped ZnO: from bulk crystals to nanostructures, *Front. Nanosci.*, 2022, 151–193.
33 J. Zagorac, J. C. Schön, B. Matović, T. Škundrić and D. Zagorac, Predicting Feasible Modifications of Ce2ON2 Using a Combination of Global Optimization and Data Mining, *J. Phase Equilib. Diffus.*, 2020, **41**, 538–549.
34 C. Buyer, H. Grossholz, S. Wolf, D. Zagorac, J. Zagorac, J. C. Schön and T. Schleid, Crystal-Structure Prediction and Experimental Investigation of the Polymorphic Lanthanum Fluoride Selenides LaFSe and La2F4Se, *Cryst. Growth Des.*, 2022, **22**, 7133–7142.
35 M. Pejić, D. Zagorac, J. Zagorac, B. Matović and J. C. Schön, Structure prediction *via* global energy landscape exploration of the ternary rare-earth compound LaOI, *Z. Anorg. Allg. Chem.*, 2022, **648**, e202200308.
36 J. Zagorac, D. Zagorac, A. Zarubica, J. C. Schön, K. Djuris and B. Matovic, Prediction of possible CaMnO3 modifications using an *ab initio* minimization data-mining approach, *Acta Crystallogr., Sect. B: Struct. Sci., Cryst. Eng. Mater.*, 2014, **70**, 809–819.
37 M. Rosić, D. Zagorac, D. Milivojević, N. Paunović, J. Zagorac, Z. Dohčević-Mitrović and B. Matović, Theoretical and experimental study of octahedral tilting of Ca1-xGdxMnO3 (x =

0.05, 0.1, 0.15, 0.2) nanometric powders, *J. Alloys Compd.*, 2016, **678**, 219–227.
38 M. Čebela, D. Zagorac, K. Batalović, J. Radaković, B. Stojadinović, V. Spasojević and R. Hercigonja, BiFeO3 perovskites: A multidisciplinary approach to multiferroics, *Ceram. Int.*, 2017, **43**, 1256–1264.
39 M. W. Lufaso and P. M. Woodward, Prediction of the crystal structures of perovskites using the software program SPuDS, *Acta Crystallogr., Sect. B: Struct. Sci.*, 2001, **57**, 725–738.
40 M. W. Lufaso and P. M. Woodward, Jahn-Teller distortions, cation ordering and octahedral tilting in perovskites, *Acta Crystallogr., Sect. B: Struct. Sci.*, 2004, **60**, 10–20.
41 V. M. Goldschmidt, Die Gesetze der Krystallochemie, *Naturwissenschaften*, 1926, **14**, 477–485.
42 R. Shannon, Revised effective ionic radii and systematic studies of interatomic distances in halides and chalcogenides, *Acta Crystallogr., Sect. A: Cryst. Phys., Diffr., Theor. Gen. Crystallogr.*, 1976, **32**, 751–767.
43 R. Hundt, *KPLOT: A Program for Plotting and Analysing Crystal Structures*, Technicum Scientific Publishing, Stuttgart, 2016.
44 R. Hundt, J. C. Schön, A. Hannemann and M. Jansen, Determination of symmetries and idealized cell parameters for simulated structures, *J. Appl. Crystallogr.*, 1999, **32**, 413–416.
45 A. Hannemann, R. Hundt, J. C. Schön and M. Jansen, A New Algorithm for Space-Group Determination, *J. Appl. Crystallogr.*, 1998, **31**, 922–928.
46 R. Hundt, J. C. Schön and M. Jansen, CMPZ - an algorithm for the efficient comparison of periodic structures, *J. Appl. Crystallogr.*, 2006, **39**, 6–16.
47 K. Momma and F. Izumi, VESTA 3 for three-dimensional visualization of crystal, volumetric and morphology data, *J. Appl. Crystallogr.*, 2011, **44**, 1272–1276.
48 E. Artacho, E. Anglada, O. Diéguez, J. D. Gale, A. García, J. Junquera, R. M. Martin, P. Ordejón, J. M. Pruneda, D. Sánchez-Portal and J. M. Soler, The SIESTA method; developments and applicability, *J. Phys.: Condens. Matter*, 2008, **20**, 064208.
49 J. P. Perdew, K. Burke and M. Ernzerhof, Generalized Gradient Approximation Made Simple, *Phys. Rev. Lett.*, 1996, **77**, 3865–3868.
50 N. Troullier and J. L. Martins, Efficient pseudopotentials for plane-wave calculations, *Phys. Rev. B: Condens. Matter Mater. Phys.*, 1991, **43**, 1993–2006.
51 H. J. Monkhorst and J. D. Pack, Special points for Brillouin-zone integrations, *Phys. Rev. B: Solid State*, 1976, **13**, 5188–5192.
52 M. R. Hestenes and E. Stiefel, Methods of conjugate gradients for solving linear systems, *J. Res. Natl. Inst. Stand. Technol.*, 1952, **49**, 409–436.
53 A. I. Liechtenstein, V. I. Anisimov and J. Zaanen, Density-functional theory and strong interactions: Orbital ordering in Mott-Hubbard insulators, *Phys. Rev. B: Condens. Matter Mater. Phys.*, 1995, **52**, R5467–R5470.
54 V. I. Anisimov, J. Zaanen and O. K. Andersen, Band theory and Mott insulators: Hubbard U instead of Stoner I, *Phys. Rev. B: Condens. Matter Mater. Phys.*, 1991, **44**, 943–954.
55 I. A. Vladimir, F. Aryasetiawan and A. I. Lichtenstein, First-principles calculations of the electronic structure and spectra of strongly correlated systems: the LDA+*U* method, *J. Phys.: Condens. Matter*, 1997, **9**, 767.
56 P. Suresh, P. D. Babu and S. Srinath, Effect of Ho substitution on structure and magnetic properties of BiFeO3, *J. Appl. Phys.*, 2014, **115**, 17D905.
57 S. Chaturvedi, M. M. Shirolkar, R. Rajendra, S. Singh, N. Ballav and S. Kulkarni, Coercivity and exchange bias of bismuth ferrite nanoparticles isolated by polymer coating, *J. Appl. Phys.*, 2014, **115**, 123906.
58 S. Chaturvedi, I. Sarkar, M. M. Shirolkar, U.-S. Jeng, Y.-Q. Yeh, R. Rajendra, N. Ballav and S. Kulkarni, Probing bismuth ferrite nanoparticles by hard x-ray photoemission: Anomalous occurrence of metallic bismuth, *Appl. Phys. Lett.*, 2014, **105**, 102910.
59 G. L. Song, G. J. Ma, J. Su, T. X. Wang, H. Y. Yang and F. G. Chang, Effect of Ho3 + doping on the electric, dielectric, ferromagnetic properties and TC of BiFeO3 ceramics, *Ceram. Int.*, 2014, **40**, 3579–3587.
60 Y. Wu, J.-g Wan, C. Huang, Y. Weng, S. Zhao, J.-m Liu and G. Wang, Strong magnetoelectric coupling in multiferroic BiFeO3–Pb(Zr0.52Ti0.48)O3 composite films derived from electrophoretic deposition, *Appl. Phys. Lett.*, 2008, **93**, 192915.
61 Z.-L. Hou, H.-F. Zhou, L.-B. Kong, H.-B. Jin, X. Qi and M.-S. Cao, Enhanced ferromagnetism and microwave absorption properties of BiFeO3 nanocrystals with Ho substitution, *Mater. Lett.*, 2012, **84**, 110–113.
62 S. M. Selbach, T. Tybell, M.-A. Einarsrud and T. Grande, The Ferroic Phase Transitions of BiFeO3, *Adv. Mater.*, 2008, **20**, 3692–3696.
63 R. Palai, R. S. Katiyar, H. Schmid, P. Tissot, S. J. Clark, J. Robertson, S. A. T. Redfern, G. Catalan and J. F. Scott, β phase and γ−β metal-insulator transition in multiferroic BiFeO3, *Phys. Rev. B: Condens. Matter Mater. Phys.*, 2008, **77**, 014110.
64 J. M. Munro, H. Akamatsu, H. Padmanabhan, V. S. Liu, Y. Shi, L.-Q. Chen, B. K. VanLeeuwen, I. Dabo and V. Gopalan, Discovering minimum energy pathways *via* distortion symmetry groups, *Phys. Rev. B*, 2018, **98**, 085107.
65 D. Zagorac, J. Zagorac, J. C. Schön, N. Stojanovic and B. Matovic, ZnO/ZnS (hetero)structures: *ab initio* investigations of polytypic behavior of mixed ZnO and ZnS compounds, *Acta Crystallogr., Sect. B: Struct. Sci., Cryst. Eng. Mater.*, 2018, **74**, 628–642.
66 S. M. Selbach, T. Tybell, M.-A. Einarsrud and T. Grande, Size-Dependent Properties of Multiferroic BiFeO3 Nanoparticles, *Chem. Mater.*, 2007, **19**, 6478–6484.
67 P. Ravindran, R. Vidya, A. Kjekshus, H. Fjellvåg and O. Eriksson, Theoretical investigation of magnetoelectric behavior in BiFeO3, *Phys. Rev. B: Condens. Matter Mater. Phys.*, 2006, **74**, 224412.

68 O. Diéguez, O. E. González-Vázquez, J. C. Wojdeł and J. Íñiguez, First-principles predictions of low-energy phases of multiferroic BiFeO${}_{3}$, *Phys. Rev. B: Condens. Matter Mater. Phys.*, 2011, **83**, 094105.

69 R. Haumont, J. Kreisel, P. Bouvier and F. Hippert, Phonon anomalies and the ferroelectric phase transition in multiferroic BiFeO3, *Phys. Rev. B: Condens. Matter Mater. Phys.*, 2006, **73**, 132101.

70 J. Singh, A. Agarwal, S. Sanghi, P. Prakash, A. Das, C. L. Prajapat and M. Rangi, Phase transformation in crystal and magnetic structure and improved dielectric and magnetic properties of Ho substituted BiFeO3multiferroics, *AIP Adv.*, 2019, **9**, 025110.

71 D. L. Golić, A. Radojković, J. Ćirković, A. Dapčević, D. Pajić, N. Tasić, S. M. Savić, M. Počuča-Nešić, S. Marković, G. Branković, Z. M. Stanojević and Z. Branković, Structural, ferroelectric and magnetic properties of BiFeO3 synthesized by sonochemically assisted hydrothermal and hydro-evaporation chemical methods, *J. Eur. Ceram. Soc.*, 2016, **36**, 1623–1631.

72 D. L. Golić, A. Radojković, A. Dapčević, D. Pajić, J. Dragović, F. Torić, J. Ćirković, G. Branković and Z. Branković, Change in structural, ferroelectric, and magnetic properties of bismuth ferrite induced by doping with gadolinium, *Ceram. Int.*, 2019, **45**, 19158–19165.

73 A. Radojković, D. L. Golić, J. Ćirković, Z. M. Stanojević, D. Pajić, F. Torić, A. Dapčević, P. Vulić, Z. Branković and G. Branković, Tuning of BiFeO3 multiferroic properties by light doping with Nb, *Ceram. Int.*, 2018, **44**, 16739–16744.

74 Y.-H. Lin, Q. Jiang, Y. Wang, C.-W. Nan, L. Chen and J. Yu, Enhancement of ferromagnetic properties in BiFeO3 polycrystalline ceramic by La doping, *Appl. Phys. Lett.*, 2007, **90**, 172507.

75 G. Catalan, K. Sardar, N. S. Church, J. F. Scott, R. J. Harrison and S. A. T. Redfern, Effect of chemical substitution on the Néel temperature of multiferroic Bi1−xCaxFeO3, *Phys. Rev. B: Condens. Matter Mater. Phys.*, 2009, **79**, 212415.

76 I. Sosnowska, R. Przeniosło, P. Fischer and V. A. Murashov, Investigation of Crystal and Magnetic Structure of BiFeO_{3} Using Neutron Diffraction, *Acta Phys. Pol., A*, 1994, **86**, 629–631.

77 C. Ederer and N. A. Spaldin, Weak ferromagnetism and magnetoelectric coupling in bismuth ferrite, *Phys. Rev. B: Condens. Matter Mater. Phys.*, 2005, **71**, 060401.

78 C. Suchomski, C. Reitz, D. Pajic, Z. Jaglicic, I. Djerdj and T. Brezesinski, Large-Pore Mesoporous Ho3Fe5O12 Thin Films with a Strong Room-Temperature Perpendicular Magnetic Anisotropy by Sol–Gel Processing, *Chem. Mater.*, 2014, **26**, 2337–2343.

79 O. Prakash and M. A. H. McCausland, Free precession of 165Ho nuclei in a single crystal of holmium iron garnet, *J. Phys. C: Solid State Phys.*, 1983, **16**, L903.

80 J. Englich, H. Lütgemeier, M. W. Pieper, K. F. A. Jülich, W. Germany, V. Nekvasil and P. Novák, Umbrella structure in Ho substituted YIG - NMR study, *Solid State Commun.*, 1985, **56**, 825–828.

materials

MDPI

Article

Synthesis, Structural and Magnetic Properties of $BiFeO_3$ Substituted with Ag

Maria Čebela [1,2,*], Pavla Šenjug [2], Dejan Zagorac [1,3], Igor Popov [4,5], Jelena Zagorac [1,3], Milena Rosić [1,*] and Damir Pajić [2,*]

1 "Vinča" Institute of Nuclear Sciences, National Institute of the Republic of Serbia, University of Belgrade, Mike Petrovića Alasa 12-14, 11351 Belgrade, Serbia; dzagorac@vin.bg.ac.rs (D.Z.); jelena@vin.bg.ac.rs (J.Z.)
2 Faculty of Science, Department of Physics, University of Zagreb, Bijenička Cesta 32, 10000 Zagreb, Croatia; psenjug@phy.hr
3 Center of Excellence "CextremeLab", "Vinča" Institute of Nuclear Sciences, National Institute of the Republic of Serbia, University of Belgrade, Mike Petrovića Alasa 12-14, 11351 Belgrade, Serbia
4 Institute for Multidisciplinary Research, University of Belgrade, Kneza Višeslava 1, 11030 Belgrade, Serbia; popov@ipb.ac.rs
5 Institute of Physics, University of Belgrade, Pregrevica 118, 11080 Belgrade, Serbia
* Correspondence: mcebela@vin.bg.ac.rs (M.Č.); mrosic@vin.bg.ac.rs (M.R.); dpajic@phy.hr (D.P.)

Abstract: Here, we report the hydrothermal synthesis of BFO (bismuth ferrite) and $Bi_{1-x}Ag_xFeO_3$ (x = 0.01, 0.02) ultrafine nanopowders. The diffraction patterns show that all obtained particles belong to the *R3c* space group. On top of that, crystal structure prediction has been accomplished using bond valence calculations (BVCs). Several promising perovskite structures have been proposed together with experimentally observed modifications of BFO as a function of silver doping. Magnetization measurements were performed on BFO, both pure and substituted with 1% and 2% of Ag. The addition of Ag in BFO did not affect the Neel temperature, T_N = 630 K for all samples; instead, the influence of Ag was observed in the increase in the value and irreversibility of magnetization, which are usual characteristics of weak ferromagnetism. Our calculations based on density functional theory (DFT) are in agreement with the experimental finding of enhanced magnetization upon Ag doping of antiferromagnetic BFO, which is assigned to the perturbation of magnetic-type interactions between Fe atoms by Ag substitutional doping. Additionally, electronic and magnetic properties were studied for all phases predicted by the BVCs study. DFT predicted half-metallicity in the γ phase of BFO, which may be of great interest for further study and potential applications.

Keywords: bismuth ferrite; multiferroics; XRD; magnetoelectric effect; crystal structure prediction; bond valence calculations; density functional theory

Academic Editor: Vladimir Shvartsman

Received: 20 February 2025
Revised: 12 March 2025
Accepted: 22 March 2025
Published: 25 March 2025

Citation: Čebela, M.; Šenjug, P.; Zagorac, D.; Popov, I.; Zagorac, J.; Rosić, M.; Pajić, D. Synthesis, Structural and Magnetic Properties of $BiFeO_3$ Substituted with Ag. *Materials* **2025**, *18*, 1453. https://doi.org/10.3390/ma18071453

1. Introduction

After many years of practical and scientific interests, perovskite-type bismuth ferrites still attract enormous attention. This is due to their ferroelectric and antiferromagnetic arrangement in only one phase [1–3]. Due to the variety of their unique behaviors, they have attracted a wide range of applications such as optoelectronic and spintronic devices, data storage, chemical resistant sensors and photocatalytic activities [4–9]. Many examinations have been conducted on the substitution of bismuth ions in $BiFeO_3$ by alkaline earth, transition and rare earth metals like Sr^{2+}, Mn^{3+}, Nb^{3+} and La^{3+} to name just a few of the numerous examples [10–12]. Perovskites with mixed metal oxides provide an important class of electric, ferroelectric, catalytic and magnetic materials [13]. From the magnetic

and ferroelectric viewpoint, the nanosized ferrite particles with appropriate shapes usually display qualitatively new properties concerning their bulk counterparts, such as changes in magnetic transition temperatures, the emergence of superparamagnetism, size dependence of the saturation magnetization and coercivity, etc. [14,15].

Under standard conditions, the known modification of bismuth ferrite crystallizes in the perovskite structure type (α) and possesses a rhombohedral space group *R3c* (no. 161) [16–19].

The location of residual porosity, microstructure, particle size, grain growth behavior and grain boundary characteristics in sintered specimens play a crucial role in determining the electrical and magnetic properties of $BiFeO_3$ [20–23]. Notably, introducing dopants in $BiFeO_3$ materials can significantly impact their structure and properties. Recent studies have successfully fabricated various morphologies of Ag-substituted $BiFeO_3$, including thin films [24–27], nanofilms [28], nanoparticles [29,30], nanopowders [31,32], nanocrystalline BFO [33] and bulk/polycrystalline ceramics [34–37].

The development of the secondary phase, weak electromagnetic coupling and weak magnetization are only some of the reasons for the limited technological application of bismuth ferrites. Doping is used to increase its multiferroic properties. Perovskite-type bismuth ferrites have the general formula of ABO_3, which is complicated by doping with various elements in appropriate stoichiometric ratios. Doping leads to a charge imbalance in the system, which can be adjusted by creating oxygen vacancies, charge disproportionality of Fe^{3+} and Fe^{5+} or partial exchange of Fe^{3+} into Fe^{4+} [13]. The element we use as a dopant in this perovskite structure will occupy the A or B site or both of them (amphoteric) depending on its ionic radius, where if it is larger, it will occupy the A site, and if it is smaller, it will occupy the B site [38]. Silver ions are used as a dopant, and since they are much larger than Fe cations, Ag will occupy the A sites. If it were not so, partial substitution of Fe for Ag would affect the change in Fe valence. The perovskite structures are governed by the Goldschmidt tolerance factor $f = (r_A + r_O)/\sqrt{2}(r_B + r_O)$ [39]. The stress in the structure is due to the mismatch between the equilibrium lengths of the A-O and B-O bonds. When the Goldschmidt tolerance factor is $f = 1$, it represents an unstressed cubic lattice. If $f > 1$ or $f < 1$, relaxed deformation occurs by distorting the structure from its ideal cubic shape. The Goldschmidt tolerance factor is 0.9309, which leads us to conclude that the observed nanometric structure could be stable.

In this study, we investigated the effects of Ag doping on the structural, electrical and magnetic properties of $BiFeO_3$. To advance the understanding of $BiFeO_3$'s magnetic behavior, we complemented experimental magnetization measurements with ab initio theoretical calculations. A central focus of this study was the intricate spin cycloid, a fundamental feature governing the multiferroic properties of $BiFeO_3$, and the development of strategies for its precise control. The investigation further extended to a detailed analysis of the structure–property relationship under Ag doping, providing new insights into the role of compositional tuning. Additionally, predictive modeling enabled the identification of novel perovskite structures alongside a comprehensive evaluation of their electronic and magnetic properties. By integrating high-resolution synthesis, XRD characterization, magnetic analysis and theoretical predictions, this work offers a profound understanding of the impact of Ag substitution on the structural and magnetic evolution of $BiFeO_3$, establishing a robust framework for tailoring its functional properties.

2. Materials and Methods

2.1. Synthesis and Structural Characterization of $Bi_{1-x}Ag_xFeO_3$ (x = 0.01, 0.02) Nanopowders

Nanocrystalline powders of $Bi_{1-x}Ag_xFeO_3$ were synthesized using the hydrothermal method, a well-established technique recognized for its energy efficiency, cost-effectiveness

and ability to yield high-purity products with controlled morphology. High-purity precursors, including bismuth nitrate ($Bi(NO_3)_3 \cdot 5H_2O$), silver nitrate ($AgNO_3$), iron nitrate ($Fe(NO_3)_3 \cdot 9H_2O$) and potassium hydroxide (KOH), were employed to ensure the reproducibility and phase purity of the final material. The synthesis involved dissolving stoichiometric amounts of $Bi(NO_3)_3 \cdot 5H_2O$, $AgNO_3$ and $Fe(NO_3)_3 \cdot 9H_2O$ in 40 mL of an 8 M KOH solution, followed by vigorous stirring for 30 min to promote homogeneous mixing and precursor reactivity. The resulting solution was then transferred into a Teflon-lined stainless steel autoclave and subjected to hydrothermal treatment at 200 °C under autogenous pressure for 6 h, facilitating crystallization under controlled conditions. Following the reaction, the system was cooled naturally to ambient temperature, and the precipitated powders were carefully collected. To eliminate residual reactants and potential secondary phases, the powders underwent multiple washing cycles involving centrifugation with distilled water. Subsequently, they were dispersed in ethanol and subjected to ultrasonication for 60 min to break up agglomerates and ensure uniform particle distribution. Finally, the purified powders were dried via controlled evaporation of ethanol using a heated mortar maintained at 60 °C, yielding nanocrystalline $Bi_{1-x}Ag_xFeO_3$ with well-defined structural characteristics [40].

Multiple syntheses of bismuth ferrite doped with two distinct concentrations of Ag were successfully performed, yielding phase-pure samples in each case. This consistency underscores the high precision and reproducibility of the synthesis process. For magnetic characterization, a representative sample was carefully selected for each doping level to ensure that the measured properties accurately reflect the intrinsic magnetic behavior of the doped bismuth ferrite system.

The structure of the obtained powder was determined by X-ray powder diffraction on a Rigaku ULTIMA IV XRPD diffractometer (Tokyo, Japan) with Cu Kα1,2 radiations, at room temperature. Data for structural refinement were taken in the 2θ range 10–110°, with a step width of 0.02° 2θ and 5 s per step. The refinement was performed with the FullProf (version 5.90) [41] computer program which adopts the Rietveld calculation method. In the present approach, the grain size broadening was represented by a Lorentzian function, and strain broadening by a Gaussian function.

2.2. Magnetic Measurements

Magnetization was measured on the MPMS 5 SQUID magnetometer (Quantum Design Inc., San Diego, CA, USA) in a wide temperature range, from 2 K to 720 K, and in fields up to 5T. The high temperatures were realized using an oven option, which enabled the measurements at the high temperatures. To measure the temperature dependence of magnetization or the so-called zero-field-cooled (ZFC) and field-cooled (FC) magnetization curves of the compounds with the high magnetic phase transition temperature, such as pure BFO (T N ~630 K), correctly through the entire temperature range, it was necessary to use the following procedure. The samples were first cooled in zero field till 2 K and measured with the standard setup (pellet in the plastic straw) until T = 400 K; then, the samples were taken out and put on a quartz tube holder of the oven option and inserted back for the measurements on the high temperatures. After completing the ZFC curve, the FC magnetization was measured while cooling from 720 K to room temperature, where again the sample was removed and put in a standard setup for the continuation of the FC curve. For all the compounds, M(T) was measured in the constant field of 1 kOe. In addition to the M(T) measurements, the field dependence was measured at temperatures of 4 K and 300 K on a standard setup.

2.3. Crystal Structure Prediction (CSP) and Bond Valence Calculations (BVC)

Our general approach and methods of crystal structure prediction (CSP) and identification of structure candidates have been given in detail elsewhere [42–45], especially including the multidisciplinary approach and previous successful applications on perovskites [46–49]. The Structure Prediction Diagnostic Software (SPuDS V2.21.05.11) [49] was used to generate potential perovskite-related structure candidates in a silver-doped $BiFeO_3$ chemical system. The SPuDS program is based on bond valence calculations (BVCs) and is used to predict the crystal structures of perovskites, including those distorted by tilting of symmetric octahedra or caused by Jahn–Teller distortions [46–49]. The stability of the predicted perovskite-related structures is determined using the global instability index (GII). The GII is obtained by comparing the calculated bond valence sums and the ideal formal valences, and it directly corresponds to the amount of the Ag quantity in $BiFeO_3$ and the different Glazer tilt systems. The symmetry of the novel predicted structures was analyzed with the algorithms SFND [50] and RGS [51], all implemented in the KPLOT version 3 program [52]. The predicted structures were visualized using the VESTA 4.6.0 software [53].

2.4. Density Functional Theory (DFT) Calculations

We utilized SIESTA 5.2 [54] implementation of DFT to determine the atomic structure, electronic and magnetic properties of investigated crystal phases. Valence electrons were modeled using norm-conserving Troullier–Martins pseudopotentials [55], incorporating partial core corrections. A double-zeta basis set was utilized, and calculations for potentials and charge density were performed on a real-space grid with a mesh cutoff energy of 350 Ry, ensuring total energy convergence within 0.1 meV per unit cell during self-consistency procedures. Generalized-gradient approximation with Coulomb interaction potential, GGA+U, [56–59] was employed. At the same time, we fixed the Hubbard U_{eff} = 3.8 eV for Fe 3d orbital and U_{eff} = 0.95 for Fe 4s orbital in all calculations, which was successfully applied in our previous calculations [40]. The crystals were modeled using conventional unit cells that contain 30 atoms (for α- and *R*-type structures) or 40 atoms (for β-, γ-, T1- and T2-type structures). The Brillouin zone was sampled by following k-point grids using the Monkhorst–Pack sampling: 8 × 8 × 4 (α-type structure), 6 × 6 × 6 (β -type structure), 8 × 8 × 8 (γ-type structure), 8 × 8 × 4 (*R*-type structure), 6 × 8 × 6 (T1- and T2-type structures). Atomic structures were relaxed using the conjugate gradient method, where the structures were considered optimized when the maximal force on atoms dropped below 0.04 eV/Angstrom. We examined a ferromagnetic (FM) configuration along with three antiferromagnetic configurations labelled AFM-a, AFM-c and AFM-g by setting up initial atomic spin moments on Fe atoms, which were allowed to relax in self-consistent cycles.

3. Results

3.1. X-Ray Powder Diffraction (XRPD) and Rietveld Refinement

The most common way to clarify the structural changes caused by Ag doping is using Rietveld refinement. This procedure requires a structural model that is an approximation of the actual structure. The starting structural model for the rhombohedral R3cH (no.161) space group using a hexagonal setting was built up with crystallographic data reported in [60].

The structure refinement was carried out on a FullProf program [61] which adopts the Rietveld calculation method. A pseudo-Voigt function was chosen as a profile function among profiles in the refinement program. The refinement of the background was performed using linear interpolation between 56 selected points. The best fit between the calculated and observed X-ray diffraction pattern is shown in Figure 1a,b, where all

allowed Bragg reflections are shown by vertical bars. Inspecting the difference between the experimental and calculated profiles indicates good agreement. Besides the difference curve (blue line), the good refinement is proven by the R (reliability) factors that have values between 1.7 and 2.7.

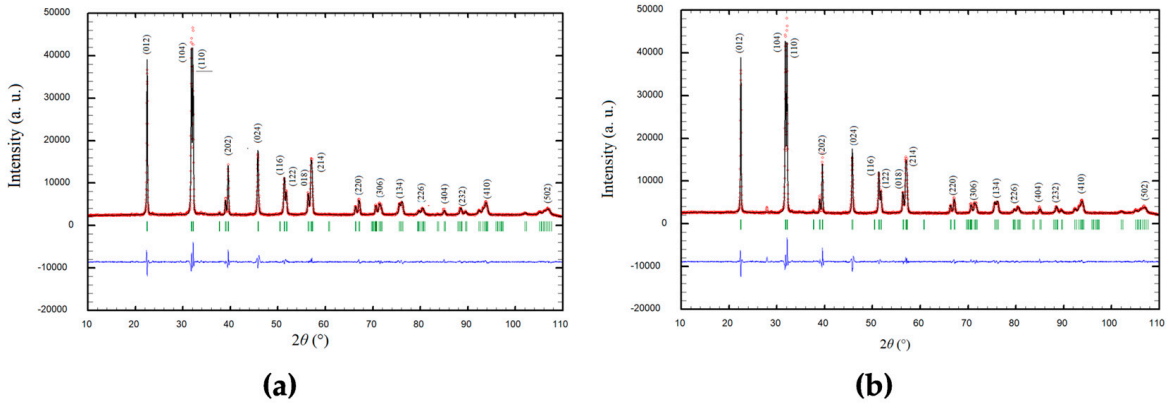

Figure 1. The structural refinement patterns of (**a**) $Bi_{0.99}Ag_{0.01}FeO_3$ and (**b**) $Bi_{0.98}Ag_{0.02}FeO_3$. A difference (observed–calculated) plot is shown beneath (blue line). Green stick marks above the different data indicate the reflection position. Red color denotes the experimental diffraction pattern.

The crystal structures of $Bi_{1-x}Ag_xFeO_3$ (x = 0.01, 0.02) are shown in Figure 2.

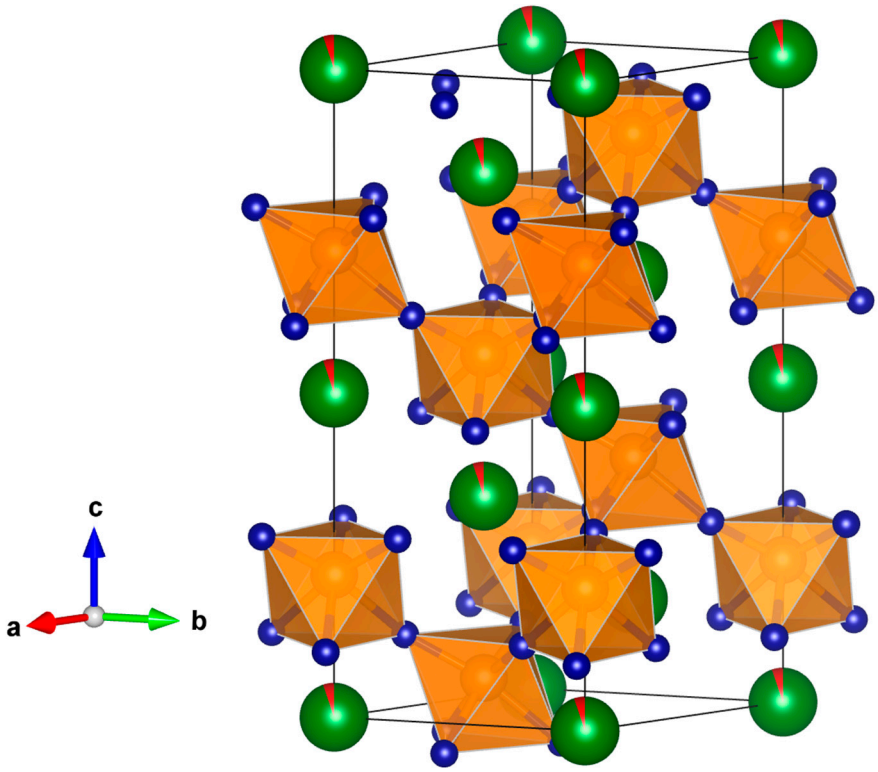

Figure 2. The refined silver-doped α-$BiFeO_3$ structure in the rhombohedral R3cH (no.161) space group using a hexagonal setting. Green spheres correspond to Bi atoms, while red color corresponds to silver doping, blue atoms correspond to oxygen and orange atoms correspond to iron, represented by Fe-O octahedra.

The results of the Rietveld refinement, including unit cell parameters, atomic positions, and average bond distances, are given in Table 1. According to [62], the ionic radii of the Ag^+ cation in coordination VI is 1.15 Å, and for the Bi^{3+} in the same coordination is 1.03 Å.

Silver, instead of bismuth in the crystal lattice, will increase the unit cell parameters. In Table 1, we can follow the effect of entering silver in the structure of $BiFeO_3$ by following values of the unit cell parameters, unit cell volume, and bond lengths. As expected, both investigated compounds have higher values for those parameters in comparison with undoped $BiFeO_3$. Furthermore, we can see the difference between $Bi_{0.98}Ag_{0.02}FeO_3$ where 2% of silver in the structure further increases the above-mentioned parameters in $Bi_{0.98}Ag_{0.02}FeO_3$ if compared with $Bi_{0.99}Ag_{0.01}FeO_3$. The changes in the crystal structure indicate the presence of silver in the structure, while the values of the occupation factors during Rietveld refinement were fixed to the nominal compositions of the powders.

Table 1. Refined structure parameters for $Bi_{0.99}Ag_{0.01}FeO_3$ and $Bi_{0.98}Ag_{0.02}FeO_3$ in comparison with pure $BiAgFeO_3$.

Sample	Structure Parameters	Distances
$Bi_{0.99}Ag_{0.01}FeO_3$	a = 5.57708(6) c = 13.8667(3) V = 373.52 Å^3 Bi/Ag 0 0 0 Fe 0 0 0.2170(2) O 0.570(1) 0.027(1) 0.9512(5)	3 × (Bi-O) = 2.5651(19) Å 3 × (Bi-O) = 2.227(6) Å Average = 2.3963 Å 3 × (Fe-O) = 2.002(4) Å 3 × (Fe-O) = 2.045(5) Å Average = 2.0231 Å
$Bi_{0.98}Ag_{0.02}FeO_3$	a = 5.57765(6) c = 13.8682(3) V = 373.64 Å^3 Bi/Ag 0 0 0 Fe 0 0 0.2208(2) O 0.562(2) 0.022(1) 0.9533(6)	3 × (Bi-O) = 2.586(3) Å 3 × (Bi-O) = 2.262(8) Å Average = 2.4244 Å 3 × (Fe-O) = 1.963(5) Å 3 × (Fe-O) = 2.075(7) Å Average = 2.0191 Å
$BiFeO_3$ [1]	a = 5.5767(3) c = 13.8639(8) V = 373.40 Å^3 Bi 0 0 0 Fe 0 0 0.2208(2) O 0.4478(4) 0.0196(5) 0.9522(2)	3 × (Bi-O) = 2.533(3) Å 3 × (Bi-O) = 2.265(3) Å Average = 2.3989 Å 3 × (Fe-O) = 1.957(5) Å 3 × (Fe-O) = 2.101(7) Å Average = 2.0289 Å

3.2. CSP of Silver-Doped $BiFeO_3$ Perovskites

A crystal structure prediction study was carried out in a bismuth ferrite system as a function of Ag concentration. Calculations were accomplished using bond valence calculations (BVCs) and SPuDS code to find possible additional structure candidates besides experimentally observed α-phase with perovskite structure type. Ten additional perovskite-related structure candidates were predicted, five with 0.1% silver in BFO and five with 0.2% Ag in BFO. Moreover, we predicted 0.5% Ag in BFO and generated an additional five structure candidates. These predicted structures are ranked according to the global instability index (GII) and tilt system and summarized in Table 2 (full structural data are presented in the Supporting Information).

The most stable $BiFeO_3$ perovskite structure with silver doping, according to the GII criterion (Table 2), is the β-type in the space group Pnma. This is in agreement with previous experimental and theoretical data where the β-type structure was found in doped bismuth ferrite [30,31,36,40,62]. The GII ranging of the β-type structure increased from 0.02601 to 0.03542 at 2% Ag doping in BFO, indicating less stability with a higher level of silver dopant in BFO. The predicted β modification in the 2% Ag-doped BFO is shown in Figure 3a.

Table 2. Computed values of the GII and tilt system of the most promising predicted structure candidates in the (a) $Bi_{0.99}Ag_{0.01}FeO_3$; (b) $Bi_{0.98}Ag_{0.02}FeO_3$ system. Calculations were carried out using the BVCs method.

Composition	**$Bi_{0.99}Ag_{0.01}FeO_3$**		
Modification	**Space Group**	**Tilt System**	**GII**
β-type	*Pnma*	$a^-b^+a^-$	0.02601
R-type	*R-3c*	$a^-a^-a^-$	0.13907
T1-type	*P4/mbm*	$a^0a^0c^-$	0.14216
T2-type	*I4/mcm*	$a^0a^0c^-$	0.14216
γ-type	*Pm-3m*	$a^0a^0a^0$	0.76254
	$Bi_{0.98}Ag_{0.02}FeO_3$		
β-type	*Pnma*	$a^-b^+a^-$	0.03542
R-type	*R-3c*	$a^-a^-a^-$	0.14136
T1-type	*P4/mbm*	$a^0a^0c^-$	0.14433
T2-type	*I4/mcm*	$a^0a^0c^-$	0.14433
γ-type	*Pm-3m*	$a^0a^0a^0$	0.75986

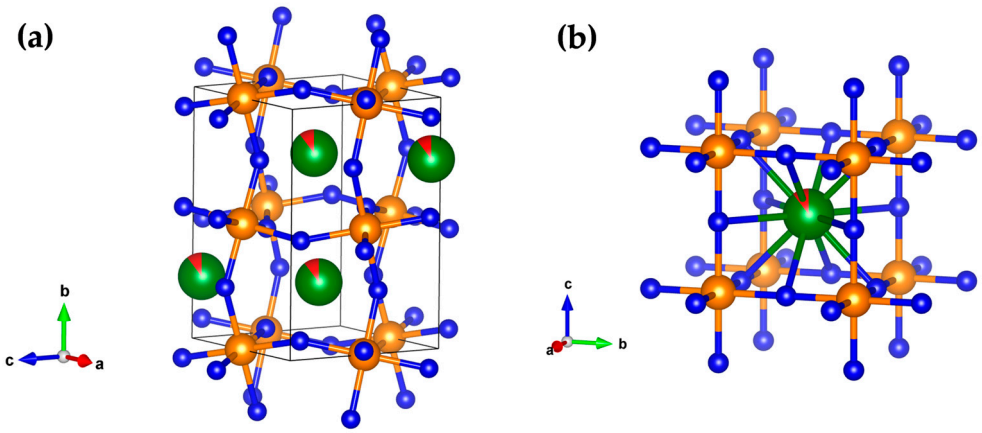

Figure 3. Visualization of the predicted: (**a**) *β*-type of structure in the space group Pnma (no. 62); (**b**) *γ*-type in the cubic Pm-3m (no. 221) space group, in the $Bi_{0.98}Ag_{0.02}FeO_3$ compound.

On the other hand, the *γ*-type of structure is the candidate with the highest level of the GII index, but the GII index is reduced with the increase in the Ag dopant, indicating that increasing silver concentration could stabilize this phase. This will be further confirmed later on in our DFT calculations (See Section 3.3). The gamma phase shows the highest cubic symmetry (Pm-3m (no. 221) space group) where the iron atoms are coordinated by six O atoms forming a perfect octahedron (Figure 3b). The *γ*-type modification was found in the experiments and theoretical studies in pure $BiFeO_3$ at high temperatures, [6,63,64] and was also found in our previous research on pure BFO [40], indicating the possible existence of the gamma phase in the silver-doped bismuth ferrite.

The next three predicted silver-doped structures in BFO, the *R*-, T1- and T2-type, are almost the same according to the GII index regardless of silver concentration, indicating the same possibility of synthesis between the beta and the gamma phase. The *R*-type appears in the rhombohedral R-3c (no. 167) space group (Figure 4a), structurally related to the experimentally observed alpha phase, making the *R*-type a bit more favorable in silver-doped bismuth ferrite. This concurs with previous experimental and theoretical research on pure $BiFeO_3$ where high-temperature rhombohedral modification of $BiFeO_3$ was identified [65,66]. On the other hand, both tetragonal T1 and T2 structures are closely related, where T2 modification appears as a

polytype of T1 [67] (Figure 4b,c). Still, both phases are easily distinguishable by symmetry, where the T1 type appears in the P4/mbm (no. 127) space group, and the T2 type shows I4/mcm (no. 140) space group. Previous literature data on various tetragonal modifications in pure $BiFeO_3$ at high temperatures [6,40,68,69] indicate that both T1- and T2-phases have a high potential for experimental synthesis in silver-doped $BiFeO_3$. In order to explore higher doping levels of Ag in BFO, we predicted these perovskite structure candidates in the $Bi_{0.95}Ag_{0.05}FeO_3$ compound. However, very small changes in structure and unit cell parameters were detected, implying that larger amounts of silver do not have a significant impact on the crystal structure of BFO (full structural data are presented in the Supporting Information).

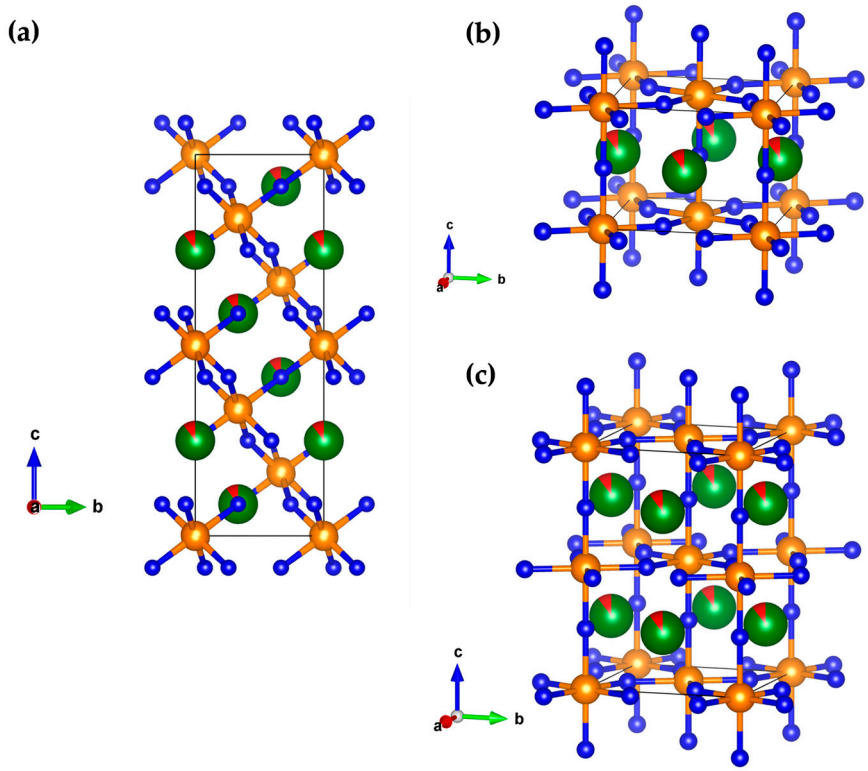

Figure 4. Visualization of the predicted: (**a**) *R*-type in the rhombohedral R-3c (no. 167) space group; (**b**) T1-type structure appearing in the space group P4/mbm (no. 127); (**c**) T2-type appearing in the I4/mcm (no. 140) space group in the $Bi_{0.98}Ag_{0.02}FeO_3$ compound.

3.3. Electronic and Magnetic Properties—Density Functional Theory Study

Using the structures predicted by the BVCs method, we analyzed the electronic and magnetic properties of the doped materials. To investigate the doped systems, we substituted one Bi atom with one Ag atom per conventional unit cell. This corresponds to doping of 12.5% (1/8) for α- and *R*-type structures and 16.6% (1/6) for remaining structural types. Unit cells that correspond to smaller, closer to experimental, doping levels are significantly larger than the unit cells which we used in the DFT calculations. Larger unit cells and the correspondingly larger number of atoms per unit cell significantly increase the number of degrees of freedom, which made geometry optimizations difficult and, for most phases, unachievable for the quantum method; atomic forces or even electron density could not converge below desired tolerance levels. However, differences between bond lengths of the doped materials predicted by the BVCs method for doping levels of 5% and 12.5% do not exceed 0.26%, which fairly justifies the utilization of the smaller unit cells. Additionally, the BVCs study indicated the stabilization of a studied crystal, particularly the γ phase, by an increase in Ag doping. Our DFT calculations, as will be shown below, confirmed this indication for a significantly larger doping concentration than that considered in BVCs. We

proceeded with DFT calculations in the following steps. First, using the conjugate gradient method, we optimized the atomic structure of the undoped crystals. The optimization was performed with atomic spins initially set up in a ferromagnetic FM, or one of the three antiferromagnetic spin orders, AFM-a, AFM-c or AFM-g. The spin orders were determined by initial spins on Fe atoms. Second, we substituted one Bi atom with one Ag atom in the optimized undoped structure. After setting up the atomic spins to the previously obtained values in undoped structures, the conjugate gradient optimization was conducted for the doped structures. Table 3 shows the energy released upon the substitution of one Bi atom by one Ag atom in the unit cell. It is calculated from the expression E_{dop} = E(doped) + E(Bi) − E(undoped) − E(Ag), where E(doped) is the energy of the doped crystal, E(undoped) is the energy of the pristine crystal and E(Bi) and E(Ag) are energies of isolated Bi and Ag atoms. For the crystals with theoretically considered high levels of Ag doping, our DFT calculations indicate that only three phases can be substitutionally doped: γ, T1 and T2 with ground states having FM, AFM-c and AFM-a spin textures, respectively. Note that, e.g., molecular dynamics simulations (MDSs) would be essential to study the thermodynamic stability of these phases at finite temperatures, from, for example, the Lindemann index. However, MDSs are very "expensive" for investigated systems, in which atomic forces and density matrices were difficult to converge in self-consistent field iterations even in the conjugate gradient structural optimizations (essentially presenting quasi-dynamics of atomic structures at the absolute zero).

Table 3. Energy (eV/unit cell) for substitution of one Bi atom by one Ag atom in the unit cell. The doping energy is calculated using the following formula: E_{dop} = E(doped) + E(Bi) − E(undoped) − E(Ag). The fields marked in blue indicate the doping energies in the ground states.

Phase	FM	AFM-a	AFM-c	AFM-g
α	0.103	2.351	N/A	N/A
β	1.357	1.639	1.737	2.077
γ	−0.350	0.127	0.704	1.531
R	0.102	1.623	N/A	N/A
T1	−0.383	−0.294	−0.609	−0.133
T2	−0.068	−0.353	1.456	−0.073

The spins were allowed to relax during self-consistent field iterations. For all investigated phases, the initial spin configurations were retained, while the obtained values of atomic spins are listed in Table S1 of the provided Supplementary Material. Two conclusions can be derived from Table S1:

1. Doping reduces the magnetization in the FM-ordered systems of all crystals by around 5% except for the R phase, for which magnetization is reduced by 7%.
2. In undoped systems, spins are perfectly compensated in AFM magnetic orders, whereas Ag doping induces net spins on Fe and O atoms in AFM magnetic textures.

Next, we show the electronic structure of the three systems with theoretically feasible high Ag doping, ferromagnetic γ-type structure, T1-type structure with AFM-c and T2-type structure with AFM-a spin textures, which are in ground electronic states according to our DFT calculations. Electronic band structures (BSs) and electronic density of states (DOS) for these phases are represented in Figure 5 in Panels (a), (b) and (c), respectively. The band structure of the ferromagnetic γ-type structure has mixed features of metal, semi-metal and half-metal. A band with a relatively large dispersion of about 2 eV starts at the center of the Brillouin zone (Γ-point at Γ-X segment) and crosses the Fermi level close to the M

point. At the segment M-Γ-R, the bottom of the conduction band is placed below the top of the valence band, indicating the semi-metallic nature of the crystal. The majority spin characterizes the energy range from around −1 eV below the Fermi level to the Fermi level, indicating the half-metallic nature of the material in the γ-type structure. The T1 phase is nearly perfectly compensated antiferromagnet with AFM-c spin texture. It is also a narrow-gap semiconductor, with a direct gap of around 0.5 eV. In contrast, the T2-type structure with AFM-a spin texture is a semiconductor with a band gap of about 0.8 eV. Its valence band is characterized primarily by minority spin, whereas the conduction band has predominantly majority spin. The T2 phase has an indirect band gap, with the top of the valence band at the Γ-point and the bottom of the condition band at the Y point. We obtained electronic BS and DOS also for α, β and R phases and all combinations of spin textures. These are included in Figures S1 and S2 of the Supplementary Material.

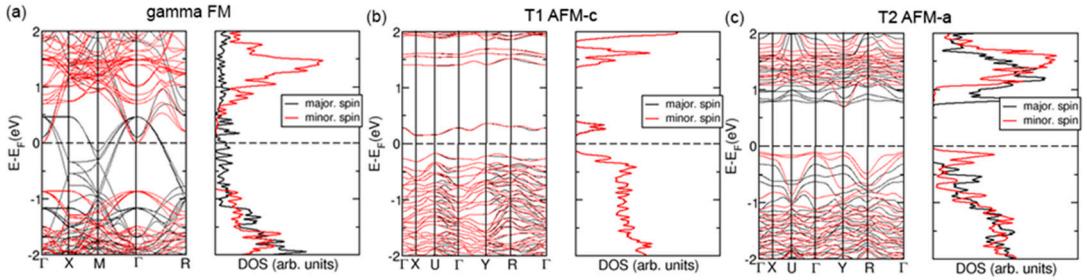

Figure 5. Electronic band structure (BS) and density of states (DOS) for ferromagnetic γ phase (**a**), T1 phase with AFM-c spin texture (**b**) and T2 phase with AFM-a spin texture (**c**). The figure on the left side of each panel represents BS, while the right-hand side figure of each panel shows DOS. The vertical scale of DOS figures matches the ones of BS. Features of majority spins are depicted by black lines, while those of minority spins are in red. Dash lines indicate Fermi's energy.

3.4. Magnetic Properties

The temperature dependence of magnetization measured on the pellets of pure BFO, and BFO with 1% and 2% of Ag is shown in Figure 6. It can be seen that the incorporation of Ag increases the value and the irreversibility of magnetization but does not change the temperature of the magnetic phase transition (T_N = 630 K). Our DFT calculations are in agreement with the experimental finding of magnetization increase by Ag doping in AFM spin orders, with spins localized at Fe and O atoms. While pure BFO is known to be an antiferromagnet with the spin cycloid magnetic order [70], often, the weak ferromagnetic moment can be found due to the microstructure of the samples. Very rarely, it is synthesized in monocrystal form, which would show the peak in the magnetization at the transition temperature, and more often it is found to be in the form of nanoparticles, where the non-compensated surface spins and the breaking of spin spiral periodicity (period 62 nm) attribute to the appearance of the magnetic moment. The substitution of nonmagnetic Ag enhances the development of the weak ferromagnetic moment, and the irreversibility of the magnetization increases as it disturbs the antiferromagnetic interaction of the Fe ions. A similar effect is also found in the substitution with other elements [71–73].

A peculiar behavior is observed in pure BFO and BFO with 1% of Ag, where the crossing of ZFC and FC curves is present around 280 K and 250 K, respectively. Such behavior was already observed and can be attributed to different origins such as the competition of the interactions between Fe in different magnetic sublattices spin freezing in surface layers of small particles and other types of canting in the antiferromagnetic spin cycloids, etc. [74,75]. Only the former origin was attainable by our DFT calculations since we modeled the systems as infinite crystals (i.e., without surfaces), and we performed collinear spin calculations that do not take into account the spin canting in an antiferromagnet.

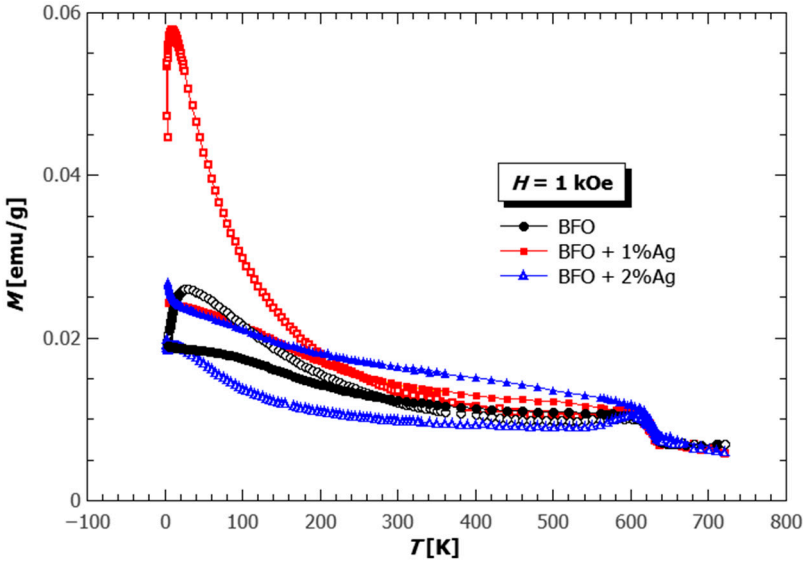

Figure 6. The temperature dependence of magnetization was measured in the magnetic field of 1 kOe on the pellets of pure BFO (black circles), BFO with 1% Ag (red rectangles) and 2% Ag (blue triangles). The empty symbols represent the ZFC, and the full symbols FC magnetization curves.

From the field dependence of magnetization at 4 K and 300 K (Figure 7), additional conclusions can be drawn in the same direction. The substitution of Ag increases the value of magnetization, which is expressed in the larger changes at the lowest fields and the additional appearance of the S-shape is superimposed on the antiferromagnetic linear dependence, which is characteristic of the weak ferromagnetic behavior. The pronounced weak ferromagnetic hysteresis is found in the BFO with 2% of Ag also at room temperature, while 0% Ag and 1% Ag curves resemble much more the shape of antiferromagnetic MH loops. This shows that even the addition of only 2% of a nonmagnetic substituent can produce a weak ferromagnetic response at ambient temperatures, thereby opening the possibilities of developing such materials towards eventual applications in different multiferroic devices.

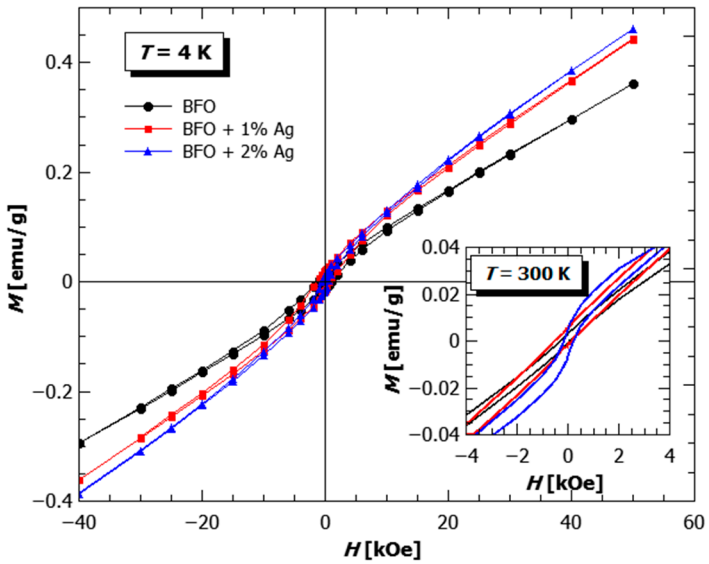

Figure 7. Field dependence of magnetization at 4 K and 300 K (inset), measured on the pellets of pure BFO (black circles), BFO with 1% Ag (red rectangles) and 2% Ag (blue triangles).

4. Conclusions

A comprehensive multidisciplinary study was conducted to investigate the impact of doping $BiFeO_3$ with Ag atoms. Nanocrystalline powders of $BiFeO_3$ and $Bi_{1-x}Ag_xFeO_3$ (with x = 0.01 and 0.02) were synthesized using the hydrothermal method. Samples doped with 1 and 2 atomic percent (at. %) of Ag were characterized using powder X-ray diffraction, and the structure refinement was carried out on a FullProf program, which adopts the Rietveld calculation method. The doped $BiFeO_3$ samples, regardless of the Ag concentration, exhibited the α-phase structure in the space group *R3cH*. To explore additional possible structures in Ag-doped $BiFeO_3$, bond valence calculations (BVCs) were employed for structure prediction. As a result, several structure candidates, including α-, β-, γ-, *R*-, T1 and T2 structures, were predicted in various Ag-doped $BiFeO_3$ systems using BVCs. We studied the electronic and magnetic properties of these structures using DFT. Our DFT results are in agreement with the experimental finding of magnetization increase upon Ag doping in antiferromagnetically ordered structures and the possibility to dope the γ phase with a high Ag dopant concentration. Additionally, DFT calculations predict the semiconducting properties of antiferromagnetic T1 and T2 phases. More importantly, the half-metallic property of the γ-type structure that DFT calculations predicted, as well as the induced weak ferromagnetism with light doping, may be of great interest for further research due to its potential physical consequences and applications in future nanodevices.

Supplementary Materials: The following supporting information can be downloaded at: https://www.mdpi.com/article/10.3390/ma18071453/s1, Figure S1: Electronic band structure and density of states for all combinations of alpha, beta, gamma and R phases on one hand and FM, AFM-a, AFM-c and AFM-g spin orders on the other hand; Figure S2: Electronic band structure and density of states for all combinations of T1 and T2 phases on one hand and FM, AFM-a, AFM-c and AFM-g spin orders on the other hand. Table S1: Calculated values of the global instability index (GII) and tilt system of the most promising $Bi_{0.99}Ag_{0.01}FeO_3$ modifications using the bond valence calculations (BVCs) method.; Table S2: Structural data of the most promising $Bi_{0.99}Ag_{0.01}FeO_3$ perovskite modifications were calculated using the BVCs method; Table S3: Calculated values of the global instability index (GII) and tilt system of the most promising $Bi_{0.98}Ag_{0.02}FeO_3$ modifications using the bond valence calculations (BVCs) method; Table S4: Structural data of the most promising $Bi_{0.98}Ag_{0.02}FeO_3$ perovskite modifications were calculated using the BVCs method; Table S5: Atomic spins (in units of Bohr magneton) were obtained by DFT calculations for each of the undoped or Ag-doped phases for FM, AFM-a, AFM-c and AFM-g spin textures. For undoped crystals, the Ag atom is not present and so spin on the Ag atom is not available (N/A). Data for Alpha and R phases in AFM-c and AFM-g spin configurations are not available as well, as these results could not converge.

Author Contributions: Conceptualization, M.Č. and D.P.; methodology, M.Č, D.Z., I.P. and J.Z.; software, D.Z. and I.P.; validation, M.R. and D.P.; formal analysis, P.Š. and J.Z.; investigation, D.Z., P.Š., J.Z. and M.R.; writing—original draft preparation, I.P. and M.Č.; writing—review and editing, M.Č., M.R. and D.P.; visualization, D.Z., P.Š. and J.Z.; supervision, D.P. All authors have read and agreed to the published version of the manuscript.

Funding: This research was funded by the Ministry of Science, Technological Development and Innovation of the Republic of Serbia, based on Contract no. 451-03-136/2025-03/200017 ("Vinča" Institute of Nuclear Sciences—National Institute of the Republic of Serbia, University of Belgrade), 451-03-66/2024-03/200053 (Institute for Multidisciplinary Research, University of Belgrade), and by the Croatian Science Foundation, Zagreb, Croatia [project IP-2022-10-6321]; M. Č. acknowledges the support from the Bilateral Project Between Serbia and Austria (OeAD-GmbH-Project no. RS 24/2022) 337-00-577/2021-09/6. DFT calculations were performed using computational resources at the Center of Surface and Nanoanalytics, Johannes Kepler University, Linz, Austria. We thank Kurt Hingerl for providing the computational resources at JKU. P.Š. and D.P. acknowledge support from the CeNIKS, Grant No. KK.01.1.1.02.0013 co-financed by the Croatian Government and the European Union

through the European Regional Development Fund—Competitiveness and Cohesion Operational Programme.

Institutional Review Board Statement: Not applicable.

Informed Consent Statement: Not applicable.

Data Availability Statement: The original contributions presented in this study are included in the article/Supplementary Material. Further inquiries can be directed to the corresponding authors.

Conflicts of Interest: The authors declare no conflicts of interest.

References

1. Monem, A.M.A.; Abd-Elmohssen, N.; El-Bahnasawy, H.H.; Makram, N.; Sedeek, K. Comparative studies by X-ray diffraction, Raman, vibrating sample magnetometer and Mössbauer spectroscopy of pure, Sr doped and Sr, Co co-doped $BiFeO_3$ ceramic synthesized via tartaric acid-assisted technique. *Ceram. Int.* **2023**, *49*, 15213–15220. [CrossRef]
2. Jin, C.; Geng, W.; Wang, L.; Han, W.; Zheng, D.; Hu, S.; Ye, M.; Xu, Z.; Ji, Y.; Zhao, J.; et al. Tuning ferroelectricity, and ferromagnetism in $BiFeO_3/BiMnO_3$ superlattices. *Nanoscale* **2020**, *12*, 9810–9816. [CrossRef]
3. Cheong, S.W.; Mostovoy, M. Multiferroics: A magnetic twist for ferroelectricity. *Nat. Mater.* **2007**, *6*, 13–20. [CrossRef] [PubMed]
4. Haruna, A.; Abdulkadir, I.; Idris, S.O. Photocatalytic activity and doping effects of $BiFeO_3$ nanoparticles in model organic dyes. *Heliyon* **2020**, *6*, e03237. [CrossRef]
5. Freitas, V.F.; Dias, G.S.; Protzek, O.A.; Montanher, D.Z.; Catellani, I.B.; Silva, D.M.; C'otica, L.F.; dos Santos, I.A. Structural phase relations in perovskite–structured $BiFeO_3$-based multiferroic compounds. *J. Adv. Ceram.* **2013**, *2*, 103–111. [CrossRef]
6. Selbach, S.M.; Tybell, T.; Einarsrudand, T.M.; Grande, T. Size-dependent properties of multiferroic $BiFeO_3$ nanoparticles. *Chem. Mater.* **2007**, *19*, 6478–6484. [CrossRef]
7. Yakout, S.M. Spintronics and innovative memory devices: A review on advances in magnetoelectric $BiFeO_3$. *J. Supercond. Nov. Magnetism.* **2021**, *34*, 317–338. [CrossRef]
8. Rizwan, S.; Awan, S.; Irfan, S. Room-temperature ferromagnetism in Gd and Sn co-doped bismuth ferrite nanoparticles and co-doped $BiFeO_3$/MXene (Ti_3C_2) nanohybrids of spintronics applications. *Ceram. Int.* **2020**, *46 Pt A*, 29011–29021. [CrossRef]
9. Neogi, S.; Ghosh, R. Behavioral remodelling of perovskite $BiFeO_3$ by Ag-doping strategies for enhanced and ppb level acetone sensing performance: An advanced enlightenment for selectivity and sensing mechanism. *Appl Mater Today* **2022**, *29*, 101611. [CrossRef]
10. Xu, H.; Xu, J.; Li, H.; Zhang, W.; Zhang, Y.; Zhai, Z. Highly sensitive ethanol and acetone gas sensors with reduced working temperature based on Sr-doped $BiFeO_3$ nanomaterial. *J. Mater. Res. Technol.* **2022**, *17*, 1955–1963. [CrossRef]
11. Liu, H.; Sun, Y. Defect chemistry for Mn-doped and Nb-doped $BiFeO_3$-based ceramics. *J. Phys. Chem. Solids* **2022**, *170*, 110951. [CrossRef]
12. Aishwarya, K.; Navamathavan, R. Effect of grain size and orthorhombic phase of La-doped $BiFeO_3$ on thermoelectric properties. *J. Alloys Compd.* **2023**, *947*, 169452. [CrossRef]
13. Nazeer, Z.; Bibi, I.; Majid, F.; Kamal, S.; Ghafoor, A.; Ali, A.; Kausar, A.; Elqahtani, Z.M.; Alwadai, N.; Iqbal, M. Microemulsion synthesis of Ga and Sr doped $BiFeO_3$ nanoparticles and evaluation of their ferroelectric, optical, dielectric and photocatalytic properties. *Phys. B* **2023**, *657*, 414788. [CrossRef]
14. Anwar, A.; Basith, M.A.; Choudhury, S. From bulk to nano: A comparative investigation of structural, ferroelectric and magnetic properties of Sm and Ti co-doped $BiFeO_3$ multiferroics. *Mater. Res. Bull.* **2019**, *111*, 93–101. [CrossRef]
15. Chowdhury, S.S.; Kamal, A.H.M.; Hossain, R.; Hasan, M.; Islam, M.F.; Ahmmad, B.; Basith, M.A. Dy doped $BiFeO_3$: A bulk ceramic with improved multiferroic properties compared to nano counterparts. *Ceram. Int.* **2017**, *43*, 9191–9199. [CrossRef]
16. Moreau, J.M.; Michel, C.; Gerson, R.; James, W.J. Ferroelectric $BiFeO_3$ X-ray and neutron diffraction study. *J. Phys. Chem. Solids* **1971**, *32*, 1315–1320. [CrossRef]
17. Kubel, F.; Schmid, H. Structure of a ferroelectric and ferroelastic monodomain crystal of the perovskite $BiFeO_3$. *Acta Crystallog. B* **1990**, *46*, 698–702. [CrossRef]
18. Wang, J.; Neaton, J.B.; Zheng, H.; Nagarajan, V.; Ogale, S.B.; Liu, B.; Viehland, D.; Vaithyanathan, V.; Schlom, D.G.; Waghmare, U.V.; et al. Epitaxial $BiFeO_3$ Multiferroic Thin Film Heterostructures. *Science* **2003**, *299*, 1719–1722. [CrossRef] [PubMed]
19. Feng, H. Magnetism and electronic properties of $BiFeO_3$ under lower pressure. *J. Magn. Magn. Mater.* **2010**, *322*, 3755–3759. [CrossRef]
20. Catalan, G.; Scott, J.F. Physics and Applications of Bismuth Ferrite. *Adv. Mater.* **2009**, *21*, 2463–2485. [CrossRef]
21. Martin, L.W.; Crane, S.P.; Chu, Y.H.; Holcomb, M.B.; Gajek, M.; Huijben, M.; Yang, C.H.; Balke, N.; Ramesh, R. Multiferroics and magnetoelectrics: Thin films and nanostructures. *J. Phys.-Condens. Mat.* **2008**, *20*, 434220. [CrossRef]

22. Wu, J.; Fan, Z.; Xiao, D.; Zhu, J.; Wang, J. Multiferroic bismuth ferrite-based materials for multifunctional applications: Ceramic bulks, thin films and nanostructures. *Prog. Mater. Sci.* **2016**, *84*, 335–402. [CrossRef]
23. Park, J.-G.; Le, M.D.; Jeong, J.; Lee, S. Structure and spin dynamics of multiferroic $BiFeO_3$. *J. Phys.-Condens. Mat.* **2014**, *26*, 433202. [CrossRef]
24. Wang, Y.; Wang, Y.; Wei, M.; Zhang, J.; Zhang, Y. Role of Ho Doping in Magnetization Mechanism of $BiFeO_3$ Thin Films. *J. Supercond. Nov. Magn.* **2019**, *32*, 3495–3501. [CrossRef]
25. Liu, Y.Q.; Wang, Y.J.; Zhang, J.; Gao, M.; Zhang, Y.J.; Wei, M.B.; Yang, J.H. Effect of Ho substitution on the structure and magnetic property of $BiFeO_3$ prepared by sol-gel method. *Mater. Sci. Semicond. Process.* **2015**, *40*, 787–795. [CrossRef]
26. Sharif, S.; Murtaza, G.; Meydan, T.; Williams, P.I.; Cuenca, J.; Hashimdeen, S.H.; Shaheen, F.; Ahmad, R. Structural, surface morphology, dielectric and magnetic properties of holmium doped $BiFeO_3$ thin films prepared by pulsed laser deposition. *Thin Solid Films* **2018**, *662*, 83–89. [CrossRef]
27. Hou, P.; Liu, B.; Guo, Z.; Zhou, P.; Wang, B.; Zhao, L. Effect of Ho doping on the crystal structure, surface morphology and magnetic property of $BiFeO_3$ thin films prepared via the sol-gel technology. *J. Alloys Compd.* **2019**, *775*, 59–62. [CrossRef]
28. Yun, Q.; Bai, A.; Zhao, S. Lattice distortion of holmium doped bismuth ferrite nanofilms. *J. Rare Earth* **2014**, *32*, 884–889. [CrossRef]
29. Islam, M.R.; Zubair, M.A.; Galib, R.H.; Hoque, M.S.B.; Tomko, J.A.; Aryana, K.; Basak, A.K.; Hopkins, P.E. Vacancy-Induced Temperature-Dependent Thermal and Magnetic Properties of Holmium-Substituted Bismuth Ferrite Nanoparticle Compacts. *ACS Appl. Mater. Interfaces* **2022**, *14*, 25886–25897. [CrossRef]
30. Chaturvedi, S.; Bag, R.; Sathe, V.; Kulkarni, S.; Singh, S. Holmium induced enhanced functionality at room temperature and structural phase transition at high temperature in bismuth ferrite nanoparticles. *J. Mater. Chem. C* **2016**, *4*, 780–792. [CrossRef]
31. Stojadinović, B.; Dohčević-Mitrović, Z.; Stepanenko, D.; Rosić, M.; Petronijević, I.; Tasić, N.; Ilić, N.; Matović, B.; Stojanović, B. Dielectric and ferroelectric properties of Ho-doped $BiFeO_3$ nanopowders across the structural phase transition. *Ceram. Int.* **2017**, *43*, 16531–16538. [CrossRef]
32. Kuang, D.; Yang, F.; Wang, W.; Yang, Z. Effects of Ho^{3+} and transition metal ion doping on optical and magnetic properties of $BiFeO_3$ nanopowders. *J. Mater. Sci.-Mater. Electron.* **2018**, *29*, 4041–4047. [CrossRef]
33. Thakuria, P.; Joy, P.A. High room temperature ferromagnetic moment of Ho substituted nanocrystalline $BiFeO_3$. *Appl. Phys. Lett.* **2010**, *97*, 162504. [CrossRef]
34. Jeon, N.; Rout, D.; Kim, I.W.; Kang, S.-J.L. Enhanced multiferroic properties of single-phase $BiFeO_3$ bulk ceramics by Ho doping. *Appl. Phys. Lett.* **2011**, *98*, 072901. [CrossRef]
35. Pradhan, S.K.; Das, J.; Rout, P.P.; Mohanta, V.R.; Das, S.K.; Samantray, S.; Sahu, D.R.; Huang, J.L.; Verma, S.; Roul, B.K. Effect of holmium substitution for the improvement of multiferroic properties of $BiFeO_3$. *J. Phys. Chem. Solids* **2010**, *71*, 1557–1564. [CrossRef]
36. Van Minh, N.; Quan, N.G. Structural, optical and electromagnetic properties of $Bi_{1-x}Ho_xFeO_3$ multiferroic materials. *J. Alloys Compd.* **2011**, *509*, 2663–2666. [CrossRef]
37. Muneeswaran, M.; Lee, S.H.; Kim, D.H.; Jung, B.S.; Chang, S.H.; Jang, J.-W.; Choi, B.C.; Jeong, J.H.; Giridharan, N.V.; Venkateswaran, C. Structural, vibrational, and enhanced magneto-electric coupling in Ho-substituted $BiFeO_3$. *J. Alloys Compd.* **2018**, *750*, 276–285. [CrossRef]
38. Li, X.; Zhang, Y.; Kang, W.; Yan, Z.; Shen, Y.; Huo, J. Anti-perovskite nitrides and oxides: Properties and preparation. *Comp. Mater. Sci.* **2023**, *225*, 112188. [CrossRef]
39. Goldschmidt, V.M. Die gesetze der krystallochemie. *Naturwissenschaften* **1926**, *14*, 477–485. [CrossRef]
40. Čebela, M.; Zagorac, D.; Batalović, K.; Radaković, J.; Stojadinović, B.; Spasojević, V.; Hercigonja, R. $BiFeO_3$ perovskites: A multidisciplinary approach to multiferroics. *Ceram. Int.* **2017**, *43*, 1256–1264. [CrossRef]
41. Rodriguez-Carvajal, J. Recent advances in magnetic structure determination by neutron powder diffraction. *Phys. B* **1993**, *192*, 55–69. [CrossRef]
42. Zagorac, D.; Schön, J.C. Energy landscapes of pure and doped ZnO: From bulk crystals to nanostructures. *Front. Nanosci.* **2022**, *21*, 151–193. [CrossRef]
43. Zagorac, J.; Zagorac, D.; Šrot, V.; Ranđelović, M.; Pejić, M.; van Aken, P.A.; Matović, B.; Schön, J.C. Synthesis, Characterization, and Electronic Properties of ZnO/ZnS Core/Shell Nanostructures Investigated Using a Multidisciplinary Approach. *Materials* **2023**, *16*, 326. [CrossRef]
44. Buyer, C.; Grossholz, H.; Wolf, S.; Zagorac, D.; Zagorac, J.; Schön, J.C.; Schleid, T. Crystal-Structure Prediction and Experimental Investigation of the Polymorphic Lanthanum Fluoride Selenides LaFSe and La_2F_4Se. *Cryst. Growth Des.* **2022**, *22*, 7133–7142. [CrossRef]
45. Pejić, M.; Zagorac, D.; Zagorac, J.; Matović, B.; Schön, J.C. Structure prediction via global energy landscape exploration of the ternary rare-earth compound LaOI. *Z.. Anorg. Allg. Chem.* **2022**, *648*, e202200308. [CrossRef]
46. Zagorac, J.; Zagorac, D.; Zarubica, A.; Schön, J.C.; Djuris, K.; Matovic, B. Prediction of possible CaMnO3 modifications using an ab initio minimization data-mining approach. *Acta Crystallogr. B Struct. Sci. Cryst. Eng. Mater.* **2014**, *70*, 809–819. [CrossRef]

47. Rosić, M.; Zagorac, D.; Milivojević, D.; Paunović, N.; Zagorac, J.; Dohčević-Mitrović, Z.; Matović, B. Theoretical and experimental study of octahedral tilting of $Ca_{1-x}Gd_xMnO_3$ (x = 0.05, 0.1, 0.15, 0.2) nanometric powders. *J. Alloys Compd.* **2016**, *678*, 219–227. [CrossRef]
48. Lufaso, M.W.; Woodward, P.M. Prediction of the crystal structures of perovskites using the software program SPuDS. *Acta Crystallogr. B* **2001**, *57*, 725–738. [CrossRef]
49. Lufaso, M.W.; Woodward, P.M. Jahn-Teller distortions, cation ordering and octahedral tilting in perovskites. *Acta Crystallogr. B* **2004**, *60*, 10–20. [CrossRef]
50. Hundt, R.; Schön, J.C.; Hannemann, A.; Jansen, M. Determination of symmetries and idealized cell parameters for simulated structures. *J. Appl. Crystallogr.* **1999**, *32*, 413–416. [CrossRef]
51. Hannemann, A.; Hundt, R.; Schön, J.C.; Jansen, M. A New Algorithm for Space-Group Determination. *J. Appl. Crystallogr.* **1998**, *31*, 922–928. [CrossRef]
52. Hundt, R. *KPLOT: A Program for Plotting and Analysing Crystal Structures*; Technicum Scientific Publishing: Stuttgart, Germany, 2016.
53. Momma, K.; Izumi, F. VESTA 3 for three-dimensional visualization of crystal, volumetric and morphology data. *J. Appl. Crystallogr.* **2011**, *44*, 1272–1276. [CrossRef]
54. Soler, J.M.; Artacho, E.; Gale, J.D.; Garcia, A.; Junquera, J.; Ordejon, P.; Sanchez-Portal, D. The SIESTA Method for Ab initio Order-N Materials Simulation. *J. Phys. Condens. Matter.* **2002**, *14*, 2745. [CrossRef]
55. Troullier, N.; Martins, J.L. Efficient Psudopotentials for Plane-wave Calculations. *Phys. Rev. B* **1991**, *43*, 1993–2006. [CrossRef]
56. Liechtenstein, A.I.; Anisimov, V.I.; Zaanen, J. Density-functional theory and strong interactions: Orbital ordering in Mott-Hubbard insulators. *Phys. Rev. B* **1995**, *52*, R5467–R5470. [CrossRef]
57. Anisimov, V.I.; Zaanen, J.; Andersen, O.K. Band theory and Mott insulators: Hubbard U instead of Stoner I. *Phys. Rev. B* **1991**, *44*, 943–954. [CrossRef]
58. Vladimir, I.A.; Aryasetiawan, F.; Lichtenstein, A.I. First-principles calculations of the electronic structure and spectra of strongly correlated systems: The LDA+ U method. *J. Phys.-Condens. Matter* **1997**, *9*, 767. [CrossRef]
59. Ivanov, S.A.; Nordblad, P.; Tellgren, R.; Ericsson, T.; Korchagina, S.K.; Rybakova, L.F.; Hewat, A. Influence of $PbZrO_3$ doping on the structural and magnetic properties of $BiFeO_3$. *Solid State Sci.* **2008**, *10*, 1875–1885. [CrossRef]
60. Roisnel, T.; Rodriguez-Carvajal, J. WinPLOTR: A Windows tool for powder diffraction pattern analysis. *Mater. Sci. Forum* **2001**, *378*, 118–123. [CrossRef]
61. Shannon, R. Revised effective ionic radii and systematic studies of interatomic distances in halides and chalcogenides. *Acta Crystallogr. A* **1976**, *32*, 751–767. [CrossRef]
62. Chaturvedi, S.; Sarkar, I.; Shirolkar, M.M.; Jeng, U.-S.; Yeh, Y.-Q.; Rajendra, R.; Ballav, N.; Kulkarni, S. Probing bismuth ferrite nanoparticles by hard x-ray photoemission: Anomalous occurrence of metallic bismuth. *Appl. Phys. Lett.* **2014**, *105*, 102910. [CrossRef]
63. Palai, R.; Katiyar, R.S.; Schmid, H.; Tissot, P.; Clark, S.J.; Robertson, J.; Redfern, S.A.T.; Catalan, G.; Scott, J.F. β phase and $\gamma-\beta$ metal-insulator transition in multiferroic $BiFeO_3$. *Phys. Rev. B* **2008**, *77*, 014110. [CrossRef]
64. Haumont, R.; Kreisel, J.; Bouvier, P.; Hippert, F. Phonon anomalies and the ferroelectric phase transition in multiferroic $BiFeO_3$. *Phys. Rev. B* **2006**, *73*, 132101. [CrossRef]
65. Selbach, S.M.; Tybell, T.; Einarsrud, M.-A.; Grande, T. The Ferroic Phase Transitions of $BiFeO_3$. *Adv. Mater.* **2008**, *20*, 3692–3696. [CrossRef]
66. Munro, J.M.; Akamatsu, H.; Padmanabhan, H.; Liu, V.S.; Shi, Y.; Chen, L.-Q.; VanLeeuwen, B.K.; Dabo, I.; Gopalan, V. Discovering minimum energy pathways via distortion symmetry groups. *Phys. Rev. B* **2018**, *98*, 085107. [CrossRef]
67. Zagorac, D.; Zagorac, J.; Schön, J.C.; Stojanović, N.; Matović, B. ZnO/ZnS (hetero)structures: Ab initio investigations of polytypic behaviour of mixed ZnO and ZnS compounds. *Acta Crystallogr. B* **2018**, *74*, 628–642. [CrossRef]
68. Ravindran, P.; Vidya, R.; Kjekshus, A.; Fjellvåg, H.; Eriksson, O. Theoretical investigation of magnetoelectric behaviour in $BiFeO_3$. *Phys. Rev. B* **2006**, *74*, 224412. [CrossRef]
69. Diéguez, O.; González-Vázquez, O.E.; Wojdeł, J.C.; Íñiguez, J. First-principles predictions of low-energy phases of multiferroic $BiFeO_3$. *Phys. Rev. B* **2011**, *83*, 094105. [CrossRef]
70. Lu, J.; Günther, A.; Schrettle, F.; Mayr, F.; Krohns, S.; Lunkenheimer, P.; Pimenov, A.; Travkin, V.D.; Mukhin, A.A.; Loidl, A. On the room temperature multiferroic $BiFeO_3$: Magnetic, dielectric and thermal properties. *Eur. Phys. J. B* **2010**, *75*, 451–460. [CrossRef]
71. Li, Y.; Liu, L.; Wang, D.; Zhang, H.; He, X.; Li, Q. The Study of Magnetic Properties for Non-Magnetic Ions Doped $BiFeO_3$. *Materials* **2021**, *14*, 4061. [CrossRef]
72. Luković Golić, D.; Radojković, A.; Dapčević, A.; Pajić, D.; Dragović, J.; Torić, F.; Ćirković, J.; Branković, G.; Branković, Z. Change in structural, ferroelectric, and magnetic properties of bismuth ferrite induced by doping with gadolinium. *Ceram. Int.* **2019**, *45*, 19158–19165. [CrossRef]

73. Radojković, A.; Luković Golić, D.; Ćirković, J.; Marinković Stanojević, Z.; Pajić, D.; Torić, F.; Dapčević, A.; Vulić, P.; Branković, Z.; Branković, G. Tuning of $BiFeO_3$ multiferroic properties by light doping with Nb. *Ceram. Int.* **2018**, *44*, 16739–16744. [CrossRef]
74. Suchomski, C.; Reitz, C.; Pajic, D.; Jaglicic, Z.; Djerdj, I.; Brezesinski, T. Large-Pore Mesoporous $Ho_3Fe_5O_{12}$ Thin Films with a Strong Room-Temperature Perpendicular Magnetic Anisotropy by Sol-Gel Processing. *Chem. Mater.* **2014**, *26*, 2337–2343. [CrossRef]
75. Englich, J.; Lütgemeier, H.; Pieper, M.W.; Jülich, K.F.A.; Germany, W.; Nekvasil, V.; Novák, P. Umbrella structure in Ho substituted YIG–NMR study. *Solid State Commun.* **1985**, *56*, 825–828. [CrossRef]

THE JOURNAL OF PHYSICAL CHEMISTRY B
A JOURNAL OF THE AMERICAN CHEMICAL SOCIETY

pubs.acs.org/JPCB

Article

Water-Mediated Interactions Enhance Alkaline Earth Cation Chelation in Neighboring Cavities of a Cytosine Quartet in the DNA Quadruplex

Branislav Milovanović, Milena Petković, Igor Popov, and Mihajlo Etinski*

Cite This: *J. Phys. Chem. B* 2021, 125, 11996–12005

Read Online

ACCESS | Metrics & More | Article Recommendations | Supporting Information

ABSTRACT: Larger Coulombic repulsion between divalent cations compared to the monovalent counterparts dictates the cation−cation distance in the central ion channel of quadruplexes. In this work, density functional theory and a continuum solvation model were employed to study bond energies of alkaline earth cations in adjacent cavities of the central ion channel. Four crystallized tetramolecular quadruplexes with various geometric constraints and structural motifs available in the Protein Data Bank were examined in order to understand how the cation binding affinities could be increased in aqueous solution. A cytosine quartet sandwiched between guanine quartets has a larger bond energy of the second alkaline earth cation in comparison with guanine and uracil quartets. Four highly conserved hydrogen-bonded water molecules in the center of the cytosine quartet are responsible for a higher electrostatic interaction with the cations in comparison with guanines' carbonyl groups. The reported findings are valuable for the design of synthetic quadruplexes templated with divalent cations for optoelectronic applications.

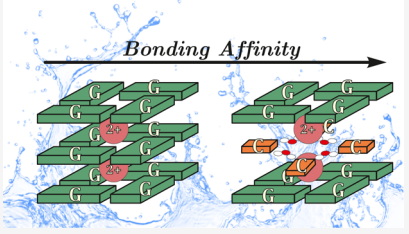

INTRODUCTION

The stability of nucleic acids' structures is determined by nucleobase-specific interactions that allow strands to adopt energetically favorable forms. A larger diversity of these nanostructures is achieved by noncanonical nucleobase pairing.[1] Particularly intriguing is the guanine quadruplex due to its stability under physiological conditions. It consists of stacked guanine quartets, in which guanine units are connected by four hydrogen bonds formed between complementary Watson−Crick and Hoogsteen edges of neighboring units. Unlike in other nucleic acid structures, guanines in quadruplexes interact directly with monovalent and divalent cations via inner sphere coordination in order to increase the stability of the overall structure.[2] While monovalent cations occupy all quadruplex vacancies in the central ion channel, divalent cations tend to avoid adjacent vacancies.[3−7]

The interactions between chelated cations and guanines provides an opportunity to modulate the electronic properties of quadruplexes by different cation types.[8−13] This can be achieved by using cations with different ionic radii and charges. Larger mobility of smaller than larger cations is favorable for trapping relaxed charge transfer excitons.[10] These collective excitations are also stabilized to a greater degree by divalent than monovalent cations.[13] Electric fields created by several divalent cations positioned in consecutive vacancies will likely stabilize charge transfer excitations below bright states. Considering the importance of these excited electronic states for nanotechnology applications, it is desirable to understand how divalent cations in the central ion channel might be stabilized with the same spacing as monovalent cations.

Several theoretical studies have addressed the stabilizing interactions between monovalent cations and a quadruplex scaffold.[2,14−18] Energy decomposition analysis (EDA) revealed that the interaction between an alkali cation and guanines in a two-layer quadruplex is overwhelmingly electrostatic.[2] The orbital interaction contribution is found to be twice smaller. This energy term mainly results from the donation of electron density from the highest occupied orbitals of guanines' oxygen atoms to the lowest unoccupied orbitals of the alkali cation. By adding the second and the third alkali cation in quadruplexes with one and two cations, respectively, Nieuwland et al. showed that electrostatic energies of the added cations decrease as a result of the electrostatic repulsion between the cations, whereas the orbital interaction does not change.[18] In the case of two alkali cations, the electrostatic interaction between the second cation and a quadruplex scaffold chelated with the first cation is slightly larger than the orbital interaction of the second cation. By adding the third alkali cation, the orbital interaction energy of this cation becomes larger than its electrostatic energy. Destabilizing the electrostatic repulsion between the hosted alkali cations is counterbalanced by electronic screening and solvation effects so that the magnitude

Received: June 24, 2021
Revised: September 30, 2021
Published: October 25, 2021

https://doi.org/10.1021/acs.jpcb.1c05598
J. Phys. Chem. B 2021, 125, 11996−12005

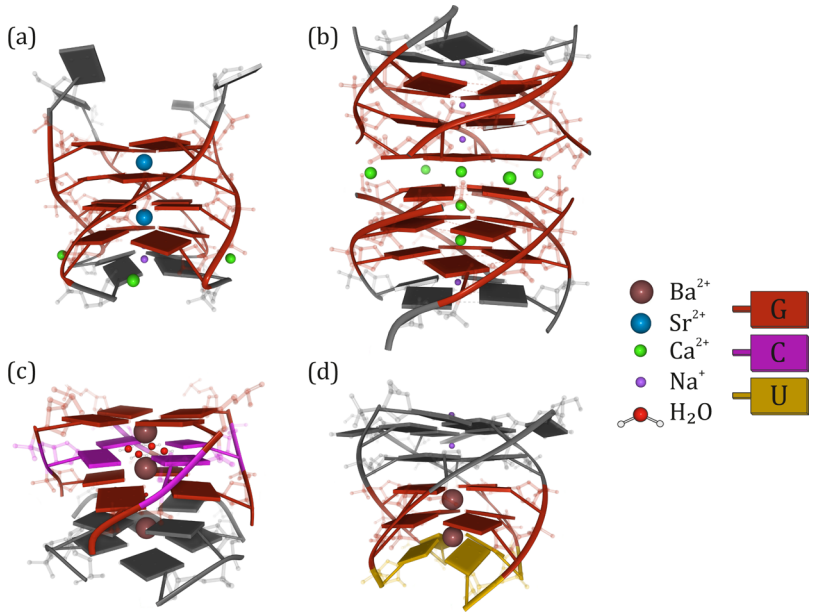

Figure 1. Crystal structures of quadruplexes coordinated with at least two alkaline earth cations: (a) $r(UG_4U)_4$,[3] (b) two end-to-end stacked $d(TG_4T)_4$,[19] (c) $d(GCGTGG)_4$[20] (thymines do not form a quartet and are not shown), and (d) $r(GAGGU)_4$.[21] The coloring scheme is adjusted to highlight the reduced computational model used in this work. Nucleobases that are not considered in the model are colored in gray.

of the energy needed for binding consecutive alkali cations remains unaltered.

Alkaline earth cations have a two times larger charge than alkali cations, and if they have been coordinated with a similar spacing along the central axis of a quadruplex as alkali cations, they experience a 4 times larger electrostatic repulsion between them. This results in a high energy penalty for alkaline earth cations binding between consecutive guanine quartets. Solution NMR faces difficulties to probe the direct response of alkaline earth cations since their spectral signatures originate from exotic nuclei such as ^{43}Ca, ^{87}Sr, and ^{137}Ba.[22,23] Due to this, the existence of two alkaline earth cations positioned in neighboring vacancies of the central ion channel has not been experimentally observed in aqueous solutions. Inspection of the Protein Data Bank (PDB) reveals three crystal quadruplex structures with at least two alkaline earth cations coordinated between successive guanine or other nucleobase quartets[19−21] (Figure 1). Two of them contain a pair of Ba^{2+} cations positioned between three consecutive layers, one of which is a pyrimidine nucleobase quartet. In the $r(GAGGU)_4$ quadruplex, a tandem of guanine quartets interacts with one Ba^{2+} cation, whereas the second Ba^{2+} cation is positioned between the guanine and uracil quartets.[21] Since the uracil quartet is at the 3′-terminus of the quadruplex, it exhibits out-of-plane deformation, which enables approximately 1 Å longer distance between the Ba^{2+} cations than those found between other cations in the quadruplex. The second structure with two Ba^{2+} cations is found in a tetramolecular quadruplex formed from a decameric oligonucleotide $d(CCA^{CNV}KGCGTGG)$ (^{CNV}K is 3-cyanovinylcarbazole) sequence.[20] The quadruplex contains a cytosine quartet, which is stabilized by four highly conserved water molecules positioned in the middle of the quartet. The oxygens of the water molecules are in the same location as the O6 of the guanines in a typical guanine quartet. In this case, a large energy penalty due to electrostatic repulsion between Ba^{2+} cations is avoided by water coordination of the cations. The oxygen atoms of four hydrogen-bonded water molecules in the interior of the cytosine quartet have enhanced electron densities relative to those in the guanine's oxygen atom, which facilitates screening of Ba^{2+} cations.[20] Lee et al. crystallized a tetramolecular $d(TG_4T)_4$ quadruplex in a mixed Na^+ and Ca^{2+} environment and found an arrangement involving both cations in the central channel.[19] The crystallographic unit contains two end-to-end stacked quadruplexes asymmetrically populated by Na^+ and Ca^{2+} cations. One quadruplex is templated with three Na^+ cations, whereas the other one has one Na^+ and two Ca^{2+} cations. There is also one Ca^{2+} cation coordinated at the interface between the quadruplexes.

The three crystallized quadruplexes[19−21] provide us with the opportunity to examine electronic energies of chelated cations for structures in aqueous solutions. As reference systems, we also study tetramolecular quadruplexes coordinated with Sr^{2+} cations between every other layer and one coordinated with Na^+ cations. Our goal is to provide insights into the importance of structural motifs and geometric constraints for enhancing chelation affinity of alkaline earth cations in neighboring vacancies. To this end, we performed EDA of the interaction energy for binding the first and the second cation and examined many-body and solvation effects in model quadruplexes consisting of three and four layers. We also determined the energy needed to exchange two Na^+ by two Ca^{2+} cations in tetramolecular quadruplexes with GGG and GCG sequences. The present results offer a comparison between the binding energies of alkaline earth cations in adjacent positions with those in systems with vacant cavities and energies of alkali cations. The computations reveal that the cytosine quartet stacked between guanine quartets has a much higher propensity for binding alkaline earth cations than the pure guanine quadruplex. This finding reveals that the design of synthetic tetramolecular quadruplexes with divalent cations in adjacent chelating sites in aqueous solutions benefits from selection of the GCG sequence motif.

https://doi.org/10.1021/acs.jpcb.1c05598
J. Phys. Chem. B 2021, 125, 11996−12005

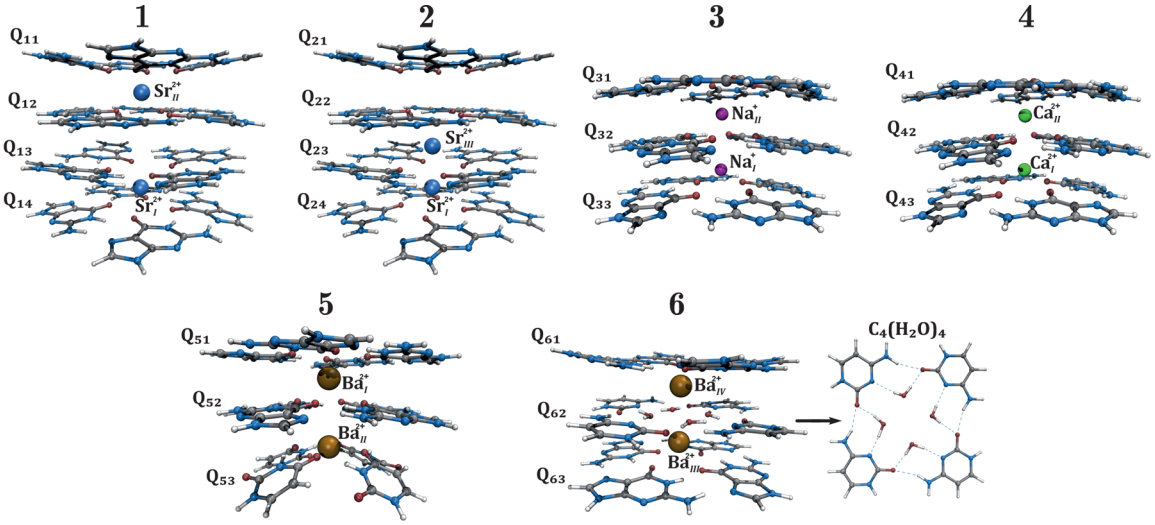

Figure 2. Geometries of quadruplexes and labels used in the present work.

METHODS

In order to make this study computationally feasible, we used a reduced quadruplex model in which the sugar−phosphate backbone is neglected. Previous computational studies showed that the presence of the backbone does not considerably alter alkali cation binding energies.[2,18] The geometries of the six examined structures are given in Figure 2, whereas cation labels and PDB IDs of quadruplexes from which atomic positions were extracted are collected in Table 1. Quadruplex **2** was created from **1** by shifting the Sr_I^{2+} cation to the midway position between the Sr_I^{2+} and Sr_{II}^{2+} cations (the new cation label is Sr_{III}^{2+}). Crystallographic positions of waters' hydrogen atoms are not given for structure **6**. Their positions were determined by performing partial optimization at the level of theory used for electronic structure calculations in this work.

Table 1. Structures, Cation Labels, and PDB IDs of Quadruplexes from Which Atomic Positions Were Extracted

structure	cation labels	PDB ID
1	G_4-Sr_I^{2+}-G_4-G_4-Sr_{II}^{2+}-G_4	1J8G[3]
2	G_4-Sr_I^{2+}-G_4-Sr_{III}^{2+}-G_4-G_4	1J8G[3]
3	G_4-Na_I^{+}-G_4-Na_{II}^{+}-G_4	2GW0[19]
4	G_4-Ca_I^{2+}-G_4-Ca_{II}^{2+}-G_4	2GW0[19]
5	G_4-Ba_I^{2+}-G_4-Ba_{II}^{2+}-U_4	1J6S[21]
6	G_4-Ba_{III}^{2+}-$C_4(H_2O)_4$-Ba_{IV}^{2+}-G_4	4U92[20]

All calculations were performed with the Turbomole program package.[24] We used density functional theory with the B-LYP functional[25,26] and Grimmes's D3 correction[27] for calculations of electronic energies. Kohn−Sham molecular orbitals were expended in the def2-TZVPP basis set.[28] Multipole accelerated resolution-of-identity was used to accelerate the calculation of the electronic Coulomb interaction. This combination of density functional and valence triple-zeta polarization basis set has been used often to study guanine self-assemblies.[2,29−32] Atomic charges were computed by using natural population analysis.[33] Solvent effects were taken into account by employing the continuum solvation model (COSMO)[34,35] with the dielectric constant of water (ϵ = 78.5). The cation radii used in the COSMO model were recalculated to reproduce experimental solvation energies of the cations.[36] The recalculated values were 1.8161, 1.9819, 2.1890, and 1.8685 Å, for Ca^{2+}, Sr^{2+}, Ba^{2+}, and Na^{+}, respectively.

The bond energy ΔE_{bond} represents the energy needed to chelate a cation to a quadruplex in aqueous solution. It was computed using structures depicted in Figure 3. In order to understand the contribution of various stabilizing and destabilizing energy terms, we decomposed the bond energy into

$$\Delta E_{bond} = \Delta E_{desolv} + \Delta E_{int} + \Delta E_{solv} \quad (1)$$

ΔE_{desolv}, ΔE_{solv}, and ΔE_{int} are the energies of desolvation, solvation, and interaction energy, respectively (see Figure 3). The desolvation and solvation energies are related to energy differences between the gas phase and aqueous solution energies. Note that binding a cation to a quadruplex results in deformation of quadruplex's geometry. The related preparation energy is relatively small (<10 kcal/mol)[18] and not accounted for in bond energies since we employed the experimental geometries. One- and two-cation interaction energies, ΔE_{int}, are decomposed by using EDA.[37] This method decomposes the electronic energy into electrostatic (ΔE_{ele}), exchange (ΔE_{ex}), repulsion (ΔE_{rep}), polarization and orbital interaction (ΔE_{pol}), and dispersion (sum of correlation and D3 dispersion energies) (ΔE_{disp}) terms. The energy needed to exchange two Na^{+} by two Ca^{2+} cations was calculated by the thermodynamic cycle shown in Figure 3. It contains the desolvation ΔE_{desolv}, solvation ΔE_{solv}, and preparation energy ΔE_{prep}, as well as two-cation interaction energies $\Delta E_{int,2Na^+}$ and $\Delta E_{int,2Ca^{2+}}$ with Na^{+} and Ca^{2+} cations, respectively.

Let us summarize approximations employed in this work. In the first place, we used molecular geometries determined for quadruplexes in a crystal environment. These structures are slightly different from those in the aqueous solution. This choice of geometries was dictated by difficulties related to geometry optimization of quadruplexes with more than two stacked quartets. Bond energies are determined in fixed molecular geometries without geometry relaxation upon cation chelation. The sugar−phosphate backbone is not taken into account, and solvent effects were modeled by a continuum model. Since cation radii are chosen to reproduce experimental free hydration energies, the computed bond energies also

https://doi.org/10.1021/acs.jpcb.1c05598
J. Phys. Chem. B 2021, 125, 11996−12005

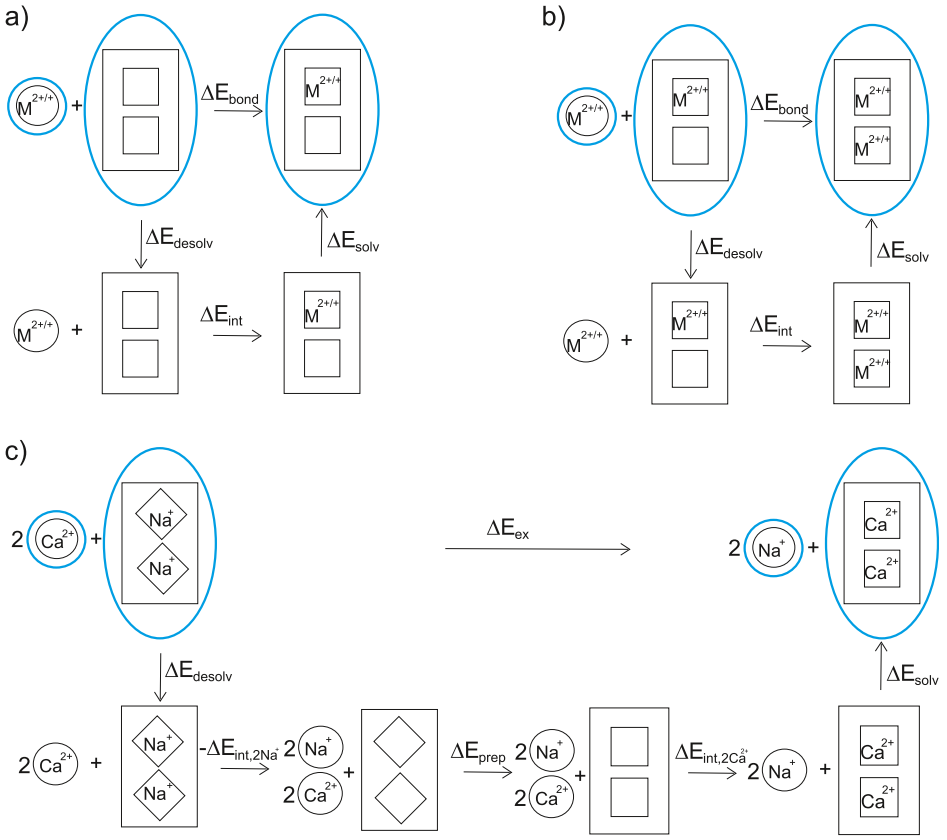

Figure 3. Thermodynamic cycles for the calculation of the bond energy [for the first (a) and the second (b) cation] and the energy needed to exchange two Na^+ by two Ca^{2+} cations (c). The fragments encircled by blue lines were computed in aqueous solutions.

Table 2. Partitioning of the Bond Energy (in kcal/mol)

quadruplex	1		2		3	
cation	Sr_I^{2+}	Sr_{II}^{2+}	Sr_I^{2+}	Sr_{III}^{2+}	Na_I^+	Na_{II}^+
E_{desolv}	456.9	516.1	456.9	516.1	191.5	197.9
E_{solv}	−186.2	−382.5	−186.2	−405.6	−110.6	−159.2
$E_{desolv} + E_{solv}$	270.7	133.5	270.7	110.5	80.9	38.4
E_{int}	−388.2	−234.9	−388.2	−129.1	−157.6	−111.8
E_{bond}	−117.4	−101.4	−117.4	−18.6	−76.7	−73.2
quadruplex	4		5		6	
cation	Ca_I^{2+}	Ca_{II}^{2+}	Ba_I^{2+}	Ba_{II}^{2+}	Ba_{III}^{2+}	Ba_{IV}^{2+}
E_{desolv}	464.9	530.7	395.1	458.7	403.3	467.0
E_{solv}	−171.0	−395.4	−159.9	−407.4	−168.2	−386.6
$E_{desolv} + E_{solv}$	293.9	135.3	235.2	51.3	235.1	80.3
E_{int}	−368.4	−158.9	−327.6	−28.9	−392.5	−167.4
E_{bond}	−74.5	−23.7	−92.4	22.4	−157.4	−87.0

implicitly take into account thermal effects of cation hydration. Nevertheless, the bond energies are not free energies since the quadruplex's scaffold thermal effects are not included. Free energies might be determined by employing molecular dynamics with polarizable force fields or approximate theories such as quasi-chemical theory.[38,39] In order to estimate the importance of entropy for binding affinities, we optimized guanine octets chelated with Na^+ and Ca^{2+} cations. Although these systems have 381 normal modes, the zero-point vibrational energy and entropy differences were found to be only 983 cm^{-1} and 4.3 kcal/mol (at 298 K), respectively, at the B-LYP-D3/def2-SVP level. This implies that quadruplexes are stiff systems toward cation exchange and that the cation−nucleobase interaction energy dominates the relative free energy difference.[40]

RESULTS AND DISCUSSION

Bond Energies. The sum of desolvation and solvation energies of a quadruplex scaffold and cations in water is positive for binding one and two cations. Since water is a more polarizable environment than crystals, cation binding in the aqueous solution will be weaker than in the solid state. The Gibbs energies of hydration for Ca^{2+}, Sr^{2+}, and Ba^{2+} cations amount to −1505, −1380, and −1250 kcal/mol,[36] respectively. These energies are much higher than those for Na^+ (−365 kcal/mol), K^+ (−295 kcal/mol), and Rb^+ (−275 kcal/mol).[36]

https://doi.org/10.1021/acs.jpcb.1c05598
J. Phys. Chem. B 2021, 125, 11996−12005

At first sight, it appears that the bond energies of alkaline earth cations are smaller in comparison with alkali cation energies. However, alkaline earth cations also interact more strongly with the quadruplex scaffold than alkali cations, which compensates the solvation effects.

Bond energies and their partition into desolvation, interaction, and solvation energies are given in Table 2. Comparison between bond energies of cations from different quadruplexes is only possible if the quadruplexes have the same chemical makeup or the cations are of the same type or have similar radii. The bond energies for chelation of the first cation in every quadruplex were strongly negative, irrespective of the cation type. By comparing bond energies of the Ca_I^{2+}, Sr_I^{2+} and Ba_I^{2+} cations chelated between guanine quartets, we found that the most strongly bound cation was Sr_I^{2+}, followed by Ba_I^{2+} and Ca_I^{2+}. This stabilization ordering is in accordance with experimental findings of Venczel and Sen,[41] although we examined both RNA and DNA quadruplexes. Ba_I^{2+} had the lowest sum of solvation and desolvation energies, but its interaction energy was considerably smaller than that of Sr_I^{2+}. Chelation of Na_I^{+} was 2.2 kcal/mol stronger than that of Ca_I^{2+} with a similar ionic radius. This unexpectedly small energy difference indicates that an increase in Ca^{2+} concentration may lead to the exchange of one Na^+ by the Ca^{2+} cation in aqueous solutions. Yet, the difference in entropic terms computed from the optimized geometries (4.3 kcal/mol at 298 K) additionally stabilizes chelation of Na^+ over the Ca^{2+} cation.

The bond energy of the Ba^{2+} cation between guanine and cytosine quartets is much higher than that between two guanine quartets. The sum of solvation and desolvation energies of the Ba_{III}^{2+} cation is equal to that of the Ba_I^{2+} cation, implying that these contributions are robust against the influence of geometric constraints and different structural motif contributions for binding of the first cation. On the other hand, we find that the solvation effects for chelating the second cation were approximately 30 kcal/mol more favorable in quadruplex **5** than in **6** due to the larger cation−cation distance.

The energy needed for binding the Na_{II}^{+} cation was almost equal to the energy of the Na_I^{+}, as has been found previously.[18] A somewhat larger energy difference is noticed for the Sr_I^{2+} and Sr_{II}^{2+} cations, but still the bond energy of Sr_{II}^{2+} was sufficiently negative to allow strong chelation of Sr_{II}^{2+} two cavities away from already occupied cavity. If the second Sr^{2+} cation is chelated in the adjacent vacancy, its bond energy is −19 kcal/mol. This value was 83 kcal/mol higher than the energy needed for chelation in every other cavity. Since electrostatic interaction has a long-range character, the third consecutive Sr^{2+} cation and every following cation would experience even larger Coulomb repulsion than the second one. Their energies would decrease and eventually become positive, which prevents chelation of the Sr^{2+} cation in the adjacent cavities of the guanine quadruplex. Therefore, alkaline earth cations prefer alternating occupation of cavities of the guanine quadruplex in the aqueous solution.

Similar to the binding of Sr^{2+} to quadruplex **2**, the bond energy of the second Ca^{2+} cation was much lower than that of the first cation. It amounted to −24 kcal/mol, which is 49 kcal/mol smaller than that for the second Na^+ cation. Hence, although chelation of two alkaline earth cations in neighboring quadruplexes' binding sites is energetically possible, their small bond energies indicate that these quadruplexes are not as stable as those templated with monovalent cations. In order to further reveal the difference in binding affinities of Na^+ and Ca^{2+} cations, we computed the energy needed to exchange two Na^+ cations in quadruplex **3** by two Ca^{2+} cations in quadruplex **4**. The exchange energy amounted to 49 kcal/mol, that is, the cation exchange was not spontaneous in the aqueous solution. The desolvation and solvation contributions were 878.6 and −570.1 kcal/mol, respectively, and their sum was 308.5 kcal/mol. The large discrepancy between the absolute values of these terms is due to the fact that water hydrates double-positive charge of the Ca^{2+} cation more strongly than a single charge of the Na^+ cation. The interaction energies $-E_{int,2Na^+}$ and $E_{int,2Ca^+}$ are 269.5 and −527.5 kcal/mol, respectively. Their sum (−258 kcal/mol) is negative since Ca^{2+} cations are more tightly bound to the quadruplex than Na^+ cations. The preparation energy term was very small (−1.5 kcal/mol), reflecting similar quadruplex scaffolds for structures with Ca^{2+} and Na^+ cations. Overall, the cation exchange in the aqueous solution was not spontaneous even when the entropic contribution would be taken into account and was dominated by the solvation penalty. In a crystallizing solution, high ion concentrations decrease the dielectric constant, which makes Ca^{2+} cations easier to desolvate than in water. As a result, there are three Ca^{2+} cations in the adjacent vacancies of the crystallized stacked guanine quadruplex.[19]

The bond energy of the second Ba^{2+} cation in quadruplex **5** was positive due to small interaction energy, implying that the constrained geometry of this quadruplex is only stable under crowding conditions in the crystal and not in the aqueous solution. The cytosine quartet sandwiched between two guanine quartets exhibits much stronger affinity for binding the second cation than the guanine quartet stacks. The bond energy of the Ba_{IV}^{2+} cation is equal to −87 kcal/mol, which was only 5 kcal/mol lower than the energy needed for binding the first Ba^{2+} cation in the guanine quadruplex.

We can indirectly compare the bond energy of the Ba_{IV}^{2+} cation with those of alkali cations. In the first place, Ba^{2+} and K^+ cations have radii which only differ by 0.02 Å. In addition, the bond energies of Na^+ and K^+ cations are up to approximately 1 kcal/mol.[2] Taking into account that the bond energy of the Ba_{IV}^{2+} cation is 14 kcal/mol higher than the energy of the second Na^+ cation in guanine quadruplex **3**, we conclude that it is plausible that the Ba_{IV}^{2+} cation is more tightly bound than alkali cations in guanine quadruplexes. We also suggest that two Ba^{2+} cations are sufficiently strongly coordinated in the tetramolecular quadruplex segment with the GCG sequence being stable in the aqueous solution.

Affinity of the $(GCG)_4$ Quadruplex toward Na^+ and Ca^{2+} Cations. The unusually high affinity of the cytosine quartet sandwiched between guanine quartets for Ba^{2+} cations might indicate that it will also hold true for other divalent cations. Yet, Liu et al. showed that this motif in a solution of Pb^{2+} and several monovalent cations bound only one Pb^{2+} cation—the cation in the adjacent vacancy was found to be Na^+.[42] Since two chelation sites of the $(GCG)_4$ quadruplex have distinct coordination geometries (bipyramidal antiprismatic and nearly square prismatic), Liu et al. argued that Pb^{2+} coordination might depend on the quartet orientation.[42] This observation motivated us to examine bond energies of Na^+ and Ca^{2+} cations in the $(GCG)_4$ quadruplex. We computed these energies at the geometries of Ba^{2+} cations in quadruplex **6**. This procedure is justified by similar ionic radii of Na^+ and Ca^{2+} cations (0.97 and 0.99 Å) and very small preparation energy for exchange of two Na^+ by two Ca^{2+} cations in the guanine

https://doi.org/10.1021/acs.jpcb.1c05598
J. Phys. Chem. B 2021, 125, 11996−12005

quadruplex. In addition, it was found that the optimized guanine quartet chelated by Na^+ and Ca^{2+} cations also had similar oxygen-cation distances, 2.26 and 2.27 Å,[17] respectively.

Table 3 contains bond energies of Na^+ and Ca^{2+} cations chelated in vacancies of quadruplex **6** and their partitioning to desolvation, solvation, and interaction energy contributions. Both the first and second bond energy of Na^+ cations were larger than those in the guanine quadruplex. Nevertheless, the larger decrease of the bond energy from the first to the second Na^+ cation in comparison with the guanine quadruplex was found. The bond energies of Ca^{2+} cations were similar to those of the Ba^{2+} cation, implying that alkaline earth cations are likely coordinated in both vacancies of this motif. Besides bond energies, we also calculated the energy needed for exchange of two Na^+ by two Ca^{2+} cations. The desolvation and solvation energies for this process were 878.6 and −561.3 kcal/mol, respectively. These values are almost equal to those for pure guanine quadruplex, that is, solvation and desolvation costs are independent of structural motifs. On the other hand, the interaction energies $-E_{int,2Na^+}$ and $E_{int,2Ca^+}$ were 330.6 and −671.4 kcal/mol, respectively, giving an exchange energy of −23.5 kcal/mol. Thus, the water-stabilized cytosine quartet stacked between guanine quartets acts as a selective ionophore for chelation of alkaline earth over alkali cations in the adjacent positions. This conclusion is based on the electronic energy contributions to the free energy.

Table 3. Partitioning of the Bond Energies of Na^+ and Ca^{2+} Cations Chelated in Vacancies of Quadruplex 6 (in kcal/mol)[a]

cation	Na_{III}^+	Na_{IV}^+	Ca_{III}^{2+}	Ca_{IV}^{2+}
E_{desolv}	191.8	200.7	464.2	527.8
E_{solv}	−113.4	−159.2	−168.1	−386.6
$E_{desolv} + E_{solv}$	78.4	41.6	296.0	141.3
E_{int}	−190.5	−140.1	−442.4	−229.0
E_{bond}	−112.0	−98.6	−146.4	−87.7

[a]The cations Na_{III}^+/Ca_{III}^{2+} and Na_{IV}^+/Ca_{IV}^{2+} are positioned in the place of the cations Ba_{III}^{2+} and Ba_{IV}^{2+}, respectively.

Structural Properties. The size of a central cavity between the quadruplex layers overwhelmingly influences the interaction between a cation and quadruplex scaffold. This property is reflected by oxygen-cation distances. Besides, coordinating oxygen atoms in quadruplexes with pyrimidine bases might have different charges than those of guanine's oxygens. Zhang et al. noticed that cytosine's N3 and O2 atoms form hydrogen bonds with water molecules in quadruplex **6**, which likely results in a rise of the electron density at the water oxygen's lone pairs.[20] Here, we analyze geometric and structural properties which determine the interaction between cations and ligands.

Table 4 shows the average oxygen-cation distances for each layer, their average values for both layers, and their differences between the layers. It also contains cation−cation distances. Quantum chemical calculations showed that an occupied cavity tends to adapt its size when a cation is hosted in the adjacent position.[18] The most frequent oxygen-cation distance was in the range 2.7−2.8 Å. This observation also includes waters' oxygens in the cytosine quartet. Deviations form these lengths indicate that there is distortion in the quadruplex scaffold. Sr^{2+} cations in quadruplex **1** with four layers were found to be symmetrically positioned between the layers. Guanine carbonyl groups were distorted toward the cations, which resulted in average oxygen-cation distances equal to 2.6 Å. In quadruplex **2**, the Sr_{III}^{2+} cation was inserted in the vacancy next to the one of the Sr_I^{2+} cation, but its oxygen-cation distances were not relaxed. The obtained average O6−Sr_{III}^{2+} length was 0.3 Å longer than the relaxed value. Quadruplexes **3** and **4** exhibited asymmetric positions of cations relative to the upper and lower quartets. This was particularly pronounced for Ca_I^{2+} and Na_{II}^+ cations. The asymmetry might originate from relatively small radii of these cations, which allow flexibility in their positions within the cavity. One consequence of this asymmetry was that the average distance between a cation and oxygens of the closer quartet was 2.5 Å. Note that average distances between oxygens of both quartets and Ca^{2+} cations were 2.8 Å, as found in other quadruplexes. In quadruplex **5**, the Ba_{II}^{2+} cation was much closer to the uracil than to the guanine quartet. The shortest and longest distance between the cations in the adjacent cavities was found in quadruplexes **2** and **5**, respectively. The distance between two Ba^{2+} cations in quadruplex **6** was 0.5 Å shorter than in quadruplex **5**.

Figure 4 shows the average oxygens' charges for each quartet. Guanine's oxygen charges were in the range from −0.57*e* to −0.76*e*. It is clearly noticeable that there was a redistribution of charges within different quartets. In the case of quadruplexes **3** and **4**, the oxygens of the central layer showed decreased electron density, whereas in the case of quadruplex **1**, every other quartet had the same average charge. Oxygens of the uracil quartet did not exhibit significantly different values than on average guanines. On the other hand, water oxygens in the cytosine quartet had in average −1.09*e*. This highly negative charge enables strong electrostatic interaction between the cations and water molecules.

Energy Decomposition Analysis. The interaction between cations and biological molecules is characterized by

Table 4. Average Distances (in Å) between the Oxygen Atoms of Guanine Quartets (Water Molecules in Structure 6) and Cations in the Quadruplexes[a]

quadruplex	1		2	3		4		5		6	
cation	Sr_I^{2+}	Sr_{II}^{2+}	Sr_{III}^{2+}	Ca_I^{2+}	Ca_{II}^{2+}	Na_I^+	Na_{II}^+	Ba_I^{2+}	Ba_{II}^{2+}	Ba_{III}^{2+}	Ba_{IV}^{2+}
lower quartet	2.61	2.60	2.90	2.53	2.68	2.75	3.10	2.74	2.35	2.66	2.82
upper quartet	2.61	2.60	2.90	3.13	2.93	2.54	2.48	2.77	3.64	2.76	2.68
average	2.61	2.60	2.90	2.83	2.80	2.64	2.79	2.76	3.00	2.71	2.75
difference	0.00	0.00	0.00	0.60	0.25	−0.21	−0.62	0.03	1.29	0.10	−0.14
d_{CC}	6.37		3.19[b]	3.59		3.49		4.39		3.86	

[a]The differences and averages are given between the values for upper and lower quartets. d_{CC} is the distance (in Å) between the cations. [b]Distance between the Sr_I^{2+} and Sr_{III}^{2+} cations.

https://doi.org/10.1021/acs.jpcb.1c05598
J. Phys. Chem. B 2021, 125, 11996−12005

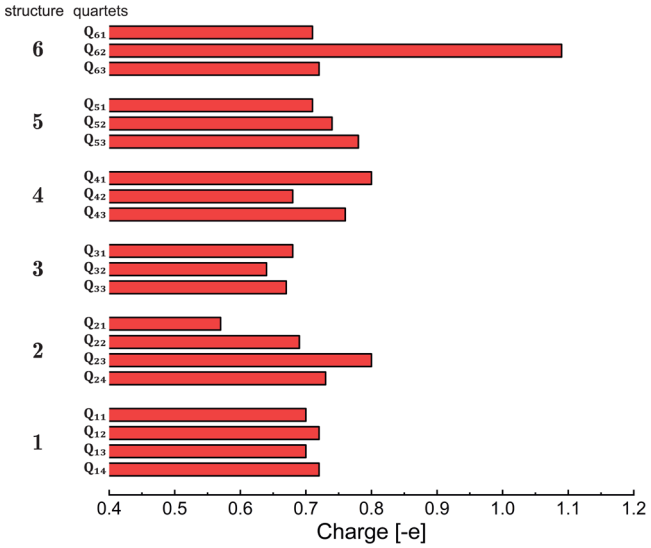

Figure 4. Average oxygens' charges for each quartet. See Figure 2 for quartet labels.

large contributions of both additive and nonadditive (many-body) polarization. Recently, Jing et al. argued that the selectivity of calcium-binding proteins for Ca^{2+} over the Mg^{2+} cation stems from the energetic cost due to the many-body polarization effect.[43] They revealed that many-body polarization is sensitive to the number and spatial arrangement of charged residues surrounding the cation. By employing the EDA, we examine to what extent polarization contributes to interaction between cations and the quadruplex scaffold. Besides, we provide insights into decreased stability of the Ba_{II}^{2+} cation.

Table 5 contains the EDA of interaction energies for binding one and two cations, cation−cation energies, and many-body effects (MBEs). Polarization contributed to a greater extent to the interaction energy for alkaline earth than alkali cations. In the former case, it amounted to around 50% of the one-cation interaction energy, whereas for alkali cations, this term was about 25%. The situation was even more drastic for the two-cation interaction energy: the sum of all other terms for quadruplexes **2** and **5** was positive, implying that their stability originated completely from the polarization energy. For other quadruplexes, polarization contributed to 70−90% of the interaction energy. Note that approximately one-third of the cation−cation Coulomb repulsion of alkaline earth cations in neighboring sites is reduced by many-body polarization energy. As expected, many-body contributions of other energy components were strictly or nearly pairwise additive.

The atomic coordinates of the quadruplex scaffold around the Sr_{III}^{2+} cation were not relaxed, so that the interaction energy of this cation was 27 kcal/mol weaker than the one of the Sr_{I}^{2+} cation. Note that interaction energies of adjacent cations in other quadruplexes can vary by up to 10 kcal/mol. Hence, we predicted that the interaction energy of the Sr_{III}^{2+} cation is approximately 20 kcal/mol underestimated. Nevertheless, this energy value does not modify the conclusions about Sr^{2+} cation chelation in the adjacent cavities of guanine quadruplexes.

Two Ba^{2+} cations in quadruplex **5** were separated by an around 1 Å larger distance than those found for other cations in the $r(GAGGU)_4$ quadruplex.[21] This resulted in 90 kcal/mol lower Coulomb repulsion between the cations. On the other hand, the Ba_{II}^{2+} is coordinated by a distorted uracil quartet whose oxygen atoms are closer to the Ba_{II}^{2+} cation than those of guanines. As a consequence of these close oxygen-cation distances, the Ba_{II}^{2+} cation experienced 150 kcal/mol larger repulsion energy than the Ba_{I}^{2+} cation. Taking into account other energy components, it was 100 kcal/mol less stable than the Ba_{I}^{2+} cation. Hence, all energy gain from longer cation−cation distance was compensated by the repulsion energy due to proximity of the uracil quartet.

Table 5. Partitioning of Cation−Cation, One- and Two-Cation Interaction Energies, and MBE (in kcal/mol)

	1-Sr_I^{2+}	**1**-Sr_{II}^{2+}	Sr_I^{2+}-Sr_{II}^{2+}	**1**-Sr_I^{2+}-Sr_{II}^{2+}	MBE
ΔE_{int}	−388.2	−384.6	205.4	−623.1	−55.7
ΔE_{ele}	−252.6	−248.8	208.5	−293.0	0.0
ΔE_{ex}	−4.3	−4.1	0.0	−8.4	0.0
ΔE_{rep}	95.2	92.6	0.0	188.3	0.5
ΔE_{pol}	−185.8	−184.1	−0.7	−429.1	−58.5
ΔE_{disp}	−40.6	−40.2	−2.4	−80.9	2.3
	2-Sr_I^{2+}	**2**-Sr_{III}^{2+}	Sr_I^{2+}-Sr_{III}^{2+}	**2**-Sr_I^{2+}-Sr_{III}^{2+}	MBE
ΔE_{int}	−388.2	−361.1	405.6	−517.3	−173.6
ΔE_{ele}	−252.6	−207.4	416.4	−43.7	0.0
ΔE_{ex}	−4.3	2.0	0.5	−2.0	−0.2
ΔE_{rep}	95.2	34.3	1.1	133.5	3.0
ΔE_{pol}	−185.8	−154.9	−11.1	−526.9	−175.1
ΔE_{disp}	−40.6	−35.0	−1.2	−78.1	1.2
	3-Na_I^{+}	**3**-Na_{II}^{+}	Na_I^{+}-Na_{II}^{+}	**3**-Na_I^{+}-Na_{II}^{+}	MBE
ΔE_{int}	−157.6	−167.4	94.1	−269.5	−38.5
ΔE_{ele}	−111.2	−118.7	95.1	−134.8	0.0
ΔE_{ex}	0.6	1.2	0.0	1.7	0.0
ΔE_{rep}	16.7	15.2	0.0	32.2	0.3
ΔE_{pol}	−39.6	−41.5	−0.4	−120.9	−39.4
ΔE_{disp}	−24.1	−23.5	−0.7	−47.7	0.6
	4-Ca_I^{2+}	**4**-Ca_{II}^{2+}	Ca_I^{2+}-Ca_{II}^{2+}	**4**-Ca_I^{2+}-Ca_{II}^{2+}	MBE
ΔE_{int}	−368.4	−376.6	364.7	−527.4	−147.0
ΔE_{ele}	−214.5	−215.3	369.8	−60.0	0.0
ΔE_{ex}	−0.3	1.5	0.1	1.3	0.0
ΔE_{rep}	43.4	29.3	0.0	73.9	1.2
ΔE_{pol}	−166.5	−162.9	−4.0	−482.1	−148.7
ΔE_{disp}	−30.6	−29.2	−1.1	−60.4	0.5
	5-Ba_I^{2+}	**5**-Ba_{II}^{2+}	Ba_I^{2+}-Ba_{II}^{2+}	**5**-Ba_I^{2+}-Ba_{II}^{2+}	MBE
ΔE_{int}	−327.6	−224.0	296.3	−356.6	−101.2
ΔE_{ele}	−216.1	−179.7	302.7	−93.2	0.0
ΔE_{ex}	−6.7	−30.8	0.1	−37.5	−0.1
ΔE_{rep}	114.6	264.5	0.0	382.3	3.2
ΔE_{pol}	−175.5	−231.0	−5.7	−517.4	−105.2
ΔE_{disp}	−43.8	−47.1	−0.9	−90.8	0.9
	6-Ba_{III}^{2+}	**6**-Ba_{IV}^{2+}	Ba_{III}^{2+}-Ba_{IV}^{2+}	**6**-Ba_{III}^{2+}-Ba_{IV}^{2+}	MBE
ΔE_{int}	−392.5	−397.7	335.0	−559.9	−104.7
ΔE_{ele}	−286.8	−297.8	344.5	−240.1	0.0
ΔE_{ex}	−8.6	−11.6	0.5	−20.1	−0.3
ΔE_{rep}	125.2	145.0	0.4	272.3	1.6
ΔE_{pol}	−174.7	−184.0	−9.5	−475.1	−106.9
ΔE_{disp}	−47.6	−49.3	−0.9	−96.9	0.9

Structure−Property Relations. Although examined quadruplexes have various geometric parameters and are chelated with different alkaline earth cation types, the cation coordination by oxygen atoms provides structure−property relations for two most stabilizing interaction energy terms: electrostatic interaction between a cation and quadruplex scaffold and the electronic shielding of cations due to many-

https://doi.org/10.1021/acs.jpcb.1c05598
J. Phys. Chem. B 2021, 125, 11996−12005

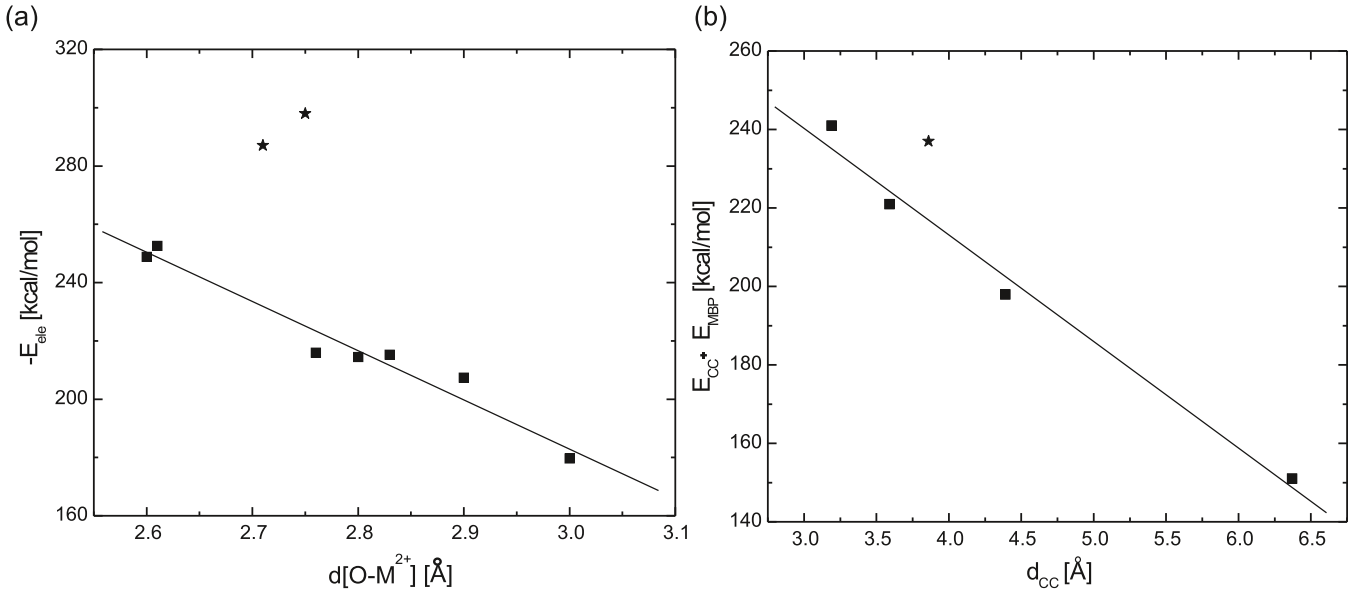

Figure 5. (a) Plot of the one-cation electrostatic energy (E_{ele}) vs the average oxygen-cation distance for both layers and (b) plot of the sum of the cation−cation Coulomb repulsion (E_{CC}) and many-body polarization energy (E_{MBP}) vs the cation−cation distance for each quadruplex. Straight lines represent linear regressions for all alkaline earth cations excluding those related to a cytosine quartet (depicted by star symbols).

body polarization. These relations hold for quadruplexes with the same chemical composition, irrespective of the chelated cations. By studying these relations, we provide insights into the excess interaction energy of the cytosine-containing quadruplex **6** relative to guanine quadruplexes.

Figure 5 shows the one-cation electrostatic energy and the sum of the cation−cation Coulomb repulsion and many-body polarization energy as functions of the average oxygen-cation and the cation−cation distance, respectively, for quadruplexes with alkaline earth cations. Both energy terms exhibited a linear correlation with the selected geometric parameters. The correlation coefficient was slightly lower for the one-cation electrostatic energy (−0.979) than for the sum of the cation−cation Coulomb repulsion and many-body polarization energy (−0.992). Note that the electrostatic energy of the Ba_{II}^{2+} cation which interacts with the uracil quartet was also nicely correlated with the energies of the other cations. The electrostatic energies of the Ba_{III}^{2+} and Ba_{IV}^{2+} cations were ≈60 kcal/mol larger than expected from the linear regression. This is a consequence of the increased water's oxygen charge relative to those of carbonyl groups. On the other hand, these cations and quadruplex **6** exhibited lower many-body polarization energy than guanine systems by 20 kcal/mol. Due to this weaker cation shielding, there is a larger decrease of the bond energy from the first to the second cation of the $(GCG)_4$ quadruplex relative to that of the guanine quadruplexes. Overall, the binding of the second Ba^{2+} cation benefits ≈40 kcal/mol from waters' oxygens in comparison with values expected from O6 oxygens.

CONCLUSIONS

The most common mode of alkaline earth cation binding to quadruplexes is the sandwich type with alternating cations and vacancies.[3−7] The goal of this study was to understand how another binding mode related to chelation in adjacent positions can be enhanced in aqueous solutions. We examined four crystallized tetramolecular quadruplexes,[19−21] two of which are associated with pyrimidine quartets. EDA of interaction energies between quadruplex scaffold and cations revealed that the binding of the second cation in a consecutive position is due to additive and many-body polarization. Solvation effects were found to be robust for different structural motifs. The common feature of all quadruplexes was that the bond energy of the second alkaline earth cation was considerably smaller than that of the first one, unlike for quadruplexes with alkali cations and alkaline earth cations in every other cavity. This indicates that each subsequent cation chelation will be even more difficult and that it is likely that only two alkaline earth cations can be bound in adjacent vacancies of hydrated quadruplexes.

Quadruplexes consisting of guanine quartets had negative energy of chelation of the second cation but these values were much smaller compared to those of alkaline cations. The energy needed to exchange two Na^{2+} by two Ca^{2+} cations is 49 kcal/mol, which shows that cation substitution is not possible in water. Could quartets composed of pyrimidine bases increase the bond energy of the second cation? Flexibility of the end-stacked uracil quartet allows elongation of the cation−cation distance by approximately 1 Å in the crystallized quadruplex. Yet, the reduced Coulomb repulsion between the cations is compensated by the large repulsion energy between uracils' oxygens and the chelated cation. Larger cation desolvation energies in water than in the crystallizing environment is responsible for positive bond energy of the cation coordinated by the uracil quartet. On the other hand, the bond energy of the second cation in the vacancy created by cytosine and guanine quartets is sufficiently large to be stable in aqueous solutions. The energy increase originates from water-mediated contacts between the cations. The increased charge of water's relative to guanine's oxygen results in stronger electrostatic attraction with cations, whereas electronic shielding is somewhat reduced. We tentatively propose that the cytosine quartet stacked between two guanine quartets has higher affinity for alkaline earth than alkali cations in water. This suggests that different structural motifs might be used to

https://doi.org/10.1021/acs.jpcb.1c05598
J. Phys. Chem. B 2021, 125, 11996−12005

synthesize quadruplexes with an unusual cation bonding mode for nanotechnology applications.

■ ASSOCIATED CONTENT

Supporting Information

The Supporting Information is available free of charge at https://pubs.acs.org/doi/10.1021/acs.jpcb.1c05598.

Cartesian coordinates of all examined systems (PDF)

■ AUTHOR INFORMATION

Corresponding Author

Mihajlo Etinski − *Faculty of Physical Chemistry, University of Belgrade, 11000 Belgrade, Serbia;* orcid.org/0000-0003-0342-7045; Phone: +381113336632; Email: etinski@ffh.bg.ac.rs

Authors

Branislav Milovanović − *Faculty of Physical Chemistry, University of Belgrade, 11000 Belgrade, Serbia*

Milena Petković − *Faculty of Physical Chemistry, University of Belgrade, 11000 Belgrade, Serbia;* orcid.org/0000-0001-6180-1854

Igor Popov − *Institute for Multidisciplinary Research, University of Belgrade, 11030 Belgrade, Serbia; Institut of Physics, University of Belgrade, 11080 Belgrade, Serbia;* orcid.org/0000-0002-2030-3530

Complete contact information is available at: https://pubs.acs.org/10.1021/acs.jpcb.1c05598

Notes

The authors declare no competing financial interest.

■ ACKNOWLEDGMENTS

The research leading to these results has been cofunded by the European Commission under the H2020 Research Infrastructures contract no. 675121 (project VI-SEEM). B.M., M.P., and M.E. acknowledge the financial support by the Ministry of Education, Science and Technological Development of Republic of Serbia contract no: 451-03-9/2021-14/200146. I.P. acknowledges the financial support from the Ministry for Education, Science and Technological development of the Republic of Serbia, contract with the Institute for Multidisciplinary Research, University of Belgrade 451-03-9/2021-14/200053, and Qatar National Research Fund (QNRF), cycle eleven, grant no NPRP11S-1126-170033.

■ REFERENCES

(1) Yatsunyk, L. A.; Mendoza, O.; Mergny, J.-L. "Nano-oddities": Unusual Nucleic Acid Assemblies for DNA-Based Nanostructures and Nanodevices. *Acc. Chem. Res.* **2014**, *47*, 1836−1844.

(2) Zaccaria, F.; Paragi, G.; Fonseca Guerra, C. The Role of Alkali Metal Cations in the Stabilization of Guanine Quadruplexes: Why K^+ is the Best. *Phys. Chem. Chem. Phys.* **2016**, *18*, 20895−20904.

(3) Deng, J.; Xiong, Y.; Sundaralingam, M. X-Ray Analysis of an RNA Tetraplex $(UGGGGU)_4$ with Divalent Sr^{2+} Ions at Subatomic Resolution (0.61 Å). *Proc. Natl. Acad. Sci. U.S.A.* **2001**, *98*, 13665−13670.

(4) Shi, X.; Fettinger, J. C.; Davis, J. T. Ion-Pair Recognition by Nucleoside Self-Assembly: Guanosine Hexadecamers Bind Cations and Anions. *Angew. Chem. Int. Ed.* **2001**, *40*, 2827−2831.

(5) Hud, N. V.; Plavec, J. *Quadruplex Nucleic Acids*; Neidle, S., Balasubramanian, S., Eds.; RSC Publishing: Cambridge, U.K., 2006, Chapter 4; pp 100−130.

(6) Fyfe, A. C.; Dunten, P. W.; Martick, M. M.; Scott, W. G. Structural Variations and Solvent Structure of r(UGGGGU) Quadruplexes Stabilized by Sr^{2+} Ions. *J. Mol. Biol.* **2015**, *427*, 2205−2219.

(7) Plank, T. N.; Skala, L. P.; Davis, J. T. Supramolecular Hydrogels for Environmental Remediation: G4-Quartet Gels that Selectively Absorb Anionic Dyes from Water. *Chem. Commun.* **2017**, *53*, 6235−6238.

(8) Dumas, A.; Luedtke, N. W. Cation-Mediated Energy Transfer in G-Quadruplexes Revealed by an Internal Fluorescent Probe. *J. Am. Chem. Soc.* **2010**, *132*, 18004−18007.

(9) Jissy, A. K.; Ashik, U. P. M.; Datta, A. Nucleic Acid G-quartets: Insights into Diverse Patterns and Optical Properties. *J. Phys. Chem. C* **2011**, *115*, 12530−12546.

(10) Hua, Y.; Changenet-Barret, P.; Improta, R.; Vayá, I.; Gustavsson, T.; Kotlyar, A. B.; Zikich, D.; Šket, P.; Plavec, J.; Markovitsi, D. Cation Effect on the Electronic Excited States of Guanine Nanostructures Studied by Time-Resolved Fluorescence Spectroscopy. *J. Phys. Chem. C* **2012**, *116*, 14682−14689.

(11) Changenet-Barret, P.; Hua, Y.; Markovitsi, D. Electronic Excitations in Guanine Quadruplexes. *Top. Curr. Chem.* **2014**, *356*, 183−201.

(12) Behmand, B.; Balanikas, E.; Martinez-Fernandez, L.; Improta, R.; Banyasz, A.; Baldacchino, G.; Markovitsi, D. Potassium Ions Enhance Guanine Radical Generation upon Absorption of Low-Energy Photons by G-Quadruplexes and Modify Their Reactivity. *J. Phys. Chem. Lett.* **2020**, *11*, 1305−1309.

(13) Milovanović, B.; Stanković, I.; Petković, M.; Etinski, M. Modulating Excited Charge-Transfer States of G-Quartet Self-Assemblies by Earth Alkaline Cations and Hydration. *J. Phys. Chem. A* **2020**, *124*, 8101−8111.

(14) Gkionis, K.; Kruse, H.; Platts, J. A.; Mládek, A.; Koča, J.; Šponer, J. Ion Binding to Quadruplex DNA Stems. Comparison of MM and QM Descriptions Reveals Sizable Polarization Effects Not Included in Contemporary Simulations. *J. Chem. Theory Comput.* **2014**, *10*, 1326−1340.

(15) Gresh, N.; Naseem-Khan, S.; Lagardère, L.; Piquemal, J.-P.; Sponer, J. E.; Sponer, J. Channeling through Two Stacked Guanine Quartets of One and Two Alkali Cations in the Li^+, Na^+, K^+, and Rb^+ Series. Assessment of the Accuracy of the SIBFA Anisotropic Polarizable Molecular Mechanics Potential. *J. Phys. Chem. B* **2017**, *121*, 3997−4014.

(16) Milovanović, B.; Petković, M.; Etinski, M. Properties of the Excited Electronic States of Guanine Quartet Complexes with Alkali Metal Cations. *J. Serb. Chem. Soc.* **2020**, *85*, 1021−1032.

(17) Milovanović, B.; Stanojević, A.; Etinski, M.; Petković, M. Intriguing Intermolecular Interplay in Guanine Quartet Complexes with Alkali and Alkaline Earth Cations. *J. Phys. Chem. B* **2020**, *124*, 3002−3014.

(18) Nieuwland, C.; Zaccaria, F.; Fonseca Guerra, C. Understanding Alkali Metal Cation Affinities of Multi-layer Guanine Quadruplex DNA. *Phys. Chem. Chem. Phys.* **2020**, *22*, 21108−21118.

(19) Lee, M. P. H.; Parkinson, G. N.; Hazel, P.; Neidle, S. Observation of the Coexistence of Sodium and Calcium Ions in a DNA G-Quadruplex Ion Channel. *J. Am. Chem. Soc.* **2007**, *129*, 10106−10107.

(20) Zhang, D.; Huang, T.; Lukeman, P. S.; Paukstelis, P. J. Crystal Structure of a DNA/Ba^{2+} G-Quadruplex Containing a Water-Mediated C-Tetrad. *Nucleic Acids Res.* **2014**, *42*, 13422−13429.

(21) Pan, B.; Xiong, Y.; Shi, K.; Deng, J.; Sundaralingam, M. Crystal Structure of an RNA Purine-Rich Tetraplex Containing Adenine Tetrads: Implications for Specific Binding in RNA Tetraplexes. *Structure* **2003**, *11*, 815−823.

(22) Kwan, I. C. M.; Wong, A.; She, Y.-M.; Smith, M. E.; Wu, G. Direct NMR Evidence for Ca^{2+} Ion Binding to G-Quartets. *Chem. Commun.* **2008**, *2008*, 682−684.

(23) Kwan, I. C. M.; She, Y.-M.; Wu, G. Nuclear Magnetic Resonance and Mass Spectrometry Studies of 2',3',5'-O-Triacetylgua-

nosine Self-Assembly in the Presence of Alkaline Earth Metal Ions (Ca^{2+}, Sr^{2+}, Ba^{2+}). *Can. J. Chem.* **2011**, *89*, 835−844.
(24) *TURBOMOLE*, version 7.0; TURBOMOLE GmbH: Karlsruhe, Germany, 2015.
(25) Becke, A. D. Density-Functional Exchange-Energy Approximation with Correct Asymptotic-Behavior. *Phys. Rev. A: At., Mol., Opt. Phys.* **1988**, *38*, 3098−3100.
(26) Lee, C.; Yang, W.; Parr, R. G. Development of the Coll-Salvetti Correlation-Energy Formula into a Functional of the Electron-density. *Phys. Rev. B: Condens. Matter Mater. Phys.* **1988**, *37*, 785−789.
(27) Grimme, S.; Antony, J.; Ehrlich, S.; Krieg, H. A Consistent and Accurate Ab Initio Parametrization of Density Functional Dispersion Correction (DFT-D) for the 94 Elements H-Pu. *J. Chem. Phys.* **2010**, *132*, 154104.
(28) Weigend, F.; Ahlrichs, R. Balanced Basis Sets of Split Valence, Triple Zeta Valence and Quadruple Zeta Valence Quality for H to Rn: Design and Assessment of Accuracy. *Phys. Chem. Chem. Phys.* **2005**, *7*, 3297−3305.
(29) Guerra, C. F.; Zijlstra, H.; Paragi, G.; Bickelhaupt, F. M. Telomere Structure and Stability: Covalency in Hydrogen Bonds, not Resonance Assistance, Causes Cooperativity in Guanine Quartets. *Chem.—Eur. J.* **2011**, *17*, 12612−12622.
(30) Wolters, L. P.; Smits, N. W. G.; Guerra, C. F. Covalency in Resonance-Assisted Halogen Bonds Demonstrated with Cooperativity in N-Halo-Guanine Quartets. *Phys. Chem. Chem. Phys.* **2015**, *17*, 1585−1592.
(31) Paragi, G.; Kupihár, Z.; Endre, G.; Fonseca Guerra, C.; Kovács, L. The Evaluation of 5-Amino-and 5-Hydroxyuracil Derivatives as Potential Quadruplex-forming Agents. *Org. Biomol. Chem.* **2017**, *15*, 2174−2184.
(32) Paragi, G.; Guerra, C. F. Cooperativity in the Self-Assembly of the Guanine Nucleobase into Quartet and Ribbon Structures on Surfaces. *Chem.—Eur. J.* **2017**, *23*, 3042−3050.
(33) Reed, A. E.; Weinstock, R. B.; Weinhold, F. Natural Population Analysis. *J. Chem. Phys.* **1985**, *83*, 735−746.
(34) Klamt, A.; Schüürmann, G. COSMO: a New Approach to Dielectric Screening in Solvents with Explicit Expressions for the Screening Energy and its Gradient. *J. Chem. Soc., Perkin Trans. 2* **1993**, *5*, 799−805.
(35) Schäfer, A.; Klamt, A.; Sattel, D.; Lohrenz, J. C. W.; Eckert, F. COSMO Implementation in TURBOMOLE: Extension of an Efficient Quantum Chemical Code Towards Liquid Systems. *Phys. Chem. Chem. Phys.* **2000**, *2*, 2187−2193.
(36) Marcus, Y. Thermodynamics of Solvation of Ions Part 5. Gibbs Free Energy of Hydration at 298.15 K. *J. Chem. Soc., Faraday Trans.* **1991**, *87*, 2995−2999.
(37) Su, P.; Li, H. Energy Decomposition Analysis of Covalent Bonds and Intermolecular Interactions. *J. Chem. Phys.* **2009**, *131*, 014102.
(38) Asthagiri, D.; Dixit, P. D.; Merchant, S.; Paulaitis, M. E.; Pratt, L. R.; Rempe, S. B.; Varma, S. Ion Selectivity from Local Configurations of Ligands in Solutions and Ion Channels. *Chem. Phys. Lett.* **2010**, *485*, 1−7.
(39) Asthagiri, D. N.; Paulaitis, M. E.; Pratt, L. R. Thermodynamics of Hydration from the Perspective of the Molecular Quasichemical Theory of Solutions. *J. Phys. Chem. B* **2021**, *125*, 8294−8304.
(40) Yu, H.; Noskov, S. Y.; Roux, B. Two Mechanisms of Ion Selectivity in Protein Binding Sites. *Proc. Natl. Acad. Sci. U.S.A.* **2010**, *107*, 20329−20334.
(41) Venczel, E. A.; Sen, D. Parallel and Antiparallel G-DNA Structures from a Complex Telomeric Sequence. *Biochemistry* **1993**, *32*, 6220−6228.
(42) Liu, H.; et al. High-Resolution DNA Quadruplex Structure Containing all the A-, G-, C-, T-Tetrads. *Nucleic Acids Res.* **2018**, *46*, 11627−11638.
(43) Jing, Z.; Liu, C.; Qi, R.; Ren, P. Many-Body Effect Determines the Selectivity for Ca^{2+} and Mg^{2+} in Proteins. *Proc. Natl. Acad. Sci. U.S.A.* **2018**, *115*, E7495−E7501.

https://doi.org/10.1021/acs.jpcb.1c05598
J. Phys. Chem. B 2021, 125, 11996−12005

7-11th October 2019
Belgrade, Serbia

http://www.sfkm.ac.rs/

The 20th Symposium on Condensed Matter Physics

BOOK OF ABSTRACTS

University of Belgrade, Faculty of Physics

Institute of Physics Belgrade

Vinca Institute of Nuclear Sciences

Serbian Academy of Sciences and Arts

Ministry of Education, Science and Technological Development, Republic of Serbia

Multifunctional Nanodevice Based on Ti_2O

Igor Popov[a,b]

[a]*Institute of Physics Belgrade, University of Belgrade, Pregrevica 118, 11080 Belgrade, Serbia*
[b]*Institute for Multidisciplinary Research, University of Belgrade, Kneza Višeslava 1, 11030 Belgrade, Serbia*

Abstract. Miniaturization of microelectronics, as integration of increasingly more transistors and hence functions per chip area, approaches its end due to the limits of the silicon technology. We propose a new concept of multifunctional nanodevices which multiple functionality is at the material's level, as replacements for common transistors. An example of such a multifunctional nanodevice based on a Ti_2O monolayer will be presented. In contrast to TiO_2 crystal, Ti_2O have not been intensively investigated even though the crystal was fabricated in 1953 for the first time. Our study based on density functional theory indicates that a Ti_2O layer is bistable for two lattice parameters, being metallic for one and semiconducting for another parameter. In a switching configuration, this provides a high current ON/OFF ratio of 10^3 when the layer is biased and stretched simultaneously. The electronic conductance of the layer is highly anisotropic. The high sensitivity of conductance to layer stretching can be utilized for electromechanical switching, the bistability provides potential for application as a nonvolatile memory bit, while the current-voltage characteristic of the material in its semiconducting phase indicates a possible use as a varistor – all in a single nanodevice.

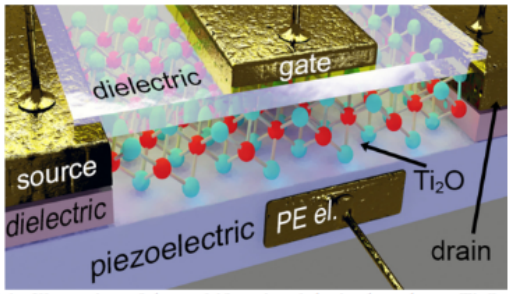

FIGURE 1. Illustration of the multifunctional device based on a Ti_2O monolayer

REFERENCES

1. E.S. Bumps, E.S., Kessler, H.D., and Hansen, M., *Trans. Am. Soc. Metals* **45**, 1008 (1953).
2. Mali, S.S, Shinde, P.S., Betty, C.A., Bhosale, P.N., Lee, W.J, and Patil, P.S., *Appl. Surf. Sci.* **257,** 9737 (2011).
3. Huang , C.H., Tsao,C.C., and Hsu, C.Y., *Ceram. Int.* **37**, 2781 (2011).
4. Furkas, B., Budai, J., Kabalci, I., Heszler,P., and Geretovszky, Z., *Appl. Surf. Sci.* **254**, 3484 (2008).
5. Bouachiba, Y., Bouabellou, A., Hanini, F., Kermiche, F., Taabouche, A., and Boukheddaden, K., *Mat. Sci.-Pol.* **32**, 1 (2014).

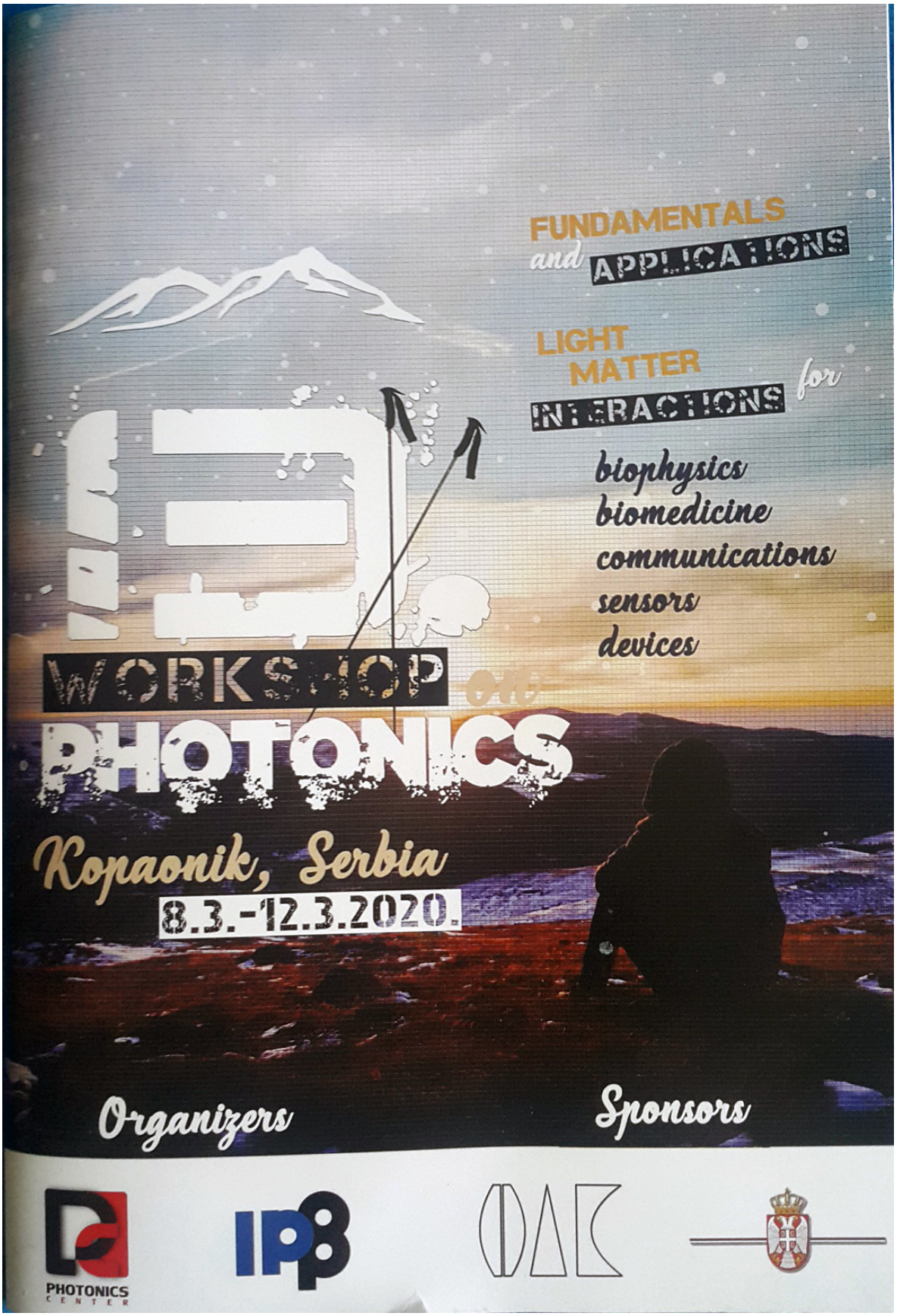
FUNDAMENTALS
and APPLICATIONS
LIGHT
MATTER
INTERACTIONS for
biophysics
biomedicine
communications
sensors
devices
WORKSHOP on
PHOTONICS
Kopaonik, Serbia
8.3.-12.3.2020.
Organizers
Sponsors
PHOTONICS
CENTER
IPB

Contents

Scientific Committee:

Wolfgang Fritzsche, *Leibniz Institute of Photonic Technology, Germany*

Lars Klimaschewski, *Innsbruck Medical University, Austria*

Srđan Antić, *Institute for Systems Genomics, Stem Cell Institute, University of Connecticut, USA*

Theo Scholtes, *Leibniz Institute of Photonic Technology, Germany*

Hrvoje Skenderović, *Institute of Physics, Zagreb, Croatia*

Gülnur Aygün Ozyuzer, *Izmir Institute of Technology, Turkey*

Ljupčo Hadžijevski, *Vinča Institute of Nuclear Sciences, Serbia*

Pavle Anđus, *Faculty of Biology, University of Belgrade, Serbia*

Branislav Jelenković, *Institute of Physics Belgrade, Serbia*

Marina Lekić, *Institute of Physics Belgrade, Serbia*

Aleksander Kovačević, *Institute of Physics Belgrade, Serbia*

Zoran Grujić, *Institute of Physics Belgrade, Serbia*

Organizing Committee:

Marina Lekić (chair), Institute of Physics Belgrade

Marija Ćurčić (secretary), Institute of Physics Belgrade

Zoran Grujić (webmaster), Institute of Physics Belgrade

Aleksander Kovačević, Institute of Physics Belgrade

Dragan Lukić, Institute of Physics Belgrade

Branislav Jelenković, Institute of Physics Belgrade

Igor Popov, Institute for Multidisciplinary Research, University of Belgrade

Multifunctional Nanodevice Based on Ti_2O

Igor Popov[1,2], Milivoj Belić[3], David Tomanek[4]

(1) Institute for Multidisciplinary Research, University of Belgrade, Kneza Višeslava 1, 11030 Belgrade, Serbia

(2) Institute of Physics Belgrade, University of Belgrade, Pregrevica 118, 11080 Belgrade, Serbia

(3) Texas A&M University at Qatar, 23874 Doha, Qatar

(4) Physics and Astronomy Department, Michigan State University, East Lansing, Michigan 48824-2320, USA

Contact: I. Popov (popov@ipb.ac.rs)

Abstract. Miniaturization of microelectronics, as integration of increasingly more transistors and hence functions per chip area, approaches its end due to the limits of the silicon technology. We propose a new concept, multifunctional nanodevices which multiple functionality is at the material's level, as replacements for common transistors. An example of such a multifunctional nanodevice based on a Ti_2O monolayer will be presented. In contrast to TiO_2 crystal, Ti_2O have not been intensively investigated even though the crystal was fabricated in 1953 for the first time. Our study based on density functional theory indicates that a Ti_2O layer is bistable for two lattice parameters, being metallic for one and semiconducting for another parameter. In a switching configuration, this provides a high current ON/OFF ratio of 10^3 when the layer is biased and stretched simultaneously. The electronic conductance of the layer is highly anisotropic. The high sensitivity of conductance to layer stretching can be utilized for electromechanical switching, the bistability provides potential for application as a nonvolatile memory bit, while the current-voltage characteristic of the material in its semiconducting phase indicates a possible use as a varistor – all in a single nanodevice.

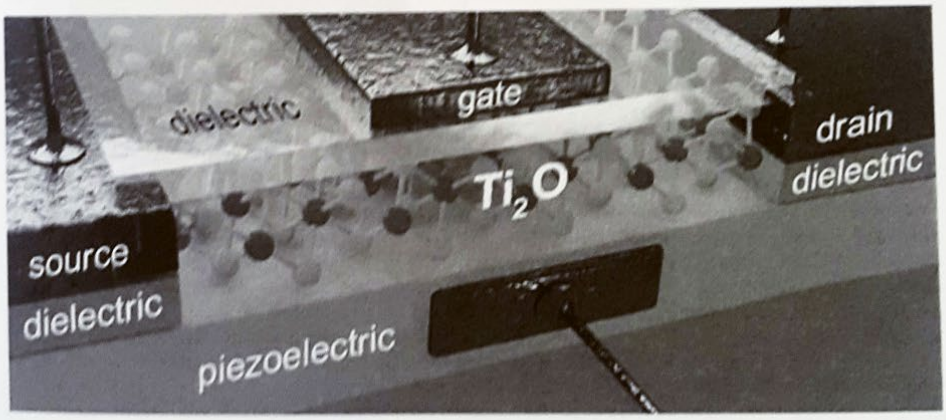

Figure 1 Illustration of the multifunctional device based on a Ti_2O monolayer.

condensed matter

MDPI

Article

Ab Initio Study of the Electronic, Vibrational, and Mechanical Properties of the Magnesium Diboride Monolayer

Jelena Pešić [1,*], Igor Popov [1,2], Andrijana Šolajić [1], Vladimir Damljanović [1], Kurt Hingerl [3], Milivoj Belić [4] and Radoš Gajić [1]

1 Laboratory for graphene, other 2D materials and ordered nanostructures, Center for Solid State Physics and New Materials, Institute of Physics Belgrade, University of Belgrade, 11080 Belgrade, Serbia; popov@ipb.ac.rs (I.P.); solajic@ipb.ac.rs (A.Š.); damlja@ipb.ac.rs (V.D.); rgajic@ipb.ac.rs (R.G.)
2 Institute for Multidisciplinary Research, University of Belgrade, Kneza Višeslava 1, 11030 Belgrade, Serbia
3 Center for Surface and Nanoanalytics, Johannes Kepler University, 4040 Linz, Austria; Kurt.Hingerl@jku.at
4 Science Program, Texas A&M University at Qatar, Doha P.O. Box 23874, Qatar; milivoj.belic@qatar.tamu.edu
* Correspondence: yelena@ipb.ac.rs

Received: 15 March 2019; Accepted: 1 April 2019; Published: 2 April 2019

Abstract: Magnesium diboride gained significant interest in the materials science community after the discovery of its superconductivity, with an unusually high critical temperature of 39 K. Many aspects of the electronic properties and superconductivity of bulk MgB_2 and thin sheets of MgB_2 have been determined; however, a single layer of MgB_2 has not yet been fully theoretically investigated. Here, we present a detailed study of the structural, electronic, vibrational, and elastic properties of monolayer MgB_2, based on ab initio methods. First-principles calculations reveal the importance of reduction of dimensionality on the properties of MgB_2 and thoroughly describe the properties of this novel 2D material. The presence of a negative Poisson ratio, higher density of states at the Fermi level, and a good dynamic stability under strain make the MgB_2 monolayer a prominent material, both for fundamental research and application studies.

Keywords: magnesium diboride; 2D materials; density functional theory

PACS: 71.15.Mb; 74.70.Ad

1. Introduction

Magnesium diboride was first synthesized and had its structure confirmed in 1953 [1]. An interest in its properties has grown ever since 2001, when it was discovered that MgB_2 exhibits the highest superconducting transition temperature T_c of all metallic superconductors. It is an inter-metallic s-wave compound superconductor with a quasi-two dimensional character [2] and a critical temperature of superconductive transition at T_c = 39 K. The experimental confirmation of the isotope effect [3] in MgB_2 indicated that it is a phonon-mediated BCS superconductor. A better definition would describe MgB_2 as self-doped semimetal with a crucial σ-bonding band that is nearly filled [4]. The basic aspects of the electronic structure and pairing is in a rather strong coupling of high frequency boron–boron stretch modes to the bonding electronic boron–boron states at the Fermi surface. The phonon-mediated mechanism with different coupling strengths between a particular phonon mode and selected electronic bands, boron σ- and π-bands [5–13], results in the presence of two superconducting gaps at the Fermi level. MgB_2 has already been fabricated in bulk, as single crystals, and as a thin film, and shows potential for practical applications.

The discovery of graphene in 2004 [14] sparked an interest in 2D materials and their properties. A variety of new properties, which distinguished graphene from graphite [14–22], inspired a search for other low-dimensional limits of layered materials and possibilities they offered. Interest in a low-dimensional limit of MgB_2 has arisen in past years, showing that it is superconductive even in a monolayer [23,24].

MgB_2 has a distinct layer structure, where boron atoms form a honeycomb layer and magnesium atoms are located above the center of the hexagons, between every boron plane. The boron layers alternate with a triangular lattice of magnesium layers. There is a noticeable structural similarity of MgB_2 to graphite-intercalated compounds (GICs), some of which also exhibit superconductivity [25–29]. Both monolayer and two-layer graphene, decorated/intercalated with atoms of alkali and alkaline earth metals, exhibit superconductivity and have been thoroughly studied using ab initio methods and isotropic and anisotropic Eliashberg theory [30–32].

Furthermore, a similarity in the electronic structure between GICs and MgB_2 exists. The peculiar and unique property of MgB_2 is a consequence of the incomplete filling of two σ bands corresponding to strongly covalent sp^2-hybrid bonding within the graphite-like boron layers [33].

Here, we present a comprehensive study of the electronic, vibrational, and mechanical properties of MgB_2 using ab initio methods, in order to provide its detail description.

2. Computational Details

MgB_2 has a hexagonal unit cell and consists of graphite-like B_2 layers stacked with the Mg atoms in between, as shown in Figure 1. The first-principles calculations were performed within the density functional theory (DFT) formalism, using a general gradient approximation (GGA) to calculate the electronic structure. For all electronic and phonon structure, the Quantum Espresso software package [34] was used with ultra-soft pseudopotentials and a plane-wave cutoff energy of 30 Ry. All calculated structures are relaxed to their minimum energy configuration, following the internal force on atoms and stress tensor of the unit cell. We used the Monkhorst-Pack $48 \times 48 \times 48$ and $40 \times 40 \times 1$ k-meshes, for the calculations of the electronic structure of the MgB_2 bulk and MgB_2 monolayer, respectively. The phonon frequencies are calculated using Density Functional Perturbation Theory (DPFT) on the $12 \times 12 \times 12$ and $20 \times 20 \times 1$ phonon wave vector mesh for the bulk and monolayer structures, respectively. In two-dimensional systems, the van der Waals (vdW) interaction was found to play an important role on the electronic structure [35]; however, as this is study on monolayer MgB_2, we do not treat vdW interactions, especially since, in this case, the effects are minor and including them would add additional computational costs but would not yield more accurate results.

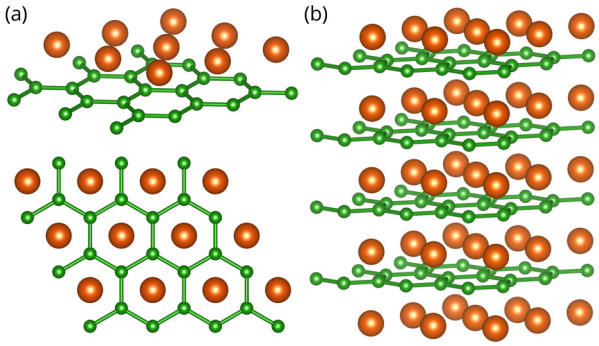

Figure 1. Crystal structure of the MgB_2 monolayer (**a**) and bulk MgB_2 (**b**), with a hexagonal unit cell. Green (orange) spheres represent Boron (Magnesium) atoms. Color online.

The crystal structure of MgB_2 and the MgB_2 monolayer are presented in Figure 1. The lattice parameters for the bulk MgB_2 are in agreement with the experimental results, $a = 3.083$ Å and

$c/a = 1.142$ [9]. In order to avoid an interlayer interaction due to the periodicity and to simulate a 2D material, an artificial vacuum layer was set to be 25 Å. When the monolayer is modelled, the structure is geometrically optimized, allowing the atoms to reach a minimum potential energy state. The bond length between neighbouring atoms remained to be 1.78 Å, but the distance from the boron layer to the Mg atoms changed from $h = 1.76$ Å to $h = 1.60$ Å.

For the molecular dynamics (MD) study, the Siesta code was utilized [36]. The super-cell is built by repeating the unit cell three times in both in-plane directions, whereas the lattice vector in the perpendicular direction is 15 Å, providing a large enough vacuum space between the 2D material and its periodic replica in order to avoid their mutual interaction. The lattice parameters and the geometry of the unit cell are initially optimized using the conjugate gradient method. The Perdew-Burke-Ernzerhof form of the exchange-correlation functional [37], the double-zeta polarized basis set, and the Troulier-Martins pseudopotentials [38] were used in all MD calculations.

The second-order elastic constants were calculated using the ElaStic software package [39]. First, the direction is projected from the strain tensor and total energies for each deformation are calculated. Elastic constants are then calculated using the second derivatives of the energy curves, dependent on the parameter η. In our calculations, the maximum positive and negative amplitudes of 5% Lagrangian strain were applied, with a step of 0.1%.

For the 2D square, rectangular, or hexagonal lattices, the non-zero second-order elastic constants, in Voigt notation, are c_{11}, c_{22}, c_{12}, and c_{66}. Due to symmetry, in hexagonal structures $c_{11} = c_{22}$ and $c_{66} = \frac{1}{2}(c_{11} - c_{12})$; so, we have 2 independent elastic constants. The layer modulus, which represents the resistance of a 2D material to stretching, is given as

$$\gamma = \frac{1}{4}(c_{11} + c_{22} + 2c_{12}).$$

The 2D Young modulus Y for strains in the (10) and (01) directions, Poisson's ratio ν and the shear modulus G are obtained from the following relations,

$$Y = \frac{c_{11}^2 - c_{12}^2}{c_{11}}, \ \nu = \frac{c_{12}}{c_{22}}, \ G = c_{66}.$$

Units for elastic constants and those parameters are N/m.

3. Results and Discussion

In order to determine the stability of a single layer of MgB_2, we perform MD simulations based on DFT and the super-cell approach. Besides the system with optimized (pristine) lattice parameters, we also consider a biaxially stretched system (up to 3% of tensile strain) and biaxially compressed system (up to 5% of compressive strain). The MD simulations are conducted in the range of temperatures between 50–300 K, with a step of 50 K, using the Nosé–Hoover thermostat [40].

Figure 2a shows the average distance between Mg and B atomic layers, as evolved over a time of 1 ps. Throughout the simulation time, there is no further evolution of the z-coordinate and the Mg atom shows only oscillatory movement around the equilibrium positions (as is shown in Figure 2) Importantly, the separation indicates that the Mg atoms do not leave the surface of the MgB_2 crystal. The plane in which the Mg atoms reside shifts away from the plane of the B atoms on average by 0.09 Å in a compressed crystal, while the distance between the planes decreases on average by 0.42 Å in the stretched system. This (relatively larger) shift in the latter case can be understood by analysing the details of the MgB_2 atomic structure. When the crystal is biaxially stretched, its Mg–B bond lengths increase, which is partially compensated by the nesting of the Mg atoms in the hollow sites closer to the B sublattice. Despite these atomic shifts, the MD simulations show the structural stability of the system. The stability from the MD simulations can be further quantitatively derived from the global Lindemann index, the dependence of which on temperature is shown in Figure 2b. It is calculated

for the pristine crystal, with a compressive strain of 5% and a tensile strain of 3%, from the local Lindemann indices, given by the formula

$$q_i = \frac{1}{N-1} \sum_{j \neq i} \frac{\sqrt{\langle r_{ij}^2 \rangle - \langle r_{ij} \rangle^2}}{\langle r_{ij} \rangle},$$

by averaging over all atoms. Here q_i is the local Lindemann index of atom i, N is number of atoms, r_{ij} is a separation between atoms i and j, and the angle brackets denote averaging over time (i.e., MD steps) [41]. The linear behaviour of the Lindemann indices indicate that systems are stable, at least up to room temperature.

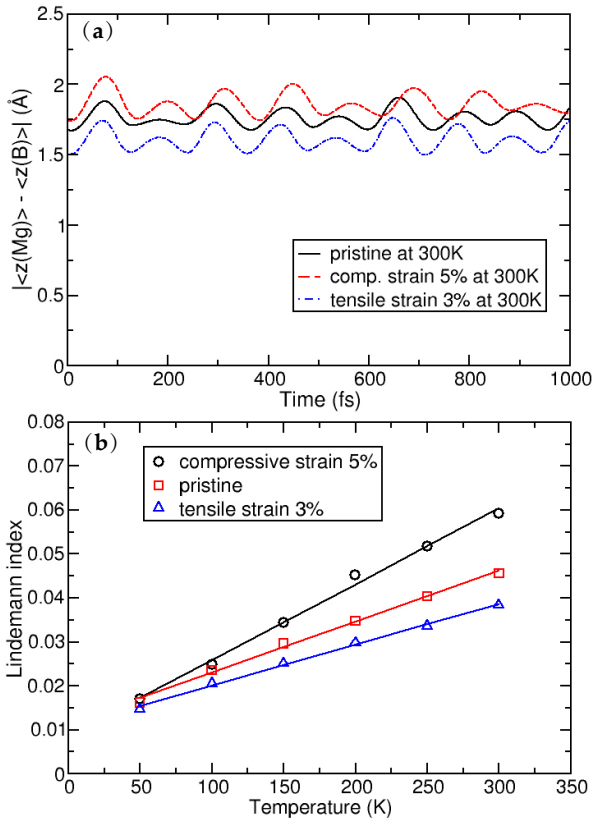

Figure 2. (**a**): Average distance between the Mg and B atomic layers; and (**b**): the dependence of the global Lindemann index as a function of temperature.

The calculated second-order elastic constants and other structural parameters for monolayer MgB_2 are given in Table 1. All elastic constants related to the bulk material (those that have 3, 4, or 5 in their subscripts), are calculated close to zero, as is expected for the monolayer. Compared to similar 2D materials, the layer modulus of MgB_2 of 30.18 N/m is relatively small (in the range of Silicene and Germanene), roughly five times smaller than that of graphene or h–BN, for example [42,43]. Similar results are obtained for the Young modulus. Compared to borophene (two-dimensional boron sheets with rectangular structures) [44], which is a hard and brittle 2D material that exhibits an extremely large Young's modulus of 398 N/m along the a direction [45], the MgB_2 monolayer has a significantly smaller value of 63.29 N/m. The most interesting observation in the elastic properties of the MgB2 monolayer is that the c_{12} constant is negative, which gives a negative Poisson ratio in the a and b directions, too—although, with a very small negative value of -0.05. However, compared to 2D borophene, which has an out-of-plane negative Poisson's ratio (that effectively holds the strong boron bonds lying along the a direction and makes the boron sheet show superior mechanical flexibility along

the b direction [46]), we obtain similar values [45]. For comparison, graphene has a Young modulus of 352.2 N/m and a Poisson ratio of 0.185 [42]. After confirming its stability and determining the elastic properties of the MgB_2 monolayer, we study its electronic properties. In Figure 3, the electronic structures of bulk MgB_2 and the MgB_2 monolayer are presented. The band structures for the bulk along the high-symmetry points Γ-K-M-Γ-A-L, and for the monolayer along Γ-K-M-Γ were calculated. The Fermi level is set to zero. The band structure of the bulk is in full agreement with previous studies [10,47–49]. The two bands crossing the Fermi level play a crucial role in the electronic properties of MgB_2. The density of the states around E_f are predominantly related to the B atoms and their p-orbitals, whereas the Mg atom contribution is negligible in this region. Previous studies described Mg as fully ionized and showed that the electrons donated to the system are not localized on the anion but, rather, are distributed over the whole crystal [6]. A similarity to graphite can be observed, with three σ bands, corresponding to the in-plane sp_xp_y (sp^2) hybridization in the boron layer and two π-bands of boron p_z orbitals [33]. Boron $p_{x(y)}$ and p_z orbitals contribute as σ and π states. Analysing projected DOS, one concludes that the σ states are considerably involved in the total density of states at the Fermi level, while the π states have only a partial contribution. It is worth emphasizing that the bulk bands of this material at the K-point above the Fermi level present a formation similar to the Dirac cones in graphene.

In the monolayer, there is an increase in the total density of states at the Fermi level from $N(E_f)_{bulk}$ = 0.72 states/eV to $N(E_f)_{mono}$ = 0.97 states/eV. In the same manner as in the bulk, the monolayer Mg atoms negligibly contribute to the density of states at the Fermi level, and the main contribution comes from the B p-orbitals. The characteristic Dirac cone-like structure is still present and closer to the Fermi level. Dg77, as the symmetry group of the MgB_2 monolayer, hosts a Dirac-like dispersion in the vicinity of the K-point in the hexagonal Brillouin zone, if the orbital wave functions belong to the 2D representation E of the C_{3v} point group of the wave vector [50,51]. In the tight-binding case, the p_x and p_y orbitals of two boron ions give rise to one E-representation (and to two one-dimensional representations), while the s-orbitals form a basis for one E-representation and p_z-orbitals form a basis for one E-representation as well. This explains the presence of the Dirac cones at the K-point in the band structure of the MgB_2 monolayer (as shown in Figure 3b).

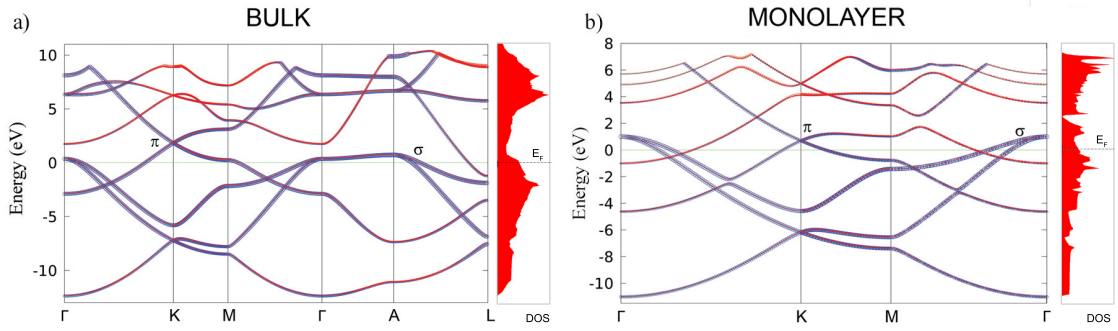

Figure 3. The electronic band structure and total density of states in bulk MgB_2 (**a**) and the MgB_2 monolayer (**b**). The blue and red colors represent the B and Mg atoms contributions to the electronic dispersion, respectively.

Table 1. The calculated elastic stiffness constants, layer modulus γ, Young's modulus Y, Poisson's ratio ν, and shear modulus G for the MgB_2 monolayer. All parameters are in units of N/m.

c_{11}	c_{12}	c_{66}	γ	Y	ν	G
63.4	−3.1	33.3	30.18	63.29	−0.05	33.3

Figure 4 shows the phonon dispersions for both the bulk and monolayer. For the bulk (in Figure 4a), there are four optical modes at the Γ point. Due to the light atomic mass of the B

atoms and the strong B–B coupling, the two high-frequency modes almost have a pure boron character. The in-plane stretching mode E_{2g} and the out-of-plane mode (where the atoms move in opposite directions B_{1g}) are the boron atom modes. E_{2g} is a doubly-degenerate Raman active mode and experimental studies [6,9] showed that this mode is very sensitive to structural changes and it has a strong electron-phonon coupling. The low-frequency modes (A_{2u}) and double degenerate (E_{1u}) are infrared active and they do not involve changes on in-plane bonds. In Figure 4b, the phonon dispersion of the MgB_2 monolayer is presented. In the phonon spectrum there are no imaginary frequencies, which confirms, once again, the dynamical stability of the system (also demonstrated earlier by the MD calculations).

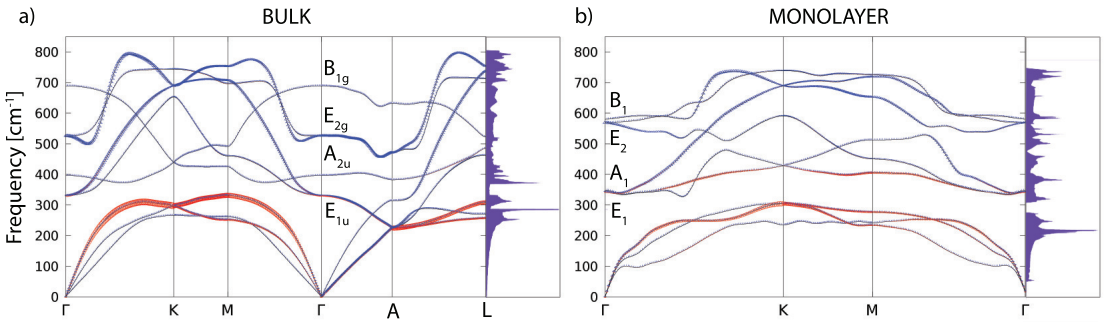

Figure 4. The phonon dispersion and the phonon density of states for the MgB_2 bulk (**a**) and monolayer (**b**). The blue and red colours represent the B and Mg atom contributions in the phonon dispersion, respectively.

At the Γ point, there are three acoustic and six optical modes (from which two pairs are doubly degenerate). The optical modes A_1, B_1, E_1, and E_2 are related to the optical modes of the parent material. Two significant differences between the bulk and monolayer spectrum can be observed: The E_1 and A_1 mode become energy degenerate in the monolayer, resulting in either a slight softening (hardening) of the modes which leads to nearly equal frequencies, which opens a gap in the phonon density of states (DOS) between the acoustic and optical modes. A more significant effect concerns the softening of the B_1 mode and hardening of the E_2 mode. As in the bulk E_{2g} mode, the monolayer E_2 mode is strongly coupled to electrons, causing the superconductivity in the monolayer in a similar fashion as in the bulk. In Figure 5, the vibrational frequencies and normal coordinates for the MgB_2 monolayer are presented. The symmetry group is C_{6v}, and the acoustic modes are A_1 and E_1. The optical modes at the Γ point are A_1, B_1, E_1, and E_2, where the infrared-active ones are A_1 and E_1. The Raman-active modes are A_1, E_1, and E_2, and B_1 is silent. In Table 2, the Raman tensor for the MgB_2 monolayer is presented [52]. Similar to graphene, the phonon eigenvectors and the normal coordinates at the Γ-point are determined by symmetry rules and, therefore, are a model independent.

Table 2. Raman tensor of the MgB_2 monolayer.

	Raman Tensors				
MgB_2-mono $Dg77 = TC_{6v}$ $O_z \,\|\|\, C_6$ $O_x \,\|\|\, \sigma_v$	A_1 $\begin{pmatrix} a & 0 & 0 \\ 0 & a & 0 \\ 0 & 0 & b \end{pmatrix}$	E_1 $\begin{pmatrix} 0 & 0 & c \\ 0 & 0 & 0 \\ c & 0 & 0 \end{pmatrix}$	$\begin{pmatrix} 0 & 0 & 0 \\ 0 & 0 & c \\ 0 & c & 0 \end{pmatrix}$	E_2 $\begin{pmatrix} d & 0 & 0 \\ 0 & -d & 0 \\ 0 & 0 & 0 \end{pmatrix}$	$\begin{pmatrix} 0 & -d & 0 \\ -d & 0 & 0 \\ 0 & 0 & 0 \end{pmatrix}$

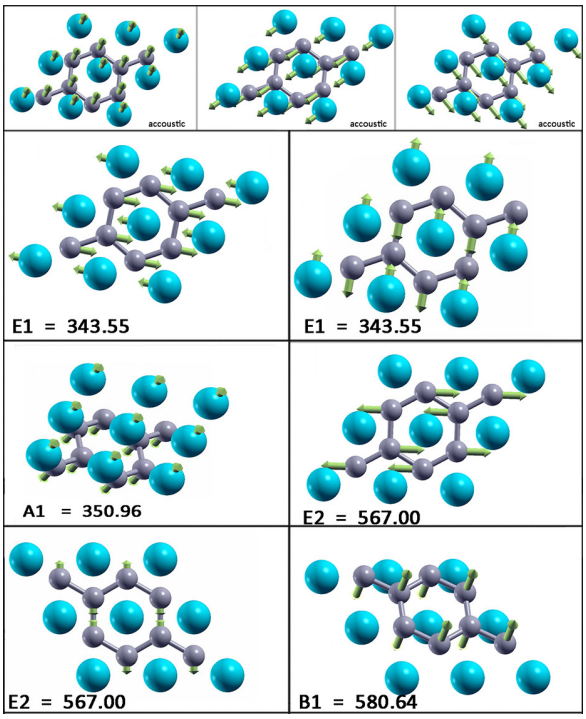

Figure 5. Vibrational frequencies (in wavenumbers) and the vibration normal coordinates at Γ for the MgB_2 monolayer.

4. Conclusions

The electronic band structure, density of states, phonon dispersion, and elastic constants have been calculated for the MgB_2 monolayer and compared to the bulk material, using first-principles calculations within the DFT framework. We demonstrated an increase of electronic density of states at the Fermi level in the monolayer (compared to the bulk) and determined its stability under various strains. These two features are crucial for the enhancement of electron–phonon coupling and they enable significant mechanical modification that increases the critical superconducting temperature. Establishing stability and offering insight into this novel 2D material, we focus on the effects of ultimate lowering of the dimensionality. The question of reduction of dimensionality to its limit, a truly atomic-scale 2D system, and the consequences of this [53–61] are highly relevant, not only to fundamental science but also to applications in nanotechnology.

Author Contributions: Conceptualization, J.P. and R.G.; Validation, K.H., M.B., R.G.; Investigation, J.P., I.P., A.Š. and V.D.; Writing—Original Draft Preparation, J.P., I.P., A.Š. and V.D.; Writing—Review & Editing, J.P.; Supervision, R.G.; Funding Acquisition, K.H., M.B. and R.G.

Funding: This research is supported by Serbian Ministry of Education, Science and Technological Development under projects OI 171005, III 45018, and III 45016 and by the Qatar National Research Fund, cycle 11, under grant number NPRP 11S-1126-170033. K.H. acknowledges the support of the European Commission under the H2020 grant TWINFUSYON.GA692034.

Acknowledgments: The DFT calculations were performed using the computational resources at Johannes Kepler University, Linz, Austria. This work was supported by the Serbian Ministry of Education, Science and Technological Development under projects OI 171005, III 45018, and III 45016.

Conflicts of Interest: The authors declare no conflict of interest.

References

1. Jones, M.E.; Marsh R.E. The preparation and structure of magnesium boride, MgB_2. *J. Am. Chem. Soc.* **1953**, *76*, 5. [CrossRef]
2. Nagamatsu, J.; Nakagawa, N.; Muranaka, T.; Zenitani, Y.; Akimitsu, J. Superconductivity at 39 K in magnesium diboride. *Nature* **2001**, *410*, 63. [CrossRef] [PubMed]
3. Bud'ko, S.L.; Lapertot, G.; Petrovic, C.; Cunningham, C.E.; Anderson, N.; Canfield, P.C. Boron Isotope Effect in Superconducting MgB_2. *Phys. Rev. Lett.* **2001**, *86*, 1877. [CrossRef] [PubMed]
4. Pickett, W. Superconductivity: 2D Physics, Unknown Mechanisms, Current Puzzles. *Emerg. Phenom. Correl. Matter Lect. Notes Autumn School Corr. Electron.* **2013**, *2013*, 45.
5. Choi, H.J.; Roundy, D.; Sun, H.; Cohen, M.L.; Steven Louie, G. The origin of the anomalous superconducting properties of MgB_2. *Nature* **2002**, *418*, 758. [CrossRef]
6. Kortus, J.; Mazin, I.I.; Belaachenko, K.D.; Antropov, V.P.; Boyer, L.L. Superconductivity of Metallic Boron in MgB_2. *Phys. Rev. Lett.* **2001**, *86*, 4656. [CrossRef]
7. An, J.M.; Pickett, W.E. Superconductivity of MgB_2: Covalent Bonds Driven Metallic. *Phys. Rev. Lett.* **2001**, *86*, 4366. [CrossRef] [PubMed]
8. Liu, A.Y.; Mazin, I.I.; Kortus, J. Beyond Eliashberg Superconductivity in MgB_2: Anharmonicity, Two-Phonon Scattering, and Multiple Gaps. *Phys. Rev. Lett.* **2001**, *87*, 087005. [CrossRef] [PubMed]
9. Kong, Y.; Dolgov, O.V.; Jepsen, O.; Andersen, O.K. Electron-phonon interaction in the normal and superconducting states of MgB_2. *Phys. Rev. B* **2001**, *64*, 020501. [CrossRef]
10. Bohnen, K.-P.; Heid, R.; Renker, B. Phonon Dispersion and Electron-Phonon Coupling in MgB_2 and AlB_2. *Phys. Rev. Lett.* **2001**, *86*, 5771. [CrossRef] [PubMed]
11. Kunc, K.; Loa, I.; Syassen, K.; Kremer, R.K.; Ahn, K. MgB_2 under pressure: phonon calculations, Raman spectroscopy, and optical reflectance. *J. Phys. Condens. Matter* **2001**, *13*, 9945. [CrossRef]
12. Choi, H.J.; Roundy, D.; Sun, H.; Cohen, M.L.; Louie, S.G. First-principles calculation of the superconducting transition in MgB2 within the anisotropic Eliashberg formalism. *Phys. Rev. B* **2002**, *66*, 020513. [CrossRef]
13. Canfield, P.C.; Crabtree, G.W. Magnesium Diboride: Better Late than Never. *Phys. Today* **2003**, *56*, 34. [CrossRef]
14. Novoselov, K.S.; Geim, A.K.; Morozov, S.V.; Jiang, D.; Zhang, Y.; Dubonos, S.V.; Grigorieva, I.V.; Firsov, A.A. Electric Field Effect in Atomically Thin Carbon Films. *Science* **2004**, *306*, 666–669. [CrossRef]
15. Katsnelson, M.I.; Novoselov, K.S.; Geim, A.K. Chiral tunnelling and the Klein paradox in graphene. *Nat. Phys.* **2006**, *2*, 620–625. [CrossRef]
16. Katsnelson, M.I. Zitterbewegung, chirality, and minimal conductivity in graphene. *Eur. Phys. J. B* **2006**, *51*, 157–160. [CrossRef]
17. Rusin, T.M.; Zawadzki, W. Zitterbewegung of electrons in graphene in a magnetic field. *Phys. Rev. B* **2008**, *78*, 125419. [CrossRef]
18. Pisana, S.; Lazzeri, M.; Casiraghi, C.; Novoselov, K.S.; Geim, A.K.; Ferrari, A.C.; Mauri, F. Breakdown of the adiabatic Born-Oppenheimer approximation in graphene. *Nat. Mater.* **2007**, *6*, 198–201. [CrossRef] [PubMed]
19. Piscanec, S.; Lazzeri, M.; Mauri, F.; Ferrari, A.C.; Robertson, J. Kohn Anomalies and Electron-Phonon Interactions in Graphite. *Phys. Rev. Lett.* **2004**, *93*, 85503. [CrossRef]
20. Novoselov, K.S.; Jiang, Z.; Zhang, Y.; Morozov, S.V.; Stormer, H.L.; Zeitler, U.; Maan, J.C.; Boebinger, G.S.; Kim, P.; Geim, A.K. Room-temperature quantum Hall effect in graphene. *Science* **2007**, *315*, 1379. [CrossRef]
21. Zhou, S.Y.; Gweon, G.-H.; Fedorov, A.V.; First, P.N.; de Heer, W.A.; Lee, D.-H.; Guinea, F.; Castro Neto, A.H.; Lanzara, A.; et al. Substrate-induced bandgap opening in epitaxial graphene. *Nat. Mater.* **2007**, *6*, 770–775. [CrossRef]
22. Zhang, Y.; Tan, Y.; Stormer, H.L.; Kim, P. Experimental observation of the quantum Hall effect and Berry's phase in graphene. *Nature* **2005**, *438*, 201–204. [CrossRef]
23. Bekaert, J.; Aperis, A.; Partoens, B. Oppeneer, P.M.; Milošević, M.V. Evolution of multigap superconductivity in the atomically thin limit: Strain-enhanced three-gap superconductivity in monolayer MgB2 *Phys. Rev. B* **2017**, *96*, 094510.
24. Morshedloo, T.; Roknabadi, M.R.; Behdani, M. First-principles study of the superconductivity in MgB_2 bulk and in its bilayer thin film based on electron–phonon coupling. *Physica C* **2015**, *509*. [CrossRef]

25. Calandra, M.; Profeta, G.; Mauri, F. Superconductivity in metal-coated graphene. *Phys. Status Solidi (b)* **2012**, *249*, 2544. [CrossRef]
26. Ludbrook, B.M.; Levy, G.; Nigge, P.; Zonno, M.; Schneider, M.; Dvorak, D.J.; Veenstra, C.N.; Zhdanovich, S.; Wong, D.; Dosanjh, P.; et al. Evidence for superconductivity in Li-decorated monolayer graphene. *Proc. Natl. Acad. Sci. USA* **2015**, *112*, 11795. [CrossRef] [PubMed]
27. Profeta, G.; Calandra, M.; Mauri, F. Phonon-mediated superconductivity in graphene by lithium deposition. *Nat. Phys.* **2012**, *8*, 131–134. [CrossRef]
28. Pešić, J.; Gajić, R.; Hingerl, K.; Belić, M. Strain-enhanced superconductivity in Li-doped graphene. *Europhys. Lett.* **2014**, *108*, 67005. [CrossRef]
29. Szczesniak, D.; Durajski, A.P.; Szczesniak, R. Influence of lithium doping on the thermodynamic properties of graphene based superconductors. *J. Phys-Condens. Mat.* **2014**, *26*, 255701. [CrossRef]
30. Durajski, A.; Skoczylas, K.; Szczesniak, R. Superconductivity in bilayer graphene intercalated with alkali and alkaline earth metals. *Phys. Chem. Chem. Phys.* **2019**, *21*, 5925. [CrossRef] [PubMed]
31. Zheng, J.-J.; Margine, E.R. First-principles calculations of the superconducting properties in Li-decorated monolayer graphene within the anisotropic Migdal-Eliashberg formalism. *Phys. Rev. B* **2016**, *94*, 064509. [CrossRef]
32. Margine, E.R.; Lambert, H.; Giustino, F. Electron-phonon interaction and pairing mechanism in superconducting Ca-intercalated bilayer graphene. *Sci. Rep.* **2016**, *6*, 21414. [CrossRef]
33. Mazin, I.I.; Antropov, V.P. Electronic structure, electron–phonon coupling, and multiband effects in MgB_2. *Phys. C Supercond.* **2003**, *385*, 49–65. [CrossRef]
34. Giannozzi, P.; Andreussi, O.; Brumme, T.; Bunau, O.; Buongiorno, N.M.; Calandra, M.; Car, R.; Cavazzoni, C.; Ceresoli, D.; Cococcioni, M. et al. Quantum espresso: A modular and open-source software project for quantum simulations of materials. *J. Phys. Condensed Matter* **2009**, *21*, 395502. [CrossRef] [PubMed]
35. Lu, N.; Guo, H.; Zhuo, Z.; Wang, L.; Wu, X.; Zeng, X.C. Twisted MX_2/MoS_2 heterobilayers: effect of van der Waals interaction on the electronic structure. *Nanoscale* **2017**, *9*, 19131–19138. [CrossRef] [PubMed]
36. Soler, J.M.; Artacho, E.; Gale, J.D.; García, A.; Junquera, J.; Ordejón, P.; Sánchez-Portal, D. The SIESTA method for ab initio order-N materials simulation. *J. Phys. Condens. Matter.* **2002**, *14*, 2745. [CrossRef]
37. Perdew, J.P.; Burke, K.; Ernzerhof, M. Generalized Gradient Approximation Made Simple. *Phys. Rev. Lett.* **1996**, *77*, 3865–3868. [CrossRef]
38. Troullier, N.; Martins, J.L. Efficient pseudopotentials for plane-wave calculations. *Phys. Rev. B* **1991**, *43*, 1993–2006. [CrossRef]
39. Golesorkhtabar, R.; Pavone, P.; Spitaler, J.; Puschnig, P.; Draxl, C.ElaStic: A tool for calculating second-order elastic constants from first principles. *Comput. Phys. Commun.* **2013**, *184*, 1861–1873. [CrossRef]
40. Nosé, S. A unified formulation of the constant temperature molecular dynamics methods. *J. Chem. Phys.* **1984**, *81*, 511. [CrossRef]
41. Lindemann, F.A. The calculation of molecular vibration frequencies. *Phys. Z.* **1910**, *11*, 609.
42. Andrew, R.C.; Mapasha, R.E.; Ukpong, A.M.; Chetty, N. Mechanical properties of graphene and boronitrene. *Phys. Rev. B* **2012**, *85*, 125428. [CrossRef]
43. Zhang, Z.; Yang, Y.; Penev, E.S.; Yakobson, B.I. Elasticity, Flexibility, and Ideal Strength of Borophenes. *Adv. Func. Mater.* **2017**, *27*, 1605059. [CrossRef]
44. Zhong, H.; Huang, K.; Yu, G.; Yuan, S. Electronic and mechanical properties of few-layer borophene. *Phys. Rev. B* **2018**, *98*, 054104. [CrossRef]
45. Mannix, A.J.; Zhou, X.F.; Kiraly, B.; Wood, J.D.; Alducin, D.; Myers, B.D.; Liu, X.; Fisher, B.L.; Santiago, U.; Guest, J.R.; et al. Synthesis of borophenes: Anisotropic, two-dimensional boron polymorphs. *Science* **2015**, *350*, 1513–1516. [CrossRef]
46. Wang, H.; Li, Q.; Gao, Y.; Miao, F.; Zhou, X.-F.; Wan, X.G. Strain effects on borophene: Ideal strength, negative Possion's ratio and phonon instability. *New J. Phys.* **2016**, *18*, 073016. [CrossRef]
47. De la Pena-Seaman, O.; de Cross, R.; Heid, R.; Bohnen, K.-P. Effects of Al and C doping on the electronic structure and phonon renormalization in MgB_2. *Phys. Rev. B* **2009**, *79*, 134523. [CrossRef]
48. Ponce, S.; Margine E.R., Verdi, C.; Giustino, F. EPW: Electron-phonon coupling, transport and superconducting properties using maximally localized Wannier functions. *Comp. Phys. Commun.* **2016**, *209*, 116–133. [CrossRef]

49. Margine, E.R.; Giustino, F. Anisotropic Migdal-Eliashberg theory using Wannier functions. *Phys. Rev. B* **2013**, *87*, 024505. [CrossRef]
50. Damljanovic, V.; Gajic, R. Existence of Dirac cones in the Brillouin zone of diperiodic atomic crystals according to group theory. *J. Phys. Condens. Matter* **2016**, *28*, 085502. [CrossRef]
51. Damljanovic, V.; Gajic, R. Addendum to 'Existence of Dirac cones in the Brillouin zone of diperiodic atomic crystals according to group theory'. *J. Phys. Condens. Matter* **2016**, *28*, 439401. [CrossRef]
52. Poulet, H.; Mathieu, J.P. *Vibration Spectra and Symmetry of Crystals*; Gordon and Breach: New York, NY, USA, 1976.
53. Szalowski, K. Critical temperature of MgB_2 ultrathin superconducting films: BCS model calculations in the tight-binding approximation. *Phys. Rev. B* **2006**, *74*, 094501. [CrossRef]
54. Zhang, C.; Wang, Y.; Wang, D.; Zhang, Y.; Liu, Z.-H.; Feng, Q.-R.; Gan, Z.-Z. Suppression of superconductivity in epitaxial MgB2 ultrathin films. *J. Appl. Phys.* **2013**, *114*, 023903. [CrossRef]
55. Ao, B.; Zhang, Z.; Tang, T.; Zhao, Y. Potential enhancement of superconductivity in MgB_2 nanosheets: First-principles calculations. *Chem. Phys. Lett.* **2014**, *591*, 185–188. [CrossRef]
56. Romero-Bermudez, A.; Garcıa-Garcıa, A.M. Shape resonances and shell effects in thin-film multiband superconductors. *Phys. Rev. B* **2014**, *89*, 024510. [CrossRef]
57. Romero-Bermudez, A.; Garcıa-Garcıa, A.M. Size effects in superconducting thin films coupled to a substrate. *Phys. Rev. B* **2014**, *89*, 064508. [CrossRef]
58. Acharya, N.; Wolak, M.A.; Cunnane, D.P.; Karasik, B.S.; Xi, X.X. MgB2 ultrathin films fabricated by hybrid physical chemical vapor deposition and ion milling. *APL Mater.* **2016**, *4*, 086114. [CrossRef]
59. Valentinis, D.; van der Marel, D.; Berthod, C. Rise and fall of shape resonances in thin films of BCS superconductors. *Phys. Rev. B* **2016**, *94*, 054516. [CrossRef]
60. Narlikar, A.V. Small Superconductors: Introduction. In *The Oxford Handbook of Small Superconductors*, 1st ed.; Narlikar, A.V., Ed.; Oxford University Press: Oxford, UK, 2017.
61. Gariglio, S.; Scheurer, M.; Schmalian, J.; Monteiro, A.M.R.V.L.; Goswami, S.; Caviglia, A. Surface and Interface Superconductivity. In *The Oxford Handbook of Small Superconductors*, 1st ed.; Narlikar, A.V., Ed.; Oxford University Press: Oxford, UK, 2017.